

Université du Québec

Institut National de la Recherche Scientifique

Centre Énergie, Matériaux et Télécommunications

Palladium-Copper-Gold Alloys for the Separation of Hydrogen Gas

by

Bruno Manuel Honrado Guerreiro, M.Sc.

A thesis submitted for the achievement of the
degree of *Philosophiae doctor* (Ph.D.) in Energy and Materials Science

December 2015

Jury Members

President of the jury:	Prof. Andreas Ruediger (INRS-EMT)
Internal Examiner:	Prof. Lionel Roué (INRS-EMT)
External Examiner:	Prof. Pierre Bénard (UQTR)
External Examiner:	Prof. Sasha Omanovic (McGill University)
Director of Research:	Prof. Daniel Guay (INRS-EMT)

Abstract

The industrial applications of hydrogen gas have made this simple diatomic molecule an important worldwide commodity in the chemical, oil and even food sectors. Moreover, hydrogen gas is a promising energy carrier that aims the delivery of clean energy, bypassing the environmental problems created by carbon-based fuels. Hydrogen production is, however, still reliant on steam reforming of natural gas and coal gasification, despite the innumerable alternatives available. In order to introduce hydrogen in the energy market, hydrogen production costs need to be reduced, and more specifically, hydrogen purification needs to be simplified. In this regard, the use of dense palladium-based membranes for hydrogen purification are especially attractive, but their wide industrial application is impaired mostly by the high cost of palladium and by hydrogen sulfide poisoning. In the current work, the potential use of palladium-copper-gold alloys as membranes for the separation of hydrogen gas was tested.

PdCuAu alloys were first prepared by pulsed electrochemical co-deposition on a titanium substrate from $\text{Pd}(\text{NO}_3)_2$, $\text{Cu}(\text{NO}_3)_2$ and $\text{Au}(\text{OH})_3$ in HNO_3 0.35 M, over a wide composition range ([Pd] = 14-74 at.%, [Cu] = 2-82 at.%, [Au] = 0-66 at.%). All alloys had a single face centered cubic (fcc) phase and were less than 1000 nm thick. The deposits presented different morphologies that were dependent on the palladium content. For example, $\text{Pd}_{14.3}\text{Cu}_{82.1}\text{Au}_{3.6}$ alloy was composed of spherical structures, while $\text{Pd}_{74.3}\text{Cu}_{18.4}\text{Au}_{7.3}$ had a more needle-like structure. Phase transition from fcc to the more H_2 -permeable body-centered cubic (bcc) phase was achieved by a simple heat treatment of 4 hours under Ar at 400°C. The aforementioned transition was found to be composition dependent, occurring for alloys with $29.5 \leq \text{Pd} \leq 45.8$; $45.3 \leq \text{Cu} \leq 63.0$; and $0.0 \leq \text{Au} \leq 17.4$, with $[\text{Pd}] + [\text{Cu}] + [\text{Au}] = 100$. The hydrogen solubility of the fcc alloys was measured in NaOH 0.1M by an electrochemical method and was found to be maximum for pure Pd. Replacement of copper with gold resulted in an increase in solubility for alloys with palladium content between 27 and 54 at.%. At the same composition, the bcc phase showed a substantial reduction in solubility when compared with the fcc phase. For example the hydrogen solubility of the fcc alloy $\text{Pd}_{33}\text{Cu}_{50}\text{Au}_{17}$ was 10.2%, while that of the corresponding bcc alloy was 0.5%.

Magnetron co-sputtering was also used for the production of fcc PdCuAu alloys on titanium substrates. The thickness of the films was below 500 nm. Phase transition from fcc to bcc upon annealing occurred in conditions analogous to the ones observed with the electrodeposited samples. Copper segregated at the surface of the alloy during heat treatment, as evidenced by X-ray photoelectron spectroscopy and cyclic voltammetry. The hydrogen solubility of both fcc and bcc phases was investigated. In the case of the fcc phase, it was found that the hydrogen solubility, as measured by an electrochemical method in NaOH 0.1M, increased with the palladium content, being maximum for pure Pd. In general, annealing of the fcc phase resulted in lower solubility either because there was a change in the crystallographic structure to the bcc phase or because of the larger crystallites formed during heat treatment. Further studies with the bcc samples by electrochemical *in situ* X-ray diffraction in H₂SO₄ 0.1M revealed that hydrogen solubility increased from 0.5 to 2.1% when palladium content increased from 40.3 to 45.6 at%, while keeping [Au]=3.5 at.%. However, no effect of gold was observed for alloys with approximate palladium concentration, in contrast to what was observed with the electrodeposited samples with fcc phase. The hydrogen solubility of both fcc and bcc phase varied linearly with the palladium content, and the increased observed was similar in both phases (0.286 and 0.295 % per [Pd] at.%, for fcc and bcc phase, respectively). This is an indication that the palladium content is the main factor governing solubility in each phase.

Gas phase testing was performed on membranes prepared from PdCuAu ternary alloys and synthesized by mechanical alloying. Alloys with four different compositions were prepared, all with approximately the same palladium composition, and increased gold content, namely, Pd₃₉Cu₆₁, Pd₄₁Cu₅₆Au₃, Pd₄₀Cu₄₃Au₇, and Pd₃₉Cu₅₁Au₁₀. NaCl was used as the process control agent at 2 wt%. The as-milled fcc alloys were first heat treated for 5 h under Ar 5% H₂ at 400°C, which promoted in general full transition to the bcc phase, in accordance with their composition. Membrane preparation from the bcc alloys involved a series of steps such as powder pressing into pellets, sintering, cold rolling, heat treatment and polishing. The final thickness of the membranes was between 277 and 327 nm. Hydrogen permeability was then measured at 464°C between 30 and 60 psig H₂ pressure. Under these conditions, hydrogen permeability was found to be composition dependent and was highest for the alloy with composition Pd₄₀Cu₄₃Au₇ ($2.1 \times 10^{-8} \text{ mol} \cdot \text{m}^{-1} \cdot \text{s}^{-1} \cdot \text{Pa}^{-0.5}$) and lowest for the alloy Pd₃₉Cu₅₁Au₁₀ ($6.9 \times 10^{-9} \text{ mol} \cdot \text{m}^{-1} \cdot \text{s}^{-1} \cdot \text{Pa}^{-0.5}$), while the hydrogen permeability of a reference 250 μm commercial foil was $1.2 \times 10^{-8} \text{ mol} \cdot \text{m}^{-1} \cdot \text{s}^{-1} \cdot \text{Pa}^{-0.5}$. The

ideal selectivity of the membranes was higher than 130. The PdCuAu ternary alloy membrane with the highest permeability was further tested at different temperatures and in the presence of hydrogen sulfide. Between 358 and 464°C, the natural logarithm of the permeability followed an Arrhenius-like relationship with $1/T$, resulting in an activation energy of $10.0 \text{ kJ}\cdot\text{mol}^{-1}$, which was lower than the value for a pure Pd reference membrane ($21.9 \text{ kJ}\cdot\text{mol}^{-1}$). Ten minutes into the test with H_2S , H_2 flow decreased to zero, indicating the formation of a hydrogen impermeable layer on the surface. Consequently, gold did not provide any extra resistance to H_2S poisoning under the tested conditions. H_2 flow resumed with time, however, post-testing SEM analysis revealed that the formation of pores had taken place. XPS analysis confirmed the presence of multiple sulfur-containing species, such as, Na_2S , $\text{Na}_2\text{S}_2\text{O}_3$, Na_2SO_3 , Cu_2S , CuS and CuSO_4 . Sulfur compounds with higher oxidation states were probably formed after H_2S testing during storage of the membrane under air.

Bruno Guerreiro

Student

Daniel Guay

Director of Research

Acknowledgements

I am especially grateful to my advisor Prof. Daniel Guay. This work would not had been possible without his support, generosity, encouragement and professionalism. But most importantly I am grateful for his enthusiasm not only towards science but also in life, and his exceptional empathy towards the well-being of those around him.

Over the four years that lasted this project, the periodical work meetings helped to enrich it with new ideas, not only from Prof. Daniel Guay but also from all the team involved, namely Prof. Lionel Roué, Julie Gaudet, Manuel Martin, Jules Galipaud and Jacques Tosques. I am also thankful for the teachings (and patience!) of Christophe Chabanier. Furthermore, I would like to thank A. Korinek for his work with the TEM images.

Many people accompanied me at the INRS, with whom I learned and laughed, namely Sébastien Garbarino, Régis Imbeault, Esen Sokullu, Denis Ferachou, Claudie Roy, Nicholas Sacré, Erwan Bertin, Teresa Simão, and many others.

These four years in Québec were made more special with the company of Lucie Côté and Luc Bergeron, who have been like a true family.

And also to my family back in Portugal, my sister, my mother and my father, I am very grateful for their support and love, in every step in life.

Finally, and most importantly, I would like to dedicate this work to the most important person in my life, Maria João; without her everything would be infinitely less complete.

Table of Contents

Abstract	I
Acknowledgements	IV
Table of Contents	V
List of Figures	IX
List of Tables	XVIII
1. Introduction.....	1
1.1. The role of hydrogen in the industrialized world	1
1.2. Hydrogen production methods	2
1.2.1. Steam reforming of natural gas and related technologies.....	3
1.2.2. Gasification technologies (coal and biomass).....	4
1.2.3. Water electrolysis and other water splitting-based methods	5
1.2.4. Biological hydrogen production.....	6
1.3. Hydrogen purification processes	7
1.3.1. Pressure swing adsorption and cryogenic distillation	7
1.3.2. Membrane Technology.....	7
1.4. Objectives of the work	9
1.5. Structure of the thesis.....	10
1.6. References	11
2. Dense palladium based metallic membranes for the separation of hydrogen gas	15
2.1. Introduction	15
2.2. Hydrogen diffusion and permeability in Pd-dense metallic membranes	16

2.3. Hydrogen solubility in palladium	24
2.4. Palladium alloys literature review	27
2.4.1. PdCu and PdAu binary alloys	27
2.4.2. PdCuAu ternary alloys.....	35
2.5. Conclusions and perspectives.....	36
2.6. References	37
3. Synthesis and characterization techniques	46
3.1. Synthesis of PdCuAu ternary alloys	46
Pd, Cu, Au metallic targets.....	46
Pd, Cu, Au metallic powders	46
3.1.1. Preparation of PdCuAu films by electrodeposition.....	47
3.1.2. Preparation of PdCuAu films by magnetron sputter deposition	50
3.1.3. Preparation of PdCuAu bulk alloys by mechanical alloying.....	52
3.1.4. Preparation of PdCuAu membranes for gas phase measurements.....	53
3.2. Physical-chemical characterization	54
3.2.1. X-Ray Diffraction (XRD).....	54
3.2.2. Scanning Electron Microscopy (SEM) and Energy Dispersive X-ray spectroscopy (EDX).....	58
3.2.3. X-ray Photoelectron Spectroscopy (XPS)	59
3.2.4. Transmission Electron Microscopy (TEM) and EELS	60
3.2.5. Electrochemical techniques	61
3.2.6. Mass of the deposits prepared by electro- or sputter deposition.....	63
3.2.7. Gas chromatography (GC).....	64
3.3. Measurement of hydrogen related properties	64

3.3.1. Electrochemical method for the measurement of hydrogen solubility.....	65
3.3.2. Electrochemical <i>in situ</i> X-ray diffraction analysis for the measurement of hydrogen solubility (E <i>in situ</i> XRD)	66
3.3.3. Gas phase method for the measurement of hydrogen permeability	70
3.4. References	74
4. Hydrogen solubility in PdCuAu alloy thin films prepared by electrodeposition	80
4.1. Synthesis and characterization	80
4.1.1. Composition analysis by EDX.....	80
4.1.2. XRD characterization	82
4.1.3. Morphology analysis by SEM.....	87
4.1.4. Characterization of annealed samples	90
4.2. Hydrogen solubility measurements	94
4.3. Conclusion.....	101
4.4. References	102
5. Hydrogen solubility in PdCuAu alloy thin films prepared by sputter deposition	105
5.1. Characterization of the as-deposited samples	105
5.2. Characterization of the annealed samples	111
5.2.1. XRD analysis	111
5.2.2. CV analysis	116
5.2.3. XPS and EDX analyses	119
5.2.4. Conclusion	125
5.3. Hydrogen solubility measurements	128
5.3.1. Electrochemical measurements in NaOH 0.1M.....	128
5.3.2. Electrochemical <i>in situ</i> XRD measurements (E <i>in situ</i> XRD) in H ₂ SO ₄ 0.1M	130

5.4. Conclusions	135
5.5. References	135
6. Hydrogen permeability of PdCuAu membranes prepared from mechanical alloyed powders	138
6.1. Synthesis and characterization of PdCuAu alloys	138
6.2. Membrane preparation from ball milled powders and characterization	143
6.2.1. Preparation method.....	143
6.2.2. EDX/SEM analysis.....	144
6.2.3. XRD analysis	147
6.2.4. Conclusions.....	153
6.3. Permeability measurements.....	153
6.3.1. Single gas experiments	153
6.3.2. H ₂ permeability in the presence of H ₂ S	169
6.4. Conclusions	185
6.5. References	186
7. Conclusions and Future work	192
7.1. Conclusions	192
7.2. Future Work	193
7.3. References	194
A1. Résumé: Alliages de Palladium-Cuivre-Or pour la Purification de l'Hydrogène	196

List of Figures

Figure 2. 1 – Schematic illustration of the mechanism of hydrogen permeation through a porous membrane (denoted PM, on the left) and a dense metallic membrane (right). The latter is referred to as the solution-diffusion mechanism and is composed of 5 steps: I – H ₂ adsorption; II – H ₂ dissociation into atomic hydrogen; III – diffusion; IV – atomic H recombination; and V) H ₂ desorption.	16
Figure 2. 2 – Boundary conditions used in the integration of Fick’s law of diffusion. The concentration gradient within the membrane is considered linear.....	18
Figure 2. 3 – Permeability vs. reciprocal temperature for bcc (Nb, V, Ta and Fe) and fcc (Pd, Ni, Cu and Pt) metals. The values were calculated from the data compiled by S.A. Steward [11]. ...	23
Figure 2. 4 – Pressure-composition-temperature phase diagram of the palladium-hydrogen system (adapted from [13, 15, 16]).....	25
Figure 2. 5 – Hydrogen solubility given by H/M ratios for PdCu [27] and PdAu [31] alloys. All measurements are made at 25°C and atmospheric pressure in H ₂ -stirred aqueous solutions.	28
Figure 2. 6 – Hydrogen permeability for PdCu and PdAu at 75 psig upstream pure hydrogen pressure as a function of the palladium content of the alloy. The measurements were made at 350°C [5]......	29
Figure 2. 7 – Variation of the permeability ratio in function of the reaction time at 350°C and at 75 psig H ₂ with 4 ppm H ₂ S; 25.4 μm thick foils were used. Time zero (t=0) is the time immediately after introducing the H ₂ S mixture into the system.	30
Figure 3. 1 – Unassembled electrodeposition cell (left) and fully functional cell (right, adapted from[12]).	49
Figure 3. 2 – Flow diagram representing the preparation of PdCuAu membranes from ball milled powders.	53

Figure 3. 3 – Variation of the potential with time (A) and variation of the current with the potential (B).	62
Figure 3. 4 – Experimental set-up for <i>E in situ</i> XRD A – general view, B – top view of cell; C – working electrode.....	68
Figure 3. 5 – Schematic representation of the experimental setup used for hydrogen permeability measurement. The retentate and the permeate sides of the permeation chamber are represented, as well as the cylinder with the gas mixture, the pressure gauges (P) and mass flow meters (MF). The arrows indicate the direction of gas flow.	71
Figure 3. 6 – Gas panel evidencing the mass flow meters (yellow dotted square on the right) and the pressure gauges (white dotted squares).	72
Figure 3. 7 – Furnace (A) and permeation chamber unassembled (B) and assembled (C). The disk at the center of panel B is the membrane (1.1 cm diameter). On each side of the membrane, the stainless steel gaskets that were used can be seen.	73
Figure 4. 1 – Variation of the relative composition of the film <i>vs</i> the relative composition of the bath: in (A) Pd, (B) Cu and (C) Au. The composition of the films was determined by EDX.	81
Figure 4. 2 – XRD patterns of CuPdAu ternary alloy thin films prepared by pulsed electrodeposition on Ti substrates. Six different compositions are shown and are organized from the highest (top curve) to the lowest Au content (bottom curve). The composition of the alloys are (A) Pd _{50.4} Cu _{9.1} Au _{40.6} , (B) Pd _{43.5} Cu _{22.5} Au ₃₁ , (C) Pd _{47.9} Cu _{25.8} Au _{26.3} , (D) Pd _{63.3} Cu _{20.2} Au _{16.5} , (E) Pd _{38.2} Cu _{57.1} Au _{4.7} , and (F) Pd _{31.2} Cu _{67.8} Au ₁ . The peak position of the pure elements is shown at the bottom for reference.	82
Figure 4. 3 – Ternary contour plot showing the variation of the experimentally determined lattice parameter (maximum standard error of 0.01Å) with the film composition.	84
Figure 4. 4 – Variation of the experimentally measured lattice parameter with respect to the lattice parameter expected from the composition of the film assuming that Vegard’s law holds true. The Gaussian shaped curve that is superimposed on the one-to-one straight line is centered at 3.82 Å and has a half width at half maximum of 0.10 Å.....	85

Figure 4. 5 – Crystallite size as a function of gold composition for PdCuAu alloys over the entire composition range (A,) and for gold concentrations above 45 at% (B,).....	87
Figure 4. 6 – SEM micrographs of PdCuAu thin films that are arranged in order of increasingly higher Pd content. In (A) Pd _{14.3} Cu _{82.1} Au _{3.6} , (B) Pd _{38.2} Cu _{57.1} Au _{4.7} , (C) Pd _{56.2} Cu _{19.2} Au _{24.6} , (D) Pd _{66.1} Cu _{7.8} Au _{26.2} , (E) Pd _{74.3} Cu _{18.4} Au _{7.3} , and (F) Pd ₁₀₀ Cu _{0.0} Au _{0.0}	88
Figure 4. 7 – High magnification micrographs (30,000 times and 100,000 times in the insets) of a pure palladium film electrodeposited on a titanium substrate.	89
Figure 4. 8 – Comparison of XRD patterns of film with composition Pd _{35.6} Cu _{60.5} Au _{3.9} (A) before (fcc phase) and (B) after (bcc phase) heat treatment at 400°C.	90
Figure 4. 9 – Ternary contour plot showing the variation of the experimentally determined lattice parameter for the bcc phase region with the film composition. The white squares are the EDX compositions of the samples used to construct this plot.	91
Figure 4. 10 – Ternary diagram showing final crystallographic phases after 4 hour-heat treatment at 400°C and under Ar. EDX compositions are used. FCC – face-centered cubic; BCC – body-centered cubic; TET – tetragonal; CUB – simple cubic.....	92
Figure 4. 11 – SEM micrographs of Pd _{38.8} Cu _{56.2} Au _{5.0} thin film (A) before (fcc phase) and (B) after heat-treatment at 400 °C (bcc phase).	93
Figure 4. 12 – Variation of the reduction and oxidation times: 2, 3, 5 and 7 minutes. Each time was applied twice.	95
Figure 4. 13 – Variation of the hydrogen solubility with the applied potential for PdCuAu alloys at different compositions. All measurements were performed in NaOH 0.1M.	96
Figure 4. 14 – Variation of the hydrogen solubility of PdCuAu alloys with the palladium content. All films are made of a fcc phase with a lattice parameter (3.885 ± 0.005) Å. The data taken from reference [22] is also shown for comparison. The copper and gold contents are shown in at.% in brackets.....	97
Figure 4. 15 – Effect of copper and gold on the hydrogen solubility of PdCuAu alloys at constant palladium content.	99

Figure 4. 16 – Variation of the hydrogen solubility with the applied potential for PdCuAu alloy in the fcc and in the bcc phase. All measurements were performed in NaOH 0.1M..... 100

Figure 5. 1 – EDX film composition as a function of the power operating on the targets. On panel A, the film composition is shown as a function of the power on the Cu target. The power of the palladium target was either 120 or 340 W, while that on the gold target was 80 W. On panel B, the film composition is shown as a function of the power on the Pd target. The power on the Cu and Au targets was 500 and 80 W, respectively..... 106

Figure 5. 2 – Diffractograms of representative samples showing that an alloy was formed and that peak shift occurs with changes in composition. The palladium content decreases from top to bottom and the composition of the samples is: (A) – Pd_{87.2}Cu_{8.2}Au_{4.6}; (B) – Pd_{76.2}Cu_{19.7}Au_{4.1}; (C) – Pd_{67.3}Cu_{29.1}Au_{3.6}; (D) – Pd_{59.1}Cu_{37.6}Au_{3.3}; (E) – Pd_{43.9}Cu_{52.4}Au_{3.7}. 107

Figure 5. 3 – Comparison between the experimental lattice parameter and the lattice parameter calculated considering Vegard’s law. 108

Figure 5. 4 – Elemental maps of Pd M45-edge, Cu L23-edge and Au M45-edge obtained with EELS at a vertical cross section of Pd_{50.8}Cu_{46.0}Au_{3.2}. The relative signals are shown here. 109

Figure 5. 5 – XRD diffractograms of alloy with composition Pd_{32.2}Cu_{63.3}Au_{4.5} taken before (A) and after (B) annealing at 400°C for 4h under Ar. The as-deposited sample shows the characteristic fcc phase peaks while a single bcc phase is observed after annealing..... 111

Figure 5. 6 – In (A), XRD patterns of fcc Pd_{67.3}Cu_{29.1}Au_{3.7} after annealing at 400°C during different times (0, 4, 8 and 48 hours). Only the region between 2θ = 66 and 73° is shown for clarity. In (B), variation of the full width at half maximum (FWHM) and peak position as a function of the annealing time. 112

Figure 5. 7 – Williamson-Hall plots for the as-deposited ternary alloy with composition Pd_{67.3}Cu_{29.1}Au_{3.7}. Left – uniform microstrain in all crystallographic directions was considered (Cauchy-Cauchy deconvolution; equation 3.7); center – anisotropic microstrain was considered (Cauchy-Cauchy deconvolution; equation 3.9); right – anisotropic microstrain was considered with Gauss-Cauchy deconvolution (equation 5.2)..... 114

Figure 5. 8 – Lattice parameter, crystallite size and uniform stress calculated for samples annealed 0, 4 and 8 hours. The crystallite size and uniform stress were calculated using equation 5.2. ...115

Figure 5. 9 – Cyclic voltammograms ($50 \text{ mV} \cdot \text{s}^{-1}$) taken before (black line; 2nd cycle) and after (red dashed line; 10th cycle) measuring the hydrogen solubility in NaOH 0.1M. The samples shown were all prepared under the same experimental conditions, except the annealing time at 400°C under Ar, which varied from 0, 4, 8 or 48 h. All samples have fcc crystallographic structure and have the same starting composition $\text{Pd}_{67.3}\text{Cu}_{29.1}\text{Au}_{3.7}$ 116

Figure 5. 10 – Cyclic voltammograms ($50 \text{ mV} \cdot \text{s}^{-1}$) taken before (black line) and after (red dashed line) measuring the hydrogen solubility in NaOH 0.1M for samples with composition $\text{Pd}_{43.9}\text{Cu}_{52.4}\text{Au}_{3.7}$. Results for both pristine (0 h) and annealed (4 h) samples are shown. Samples have fcc and bcc structure before and after annealing, respectively. 118

Figure 5. 11 – Variation of the Pd and Cu content as a function of heat treatment. Composition was determined by EDX and XPS. Two different ternary PdCuAu alloys were investigated alloy 1 ($\text{Pd}_{50.8}\text{Cu}_{46.0}\text{Au}_{3.2}$), on the left, with no heat treatment; and alloy 2 ($\text{Pd}_{67.3}\text{Cu}_{29.1}\text{Au}_{3.6}$), on the right, annealed at 400 °C during 48 hours. 119

Figure 5. 12 – Copper $2p_{3/2}$ high resolution spectra for alloy 1 ($\text{Pd}_{50.8}\text{Cu}_{46.0}\text{Au}_{3.2}$; panels 1, 2 and 3), alloy 2 ($\text{Pd}_{67.3}\text{Cu}_{29.1}\text{Au}_{3.6}$ panels 4 and 5), and copper film on silicon substrate (panel 6). Alloy 1 was not heat treated while alloy 2 was annealed for 48 hours at 400°C under Ar..... 121

Figure 5. 13 – Comparison between the copper content measured by EDX before and after hydrogen solubility measurements in NaOH 0.1M (for the fcc phase) or 0.1M H_2SO_4 (bcc phase).The dashed line represents the equality, when the final and initial concentrations are the same..... 125

Figure 5. 14 – Variation of the lattice parameter of the bcc phase with respect to the palladium content taken after the hydrogen solubility measurements. A comparison is performed between the experimental values for PdCuAu alloys and literature values for PdCu [16]. Dashed and dotted lines represent the best linear regression to each set of data ($\text{PdCuAu}_{3.5}$ and PdCu alloys, respectively)..... 126

Figure 5. 15 – Hydrogen solubility of the fcc phase in function of the (A) lattice parameter and (B) palladium content. The results are for both as-deposited samples and for samples annealed at 400°C during different times.	129
Figure 5. 16 – E <i>in situ</i> XRD for bcc alloy with composition Pd _{40.4} Cu _{56.1} Au _{3.5} showing the diffractograms recorded before applying any potential (OCP), during charging (-600 mV) and during discharging (+300 mV). Two different 2θ regions (37-45 and 75-81°) are shown.....	131
Figure 5. 17 – Peak fitting of Ti (112) peak and (221) bcc alloy peak collected at open circuit potential before applying any potential. The composition of the alloy is Pd _{40.4} Cu _{56.1} Au _{3.5}	132
Figure 5. 18 – Hydrogen solubility of the bcc phase in function of the lattice parameter (A) and the palladium content (B). Gold content of the samples is given aside the data points in at.%..	133
Figure 5. 19 – Comparison between the hydrogen solubility of the bcc phase with fcc phase in function of the palladium content. Dashed lines represent the best linear fit for each set of data. Values aside the data points represent the gold content of the alloy.	134
Figure 6. 1 – Micrographs of A) Pd ₄₀ Cu ₅₃ Au ₇ (synthesis 3 in Table 6.1) and B) pure Pd, both at 600 times magnification, after 18 hours of ball milling. Grains of NaCl are clearly visible in micrograph B.	139
Figure 6. 2 – Diffractograms of the as-milled powders (panel 1) and after 5-hour heat treatment (panel 2) arranged by increasing gold content from 0% (A) to 10% (D) (A – Pd ₃₉ Cu ₆₁ ; B – Pd ₄₁ Cu ₅₆ Au ₃ ; C – Pd ₄₀ Cu ₄₃ Au ₇ ; D – Pd ₃₉ Cu ₅₁ Au ₁₀).....	140
Figure 6. 3 – Experimental lattice parameter as a function of gold content for as-milled powders (A) and annealed samples (B).....	141
Figure 6. 4 – Comparison between the experimental and Vegard’s lattice parameter for the mechanically alloyed powders.....	142
Figure 6. 5 – Method for the production of PdCuAu membranes from mechanically alloyed PdCuAu powder (same as Fig. 3.2).	143

Figure 6. 6 – EDX mapping of the membranes’ surface. Each row represents one different composition (A – Pd₄₀Cu₆₀; B – Pd₄₀Cu₅₇Au₃; C – Pd₃₉Cu₅₃Au₇; D – Pd₄₀Cu₄₉Au₁₁) and each column represents one element (from left to right, Pd L α ₁, Cu K α ₁ and Au L α ₁). 145

Figure 6. 7 – SEM micrographs at 500 times magnification of membranes after the second heat treatment (step 6 in Fig. 6.5); A – Pd₄₀Cu₆₀; B – Pd₄₀Cu₅₇Au₃; C – Pd₃₉Cu₅₃Au₇; D – Pd₄₀Cu₄₉Au₁₁. 146

Figure 6. 8 – SEM micrograph before (left) and after (center and right) polishing was performed. Membrane with composition Pd₃₉Cu₅₃Au₇ is shown as an example. 147

Figure 6. 9 – X-ray diffractogram of Pd₄₀Cu₄₃Au₇ powder after the first heat treatment (step 2), and pellet after sintering (step 4), cold rolling (step 5) and after second heat treatment (step 6). The dotted line indicates the average peak center (42.8°) for all samples except the one that underwent cold rolling. The inset shows the diffratogram of the cold rolled sample between 38 and 59° in order to emphasize the presence of the fcc peaks. 148

Figure 6. 10 – X-ray diffractogram of Pd₄₀Cu₄₃Au₇ powder after ball milling (step 1), and of Pd₄₀Cu₄₃Au₇ pellet after cold rolling (step 5) and after second heat treatment (step 6). The latter was acquired in both Bragg-Brentano (curve in magenta) and in grazing incidence (GI) with $\theta=5^\circ$ (curve in green) configurations. The (111) and (200) fcc peaks are visible, as is also the (110) bcc peak. 149

Figure 6. 11 – Bragg-Brentano X-ray diffractograms of the membranes after the second heat treatment (step 6 in diagram of Fig. 6.5) arranged by increasing gold content from 0% (A) to 10% (D) (A – Pd₄₀Cu₆₀; B – Pd₄₀Cu₅₇Au₃; C – Pd₃₉Cu₅₃Au₇; D – Pd₄₀Cu₄₉Au₁₁)..... 151

Figure 6. 12 – Williamson-Hall analysis (equation 3.13) applied to PdCuAu alloys after ball milling (step 1) and after the second heat treatment (step 6). Results for the strain energy density (A) and the crystallite size (B) are shown. 152

Figure 6. 13 – Micrograph of membrane with composition Pd_{38.9}Cu_{54.5}Au_{6.6} that failed the He leak test after the H₂ permeation experiment. Regions A and B are shown in more detail in the insets. 154

Figure 6. 14 – Variation of H₂ flow with time at 30, 45 and 60 psig H₂ feed pressure and 464°C. The permeate side was not submitted to any pressure control and no sweeping gas was used.

Measurements were made with the following membranes: Pd 250 μm commercial foil form Alfa Aesar (A), a Pd pellet prepared from commercial Pd powder (B; 250 μm) and the four PdCuAu alloys prepared, Pd₄₀Cu₆₀Au₀ (C; 327 μm), Pd₄₀Cu₅₇Au₃ (D; 300 μm), Pd₄₀Cu₅₃Au₇ (E; 277 μm); Pd₄₀Cu₄₉Au₁₁ (F; 304 μm). 156

Figure 6. 15 – Hydrogen flux in function of the difference of the square root of pressure drop across the membrane at 464°C. The dotted lines represent the calculated linear regressions. All membranes showed 0.00 ml·min⁻¹ He flow before and after the H₂ testing. Measurements were made with the following membranes: Pd 250 μm commercial foil form Alfa Aesar (A), a Pd pellet prepared from commercial Pd powder (B; 250 μm) and the four PdCuAu alloys prepared, Pd₄₀Cu₆₀Au₀ (C; 327 μm), Pd₄₀Cu₅₇Au₃ (D; 300 μm), Pd₄₀Cu₅₃Au₇ (E; 277 μm); Pd₄₀Cu₄₉Au₁₁ (F; 304 μm). 158

Figure 6. 16 – Experimentally determined H₂ permeability of membranes prepared from the consolidation of PdCuAu mechanically alloyed powders (membranes C to F in Figs. 6.13 and 6.14 and table 6.1). Literature permeability values for PdCu alloys 25.4 foils μm [11] are also shown, along with indication of the crystallographic phase for the PdCu alloys (α - fcc phase; β - bcc phase) [1]. 162

Figure 6. 17 – H₂ permeability of the PdCuAu ternary alloy membranes at 464°C in function the gold content. As a reference, results for Pd foil and for a pellet prepared from Pd powder are also shown. 164

Figure 6. 18 – Variation of H₂ flow with time at 464°C. The H₂ feed pressure was constant at 45 psig for all experiments, except for sample A which was kept at 30, 45 and 60 psig for 2, 0.5 and 0.5 hours, respectively. The permeate side was not submitted to any pressure control and no sweeping gas was used. Measurements were made with the following membranes: Pd 250 μm commercial foil form Alfa Aesar (A), a Pd pellet prepared from commercial Pd powder (B; 250 μm) and the four PdCuAu alloys prepared, Pd₄₀Cu₆₀Au₀ (C; 327 μm), Pd₄₀Cu₅₇Au₃ (D; 300 μm), Pd₄₀Cu₅₃Au₇ (E; 277 μm); Pd₄₀Cu₄₉Au₁₁ (F; 304 μm). 165

Figure 6. 19 – Permeability vs. 1/T for Pd 250 μm foil from Alfa Aesar and Pd₄₀Cu₅₃Au₇ membrane. The dotted lines represent the best linear regression of the data, considering an Arrhenius-type relationship. 166

Figure 6. 20 – Variation of flow with time when the membranes are exposed to either pure H₂ or a mixture of H₂ and 941 ppm H₂S. Two different membranes were analyzed: Pd 250 μm foil from Alfa Aesar (left panel) and Pd₃₉Cu₅₄Au₇ membrane E-2 (right panel). Experiments were performed at 464°C. 169

Figure 6. 21 – Diffractograms of Pd 250 μm foil (panel 1) and membrane E-2 Pd₃₉Cu₅₄Au₇ (panel 2) after exposure to H₂S. Both retentate (panels A) and permeate (panels B) sides of the membrane were analyzed. 173

Figure 6. 22 – Grazing incidence X-ray diffractograms ($\theta = 5^\circ$) for membrane E-2 Pd₃₉Cu₅₄Au₇, after exposure to H₂S, for both retentate and permeate sides. A comparison is made with the pristine sample. 174

Figure 6. 23 – SEM micrographs for the Pd 250 μm foil (top) and membrane E-2 Pd₃₉Cu₅₄Au₇ (bottom). Both retentate (left) and permeate sides (right) of the membranes are shown. 176

Figure 6. 24 – Variation of composition as determined by EDX measurements for membrane E-2. The data were taken on both surfaces of the membrane and at various locations on the cross section: (1) surface of pristine sample; (2) surface of retentate upon exposure to H₂S treatment; (3) surface of permeate upon exposure to H₂S; (4) cross section close to retentate side; (5) middle of cross section; (6) cross section close to permeate side. 177

Figure 6. 25 – Pd, Cu, Au, Na and S concentration profile of membrane E-2 that was in contact with H₂S 941 ppm gas mixture. Analysis started at the retentate side of the membrane here referenced as 0 nm depth. Depth was estimated using equation 3.15. 180

Figure 6. 26 – Cu 2p_{3/2} high resolution spectra for membrane E-2 after being in contact with H₂S 941 ppm. Both sides of the membrane were analyzed and are compared with a pristine sample. Analyzes were performed without (panel 1) and with etching (panel 2). 181

Figure 6. 27 – S 2p high resolution spectra for membrane E-2 after being in contact with H₂S 941 ppm. Both sides of the membrane were analyzed. Analyzes were performed without (panel 1) and with etching (panel 2). 182

List of Tables

Table 2. 1 – Hydrogen permeability for different metals at 500°C.....	21
Table 2. 2 – Literature review of the hydrogen permeability of PdCu and PdAu alloys and the effect of hydrogen sulfide.....	31
Table 3. 1 – Comparison between the preparation methods used for the synthesis of PdCuAu alloys.	46
Table 3. 2 – Different ball milling conditions used to prepare the PdCuAu alloys.	53
Table 5. 1 – Binding energies (B.E.) and amount of reduced surface copper for samples shown in Fig. 5.12 and literature values for comparison.	123
Table 6. 1 – Nominal and EDX compositions for the 4 synthesis performed.	138
Table 6. 2 – Membranes’ properties including, composition, thickness, H ₂ and He permeability at 464°C, and ideal selectivity factors. H ₂ and He permeability is given in mol·m ⁻¹ ·s ⁻¹ ·Pa ^{-0.5}	160
Table 6. 3 – Pre-exponential factor and activation energy for the H ₂ permeation assuming that an Arrhenius-type relationship between the logarithm of the permeability and 1/T is valid. Both experimental results and literature values are shown. All values are calculated considering that the H ₂ permeability is a diffusion-limited process.	167
Table 6. 4 – Literature results for the effect of H ₂ S in the H ₂ permeability of Pd and Pd alloys.	170
Table 6. 5 – Binding energy and composition of membrane E-2 after being in contact with H ₂ S gas mixture. Analyses were made on the retentate and permeate sides of the membrane with and	

without etching. The results are compared to the pristine sample. (1) refers to the bulk EDX composition of the pristine sample, and reference values are from [42].178

Table 6. 6 – Published results of the S 2p binding energy for common sulfur compounds with copper or sodium.....183

1. Introduction

1.1. The role of hydrogen in the industrialized world

Hydrogen is the most abundant element in the universe. On Earth, at the surface of the globe, is the third most abundant element after oxygen and silicon [1]. Hydrogen is a colorless, tasteless and odorless gas with low solubility in liquid solvents, while being quite unreactive at room temperature. Hydrogen's chemical and physical properties have shaped its use in the modern society where it is seen as commodity with innumerable applications [2]. The largest application of hydrogen is, by far, in the chemical industry where the Haber-Bosch process for the production of ammonia is the most important. In this process, ammonia is prepared from the reaction of N_2 and H_2 at high temperatures and pressures (typically $400^\circ C$ and 200 atm) in the presence of iron catalysts. Apart from ammonia, other bulk chemicals are also prepared directly from hydrogen gas. Such is the case of methanol, which is obtained from the reaction of carbon monoxide and hydrogen in the presence of a cobalt catalyst. Hydrogen chloride can also be directly produced by reacting hydrogen with chloride. Smaller scale applications of hydrogen in the chemical industry include the production of metal hydrides and complex metal hydrides. Hydrogen is also present in the food industry where it is used in the nickel-catalyzed hydrogenation of vegetable oils to produce solid fats sold as margarines. Other domains of human activity that use hydrogen include: metallurgy (reduction of oxides to metals such as Mo and W), steelmaking (direct reduction of iron ore), space program (liquid fuel), welding and cutting (oxyhydrogen and atomic hydrogen torches) [1].

The greatest challenge for hydrogen in the future is its use as an energy carrier especially as a fuel in transportation [3, 4]. In fact, cars powered by hydrogen are already available on the market, and more and more powering stations are being built in Japan, Europe and North America. Consuming H_2 either in a fuel cell or in an internal combustion engine yields only water. It is the cleanliness of this fuel (zero production of CO_2 , if H_2 production from fossil fuels is combined with CO_2 sequestration technologies) that attracts attention of supporters of the called hydrogen economy, as a way to reduce anthropogenic-related CO_2 levels in the atmosphere [5]. However,

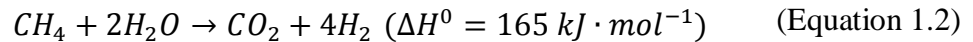
the success of this new venue for hydrogen will be dictated by the cost of its implementation. Bearing this in mind, it is crucial to lower the cost of hydrogen production and the efficiency of the methods used. In fact, 50-80% of the capital investment for the large scale production of H₂ is directed for separation/purification operations only [5]. This means that lowering the cost of the purification process will substantially decrease the final cost of the H₂ produced. This issue will be further discussed in section 1.3, after presenting different hydrogen production methods.

1.2. Hydrogen production methods

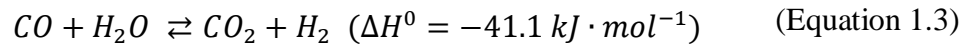
Different feedstocks are available for the production of H₂, namely, hydrocarbons (such as methane, the main constituent of natural gas), coal, water and biomass. The production method is chosen accordingly. For example, when producing hydrogen from hydrocarbons, steam reforming, partial oxidation and autothermal reforming methods can be used, while gasification processes are required for coal and biomass. Electrolysis is the method of choice when using water as the starting material. Nonetheless, this flexibility in terms of feedstock is not represented in the industry where the use of petrochemicals is still prevalent. In fact, 78% of the worldwide hydrogen production derives from petrochemicals, of which natural gas corresponds to 48% while petroleum corresponds to the remaining 30%. Coal gasification and water electrolysis account for 18 and 4% of the total hydrogen production, respectively. In the case of the US, 95% of hydrogen is produced from natural gas. Coal gasification is more important in areas where extensive coal deposits are accessible (for example, the US has 250 years reserves of coal [6, 7]), while water electrolysis is usually restricted to locations where electricity is abundant and inexpensive. Hydrogen is also the byproduct of some industrial processes, such as brine electrolysis [1, 8, 9]. The predominance of petrochemicals and coal in the production of hydrogen is justified by their lower prices, and the efficiency and the know-how of the technologies involved. However, when using carbon-based fuels, carbon dioxide, an important greenhouse gas, is concomitantly produced, which contributes to the global warming phenomenon. To mitigate the environmental drawbacks of the use of these fuels, carbon sequestration techniques are required, or other more sustainable hydrogen sources need to be pursued [10]. A brief description of the more relevant methods for hydrogen production follows.

1.2.1. Steam reforming of natural gas and related technologies

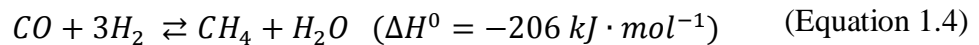
Steam reforming (SR) is one of the most efficient methods for the production of hydrogen from natural gas [11]. Natural gas is first desulfurized, in order to avoid deactivation of the catalyst. The feedstock gas is then mixed with process steam at 700-1000°C and 3-25 bar. Under these conditions, and in the presence of a Ni catalyst, the hydrocarbon is converted to carbon monoxide, hydrogen and carbon dioxide, as shown by equations 1.1 and 1.2:



The reactions above are endothermic [12] and require an external heat source. This is achieved by burning off some of the methane. The resulting gas mixture (called synthesis gas or syngas) is composed of about 12% carbon monoxide that can react further with steam and produce more hydrogen gas (equation 1.3):



The previous reaction is commonly known as the water gas shift (WGS) reaction. As the reaction is exothermic, higher conversion efficiency to hydrogen is favored at lower temperatures. Commonly, there are two WGS reactors in series downstream of the SR reactor. The first WGS reactor operates at > 350°C with an iron catalyst, while the second one operates at 200°C and uses a copper catalyst (a third WGS reactor may be used that operates at intermediate temperatures, 220-270°C). CO levels go down from 12 (syngas) to 2.5 (first WGS, [13]) and finally 0.2 vol% in the second WGS reactor. Methanation reactions (equation 1.4) can also be used that will result in CO levels lower than 10 ppm, but at the expense of hydrogen gas [1, 12].

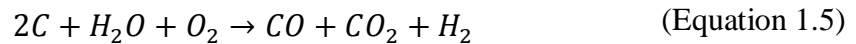


At this point, hydrogen is mixed with CO, CO₂, H₂O, and unreacted methane, along with any impurities that were already present in the natural gas, such as H₂S. This means that after steam reforming, the hydrogen gas needs to be purified. The different methods available are

discussed in section 1.3. Other hydrocarbons can be used in steam reforming (for instance methanol) and there are also other reforming technologies available, such as partial oxidation and autothermal reforming. The first step of any of these methods is the production of syngas, which can then be treated in the same way as described for the steam reforming method.

1.2.2. Gasification technologies (coal and biomass)

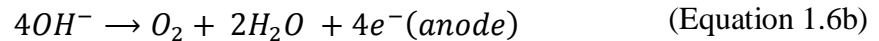
Reforming is not the only process that allows the production of syngas. Gasification is one alternative where a carbon source – coal or biomass – reacts with steam and oxygen at high temperatures. The main difference between the two sources of carbon is that biomass has low thermal efficiency, as a result of the moisture content, which also needs to be vaporized [11]. The following general equation can be written (equation 1.5):



Similarly with what happens with steam reforming, the syngas produced by gasification can be used in WGS reactions in order to maximize the conversion to hydrogen. Currently, all the hydrogen that is produced from coal uses gasification technologies. In fact, gasification of coal is considered a viable alternative to methane steam reforming in parts of the world where the reserves of coal are plentiful. Notwithstanding, biomass is a more versatile and sustainable source of carbon, being perhaps universally available. Common sources of biomass include agriculture crop residues, forest residues, special crops grown specifically for energy use, organic municipal solid waste, and animal wastes [14]. Interestingly, when using biomass, the gasification process may be considered neutral in terms of CO₂ production, because the same amount of CO₂ will be captured in the next cycle when biomass is grown. As equation 1.5 implies, the hydrogen produced through gasification is not pure and needs to be separated from the CO and CO₂ gases. Other impurities may be present, especially when dealing with coal, which need to be removed from the gas stream, such as H₂S, COS (carbonyl sulfides), and other trace elements, such as mercury or arsenic.

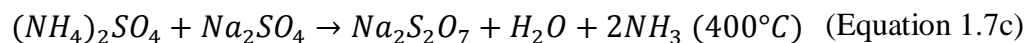
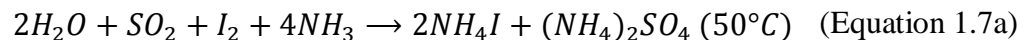
1.2.3. Water electrolysis and other water splitting-based methods

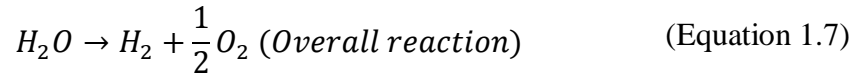
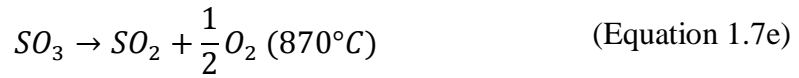
In water electrolysis, water is split into hydrogen and oxygen using electricity. An electrolytic cell is essentially composed by the electrolyte, two electrodes (commonly made of nickel) and a direct current power supply [15]. The reactions occurring in an alkaline system are the following [16]:



The gases produced at the electrodes are primarily pure oxygen (at the anode) and hydrogen (at the cathode), requiring little or no purification, depending on their final application. Other electrolyzers, such as proton exchange membrane electrolyzers and solid oxide electrolysis cells, are being developed that consist essentially of fuel cells operating in reverse. Unfortunately, these are still lacking commercial implementation [11]. In water electrolysis there is no CO₂ production, except if the electricity used in the process was generated from burning coal or natural gas. If that is the case, then gasification and steam reforming would be more direct ways to produce hydrogen gas.

The splitting of water for the production of hydrogen is also available by other routes that do not rely on electricity. Most notably, there are thermochemical and photoelectrochemical water splitting methods. In the former method, water decomposition is achieved through the combination of temperature and chemical reactions. There are many possible systems that are described in the literature. One example is given below that demonstrates the complexity of such systems [11, 17]:





Hydrogen is produced in reaction 1.7b and oxygen is produced in reaction 1.7e. Overall, only water is consumed (about 17% conversion) whereas all other chemicals are recovered in the process. The heat required can be supplied by concentrating sunlight onto a reactor or by recycling waste heat from nuclear reactors [18]. Without chemical reagents, the water splitting reaction would occur at temperatures as high as 2500-3000°C and only about 10% of water would be decomposed into oxygen and hydrogen. However, since it is based on a rather complex process, thermochemical water splitting is not a mature technology and can only be achieved at high pressures and in very corrosive conditions. In the end, hydrogen (and oxygen) still need to go through a purification step.

In photoelectrochemical water splitting, also called photoelectrolysis, sunlight is used to decompose water with the help of semiconductors, similar to those used in the generation of electricity by photovoltaics. Although promising, this technology is still far from being commercialized.

1.2.4. Biological hydrogen production

Numerous alternatives are currently being studied that use biological systems for the production of hydrogen. Two different feedstocks are available for biological hydrogen production, namely, water and biomass. In the first case, the processes being developed are based on water splitting by green algae or cyanobacteria, whereas the second process relies on the fermentation of biomass [11]. Most of the research work is focused on the identification and characterization of potential microorganism for the efficient conversion to H₂. Genetic modifications of those microorganisms are also being considered to increase the conversion efficiency.

1.3. Hydrogen purification processes

The two processes described below are mostly relevant for hydrogen that has been produced by steam reforming or gasification technologies, these being the two most common methods used in hydrogen production. All the other methods described in section 1.2 are either still in research stage or do not require extensive purification, such as is the case of the water electrolysis method.

1.3.1. Pressure swing adsorption and cryogenic distillation

In pressure swing adsorption (PSA), hydrogen is purified using molecular sieves, such as zeolites, which adsorb CO and CO₂ and other impurities at high pressure. With PSA, the final purity of the hydrogen stream is higher than 99.9%. The sieves are regenerated by reducing the pressure and temperature. Part of the purified hydrogen is used in a purging step, which reduces total hydrogen recovery to 70-85% [19]. PSA is the most common used method in gas purification.

Cryogenic separation is based on the different condensation points of the gases composing the starting mixture. It is a method mostly used for applications where low purity hydrogen (90-98%) is required. The hydrogen recovery rates are around 95% [19].

Both methods are highly energy demanding and none of the two is able to provide hydrogen pure enough to use, for example, with fuel cells, that require hydrogen 99.9995% pure to prevent poisoning the catalyst [20]. To address this demand of ultrapure hydrogen, membranes for hydrogen purification are being developed.

1.3.2. Membrane Technology

The use of membranes for hydrogen separation is a method that has been commercialized since the 1960s for small scale applications only. Many materials have been developed, such as polymeric, microporous ceramic, porous carbon, dense metallic and proton conducting dense ceramic materials. The mechanism of hydrogen transport through these membranes is dependent on the material and if the membrane is porous or dense. However, for all the membranes, the driving force for the separation is the difference in pressure (or chemical potential) of the hydrogen present upstream and downstream of the membrane [21].

Dense palladium-silver alloys are the benchmark material for hydrogen separation membranes. When using this type of material, 99% recovery of hydrogen with purity exceeding 99.9999% is possible [19]. However, these membranes are rapidly deactivated in the presence of hydrogen sulfide [22], a gas present at the exit of a natural gas steam reformer and coal gasification units. Moreover, palladium is also a costly metal. These two drawbacks justify the small scale application of this type of purification method.

One possible approach to increase the commercial competitiveness of Pd-based membranes is cost reduction by decreasing the thickness of the membranes. This means that a porous substrate (stainless steel, alumina, or other) that provides mechanical support may be required. The US Department of Energy (DOE) has set a price target for the palladium membranes at less than 1080 USD/m² by 2015 [23] that has not yet been achieved.

Another alternative to overcome the hurdles of palladium and palladium-silver membranes is to use other palladium alloys that offer the same performance as Pd-Ag but requiring less amount of palladium while providing higher H₂S resistance. In this regard palladium-copper or palladium-gold alloys seem promising [24-34]. For example, the latter alloys are able to keep higher hydrogen flux when compared to both PdCu and PdAg alloys [22]. On the other hand, a Pd₄₇Cu₅₃ membrane is able to maintain 70% of the flux of a Pd₇₃Ag₂₇ membrane¹ (0.208 vs. 0.298 scfh, respectively) of the same thickness and at the same conditions of pressure and temperature, while decreasing the amount of palladium required by 18% (mass based) [22]. The high hydrogen flux through a membrane made of PdCu alloys with low Pd content is attributed to the existence of a body-centered cubic structure, which is observed at Pd concentrations between 34 and 47 at %, for which the diffusion of hydrogen is facilitated [35-37]. Palladium-based membranes will be further discussed in chapter 2.

¹ Throughout this thesis, the alloys composition, for example Pd_xCu_{1-x}, is always given in atomic percent, except if clearly stated otherwise.

1.4. Objectives of the work

The current work aims to contribute to the development of palladium-based membranes that are both inexpensive and resistant to poisoning. In this regard, the work will focus on PdCuAu ternary alloys in an attempt to combine in one single alloy the high hydrogen flux at low Pd content of PdCu with the high H₂S poisoning resistance of PdAu. The main goal is to study the ternary alloys in respect to their solubility and permeability to hydrogen.

The objectives of the present work may be divided in two distinct sections: *section 1* which deals with PdCuAu thin films and the electrochemical measurement of hydrogen solubility, while *section 2* is dedicated to the fabrication and testing of unsupported PdCuAu alloy-membranes. A description of the objectives follows.

Objectives section 1 – thin films and hydrogen solubility

1. Use thin film deposition technologies, namely electrodeposition and sputter deposition, to prepare PdCuAu alloys over a wide composition range.
 - a. Characterize as-deposited samples in regard of their crystal structure, composition and morphology, using X-ray diffraction (XRD), Energy Dispersive X-ray spectroscopy (EDX), X-ray Photoelectron Spectroscopy (XPS), and Scanning Electron Microscopy (SEM).
2. Identify the composition of the PdCuAu alloys where the body-centered cubic (bcc) phase is stable by subjecting the as-deposited samples to heat treatment, followed by characterization (XRD, SEM/EDX, XPS and cyclic voltammetry, CV).
3. Measure the hydrogen solubility of the as-deposited (face-centered cubic phase, fcc) and annealed samples (fcc and bcc phase) by an electrochemical method or by an electrochemical *in situ* XRD method.

Objectives section 2 – unsupported membranes and hydrogen permeability

1. Validate the experimental setup built for the gas phase measurement of hydrogen flux using a commercial palladium foil as a standard.
2. Prepare the bcc PdCuAu alloy-membranes for gas phase measurement:

- a. Choose appropriate composition according to the information gathered previously in the study of thin films;
 - b. Prepare the bulk PdCuAu alloys by mechanical alloying of the pure metal powders;
 - c. Develop a method to prepare functional dense metallic membranes from the mechanically alloyed powders.
3. Measure the hydrogen flux through the membranes in the presence of pure hydrogen and hydrogen mixtures with H₂S.

1.5. Structure of the thesis

This thesis is organized in 7 different chapters. In **chapter 1**, an introduction is made to the hydrogen production and purification methods, providing the context of the present work. **Chapter 2** provides a detailed analysis of the current developments and most promising perspectives for Pd-based membranes. The experimental conditions and techniques are all thoroughly described in **chapter 3**. The results are summarized in chapters 4, 5 and 6. Chapters 4 and 5 correspond to section 1 and chapter 6 corresponds to section 2, as described in the objectives. **Chapter 4** deals with the electrodeposition of thin films, their characterization and the measurements of their hydrogen solubility properties, especially alloys with fcc structure. **Chapter 5** is analogous to chapter 4 but is focused on samples prepared by sputter deposition and more emphasis is given to samples with bcc structure. **Chapter 6** presents the preparation of unsupported PdCuAu alloy-membranes and their performance in the gas phase measurements. Finally, **chapter 7** presents the conclusion and a description of future work that will need to be performed. A summary in French is available in section A1.

1.6. References

- [1] Greenwood NN, Earnshaw A. Chemistry of the Elements. Second ed: Butterworth-Heinemann; 1997.
- [2] Ramachandran R, Menon RK. An overview of industrial uses of hydrogen. *International Journal of Hydrogen Energy*. 1998;23:593-8.
- [3] Winter C-J. Hydrogen energy — Abundant, efficient, clean: A debate over the energy-system-of-change. *International Journal of Hydrogen Energy*. 2009;34:S1-S52.
- [4] Singh S, Jain S, Ps V, Tiwari AK, Nouni MR, Pandey JK, et al. Hydrogen: A sustainable fuel for future of the transport sector. *Renewable and Sustainable Energy Reviews*. 2015;51:623-33.
- [5] Nenoff TM, Spontak RJ, Aberg CM. Membranes for hydrogen purification: An important step toward a hydrogen-based economy. *Mater Res Soc Bull*. 2006;31:735-41.
- [6] http://www1.eere.energy.gov/hydrogenandfuelcells/production/coal_gasification.html.
- [7] Gabitto J, Tsouris C. Sulfur poisoning of metal membranes for hydrogen separation. *International Review of Chemical Engineering*. 2009;1:394-411.
- [8] http://www1.eere.energy.gov/hydrogenandfuelcells/production/natural_gas.html;
- [9] http://en.wikipedia.org/wiki/Hydrogen_economy.
- [10] Turner JA. Sustainable Hydrogen Production. *Science*. 2004;305:972-4.
- [11] Holladay JD, Hu J, King DL, Wang Y. An overview of hydrogen production technologies. *Catalysis Today*. 2009;139:244-60.
- [12] Hoogers G. *Fuel Cell Technology Handbook*. Boca Raton: CRC Press; 2003.

- [13] http://www.linde-engineering.com/en/process_plants/hydrogen_and_synthesis_gas_plants/gas_generation/co_shift_conversion/index.html.
- [14] <http://energy.gov/eere/fuelcells/hydrogen-production-biomass-gasification>.
- [15] Zeng K, Zhang D. Recent progress in alkaline water electrolysis for hydrogen production and applications. *Progress in Energy and Combustion Science*. 2010;36:307-26.
- [16] Esswein AJ, McMurdo MJ, Ross PN, Bell AT, Tilley TD. Size-Dependent Activity of Co_3O_4 Nanoparticle Anodes for Alkaline Water Electrolysis. *The Journal of Physical Chemistry C*. 2009;113:15068-72.
- [17] Rosen MA. Exergy analysis of hydrogen production by thermochemical water decomposition using the Ispra Mark-10 Cycle. *International Journal of Hydrogen Energy*. 2008;33:6921-33.
- [18] <http://energy.gov/eere/fuelcells/hydrogen-production-thermochemical-water-splitting>.
- [19] Grashoff GJ, Pilkington CE, Corti CW. Purification of hydrogen. *Platinum Metals Review*. 1983;27:157-69.
- [20] Ockwig NW, Nenoff TM. Membranes for Hydrogen Separation. *Chemical reviews*. 2007;107:4078-110.
- [21] Hägg M-B. Membranes in gas separation. In: Pabby AK, Rizvi SSH, Satre AM, editors. *Handbook of Membrane Separations - Chemical, Pharmaceutical, Food, and Biotechnological Applications*: CRC Press; 2009.
- [22] Mckinley DL. Metal alloy for hydrogen separation and purification. United States: US patent 3,350,845; 1967.

- [23] Phair JW, Donelson R. Developments and Design of Novel (Non-Palladium-Based) Metal Membranes for Hydrogen Separation. *Industrial & Engineering Chemistry Research*. 2006;45:5657-74.
- [24] Kamakoti P, Morreale BD, Ciocco MV, Howard BH, Killmeyer RP, Cugini AV, et al. Prediction of Hydrogen Flux Through Sulfur-Tolerant Binary Alloy Membranes. *Science*. 2005;307:569-73.
- [25] Coulter KE, Way JD, Gade SK, Chaudhari S, Sholl DS, Semidey-Flecha L. Predicting, Fabricating, and Permeability Testing of Free-Standing Ternary Palladium-Copper-Gold Membranes for Hydrogen Separation. *Journal of Physical Chemistry C*. 2010;114:17173-80.
- [26] Coulter KE, Way JD, Gade SK, Chaudhari S, Alptekin GO, DeVoss SJ, et al. Sulfur tolerant PdAu and PdAuPt alloy hydrogen separation membranes. *Journal of Membrane Science*. 2012;405-406:11-9.
- [27] Gade SK, Payzant EA, Park HJ, Thoen PM, Way JD. The effects of fabrication and annealing on the structure and hydrogen permeation of PdAu binary alloy membranes. *Journal of Membrane Science*. 2009;340:227-33.
- [28] Flanagan TB, Wang D. Hydrogen Permeation through fcc Pd-Au Alloy Membranes. *Journal of Physical Chemistry C*. 2011;115:11618-23.
- [29] Gallucci F, Fernandez E, Corengia P, van Sint Annaland M. Recent advances on membranes and membrane reactors for hydrogen production. *Chemical Engineering Science*. 2013;92:40-66.
- [30] Peters TA, Kaleta T, Stange M, Bredesen R. Hydrogen transport through a selection of thin Pd-alloy membranes: Membrane stability, H₂S inhibition, and flux recovery in hydrogen and simulated WGS mixtures. *Catalysis Today*. 2012;193:8-19.

- [31] Hatlevik Ø, Gade SK, Keeling MK, Thoen PM, Davidson AP, Way JD. Palladium and palladium alloy membranes for hydrogen separation and production: History, fabrication strategies, and current performance. *Separation and Purification Technology*. 2010;73:59-64.
- [32] Semidey-Flecha L, Ling C, Sholl DS. Detailed first-principles models of hydrogen permeation through PdCu-based ternary alloys. *Journal of Membrane Science*. 2010;362:384-92.
- [33] Sonwane CG, Wilcox J, Ma YH. Solubility of Hydrogen in PdAg and PdAu Binary Alloys Using Density Functional Theory. *The Journal of Physical Chemistry B*. 2006;110:24549-58.
- [34] Gade SK, DeVoss SJ, Coulter KE, Paglieri SN, Alptekin GO, Way JD. Palladium–gold membranes in mixed gas streams with hydrogen sulfide: Effect of alloy content and fabrication technique. *J Membr Sci*. 2011;378:35-41.
- [35] Subramanian PR, Laughlin DE. Cu-Pd (Copper-Palladium). *Journal of Phase Equilibria*. 1991;12:231-43.
- [36] Howard BH, Killmeyer RP, Rothenberger KS, Cugini AV, Morreale BD, Enick RM, et al. Hydrogen permeance of palladium-copper alloy membranes over a wide range of temperatures and pressures. *Journal of Membrane Science*. 2004;241:207-18.
- [37] Piper J. Diffusion of hydrogen in copper-palladium alloys. *J Appl Phys*. 1966;37:715-21.

2. Dense palladium based metallic membranes for the separation of hydrogen gas

2.1. Introduction

The discovery by T. Graham that palladium absorbs hydrogen dates back from 1866. T. Graham observed that Pd absorbs 935 times its own volume of H₂ while cooling down from red hot, corresponding to a composition of PdH_{0.5}. The gas is released again upon heating of the metal [1, 2]. The hydrogen absorption decreases the metallic conductivity of palladium, but the ductility of the metal is kept constant. T. Graham took his studies further by testing a palladium tube built by George Matthey (co-founder of Johnson Matthey company, along with Percival Norton Johnson) [3]. When subjecting the palladium tube to coal-gas (a mixture of hydrogen, carbon monoxide, methane, carbon dioxide and nitrogen) at 270°C, T. Graham noticed that “the penetrating gas had no odor of coal-gas, contained no trace of carbon, and appeared to be absolutely pure hydrogen” [3]. This may well be considered the first account of a dense palladium-based metallic membrane. Additional work of T. Graham involved the study of palladium-silver alloys, that later on, in the 1960s, started being commercialized by Johnson Matthey, for small scale production of ultrapure hydrogen [2, 4].

The pioneer work of D. L. McKinley in 1960s is considered a breakthrough in the development of Pd-based membranes. D.L. McKinley intensively studied Pd alloys of copper, silver and gold at different conditions of temperature, pressure and inlet gas composition [5, 6]. He was the first investigator to identify a palladium-copper alloy at 47 at% Pd that has the same performance of pure palladium [5], and also the first to report on the effect of gold in preventing the catalytic poisoning of the membrane by hydrogen sulfide gas [6].

This chapter will first introduce the concepts of hydrogen diffusion and permeability through a dense metallic membrane, along with the mechanisms of hydrogen transport. A description of the palladium-hydrogen interaction will follow. Finally, a literature review on palladium alloys (specifically: PdCu, PdAu and PdCuAu) will be presented.

2.2. Hydrogen diffusion and permeability in Pd-dense metallic membranes

In broad terms, a membrane is a barrier that allows the selective passage of a substance, while retaining others. In gas separation, dense metallic membranes are a particular type of membranes that operate through a mechanism of solution-diffusion, in contrast with porous membranes that are mostly based on size exclusion separation mechanisms. These mechanisms are illustrated in Fig. 2.1.

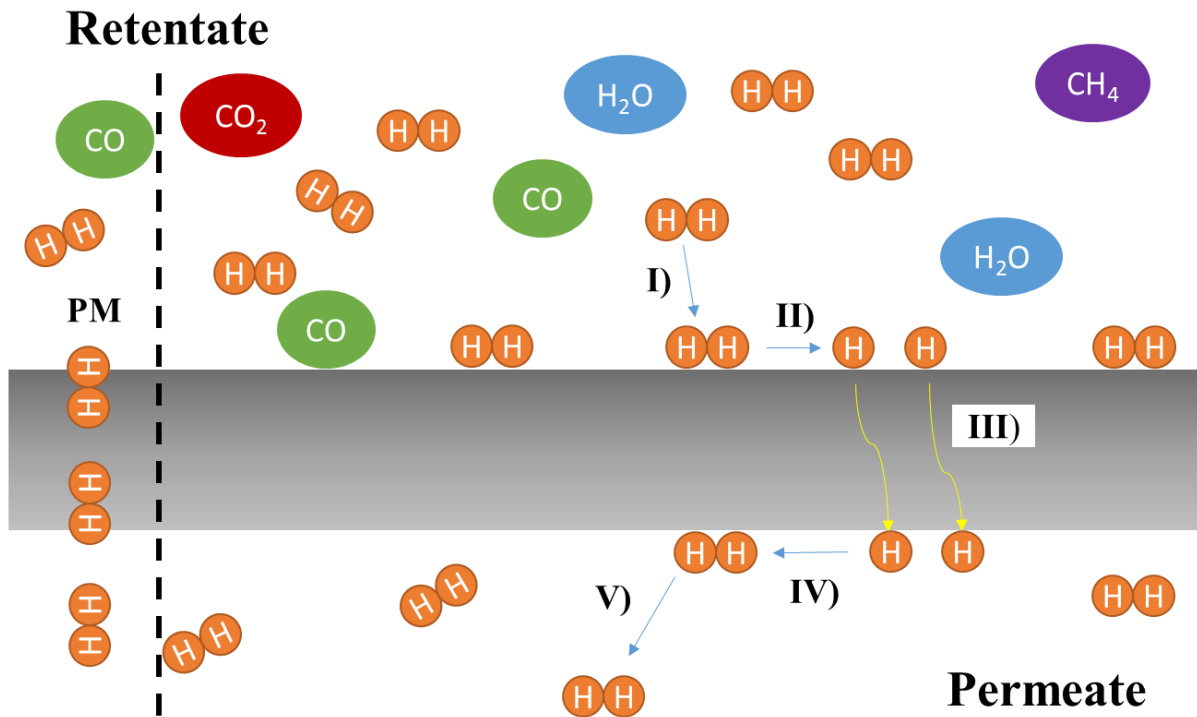


Figure 2. 1 – Schematic illustration of the mechanism of hydrogen permeation through a porous membrane (denoted PM, on the left) and a dense metallic membrane (right). The latter is referred to as the solution-diffusion mechanism and is composed of 5 steps: I – H₂ adsorption; II – H₂ dissociation into atomic hydrogen; III – diffusion; IV – atomic H recombination; and V) H₂ desorption.

Independent of the type of membrane, namely porous or dense metallic, the separation is always driven by a difference in the hydrogen partial pressure between the feed (high pressure, retentate or upstream) and the permeate (low pressure or downstream) sides of the membrane. In this sense, the hydrogen flux, defined as the amount of hydrogen transported through the membrane per unit time and unit area ($\text{mol}\cdot\text{s}^{-1}\cdot\text{m}^{-2}$), occurs from the feed to the permeate side. As shown in Fig. 2.1, the solution-diffusion mechanism is divided in 5 steps. First, on the feed side, H_2 is adsorbed on the surface of the palladium. After, the H-H bond is cleaved by palladium (step II, Fig. 2.1) and the hydrogen atoms are consequently inserted in the octahedral interstices of the palladium fcc lattice. In fact, it is generally accepted that the combined s-d bands of palladium accept the electron of the hydrogen atom[7] and it is the proton that will be positioned in the octahedral interstices, even if palladium and hydrogen have comparable electronegativities. At the temperatures at which these membranes are usually operated ($>300^\circ\text{C}$), the H atoms hop between neighboring sites through activated thermal jumps (step III, Fig. 2.1) [8]. Finally, when reaching the permeate side, the hydrogen atoms recombine to form molecular hydrogen and desorb from the surface of the membrane (steps IV and V of Fig 2.1, respectively). As hydrogen atoms are the only ones that are able to diffuse through the palladium lattice, the palladium membranes are highly selective and, at least theoretically, 100% pure H_2 may be produced. In the case of porous membranes (designated by PM on the left side of Fig. 2.1), it is the relative size of the gas molecules versus the size of the pores that is ruling the separation. This type of membranes do not require any palladium in their composition and can be produced from much less expensive materials such as carbon. Porous membranes may be more cost effective but are not usually able to achieve the selectivity that can be reached by dense Pd-based membranes. In fact, the existence of pores in dense metallic membranes is highly undesirable as their presence will reduce the quality of the separation. Porous membranes are out of the scope of the present work.

The diffusion of hydrogen atoms through a palladium membrane can mathematically be represented by Fick's law (equation 2.1) that relates the flux of hydrogen atoms (J_H) with the diffusion coefficient (D_H) and the concentration gradient across the membrane (dC_H/dx , C_H being the concentration of H atoms dissolved in the membrane):

$$J_H = -D_H \frac{dC_H}{dx} \quad (\text{Equation 2.1})$$

The conditions used for the integration of equation 2.1 are schematically illustrated in Fig. 2.2.

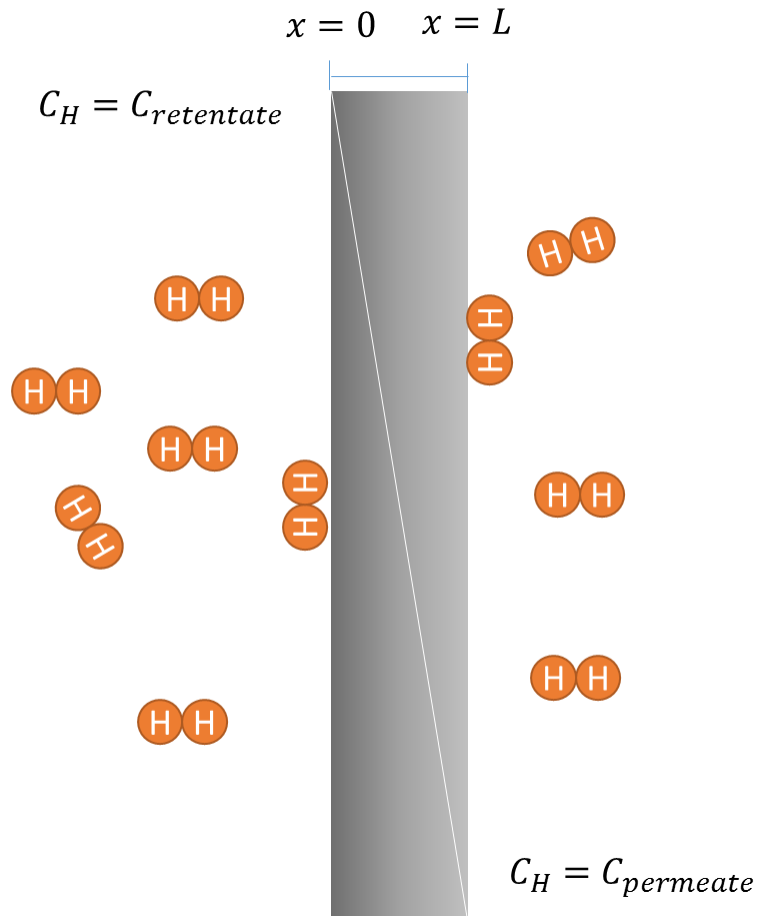


Figure 2. 2 – Boundary conditions used in the integration of Fick’s law of diffusion. The concentration gradient within the membrane is considered linear.

Using the boundary conditions set in Fig 2.2, where the concentration gradient within the membrane is considered linear, and considering steady state conditions, the integrated version of equation 2.1 can be written as:

$$J_H \int_0^L dx = -D_H \int_{C_{retentate}}^{C_{permeate}} dC_H \quad (\text{Equation 2.2})$$

Equation 2.2 simplifies to:

$$J_H = \frac{D_H}{L} (C_{retentate} - C_{permeate}) \quad (\text{Equation 2.3})$$

Equation 2.3 establishes that the flux of atomic hydrogen depends only on the hydrogen diffusion coefficient, the thickness L of the membrane and the concentration of H dissolved on both sides of the membrane (retentate and permeate). The only thing left to do is to find a way to quantify the amount of hydrogen that is dissolved in the membrane. The following chemical equilibrium is set between the hydrogen in the gas phase (molecular hydrogen) and the hydrogen dissolved in the metal (atomic hydrogen):



The corresponding equilibrium constant is given by:

$$K_S = \frac{C_H^2}{P_{H_2}} \Leftrightarrow C_H = K_S \sqrt{P_{H_2}} \quad (\text{Equation 2.5})$$

Equation 2.5 is commonly known by the Sievert's law, and the equilibrium constant is often referred to as the Sievert's constant or the solubility (K_S). This equation provides a relation between the gas pressure above the surface of the metal and the concentration of hydrogen that is dissolved in the membrane. Combining equations 2.3 and 2.5 gives the following relation:

$$J_H = \frac{D_H K_S}{L} [(P_{H_2}^{retentate})^{1/2} - (P_{H_2}^{permeate})^{1/2}] \quad (\text{Equation 2.6})$$

Noting that the flow of hydrogen gas is half the flow of atomic hydrogen, equation 2.6 becomes:

$$J_{H_2} = \frac{D_H K_S}{2L} \left[(P_{H_2}^{retentate})^{\frac{1}{2}} - (P_{H_2}^{permeate})^{\frac{1}{2}} \right] \quad (\text{Equation 2.7})$$

Equation 2.7 is known as the Richardson equation and can be further rearranged to:

$$J_{H_2} = \frac{\phi}{L} \left[(P_{H_2}^{retentate})^{\frac{1}{2}} - (P_{H_2}^{permeate})^{\frac{1}{2}} \right] \quad (\text{Equation 2.8})$$

With

$$\phi = \frac{D_H K_S}{2} \quad (\text{Equation 2.9})$$

In equations 2.8 and 2.9, ϕ represents the permeability of hydrogen gas and is usually presented in $\text{mol} \cdot \text{m}^{-1} \cdot \text{s}^{-1} \cdot \text{Pa}^{-0.5}$. As defined by equation 2.9, permeability is the product of the diffusion with the solubility of hydrogen in the membrane. The permeability can be calculated by measuring the flux of hydrogen through a membrane of known thickness L at a pressure difference. It is a property that reflects the membrane's capability to separate the hydrogen gas from a mixture and it may be used as a comparison between different types of membranes in order to evaluate their relative performance. The hydrogen permeability of common metals is summarized in table 2.1 [9].

Table 2. 1 – Hydrogen permeability for different metals at 500°C.

Metal	Crystal structure	ϕ (mol·m ⁻¹ ·s ⁻¹ ·Pa ^{-0.5})	ϕ_{Pd}/ϕ_M
Niobium	bcc	1.6×10^{-6}	0.01
Tantalum	bcc	1.3×10^{-7}	0.1
Vanadium	bcc	1.9×10^{-7}	0.1
Palladium	fcc	1.9×10^{-8}	1
Iron	bcc	1.8×10^{-10}	105
Nickel	fcc	7.8×10^{-11}	244
Copper	fcc	4.9×10^{-12}	3877
Platinum	fcc	2.0×10^{-12}	9500

As shown in table 2.1, most of the bcc metals, namely, Nb, Ta and V, have higher hydrogen permeability than pure Pd, whereas the permeability of Pt and Cu, for example, is two orders of magnitude lower than that of Pd. And also, Nb, Ta and V are less expensive than palladium. At first sight, the bcc metals should be the preferred metals for hydrogen separation. However, the permeability is often inhibited due to the formation of surface oxides and due to the poor catalytic activity of these metals towards molecular hydrogen splitting. Furthermore, the hydrides of these metals are usual brittle, giving the membranes low mechanical stability. Nevertheless, there is a considerable amount of research being performed with bcc metals that uses Pd or Pd alloys as the active catalyst to help the dissociation of molecular H₂. These membranes – often referred to as “palladium-free” membranes – are the most direct competitors of palladium-based membranes, but a viable commercial option has yet to be presented.

A more general empirical relation between hydrogen flux and pressure gradient can be written by adapting equation 2.8:

$$J_{H_2} = \frac{\phi}{L} \left[(P_{H_2}^{retentate})^n - (P_{H_2}^{permeate})^n \right] \quad (\text{Equation 2.10})$$

Where n is a coefficient that reflects the limiting step in the transport of hydrogen. The balance between the rate of hydrogen diffusion through the membrane and the rate at which the dissociation/recombination of hydrogen occurs at the surface, is, ultimately, the factor ruling the concentration of hydrogen incorporated in the membrane. In equilibrium, Sievert's law is valid and $n = 0.5$, as demonstrated before, and in this case the rate of dissociation/association of hydrogen is not important to the overall flux. However, if the surface reactions become the limiting step, the system gets away from equilibrium, and Sievert's law is no longer valid. In this situation, n approaches unity values, and it will be equal to one in systems that are exclusively limited by the surface reactions. In general, Pd membranes with thickness higher than 10 μm are diffusion limited, whereas below that value it is more common to find membranes limited by surface reactions. In the current work, measures of both solubility and permeability were performed, and permeability measurements were always taken in the diffusion limited regime, this is with membranes with thicknesses higher than 10 μm .

Both diffusion and solubility are properties that are temperature dependent, which makes permeability, the product of the two, also dependent on temperature. For the case of diffusion-limited transport, the permeability's variation with temperature is described by an Arrhenius-like equation:

$$\phi = \phi_0 \exp(-E_a/RT) \quad (\text{Equation 2.11})$$

Where ϕ_0 is the pre-exponential factor, E_a is the activation energy, R is the perfect gas constant and T is the temperature. The activation energy for the permeability is in fact the sum of the activation energy for diffusion with the enthalpy variation that occurs during hydrogen absorption [10]. The variation of permeability with temperature is shown for some metals in Fig. 2.3.

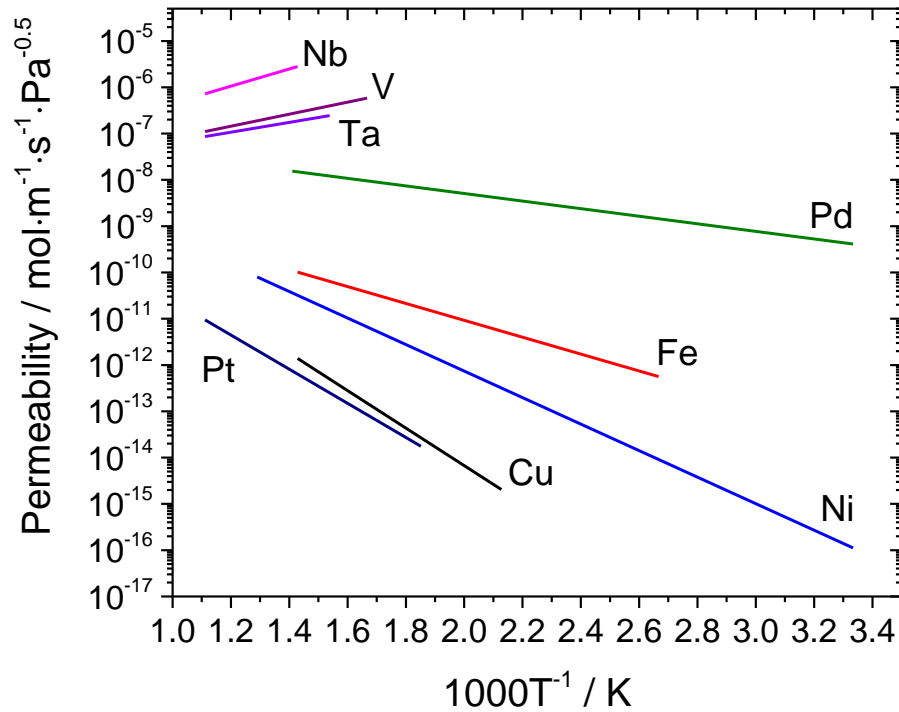


Figure 2. 3 – Permeability vs. reciprocal temperature for bcc (Nb, V, Ta and Fe) and fcc (Pd, Ni, Cu and Pt) metals. The values were calculated from the data compiled by S.A. Steward [11].

As illustrated in Fig. 2.3, the bcc metals (Nb, V and Ta) show a decrease in permeability with increasing temperature, whereas fcc metals (Pd, Ni, and Cu) show the opposite trend. For example, the permeability of Nb decreases from $3.3 \times 10^{-6} \text{ mol}\cdot\text{m}^{-1}\cdot\text{s}^{-1}\cdot\text{Pa}^{-0.5}$ at 400°C [11, 12] to $1.6 \times 10^{-6} \text{ mol}\cdot\text{m}^{-1}\cdot\text{s}^{-1}\cdot\text{Pa}^{-0.5}$ at 500°C (Table 2.1). For palladium, on the other hand, the permeability increases from $1.5 \times 10^{-8} \text{ mol}\cdot\text{m}^{-1}\cdot\text{s}^{-1}\cdot\text{Pa}^{-0.5}$ at 400°C [11, 12] to $1.9 \times 10^{-8} \text{ mol}\cdot\text{m}^{-1}\cdot\text{s}^{-1}\cdot\text{Pa}^{-0.5}$ at 500°C (table 2.1). This difference is a consequence of the fact that the permeability is defined by the product of two properties, the solubility and the diffusion (equation 2.9) that do not necessarily vary the same way with the temperature.

The performance of the membranes to separate hydrogen from another gas may be quantified by the ideal separation factor, $\alpha_{H_2,j}^*$ which is given by the ratio of the pure gas permeabilities of each individual components of the gas mixture:

$$\alpha_{H_2,j}^* = \frac{\phi_{H_2}}{\phi_j} \quad (\text{Equation 2.12})$$

In a dense metallic membrane, no other gas apart from hydrogen can permeate the membrane because of the absence of pores. In theory, this results in zero permeability for any gas except H₂, this is, $\phi_j = 0$. Consequently, the ideal separation factor is infinite for dense metallic membranes.

The separation factor for gases in mixtures (also called the selectivity of the membrane), $\alpha_{H_2,j}$, is given by the mole fractions of the components in the feed (x) and in the permeate (y):

$$\alpha_{H_2,j} = \frac{y_{H_2}/y_j}{x_{H_2}/x_j} \quad (\text{Equation 2.13})$$

Commonly, the separation factors are lower than the corresponding ideal values. The greatest challenge in the preparation of dense membranes is to guarantee the absence of any pores or pinholes that may reduce the selectivity of the membrane. This is particularly important when dealing with thin membranes, that is, membranes whose thicknesses are below 10 μm .

2.3. Hydrogen solubility in palladium

As previously illustrated in Fig. 2.1, the dissolution of hydrogen in palladium starts first by the adsorption of molecular hydrogen on the surface of the palladium, followed by the catalytic cleavage of the H-H bond. Atomic hydrogen will subsequently migrate to the bulk of the Pd, with hydrogen occupying the octahedral interstices [13, 14]. The amount of hydrogen that can be dissolved by the palladium is both temperature and pressure dependent. This is shown in Fig. 2.4.

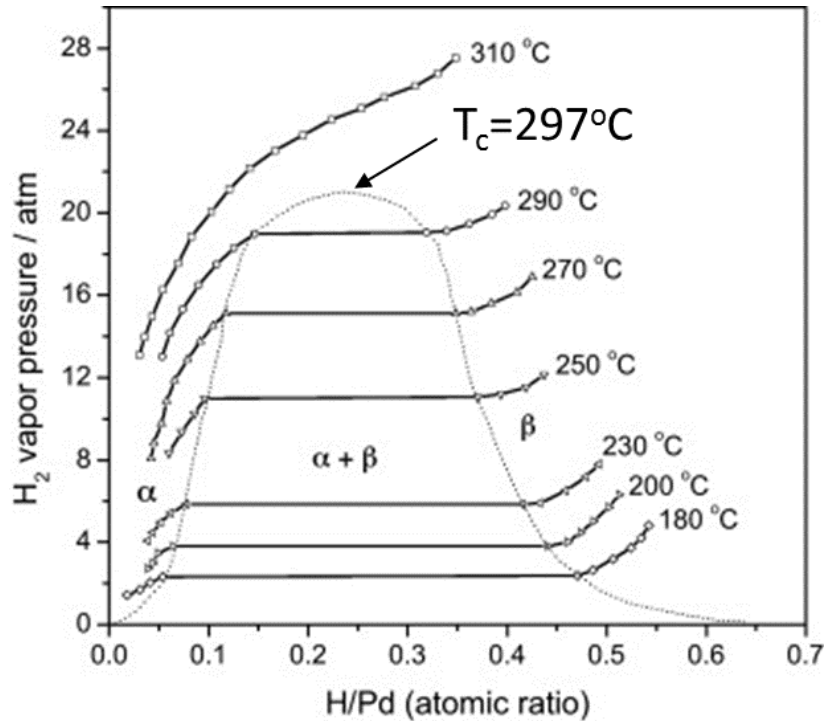
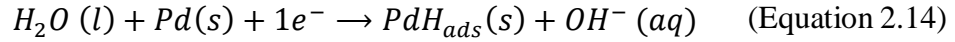


Figure 2. 4 – Pressure-composition-temperature phase diagram of the palladium-hydrogen system (adapted from [13, 15, 16])

As shown in Fig. 2.4, at temperatures below 297°C, the palladium hydrogen system exhibits two distinct phases, commonly designated by α and β phases, for the low and high H/Pd atomic ratios, respectively. As hydrogen is introduced in the metal lattice, the α phase is formed. Dissolving more hydrogen leads to the formation of the β phase also called the hydride phase. Introducing more hydrogen to the lattice will lead to an increase of the fraction of the β phase till a point where only the β phase is present. In the region of coexistence of the two phases, this is at temperatures below 297°C (the critical temperature), the hydrogen pressure is constant as required by the phase rule [17]. As the β phase is formed, the volume of the Pd-H system expands by 10.4% [13]. This is a consequence of the change in lattice parameter, from 3.894 (α phase) to 4.025Å (β phase). The lattice mismatch of these two phases may lead to embrittlement of the membrane and consequent failure. To avoid this, pure Pd membranes need to operate at temperatures above 300°C, where only the β phase is present [13, 15, 16]. Alternatively, Pd could be alloyed with other metals that will decrease the critical temperature of the membrane (section 2.4) and facilitate their use in an industrial environment.

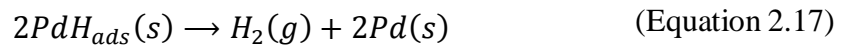
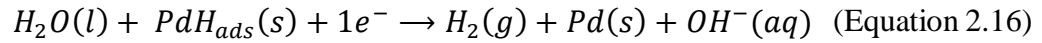
The introduction of H₂ into the Pd lattice is also possible by an electrochemical procedure, either in acidic or alkaline medium. In electrochemical hydrogen absorption, the palladium is immersed in the electrolyte and is connected to a potentiostat. Upon application of a negative potential, hydrogen uptake can occur. The electrochemical absorption of hydrogen is a two-step process [18, 19]. First, atomic hydrogen is adsorbed on the metal surface:



Where PdH_{ads} represents the hydrogen adsorbed on the surface. Equation 2.14 is also known as the Volmer reaction. Afterwards, the adsorbed hydrogen diffuses from the surface to the bulk of the electrode:



Where PdH_{abs} represents the hydrogen that was inserted in the palladium lattice by diffusion. The adsorbed hydrogen may recombine to give hydrogen gas, according to equations 2.16 (Heyrovsky reaction) and 2.17 (Tafel reaction):



Equations 2.16 and 2.17 are side reactions that do not contribute to the absorption of hydrogen. In the current work, with the aim of studying hydrogen solubility, hydrogen absorption was electrochemically promoted. The amount of hydrogen absorbed was then determined by one of two methods: electrochemical H desorption with measurements of (i) the current charge or (ii) with measurement of the changes occurring with the lattice parameter (electrochemical *in situ* X-ray diffraction). The solubility is typically represented by the ratio H/M (or nH/nM) that represents the ratio between the number of hydrogen moles dissolved with the number of moles that constitute the metal.

2.4. Palladium alloys literature review

Pure Pd membranes present several constraints that prevent their widespread use at an industrial scale. The major drawbacks are cost, hydrogen embrittlement due to the α - β phase transition and H₂S-poisoning. The presence of H₂S is particularly important in coal-derived syngas. Alloying of Pd with other elements is a way to overcome some of its intrinsic limitations, and to improve the performance of palladium based-membranes. Their use in large scale production is still far from reality but it is a promising alternative to increase the production of hydrogen and to decrease its cost, making it more available to implement the hydrogen energy economy [9, 13, 20-25].

The number of possible Pd-alloys is vast and there are reports of alloys of palladium with numerous elements such as vanadium, titanium, silver, copper, gold, yttrium, zirconium, iron, manganese, platinum, ruthenium, molybdenum, niobium, tantalum, and others. Moreover, not only binary but also ternary and quaternary alloys have been prepared. Most relevant for the current work are the alloys of PdCu, PdAu and PdCuAu. A detailed analysis of these alloys will follow.

2.4.1. PdCu and PdAu binary alloys

2.4.1.1. Solubility measurements

Hydrogen absorption by palladium and palladium alloys causes volume expansion. This needs to be taken into account, along with the thermal volume expansion, when designing the membrane module. In this sense, it is important to know how much hydrogen newly prepared alloys are able to uptake. In general, and in accordance with what happens with pure Pd, the hydrogen atoms occupy the octahedral interstitial sites of the alloys ([26] and references therein).

The solubility of PdCu [27-29] and PdAu [30, 31] alloys has been studied extensively. Some representative results are shown in Fig. 2.5.

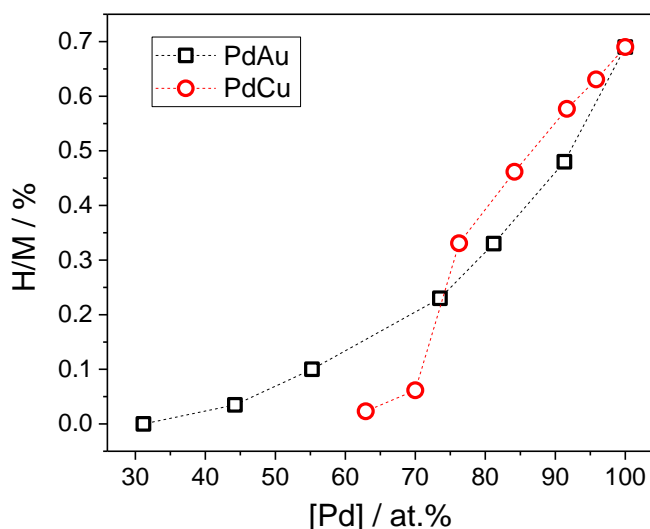


Figure 2. 5 – Hydrogen solubility given by H/M ratios for PdCu [27] and PdAu [31] alloys. All measurements are made at 25°C and atmospheric pressure in H₂-stirred aqueous solutions.

In Fig. 2.5 the hydrogen solubility is given by the ratio between the number of hydrogen moles (H) that can be introduced in the alloys' lattice and the number of moles of the alloy (M). As seen in Fig. 2.5, the hydrogen solubility is maximum for pure Pd with $\frac{H}{M} = 0.69$ [32]. Reducing the palladium content by replacing it with copper or gold leads to a decrease in solubility. This is a consequence of the fact that neither copper nor gold absorb hydrogen to a significant extent, as they do not present catalytic activity to cleave H-H bond in the gas phase. For palladium content higher than 70 at.% the hydrogen solubility is higher for PdCu than is for PdAu alloys. Both PdCu and PdAu alloys show lower critical temperatures than pure Pd. For example, Pd₆₅Cu₃₅ [27] and Pd₈₃Au₁₇ [30] only show one phase upon hydrogen absorption at 25°C, while two phases (α and β phases) co-exist in pure Pd till 297°C, as seen in Fig. 2.4.

2.4.1.2. Permeability measurements with and without H₂S

PdCu and PdAu binary alloys were extensively studied by McKinley [5, 6] in the late 1960s. In his work he used foils 25.4 μm thick supported on porous stainless steel substrates. The hydrogen permeability of these alloys as a function of the palladium content is shown in Fig. 2.5.

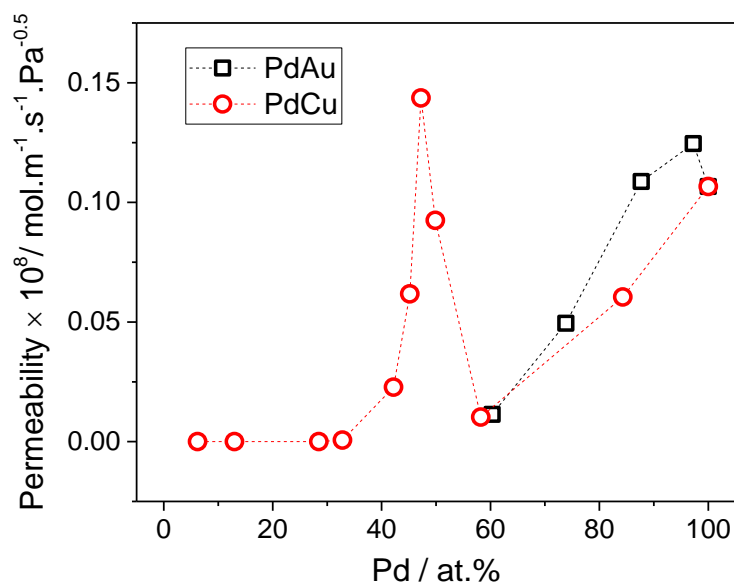


Figure 2. 6 – Hydrogen permeability for PdCu and PdAu at 75 psig upstream pure hydrogen pressure as a function of the palladium content of the alloy. The measurements were made at 350°C [5].

As shown in Fig. 2.6, there are compositions at which the hydrogen permeability of the alloy is higher than that of pure palladium. That is the case of Pd₉₇Au₃ and Pd₄₇Cu₅₃ with 1.3×10^{-8} and $1.4 \times 10^{-8} \text{ mol}\cdot\text{m}^{-1}\cdot\text{s}^{-1}\cdot\text{Pa}^{-0.5}$ permeability values, respectively, whereas in the case of Pd the H₂ permeability is $1.1 \times 10^{-8} \text{ mol}\cdot\text{m}^{-1}\cdot\text{s}^{-1}\cdot\text{Pa}^{-0.5}$. If membranes of the same thickness are considered, the increased permeability translates into higher hydrogen fluxes, namely 27 and 18% higher for the PdCu and the PdAu alloys, respectively, in comparison to a membrane of pure Pd. The increase in permeability in the case of the PdAu alloy is justified by the increase in lattice parameter caused by the introduction of gold atoms in the Pd host lattice. The higher permeability of PdCu is the result of the bcc crystal structure and its inherent higher H₂ diffusion coefficient. Indeed, at 47 at.% Pd, the diffusion coefficient of PdCu is $5 \times 10^{-5} \text{ cm}^2\cdot\text{s}^{-1}$ which is about 250 times higher than the corresponding value for pure fcc Pd ($2 \times 10^{-7} \text{ cm}^2\cdot\text{s}^{-1}$) [33]. BCC lattices have lower packing factors than fcc structures (68 vs. 74%) which ultimately facilitates hydrogen diffusion. The bcc phase of PdCu alloys is only present at temperatures below 595°C and between 34 and 47 at.% Pd [34]. Looking at the sharp peak in permeability shown in Fig. 2.6 for PdCu alloys, one may

conclude that a precise control of the composition is required if the H₂ flux is to be maximized. In fact, a variation of the composition of only 2 at.% Pd results in a decrease in permeability between 36 and 57% depending on whether the Pd content is increased or decreased, respectively.

McKinley also studied the interaction of the PdCu and PdAu alloys with H₂S [6]. These results are shown in Fig. 2.7.

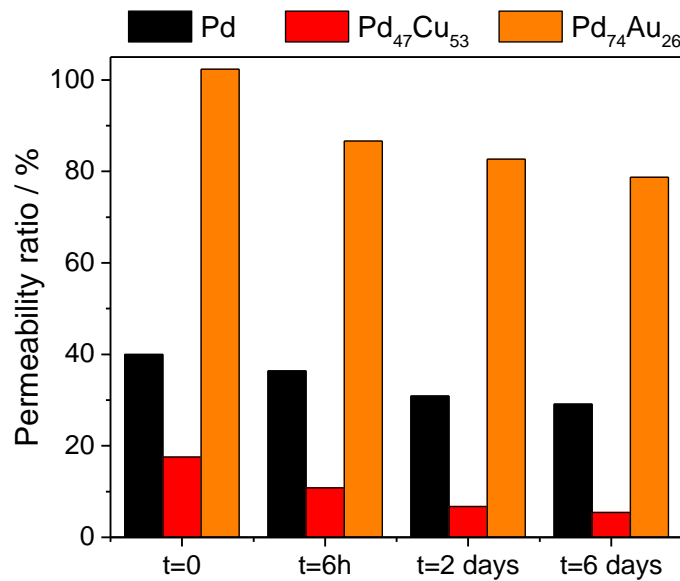


Figure 2. 7 – Variation of the permeability ratio in function of the reaction time at 350°C and at 75 psig H₂ with 4 ppm H₂S; 25.4 μm thick foils were used. Time zero (t=0) is the time immediately after introducing the H₂S mixture into the system.

The permeability ratio shown in Fig 2.7 is calculated by dividing the H₂ permeability of the alloy in the presence of H₂ plus H₂S 4 ppm with the H₂ permeability in the presence of pure hydrogen. This is equivalent to say that if a membrane presents a permeability ratio of 100%, that membrane's performance is not affected by the H₂S gas. As soon as the membranes get in contact with H₂S, t=0 in Fig. 2.7, the permeability ratios of pure Pd and Pd₄₇Cu₅₃ decrease to 40 and 18%, respectively, while that of Pd₇₄Au₂₆ is close to 100%. (These alloys have the same palladium content if using a wt.% scale, this is Pd₄₀Cu₆₀ and Pd₄₀Au₆₀). After 6 days, the PdAu alloy still

shows permeability ratio of about 80%, which is much higher than those of palladium (29%) or palladium copper alloy (5%). This experiment shows that palladium gold alloys have more tolerance to poisoning than pure palladium or palladium copper alloys. When the H₂S mixture is replaced with pure H₂, all membranes fully recover their initial H₂ permeability.

Other researchers have more recently studied the behavior of PdCu and PdAu alloys. Some of the results are summarized in table 2.2.

Table 2. 2 – Literature review of the hydrogen permeability of PdCu and PdAu alloys and the effect of hydrogen sulfide.

Membrane	Support	Preparation method	Permeability (mol·m ⁻¹ ·s ⁻¹ ·Pa ^{-0.5})	H ₂ S interaction	Ref.
Pd ₄₈ Cu ₅₂ 2 μm	Al ₂ O ₃ modified with ZrO ₂	Electroless deposition	3.1×10 ⁻⁹ at 350°C	n.a.	[35]
Pd-Cu 5-10 μm films from 83.7 to 45.6 at.% Pd	Prepared on Si substrate; tested on stainless steel plate	Magnetron sputtering	Permeability tested between 350 and 450°C; permeability at 20% of pure Pd values	n.a.	[36]
Pd ₄₇ Cu ₅₃ 25 μm foil	Not mentioned	Commercial	1.3×10 ⁻⁸ at 350°C	Complete flow inhibition after 5 min under 1000 ppm H ₂ S	[37]
Pd ₇₀ Cu ₃₀ 1000 μm tube	Not supported	Commercial	From 3×10 ⁻⁹ at 350°C to 3×10 ⁻⁸ at 900°C	Only H ₂ O, CO and CO ₂ were studied; higher inhibition occurred at 635°C and above	[38]
Pd-Cu 100 μm foils; 40-70 at.% Pd	Supported on 1 mm thick porous Hastelloy disk	Vacuum-arc melting of the unalloyed metal powders	Measurements of the permeability of the three alloys between 330 and 850°C were made.	1000 ppm H ₂ S: fcc 0-10% decrease in permeability; bcc up to 2 orders of magnitude less in permeability	[39]

			followed by rolling			
Pd-Cu 1.7-2.8 μm films 47-100 at.% Pd	Prepared on Si substrate; tested on stainless steel plate	Magnetron sputtering	At 400°C, permeability decreases from 1×10^{-8} (pure Pd) to 2×10^{-9} (60 at.% Pd) and increases to 8.2×10^{-9} (47 at.% Pd)	n.a.	[40]	
$\text{Pd}_{46}\text{Cu}_{54}$ 16.7 μm thick film	Stainless steel	Electroless plating	1.33×10^{-8} at 400°C	n.a.	[41]	
Pd-Cu 100 μm foils 28.5 to 70.5 at.%Pd	Tested on porous Hastelloy	Commercial	Membranes tested from 350 to 900°C; permeability is always lower than that of pure Pd and is dependent on temperature, composition and crystal structure.	n.a.	[21]	
$\text{Pd}_{95}\text{Au}_5$ 2.5 μm films	Prepared on Si substrate; tested on stainless steel plate	Magnetron sputtering	1.1×10^{-8} at 400°C	n.a.	[40]	
$\text{Pd}_{86.1}\text{Au}_{13.9}$ 4.8 μm film	Stainless steel coated with zirconia	Electroless plating	1.25×10^{-8} at 400°C (70% reduction in the presence of syngas) 1.55×10^{-8} at 500°C (75% reduction in the presence of syngas)	20 ppm H_2S in syngas reduces permeability to 71% (51%) of its initial value in syngas at 500°C (400°C)	[42]	
Pd-Au 25.4 μm foils from 100 to 75 at.% Pd	Tested on stainless steel support	Cold working	Membranes tested from 200 to 500°C; maximum permeability at 500°C for alloy with 2.8 at.% Au (1.9×10^{-8})	n.a.	[43]	
Pd-Au 8-31 μm films from 97 to 94 at.% Pd	Prepared on Si substrate; tested on stainless steel plate	Magnetron sputtering	Membranes tested from 200 to 500°C; maximum permeability at 500°C for alloy with 2.8-5.7 at.% Au (2.3×10^{-8})	n.a.	[43]	

Pd-Au 7-13 μm films from 100 to 86.8 at.% Pd	Stainless steel	Electroless plating	Highest permeability at 400°C for alloy with 2.3 at.% Au (1.1×10^{-8})	n.a.	[44]
Pd ₉₄ Au ₆ 24 μm film	Prepared on Si substrate; tested on stainless steel plate	Magnetron sputtering	1.82×10^{-8} at 400°C	In the presence of syngas the permeability is 64% of the initial one; with syngas plus 20 ppm H ₂ S, the permeability is 25% of the initial	[45]
Pd-Au 10-27 μm films 95.4-94.3 at.% Pd	Prepared on Si substrate; tested on stainless steel plate	Magnetron sputtering	Permeability tested between 350 and 450°C; permeability at 124% of pure Pd values for alloy with 4.6 at.% Au	n.a.	[36]
Pd ₉₁₋₉₂ Au ₉₋₈ 12 μm	Porous stainless steel with ZrO ₂	Electroless deposition	1.1×10^{-8} to 1.5×10^{-8} at 400-450°C	n.a.	[46]
PdAu 100-150 μm foils 100-75 at.% Pd	Not mentioned	Arc-melting	Permeability tested at 150-300°C and it is maximum for alloy with 11 at.% Au	n.a.	[47]
Pd ₉₁ Au ₉ 14 μm film	Zirconia-modified porous stainless steel	Electroless plating	1.1×10^{-8} at 400°C	Permeability at 40% of initial values in the presence of H ₂ S 100 ppm at 400°C; 80% of H ₂ flux recovery when going back to pure H ₂	[48]

As evidenced by table 2.2, there are different methods available for preparing PdCu and PdAu alloy-membranes. In general, metallurgical methods such as vacuum arc melting, casting, cold working and rolling are used for the preparation of stand-alone membranes [21, 37-39, 43, 47, 49-52], while thin film techniques, for example electroless deposition [35, 41, 42, 44, 46, 48, 53-57] or magnetron sputtering deposition [36, 40, 43, 45, 52], are preferred for supported

membranes. Due to their thicknesses, membranes prepared by metallurgical methods may need to be positioned in the permeation chamber on top of a porous support while thin films may be detached from their initial substrate and transferred to a porous one as well. During the permeation testing the support provides mechanical strength to the membrane, preventing it do deform or rupture in the presence of the high gas pressure difference. Metallic (for example stainless steel) and ceramic (sintered alumina, yttria, zirconia or others) porous supports are available. Metallic supports are commonly used in combination with a diffusion barrier placed between the support and membrane. This is a strategy aims to prevent intermetallic mixing between the elements of the membrane and those of the support that could otherwise lead to decreased permeability values [21]. Both planar membranes and cylindrical structures are possible [38].

Consistently with the work of McKinley shown in Fig. 2.6 above, these most recent studies have emphasized the fact that the permeability of PdCu and PdAu alloys is dependent on the composition, temperature and crystal structure, the latter in the case of PdCu. The alloys with the highest permeability, which is comparable with that of pure Pd are the bcc-Pd₄₇Cu₅₃ [5, 21, 40] and PdAu with Au content of 3-10 at.% [5, 43, 44]. The experimental results are to a great extent in agreement with theoretical calculations [36, 47, 58-65].

Pure palladium reacts with H₂S that decomposes on the surface of the palladium forming most of the times PdS₄. PdS₄ decreases the capacity of the palladium to cleave the H-H bond, and the overall result is that the flow of hydrogen decreases substantially [66]. PdCu and PdAu alloys do show less poisoning to H₂S as shown in table 2.2. As examples, the alloy with composition Pd₇₁Cu₂₉ shows no flux inhibition in the presence of 1000 ppm H₂S at temperatures between 330 and 727°C [39], while Pd₇₃Au₂₇ shows about 20% reduction in H₂ flow in the presence of 4 ppm H₂S [6]. Prevention of poisoning could be due to a dilution effect of palladium at the surface of these alloys contributing to unfavorable structures for the reaction of palladium with the hydrogen sulfide to take place [52, 67]. However, many factors influence the interaction of H₂S with the alloy, namely the alloy composition, temperature, concentration of H₂S and the crystal structure. Unfortunately, the alloys of PdCu and PdAu with the highest permeability are also the ones that show the highest deactivation in the presence of H₂S. For example, at temperatures lower than 600°C and in contact with 1000 ppm H₂S, the bcc alloy Pd₄₇Cu₅₃ shows permeabilities between 1

to 20% of the initial H₂S-free permeability. For higher temperatures, where only the fcc phase is present, no decrease in permeability is observed [39]. In the case of the alloy Pd₉₄Au₆, the presence of syngas with 20 ppm H₂S leads to a 75% decrease in permeability at 400°C [45].

2.4.2. PdCuAu ternary alloys

Several research groups have investigated the applicability of PdCuAu alloys for the purification of hydrogen. The PdCuAu ternary alloys previously reported in the literature have been prepared using several physical methods such as arc melting [68], vacuum melting [69-71], vacuum arc melting [72], or dc magnetron sputtering [36, 40, 73], followed or not by several annealing and (cold) rolling steps. Pulsed laser deposition has also been used [74]. The studies have concentrated on the measurement of the thermodynamic and hydrogen solubility properties [68, 74], and the measurements of hydrogen permeability [36, 40, 73]. Detailed first-principles calculations are also available [36, 73, 75, 76]. The group of Y. Sakamoto *et al.* [68] prepared PdCuAu alloys by arc melting up to 20% (Cu+Au), where the fraction of copper equals the fraction of gold. From gas phase measurements, they concluded that these membranes have smaller low pressure solubility but larger high pressure solubility than PdCu membrane with the same Pd content. Furthermore, there is no α to β phase transition for concentrations above 26% (Cu+Au). However, the hydrogen solubility in the ternary alloys is never higher than that of pure Pd. Accordingly, the atomic ratios H/M decrease from 0.61 to 0.38 as the (Cu+Au) content is increased from 5 to 20 at.%. The groups of L. Semidey-Flecha *et al.* [75] and of K. E. Coulter *et al.* [36] have both performed calculations to predict the behavior of the PdCuAu alloys towards hydrogen purification. Thin films were also prepared by dc magnetron sputtering and the permeability of hydrogen was measured in the gas phase. At 350°C, the membrane with the best performance had a composition of Pd_{83.8}Cu_{9.5}Au_{6.6} and a permeability which is about 80% of that of pure palladium. These experimental results are consistent with the DFT calculations [75]. Finally, the group of T.A. Peters *et al.* [40] showed that the hydrogen permeability decreases from 1.0×10^{-8} to 4.2×10^{-9} and to $3.3 \times 10^{-9} \text{ mol} \cdot \text{m}^{-1} \cdot \text{s}^{-1} \cdot \text{Pa}^{-0.5}$ for Pd, Pd₇₂Cu₂₇Au₁ and Pd₇₀Cu₃₀, respectively.

More recently, Tarditi and coworkers [54] published their results on the hydrogen permeability of 14 μm thick PdCuAu membranes prepared by electroless plating on porous stainless steel disks. Three different compositions were prepared, namely: Pd₇₀Cu₂₅Au₅,

Pd₆₀Cu₃₇Au₃, and Pd₆₉Cu₁₄Au₁₇. Their H₂ permeability at 400°C was 1.9, 2.9 and 9.7×10⁻⁹ mol·m⁻¹·s⁻¹·Pa^{-0.5}, respectively. These permeabilities correspond to 16, 24 and 73% of their Pd reference, respectively. In the presence of H₂S, the permeability of the alloys decreases by about 50-57%, whereas pure Pd decreases by 85%. These alloys do show less H₂S poisoning, and are a promising alternative to pure Pd. All the alloys are less expensive than pure Pd, except the alloy with 17 at.% Au (1 g of this alloys would cost about 27 USD, but 1 g of Pd is about 24 USD [77]).

2.5. Conclusions and perspectives

Dense palladium membranes are an important alternative to pressure swing adsorption or cryogenic distillation that could decrease operational costs in hydrogen purification and production. In this context, alloys of palladium with copper and gold (binary or ternary) are particularly interesting because they show less or no embrittlement, reduce H₂S poisoning (depending on composition) and are potentially less expensive than pure Pd. Several studies have been published that investigate the PdCu, PdAu and also PdCuAu alloys applicability towards hydrogen purification. However, all of the studies are concerned with the fcc phase of PdCuAu, while the bcc phase continues practically unexplored in its applications towards hydrogen permeability. The bcc-PdCuAu is expected to have as high permeability as the binary alloy bcc-PdCu, and higher H₂S-poisoning resistance due to the presence of gold. In the current work, we aim to study in detail PdCuAu ternary alloys, not only the fcc phase, but most importantly, the bcc phase. Bearing this aim in mind, PdCuAu alloys were prepared by three different methods (electrodeposition, sputter deposition and mechanical alloying), and the hydrogen solubility and hydrogen permeability was measured. The influence of composition and crystallographic structure were evaluated. Most importantly, this work aims to verify if bcc-PdCuAu alloys have a permeability comparable with that of pure palladium or bcc-PdCu alloys and to verify if bcc-PdCuAu alloys are resistant to H₂S poisoning.

2.6. References

- [1] Greenwood NN, Earnshaw A. Chemistry of the Elements. Second ed: Butterworth-Heinemann; 1997.
- [2] Grashoff GJ, Pilkington CE, Corti CW. Purification of hydrogen. Platinum Metals Review. 1983;27:157-69.
- [3] Graham T. On the Absorption and Dialytic Separation of Gases by Colloid Septa. Philosophical Transactions of the Royal Society of London. 1866;156:399-439.
- [4] Cottington IE. Palladium; or New Silver - no stranger to scientific controversy. Platinum Metals Review. 1991;35:141-51.
- [5] Mckinley DL. Method for hydrogen separation and purification. United States: US Patent 3,439,474; 1969.
- [6] Mckinley DL. Metal alloy for hydrogen separation and purification. United States: US patent 3,350,845; 1967.
- [7] Allard KD, Maeland AJ, Simons JW, Flanagan TB. Application of the electron-donation model for hydrogen absorption to palladium-rich alloys. Hydrogen-gold-palladium. The Journal of Physical Chemistry. 1968;72:136-43.
- [8] Fletcher S. PhD Thesis:Thin Film Palladium-Yttrium Membranes for Hydrogen Separation. Birmingham: The University of Birmingham; 2009.
- [9] Phair JW, Donelson R. Developments and Design of Novel (Non-Palladium-Based) Metal Membranes for Hydrogen Separation. Industrial & Engineering Chemistry Research. 2006;45:5657-74.

- [10] Flanagan TB, Wang D. Temperature dependence of H permeation through Pd and Pd alloy membranes. *The journal of physical chemistry A*. 2012;116:185-92.
- [11] Steward SA. Review of Hydrogen Isotope Permeability Through Materials. Lawrence Livermore National Laboratory; 1983.
- [12] Dolan MD. Non-Pd BCC alloy membranes for industrial hydrogen separation. *Journal of Membrane Science*. 2010;362:12-28.
- [13] Adams BD, Chen A. The role of palladium in a hydrogen economy. *Materials Today*. 2011;14:282-9.
- [14] Cser L, Torok G, Krexner G, Prem M, Sharkov I. Neutron holographic study of palladium hydride. *Applied Physics Letters*. 2004;85:1149-51.
- [15] Yun S, Oyama S. Correlations in palladium membranes for hydrogen separation: A review. *Journal of Membrane Science*. 2011;375:28-45.
- [16] Lewis FA. *The Palladium Hydrogen System*. New York: Academic Press; 1967.
- [17] Flanagan TB, Sakamoto Y. Hydrogen in disordered and ordered palladium alloys. *Platinum Metals Review*. 1993;37:26-37.
- [18] Kleperis J, Wójcik G, Czerwinski A, Skowronski J, Kopczyk M, Beltowska-Brzezinska M. Electrochemical behavior of metal hydrides. *Journal of Solid State Electrochemistry*. 2001;5:229-49.
- [19] Birry L, Lasia A. Effect of crystal violet on the kinetics of H sorption into Pd. *Electrochimica Acta*. 2006;51:3356-64.

- [20] Ockwig NW, Nenoff TM. Membranes for Hydrogen Separation. *Chemical reviews*. 2007;107:4078-110.
- [21] Howard BH, Killmeyer RP, Rothenberger KS, Cugini AV, Morreale BD, Enick RM, et al. Hydrogen permeance of palladium-copper alloy membranes over a wide range of temperatures and pressures. *Journal of Membrane Science*. 2004;241:207-18.
- [22] Nenoff TM, Spontak RJ, Aberg CM. Membranes for hydrogen purification: An important step toward a hydrogen-based economy. *Mater Res Soc Bull*. 2006;31:735-41.
- [23] Anthony F. Sammells MVM. *Nonporous Inorganic Membranes* Wiley-VCH; 2006.
- [24] Adhikari S, Fernando S. *Hydrogen Membrane Separation Techniques*. *Industrial & Engineering Chemistry Research*. 2006;45:875-81.
- [25] Ma YH, Mardilovich IP, Engwall EE. Thin Composite Palladium and Palladium/Alloy Membranes for Hydrogen Separation. *Annals of the New York Academy of Sciences*. 2003;984:346-60.
- [26] Baranowski B, Majchrzak S, Flanagan TB. Volume increase of fcc metals and alloys due to interstitial hydrogen over a wide-range of hydrogen contents. *Journal of Physics F-Metal Physics*. 1971;1:258-61.
- [27] Flanagan TB, Chisdes DM. Solubility of hydrogen (1 atm, 298 K) in some copper/palladium alloys. *Solid State Communications*. 1975;16:529-32.
- [28] Martin MH, Galipaud J, Tranchot A, Roué L, Guay D. Measurements of hydrogen solubility in $\text{Cu}_x\text{Pd}_{100-x}$ thin films. *Electrochimica Acta*. 2013;90:615-22.

- [29] Galipaud J, Martin MH, Roué L, Guay D. Measurement of Hydrogen Solubility in Pd_xCu_{100-x}Thin Films Prepared by Pulsed Laser Deposition: An Electrochemical in Situ X-Ray Diffraction Analysis. *The Journal of Physical Chemistry C*. 2013;117:2688-98.
- [30] Maeland A, Flanagan TB. X-Ray and Thermodynamic Studies of the Absorption of Hydrogen by Gold-Palladium Alloys. *The Journal of Physical Chemistry*. 1965;69:3575-81.
- [31] Maeland AJ, Flanagan TB. Comparison of hydrogen and deuterium solubility in palladium-rich alloys, gold-palladium. *The Journal of Physical Chemistry*. 1967;71:1950-2.
- [32] Flanagan TB, Lewis FA. Electrode Potentials of the Palladium—Hydrogen System. *The Journal of Chemical Physics*. 1958;29:1417-8.
- [33] Piper J. Diffusion of Hydrogen in Copper-Palladium Alloys. *Journal of Applied Physics*. 1966;37:715.
- [34] Subramanian PR, Laughlin DE. Cu-Pd (Copper-Palladium). *Journal of Phase Equilibria*. 1991;12:231-43.
- [35] Yuan L, Goldbach A, Xu H. Segregation and H₂ Transport Rate Control in Body-Centered Cubic PdCu Membranes. *The Journal of Physical Chemistry B*. 2007;111:10952-8.
- [36] Coulter KE, Way JD, Gade SK, Chaudhari S, Sholl DS, Semidey-Flecha L. Predicting, Fabricating, and Permeability Testing of Free-Standing Ternary Palladium-Copper-Gold Membranes for Hydrogen Separation. *Journal of Physical Chemistry C*. 2010;114:17173-80.
- [37] O'Brien CP, Howard BH, Miller JB, Morreale BD, Gellman AJ. Inhibition of hydrogen transport through Pd and Pd₄₇Cu₅₃ membranes by H₂S at 350°C. *Journal of Membrane Science*. 2010;349:380-4.

- [38] Iyoha O, Howard B, Morreale B, Killmeyer R, Enick R. The Effects of H₂O, CO and CO₂ on the H₂ Permeance and Surface Characteristics of 1 mm Thick Pd80wt%-Cu Membranes. *Top Catal.* 2008;49:97-107.
- [39] Morreale B. Effect of hydrogen-sulfide on the hydrogen permeance of palladium-copper alloys at elevated temperatures. *Journal of Membrane Science.* 2004;241:219-24.
- [40] Peters TA, Kaleta T, Stange M, Bredesen R. Development of thin binary and ternary Pd-based alloy membranes for use in hydrogen production. *Journal of Membrane Science.* 2011;383:124-34.
- [41] Gade SK, Thoen PM, Way JD. Unsupported palladium alloy foil membranes fabricated by electroless plating. *Journal of Membrane Science.* 2008;316:112-8.
- [42] Lewis AE, Zhao H, Syed H, Wolden CA, Way JD. PdAu and PdAuAg composite membranes for hydrogen separation from synthetic water-gas shift streams containing hydrogen sulfide. *Journal of Membrane Science.* 2014;465:167-76.
- [43] Gade SK, Coulter KE, Way JD. Effects of fabrication technique upon material properties and permeation characteristics of palladium-gold alloy membranes for hydrogen separations. *Gold Bulletin.* 2010;43:287-97.
- [44] Gade SK, Payzant EA, Park HJ, Thoen PM, Way JD. The effects of fabrication and annealing on the structure and hydrogen permeation of Pd–Au binary alloy membranes. *Journal of Membrane Science.* 2009;340:227-33.
- [45] Coulter KE, Way JD, Gade SK, Chaudhari S, Alptekin GO, DeVoss SJ, et al. Sulfur tolerant PdAu and PdAuPt alloy hydrogen separation membranes. *Journal of Membrane Science.* 2012;405-406:11-9.

- [46] Tarditi A, Gerboni C, Cornaglia L. PdAu membranes supported on top of vacuum-assisted ZrO₂-modified porous stainless steel substrates. *Journal of Membrane Science*. 2013;428:1-10.
- [47] Flanagan TB, Wang D. Hydrogen Permeation through fcc Pd-Au Alloy Membranes. *Journal of Physical Chemistry C*. 2011;115:11618-23.
- [48] Braun F, Tarditi AM, Miller JB, Cornaglia LM. Pd-based binary and ternary alloy membranes: Morphological and perm-selective characterization in the presence of H₂S. *Journal of Membrane Science*. 2014;450:299-307.
- [49] Iyoha O, Enick R, Killmeyer R, Morreale B. The influence of hydrogen sulfide-to-hydrogen partial pressure ratio on the sulfidization of Pd and 70 mol% Pd–Cu membranes. *Journal of Membrane Science*. 2007;305:77-92.
- [50] Morreale BD, Ciocco MV, Enick RM, Morsi BI, Howard BH, Cugini AV, et al. The permeability of hydrogen in bulk palladium at elevated temperatures and pressures. *Journal of Membrane Science*. 2003;212:87-97.
- [51] Matsumura Y. A basic study of high-temperature hydrogen permeation through bcc Pd–Cu alloy foil. *Separation and Purification Technology*. 2014;138:130-7.
- [52] Gade SK, DeVoss SJ, Coulter KE, Paglieri SN, Alptekin GO, Way JD. Palladium–gold membranes in mixed gas streams with hydrogen sulfide: Effect of alloy content and fabrication technique. *Journal of Membrane Science*. 2011;378:35-41.
- [53] Pan X, Kilgus M, Goldbach A. Low-temperature H₂ and N₂ transport through thin Pd₆₆Cu₃₄H_x layers. *Catalysis Today*. 2005;104:225-30.

- [54] Tarditi AM, Imhoff C, Braun F, Miller JB, Gellman AJ, Cornaglia L. PdCuAu ternary alloy membranes: Hydrogen permeation properties in the presence of H₂S. *Journal of Membrane Science*. 2015;479:246-55.
- [55] Kulprathipanja A, Alptekin GO, Falconer JL, Way JD. Pd and Pd–Cu membranes: inhibition of H₂ permeation by H₂S. *Journal of Membrane Science*. 2005;254:49-62.
- [56] Chen C-H, Ma YH. The effect of H₂S on the performance of Pd and Pd/Au composite membrane. *Journal of Membrane Science*. 2010;362:535-44.
- [57] Pomerantz N, Ma YH. Effect of H₂S on the Performance and Long-Term Stability of Pd/Cu Membranes. *Industrial & Engineering Chemistry Research*. 2009;48:4030-9.
- [58] Huang W, Opalka SM, Wang D, Flanagan TB. Thermodynamic modelling of the Cu–Pd–H system. *Calphad*. 2007;31:315-29.
- [59] Kamakoti P, Morreale BD, Ciocco MV, Howard BH, Killmeyer RP, Cugini AV, et al. Prediction of hydrogen flux through sulfur-tolerant binary alloy membranes. *Science*. 2005;307:569-73.
- [60] Kamakoti P, Sholl D. Ab initio lattice-gas modeling of interstitial hydrogen diffusion in CuPd alloys. *Physical Review B*. 2005;71.
- [61] Kamakoti P. A comparison of hydrogen diffusivities in Pd and CuPd alloys using density functional theory. *Journal of Membrane Science*. 2003;225:145-54.
- [62] Semidey-Flecha L, Sholl DS. Combining density functional theory and cluster expansion methods to predict H₂ permeance through Pd-based binary alloy membranes. *The Journal of Chemical Physics*. 2008;128:144701.

- [63] Chandrasekhar N, Sholl DS. Computational study of hydrogen induced lattice rearrangement and its influence on hydrogen permeance in Pd–Au alloys. *Journal of Alloys and Compounds*. 2014;609:244-52.
- [64] Sonwane CG, Wilcox J, Ma YH. Achieving optimum hydrogen permeability in PdAg and PdAu alloys. *The Journal of Chemical Physics*. 2006;125:184714.
- [65] Xu S, Sood P, Liu ML, Bongiorno A. First-principles study of hydrogen permeation in palladium-gold alloys. *Applied Physics Letters*. 2011;99:181901.
- [66] O'Brien CP, Gellman AJ, Morreale BD, Miller JB. The hydrogen permeability of Pd₄S. *Journal of Membrane Science*. 2011;371:263-7.
- [67] Venezia AM, La Parola V, Nicolì V, Deganello G. Effect of Gold on the HDS Activity of Supported Palladium Catalysts. *Journal of Catalysis*. 2002;212:56-62.
- [68] Sakamoto Y, Ishimaru N, Mukai Y. Thermodynamics of Solution of Hydrogen in Pd-Cu and Pd-Cu-Au Solid Solution Alloys. *Berichte der Bunsen-gesellschaft fuer physikalische Chemie*. 1991;95:680-8.
- [69] Winn H, Udoh K, Tanaka Y, Hernandez RI, Takuma Y, Hisatsune K. Phase transformations and age-hardening behaviors related to Au₃Cu in Au-Cu-Pd alloys. *Dental Materials Journal*. 1999;18:218-34.
- [70] Winn H, Tanaka Y, Shiraishi T, Udoh K, Miura E, Hernandez RI, et al. Two types of checkerboard-like microstructures in Au-Cu-Pd ternary alloys. *Journal of Alloys and Compounds*. 2000;306:262-9.
- [71] Ohta M, Shiraishi T, Yamane M. Phase-transformation and age-hardening of Au-Cu-Pd ternary alloys. *Journal of Materials Science*. 1986;21:529-35.

- [72] Volkov AY. Structure and mechanical properties of CuAu and CuAuPd ordered alloys. *Gold Bulletin*. 2004;37:208-15.
- [73] Coulter KE. High permeability ternary palladium alloy membranes with improved sulfur and halide tolerance U.S. Department of Energy National Energy Technology Laboratory; 2011.
- [74] Galipaud J, Martin MH, Roué L, Guay D. Pulsed Laser Deposition of PdCuAu Alloy Membranes for Hydrogen Absorption Study. *The Journal of Physical Chemistry C*. 2015;119:26451-8.
- [75] Semidey-Flecha L, Ling C, Sholl DS. Detailed first-principles models of hydrogen permeation through PdCu-based ternary alloys. *Journal of Membrane Science*. 2010;362:384-92.
- [76] Kamakoti P, Morreale BD, Ciocco MV, Howard BH, Killmeyer RP, Cugini AV, et al. Prediction of Hydrogen Flux Through Sulfur-Tolerant Binary Alloy Membranes. *Science*. 2005;307:569-73.
- [77] <http://www.kitco.com/> (2015-07-06).

3. Synthesis and characterization techniques

In this chapter, the methods used for the synthesis of the palladium-copper-gold alloys will be presented (section 3.1), followed by a description of the method used in the preparation of standalone membranes (section 3.2). Finally, an introduction to the characterization techniques will be given in section 3.3.

3.1. Synthesis of PdCuAu ternary alloys

Palladium-copper-gold alloys were prepared by three different methods, namely electrodeposition, sputter deposition and mechanical alloying. The first two methods allowed the production of thin films supported on a Ti substrate, while mechanical alloying was used to prepare the bulk material. Some of the characteristics of the aforementioned methods are compared in table 3.1.

Table 3. 1 – Comparison between the preparation methods used for the synthesis of PdCuAu alloys.

	Electrodeposition	Sputter deposition	Mechanical alloying
Starting materials	Pd(NO ₃) ₂ , Cu(NO ₃) ₂ and Au(OH) ₃	Pd, Cu, Au metallic targets	Pd, Cu, Au metallic powders
Synthesis time	minutes	minutes	hours
Substrate	Conductive	Conductive and non- conductive	Bulk synthesis
Film thickness for 10 min deposition (nm)	<1000	<500	Not applicable
Scaling up	Easy	Easy	Extremely easy
Instruments maintenance	Practically inexistent	Clean-up of vacuum chamber required after each session	Every ~100 hours of milling
Relative cost	Low	High	Low

Although the three methods are fundamentally different, they all succeed in producing single-phase ternary alloys, as it will be shown in chapters 4, 5 and 6. In electrodeposition, the starting materials are salts of the metals in oxidation state +2 (Pd and Cu) or +3 (Au), while the other two methods rely on the use of metallic targets and metallic powders (zero oxidation state). Both electrodeposition and sputter deposition allow the production of thin films less than 1000 and 500 nm, respectively, in a matter of minutes, while mechanical alloying produces bulk alloy powders within a few hours. In sputter deposition both conductive and non-conductive substrates can be use, while electrodeposition requires the substrates to be conductive. However in the current work only Ti, which is electrically conductive, was employed. Interestingly, thin films can be prepared from the alloy powder produced by mechanical alloying, by resorting to some dispersing technology, such as cold spray deposition [1], colloidal spray deposition [2], or paste-painting method [3]. Electrodeposition and mechanical alloying are relatively inexpensive when compared to sputter deposition and maintenance of the equipment is also not as costly or difficult. From the three methods, mechanical alloying seems to be the easiest one to scale up the production of the alloys if industrial application is required. In the context of this work, electrodeposition and sputter deposition were used as tools to access the range of compositions at which the ternary fcc and bcc phase alloys are stable, and to measure the electrochemical uptake of hydrogen. Therefore, the preparation of the films by these two techniques was not optimized, in terms of thickness and morphology for the use in gas phase separation. A more detailed description of each method follows.

3.1.1. Preparation of PdCuAu films by electrodeposition

3.1.1.1. Background

Electrodeposition involves the reduction of metal ions on a substrate using an external supply of electrons [4]. It finds application in a variety of areas, such as computer technology (fabrication of integrated circuits and magnetic recording devices), coatings (protective or decorative) [5, 6], and others like in the development of thermoelectric materials [7], or hydrogen permeable membranes.

The first step of electrodeposition is the migration of the hydrated metal ions from the solution to the surface of the substrate acting as the cathode. Migration occurs by diffusion,

convection and also as a result of the imposed electrical field [6]. Surfaces usually have defects, (vacancies, impurities, grain boundaries, and dislocations) that can be seen as crystallization seeds promoting the adsorption of the metal cations. In particular, kink sites are considered the places where cations are adsorbed and reduced [4]. Afterwards, formation of the deposit occurs through different mechanisms (layer growth or three dimensional crystallite growth).

Not only individual metals can be deposited, but most importantly, a combination of two, three or even more elements may be co-deposited provided the experimental conditions are adequate. Co-deposition is advantageous for alloys whose properties (mechanical, electrical or others) can be different from the properties of the individual metals. The standard electrode potential of different metals should not differ much from one another for the metals to co-deposit. Nonetheless, there are methods to bring closer together the standard potentials of two metals that would otherwise not co-deposit. The use of complexing agents is one of the available strategies which has been applied, for example, to the much studied copper-zinc system. In this case, cyanide is used to complex the copper ions [8, 9] and make the deposition successful. Another possibility is by individually deposit each metal, layer by layer. In that case, alloy formation is achieved by a subsequent heat-treatment that promotes interdiffusion and consequently alloy formation [8]. In our system, Pd, Cu and Au were co-deposited without recurring to such strategies, as described below (section 3.1.1.2).

3.1.1.2. Experimental considerations

$\text{Pd}(\text{NO}_3)_2$ (Alfa Aesar, 99.9% metal basis), $\text{Cu}(\text{NO}_3)_2$ (Alfa Aesar Puratronics, 99.999% metal basis) and $\text{Au}(\text{OH})_3$ (Aldrich, 99.5% metal basis) were used to prepare three 10 mM stock solutions in 0.35 M HNO_3 . The nitric acid solution was prepared by dilution from concentrated (69.2% w/w) commercially available HNO_3 solution (Fischer Scientific, trace metal grade). Contrary to the palladium and copper nitrate salts which are both very soluble in diluted nitric acid, gold (III) hydroxide is only sparingly soluble in that solution. For this reason, $\text{Au}(\text{OH})_3$ was first dissolved in a 1:3 mixture of concentrated HNO_3 :HCl before being added to the 0.35 M HNO_3 solution. The final concentration of HCl in the electrolytic bath was never higher than 4 vol%. De-ionized water with a resistivity better than $18 \text{ M}\Omega \text{ cm}^{-1}$ (Millipore, Milli-Q gradient) was used. Argon gas (5.0 from Praxair) was used whenever an inert atmosphere was required.

The deposits were made on titanium substrates. The titanium was acquired from Alfa Aesar either in the form of rods or plates that were then cut to fit to the dimensions of the electrochemical cell used for the electrodeposition. For better adhesion of the metallic film to the surface of the titanium, the substrates were heated in a saturated oxalic acid (Fisher Scientific) solution for about one hour [10]. During this heating period, the oxalic acid solution changes color from transparent to brownish, indicating the formation of titanium oxalate soluble complexes [11], and the end point of the etching. By reacting with substrates, the oxalic acid effectively removes the titanium surface oxide layer. The substrates were then rinsed with de-ionized water, dried with paper tissues, polished with SiC sandpaper (BuehlerMetII 320/P400 grit from Buehler), and finally washed with de-ionized water before being dried. The pretreatment of the substrates was made on the same day of the electrodeposition experiments.

The co-electrodeposition procedure was performed in an in-house developed electrochemical cell [12, 13] which is represented in Fig. 3.1.

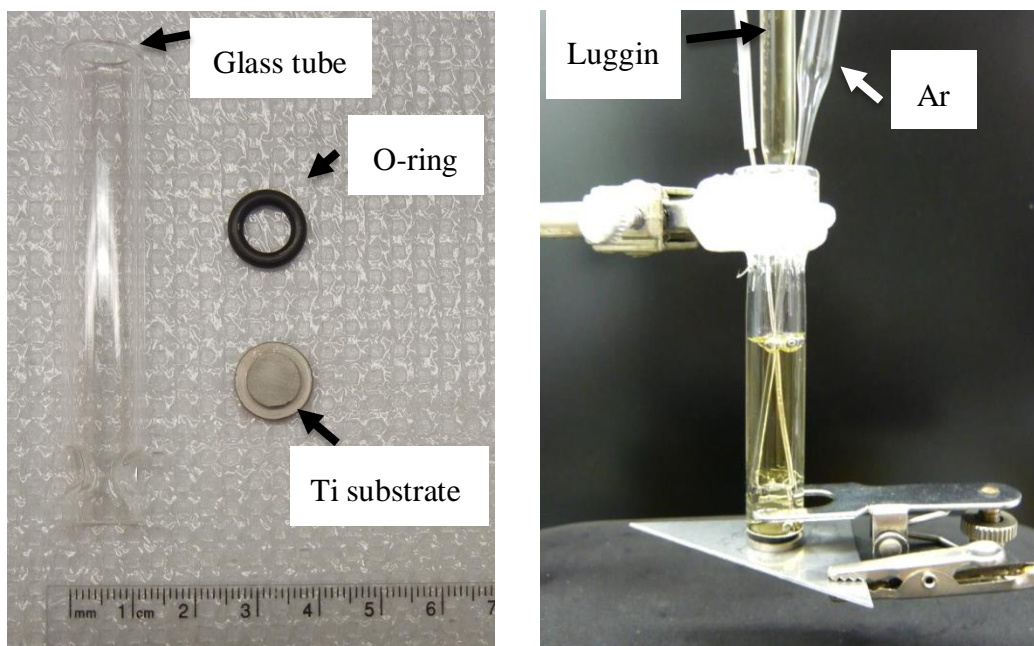


Figure 3. 1 – Unassembled electrodeposition cell (left) and fully functional cell (right, adapted from[12]).

Essentially the electrochemical cell that was used (Fig 3.1) consists of a glass tube 7 cm high with 1.2 and 0.9 cm of outer and inner diameter, respectively. This tube is placed vertically and is sitting on top of the substrate. The electrolytic bath (less than 5 ml) is poured inside the cell and leaks are prevented by the use of an o-ring clamped between the substrate and the glass rim of the tube. A titanium wire is used as the counter-electrode and the potential is controlled by a Biologic SP300 instrument with EC-lab V10.02 software. A saturated calomel electrode (SCE, from Accumet) with a Luggin capillary was used as the reference electrode. All experiments were performed at room temperature and Ar was bubbled in the solution at all times. The ternary alloy films were prepared by pulsed co-electrodeposition, with $t_{on} = 5$ ms; $t_{off} = 5$ ms; $E_{on} = -0.5$ V; $E_{off} = -0.1$ V, during ten minutes, following a procedure that was developed by Allemand and coworkers [14]. The composition of the electrolytic bath was varied by mixing different proportions of the Pd(II), Cu(II) and Au(III) stock solutions. The geometrical surface area of the deposits exposed to the solution was 0.6 cm², which corresponds to the area limited by inner diameter of the glass tube. Deposits were less than 1000 nm thick.

3.1.2. Preparation of PdCuAu films by magnetron sputter deposition

3.1.2.1. Background deposition

Over the years, magnetron sputter deposition has become increasingly present in the industry for the production of films and coatings [15, 16]. Sputtering occurs when charged particles collide with a target (cathode), causing the ejection of atoms from the surface [17-20]. The ejected atoms will deposit upon impact on a substrate (anode) usually located opposite to the target. The colliding particles used in magnetron sputter deposition originate from a plasma produced from the electrical discharge of an inert gas. Magnets are placed behind the cathode [19] to confine electrons closer to the target. Consequently, there is an increase of the ionization efficiencies [16] and the inert gas working pressure can be lowered, decreasing the possibility of incorporating inert gas atoms, such as Ar, in the lattice of the growing film [21]. The latter effect is not only undesirable, as it introduces strain to the growing lattice, but is most times irreversible, even with subsequent annealing [22]. Both conductors and insulators may be used as target materials, provided that in the latter case a radio frequency (rf) diode is used instead of a direct current (dc) diode. This strategy avoids the build-up of a positive surface charge at the surface of the insulator that would otherwise annihilate the plasma [21]. In the present work, both rf and dc sources were

used, not because of the electrical properties of the targets, but because it was the only configuration available that allowed operating the three targets, palladium, copper and gold, at the same time.

3.1.2.2. Experimental considerations

Sputter deposition was performed on titanium $1.5 \times 1.5 \text{ cm}^2$ substrates cut from commercially available titanium foils 0.25 mm thick (Alfa Aesar). The substrates' surface was first made rougher with the help of SiC sandpaper (BuehlerMetII 320/P400 grit from Buehler) in order to improve the adhesion of the sputtered films and to prevent delamination upon hydrogen absorption. A simple cleaning of the substrates followed which involved first sonicating in acetone for 15 minutes and then another 15 minutes in isopropanol. Finally, the substrates were rinsed with isopropanol and quickly dried with a nitrogen stream.

Thin films of PdCuAu ternary alloys on the Ti substrates were prepared by dc/rf magnetron sputtering (CMS-18 from Kurt J. Lesker Company) at the Laboratory of Micro- and Nanofabrication at INRS-EMT. Targets of the pure metals (>99.5%) were acquired from Kurt J. Lesker Company. The system was operated at 7×10^{-7} Pa background pressure and 0.5 Pa Ar deposition pressure. All depositions were performed for 3 minutes by sputtering all three metal targets at the same time, while the substrates were rotated at 10 rpm. Different compositions of the films were obtained by varying the power applied on each metallic target. For Pd (dc power source), the power varied from 120 to 340 W, which is equivalent to an increase in the deposition rate from 5 to $16 \text{ \AA} \cdot \text{s}^{-1}$. In the case of Cu (rf power source,) the power used was between 100 and 500 W, corresponding to 4.1 and $7.3 \text{ \AA} \cdot \text{s}^{-1}$ deposition rate, respectively, while the power of the Au target (rf power source) was 80 W (corresponding to a deposition rate of $0.9 \text{ \AA} \cdot \text{s}^{-1}$). The deposition rates were estimated with a microbalance using previous calibration of the equipment. The films are on average 300 nm thick.

3.1.3. Preparation of PdCuAu bulk alloys by mechanical alloying

3.1.3.1. Background

The metallurgical process of mechanical alloying is achieved by high-energy ball milling. It is a relatively new technique, first developed at the end of the 1960s at the International Nickel Company [23, 24]. From an experimental point of view this is a very simple process, which involves milling of the precursor powders in a grinding material. The milling occurs inside a vessel which is energetically shaken for a certain amount of time. It is generally agreed that the mechanical alloying proceeds through continuous cold welding and fracturing of the powder particles [24, 25]. When working with ductile materials, welding is favored and a process control agent (PCA), such as NaCl, is added in order to avoid extensive welding. Upon collision of the balls and collisions with the walls of the vessel, the powders trapped in between are continuously deformed in a process called cold welding, leading to the formation of a laminated structure. Atomic interdiffusion is promoted with further deformation of this layered structure. Notwithstanding, a raise in temperature as result of the collisions may occur that will also contribute to atomic interdiffusion, ultimately leading to the formation of the alloy, provided enough time is given.

Mechanical alloying is used especially in systems that are difficult to prepare by other metallurgical techniques [25]. The powders obtained from ball milling may be used in a variety of ways, for instance in coatings [1, 2, 23], as the starting constituents of wrought materials [23] or they can be consolidated in pellets [26]. The latter strategy was the one used in the current work.

3.1.3.2. Experimental considerations

Palladium (99.99%, 200 mesh, ACI Alloys inc.), copper (99.9%, -170 to +270 mesh, Alfa Aesar), and gold (99.9%, -200 mesh, Alfa Aesar) were charged into a cylindrical stainless steel crucible along with NaCl (PCA, 2 wt%) and three stainless steel milling balls (one of 2 g and two of 1 g). Crucibles and balls were cleaned before the syntheses by two twenty minute-steps of milling, firstly by charging the crucible with balls, ethanol and glass, and secondly just with the balls and ethanol. The amounts used of each solid in the different preparations are listed in table 3.2. The sealing of the crucible and weighting of the solids was made inside an Ar-filled glove

box. Afterwards, the crucible was transferred to a Spex[®] SamplePrep 8000M mixer/mill and milling was performed during 18h.

Table 3. 2 – Different ball milling conditions used to prepare the PdCuAu alloys.

Nominal composition (at.%)	Pd (g)	Cu (g)	Au (g)	NaCl (g)	Total solids (g)	Ball to powder mass ratio (%)
Pd ₄₀ Cu ₆₀	1.034	0.926	0.000	0.040	2.000	2
Pd ₄₀ Cu ₅₇ Au ₃	0.985	0.838	0.137	0.040	2.000	2
Pd ₄₀ Cu ₅₃ Au ₇	0.927	0.733	0.300	0.040	2.000	2
Pd ₄₀ Cu ₄₉ Au ₁₁	0.875	0.640	0.445	0.040	2.000	2

3.1.4. Preparation of PdCuAu membranes for gas phase measurements

The preparation of PdCuAu alloy membranes from ball milled powders involved a series of steps that comprised pellet pressing, two different heat treatments, sintering, cold rolling and polishing. All heat treatments were performed under a gas mixture of Ar 5% H₂ (Air Liquide), except when using pure palladium. In the latter case, the samples were heated under a pure Ar atmosphere. A schematic diagram is shown in Fig 3.2.

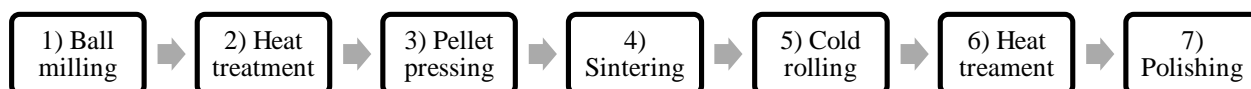


Figure 3. 2 – Flow diagram representing the preparation of PdCuAu membranes from ball milled powders.

Step 1 in Fig. 3.2 was already described in section 3.1.3.2. After ball milling, the powders were heat treated at 400°C (step 2) for 5 hours. Then, the powders were pressed into pellets, using

a bench-top hydraulic press from Carver, Inc. (step 3). Typically, 300 mg of the PdCuAu alloy was pressed (20 tons load for 10 min) into a 1.1 cm diameter disk with about 450 μm thickness. Next, the pellets were sintered (step 4) for one hour at 900°C. Cold rolling (step 5) was performed on a Durston Rolling Mill. The rolls distance was started at 500 μm and was decreased by 25 μm steps till a homogenous shine on the pellet was achieved (final rolls distance was typically 350-300 μm). Each pellet was rolled four times at each rolls distance, the sample being rotated by 90 degrees each time. A last heat treatment was performed (step 6) at 400°C for 5 hours. Finally, all membranes were polished (step 7), using SiC sanding paper (P800 – P1500 – P2500 all from Buehler) rotating at 240 rpm on an EcoMet® 250 grinder and polisher (Buehler). Polishing was finished with Al₂O₃ 1 μm paste on a MicroCloth™. Both sides of the membrane were polished till a mirror-like finish was obtained. However, sometimes a few scratches remained.

Steps 1 and 2 were omitted when preparing a membrane composed only of Pd. In this case, the polishing was also adapted. Diamond paste (6 μm and 1 μm , MetaDi Supreme Diamond) on a TexMet™ C pad rotating at 150 rpm was used instead of SiC P2500 and Al₂O₃ 1 μm , according with the Buehler guidelines [27].

3.2. Physical-chemical characterization

Different techniques were used for the characterization of the films and the bulk materials that were prepared. A description of each technique follows.

3.2.1. X-Ray Diffraction (XRD)

3.2.1.1. Background

X-Ray diffraction (XRD) is a commonly used technique to elucidate the crystallographic phase and the microstructure (strain and crystallite size) of materials. It is based on the observation that crystals diffract X-rays in a way that is dependent on the periodical arrangement of the atoms (or molecules) in a crystal [28]. The conditions upon which diffraction occurs are summarized by the Bragg's law [28, 29] which relates the wavelength (λ) of the incident radiation and the incidence angle (θ) with the inter-planar spacing (d):

$$\lambda = 2d\sin\theta \quad (\text{Equation 3.1})$$

The inter-planar spacing is a function of the Miller indices (hkl), the lattice constants (a,b,c,α,β,γ) and the crystal system. From the 7 crystal systems, the cubic one ($a = b = c; \alpha = \beta = \gamma = 90^\circ$) is the most relevant for the current work. In this case, the following relation for the inter-planar spacing can be written [28]:

$$d_{hkl} = \frac{a}{\sqrt{h^2 + k^2 + l^2}} \quad (\text{Equation 3.2})$$

A combination of equations 3.1 and 3.2 provides the tool for calculating the lattice parameter of a crystal from the diffraction data:

$$a_{hkl} = \frac{\lambda \sqrt{h^2 + k^2 + l^2}}{2 \sin \theta_{hkl}} \quad (\text{Equation 3.3})$$

Equation 3.3 was extensively used throughout this work and will be referred to several times. The diffractograms also provide us with useful information about the crystallite size and strain, which are two properties that are known to influence peak broadening [28-30], apart from instrumental effects. The crystallite size, this is, the effective thickness of the crystallite in a direction perpendicular to the reflecting planes² (D_{hkl}), can be calculated with the help of the Scherrer equation [31, 32]:

$$D_{hkl} = \frac{K\lambda}{B_{hkl} \cos \theta} \quad (\text{Equation 3.4})$$

Where K is the crystallite shape factor and is equal to 0.9, and B_{hkl} is the full width at half maximum (FWHM) in radians. The value of K has to be adjusted not only according to the crystallite shape but also to the definition that is being used for B_{hkl} (in some cases B is considered to be the integral breadth). Scherrer's equation is valid only for crystallite sizes below 100-200 nm [31] and for non-strained samples.

² Crystallite size may also be defined as the cube root of volume of the crystallite ([30] Klug HP, Alexander LE. X-ray Diffraction Procedures for Polycrystalline and Amorphous Materials: John Wiley & Sons, Inc.; 1954.). In the present work we will use only the definition presented in the main text.

Non-uniform strain in crystals can arise from a plethora of phenomena such as dislocations, stacking faults, vacancies, interstitial and substitutional defects. The consequent broadening of the diffraction peaks is described by the Wilson equation [29]:

$$B_{hkl} = 4\varepsilon \tan\theta \quad (\text{Equation 3.5})$$

Where ε represents the lattice strain or microstrain which is a dimensionless property given by the variation in d-spacing:

$$\varepsilon = \delta d/d \quad (\text{Equation 3.6})$$

As the two factors leading to peak broadening are not always easy to dissociate from one another, Williamson and Hall [33] developed a method that combines the Scherrer and the Wilson equations into one. The now called Williamson-Hall method is given by:

$$\begin{aligned} B_{hkl} &= \frac{\lambda}{D \cos\theta_{hkl}} + 4\varepsilon \tan\theta_{hkl} \Leftrightarrow \\ \Leftrightarrow B_{hkl} \cos\theta_{hkl} &= \frac{\lambda}{D} + 4\varepsilon \sin\theta_{hkl} \end{aligned} \quad (\text{Equation 3.7})$$

Equation 3.7 predicts a linear relation between $B_{hkl} \cos\theta_{hkl}$ and $\sin\theta_{hkl}$. The crystallite size and the microstrain can be evaluated from the intercept, b , and from the slope, m , respectively, using the relations: $D = \lambda/b$ and $\varepsilon = m/4$.

There are variations to the Williamson-Hall method that take into account, for example, the anisotropy of the microstrain [34]. In other words, the microstrain may vary with the crystallographic direction in accordance with equation 3.8:

$$\varepsilon_{hkl} = \frac{\sigma}{E_{hkl}} \quad (\text{Equation 3.8})$$

Where σ is the uniform stress (TPa) and E_{hkl} is the Young's modulus in the hkl direction. From the combination of equations 3.7 and 3.8 we can write the following relation:

$$B_{hkl} \cos\theta_{hkl} = \frac{\lambda}{D} + \frac{4\sigma \sin\theta_{hkl}}{E_{hkl}} \quad (\text{Equation 3.9})$$

Similarly, D and σ can be calculated from the intercept and the slope, respectively. The Young's modulus for cubic systems are given by:

$$E_{hkl}^{-1} = s_{11} - (2s_{11} - 2s_{12} - s_{44})(k^2l^2 + l^2h^2 + h^2k^2)/(h^2 + k^2 + l^2)^2 \quad (\text{Equation 3.10})$$

Where s_{11} , s_{12} and s_{44} are the elastic compliances. The elastic compliances for the $\text{Pd}_x\text{Cu}_y\text{Au}_{1-(x+y)}$ alloys were calculated using a linear interpolation of the values of the pure metals [35]:

$$s_{ij} = xs_{ij}^{\text{Pd}} + ys_{ij}^{\text{Cu}} + (1 - x - y)s_{ij}^{\text{Au}} \quad (\text{Equation 3.11})$$

Another refinement presented by Rosenberg and coworkers [34] is to consider that the anisotropic microstrain depends on a uniform density of deformation energy u :

$$\varepsilon_{hkl} = \sqrt{\frac{2u}{E_{hkl}}} \quad (\text{Equation 3.12})$$

Combining equations 3.7 and 3.12 gives:

$$B_{hkl} \cos \theta_{hkl} = \frac{\lambda}{D} + 4 \sqrt{\frac{2u}{E_{hkl}}} \sin \theta_{hkl} \quad (\text{Equation 3.13})$$

Again the parameters D and u may be calculated from the slope and intercept, respectively. Depending on the system being studied, different approximations (Equations 3.7, 3.9 and 3.13) may be valid. We shall discuss this point further when presenting the results for our PdCuAu alloys.

An alternative to the Williamson-Hall method to separate the effect of the crystallite size and strain on peak broadening is based on the fitting of a single peak [29]. In this case, it is considered that the broadening of the peak caused by the crystallite size is better described by a Lorentzian profile, whereas the broadening caused by strain is given by a Gaussian profile. When fitting the peak in question with a Voigt function, for example, it is possible then to deconvolute both Lorentzian and Gaussian contributions (B_L and B_G). These values can thus be used in the Scherrer and Wilson equations, respectively, in order to calculate the size and strain present in the sample.

3.2.1.2. Experimental details

XRD measurements were performed on a Bruker D8 Advance instrument with Cu K_α radiation source (weighted average wavelength of 1.54184 Å) operating at 40 kV and 40 mA. The

angular step size was of 0.05° and the data acquisition time was of 5 s per step. As-prepared samples were analyzed from $2\theta = 30$ to 90° and heat treated samples from $2\theta = 20$ to 100° . Both Bragg-Brentano and grazing incidence ($\theta = 5^\circ$) configurations were used. Peak position and FWHM were calculated by performing peak fitting using a Voigt function with the help of the OriginLab[®] software. EVA V14 software was also used in the cases where only information of the lattice parameter was required.

3.2.2. Scanning Electron Microscopy (SEM) and Energy Dispersive X-ray spectroscopy (EDX)

3.2.2.1. Background

SEM makes it possible to analyze the surface topography in detail, with magnifications that can go up to $800,000\times$ [36] and with ~ 1 nm resolution [37]. In general, sample preparation procedures are straightforward and non-destructive, compared for instance, with TEM procedures. In SEM, a beam of accelerated electrons (0.1-30 keV) is focused on the sample's surface. Upon impact, secondary electrons and X-rays are produced, among other particles, such as Auger electrons or backscattered electrons. As the sample is being bombarded with electrons, there will be charge accumulation on the surface if the sample is not enough conductive. To avoid such issues, a conductive film is sometimes deposited on the surface.

There are different types of SEM techniques, depending on the type of particles (for example secondary electrons or backscattered electrons) that are collected by the detector. Secondary electrons (SE) are produced by inelastic collisions between the incoming electrons and the sample atoms. SE have an energy lower than 50 eV, which means that only the ones produced close to the surface (no more than several angstroms deep [38]) are able to escape to vacuum and be detected. In practice, the lower the energy of the incoming beam, the more surface detail the image will have [37]. The incoming electron beam also leads to the emission of X-rays that are characteristic of the element which produces them. This leads not only to the identification of the emitting atoms (with atomic number higher than boron) but it also allows quantification analysis (detection limit of $\sim 0.1\%$ for most elements [36]) within ~ 1 μm below the surface.

3.2.2.2. *Experimental details*

SEM analyses by secondary electrons took place on a JEOL JSM-6300 microscope at an accelerating voltage of 20 keV at different magnifications, ranging from 25 to 100,000 \times . Information about the composition of the samples was acquired with an EDX spectroscope from Oxford Instruments with Si(Li) detector. The magnification used for the elemental analysis was 2,500 \times . The composition was calculated by taking the average of the measurements performed at three different locations of the sample. In all cases, the standard deviation of the measurements was below 2%.

EDX mapping was also used by selecting Pd $L\alpha_1$ (2.838 keV), Cu $K\alpha_1$ (8.047 keV) and Au $L\alpha_1$ (9.7111 keV). A magnification of 2,500 \times was used and 15 frames were acquired on each sample.

3.2.3. X-ray Photoelectron Spectroscopy (XPS)

3.2.3.1. *Background*

In XPS, a beam of X-rays promotes the emission of electrons from the sample, a process that is known by photoemission or by photoelectric effect. The kinetic energy (KE) of these electrons is dependent on their initial energy (the binding energy, BE), the energy of the X-ray source ($h\nu$) and the work function (Φ_s , minimum energy required to eject an electron from the highest occupied level into vacuum) [36, 38, 39]:

$$KE = h\nu - BE - \phi_s \quad (\text{Equation 3.14})$$

In equation 3.14, Φ_s and $h\nu$ are known for each particular system, which means that by measuring the kinetic energy of the ejected electrons, we can calculate the binding energy and hence identify and quantify the atoms present. This is true for all elements except hydrogen and helium. The detection limit of this technique is ~0.01-0.1 at% [36]. XPS provides us with information of the first 10 nm of the sample even if the X-rays are able to penetrate the sample several micrometers [36]. This is so because the electrons generated deeper than ~ 10 nm do not have enough energy to escape the sample and reach the detector, as they are subjected to multiple inelastic collisions. In fact, even within the 10 first nanometers only the electrons that go through little inelastic collisions will give rise to peaks in the spectra while the remaining electrons will

contribute to the spectral background. In order to probe the sample deeper, one may etch the surface first and then perform another XPS measurement.

XPS allows not only to identify which elements are present in the sample but also to know the oxidation state presented by each element. In the former case survey spectra are required, while in the latter case high resolution spectra are needed.

3.2.3.2. *Experimental details*

The surface composition of samples prepared by sputter deposition was measured with XPS, using a VG Escalab 220i-XL instrument equipped with Al K α (1486.6 eV) monochromatic source. A hemispherical analyzer and a six-channel detector were both used. The pressure inside the analysis chamber was below 1×10^{-9} mbar. A survey from 0 to 1300 eV (100 eV pass energy) was first acquired and high resolution core level spectra (20 eV pass energy) were then recorded (Pd 3d 330-360 eV; Cu 2p 925-970 eV; Au 4f 75-95 eV; and C 1s 275-295 eV). In the case of the H₂S-treated PdCuAu membrane additional Na 1s (1061-1081 eV) and S 2p (158-178 eV) high resolution spectra were acquired. The analysis of the PdCuAu membranes was made with Al K α polychromatic source. In all cases, the energy scale was calibrated for C 1s at 284.5 eV [40]. Element quantification was achieved by fitting the core level spectra with mixed Gaussian-Lorentzian functions while considering a Shirley type baseline. The fitting was performed with the help of CasaXPS software.

In some cases, Ar etching was performed. An estimation of the etch rate was made using the following equation [41]:

$$Etch\ rate\ (nm \cdot s^{-1}) = \frac{IYw}{\rho AeN} \quad (\text{Equation 3.15})$$

Where, I is the etching beam current, Y is the sputter yield, w is the atomic weight of the ablated species and ρ is its density, A is the area of the sputtered surface, e is the electron charge, and N is the Avogadro's constant.

3.2.4. **Transmission Electron Microscopy (TEM) and EELS**

In TEM, an accelerated electron beam is focused on a sample thin enough to allow the transmission of the incident electrons. In many regards, the TEM can be seen as an optical

microscope with a much higher imaging resolution, while also providing information about the sample's morphology, structure, grain size, chemical composition and composition distribution [36]. Compared to the SEM, the resolution of the TEM is about one order of magnitude higher [38]. If the energy of the transmitted electron beam, namely the energy of the inelastically scattered electrons, is analyzed, the composition of the sample can be discerned in a technique that is called electron energy-loss spectroscopy (EELS).

The samples prepared by sputtering deposition were analyzed by TEM/EELS at the Canadian Center for Electron Microscopy (Brockhouse Institute for Material Research) at McMaster, Hamilton. The sample preparation and analysis was performed by A. Korinek. Briefly, the cross sections of the films were prepared on a Zeiss NVision 40 focused ion beam instrument. The TEM analysis was carried out on a FEI Titan cubed microscope, operated at 300kV. The microscope is equipped with a CEOS hexapole image and probe corrector. EELS mapping was done using a Gatan Quantum GIF at 300kV. The scanning step size of the maps was ~1nm, the convergence semi-angle was 19 mrad and the GIF acceptance angle was 40.0 mrad. The exposure time for each spectrum was 20 ms. EELS processing was performed using Gatan Digital Micrograph.

3.2.5. Electrochemical techniques

3.2.5.1. Cyclic Voltammetry (CV)

Cyclic voltammetry is one of the techniques that is first used when exploring the electrochemical properties of a given system [42, 43]. In this technique, the electrochemical potential is varied continuously up to a certain limit, and then it is reversed at the same scan rate to the initial values, while monitoring the changes in current. This is better illustrated in Fig. 3.3.

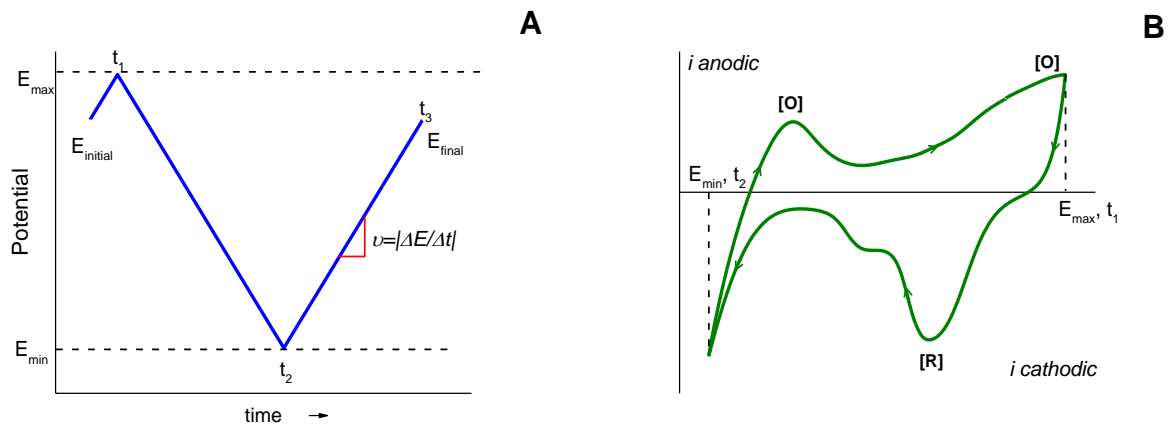


Figure 3. 3 – Variation of the potential with time (A) and variation of the current with the potential (B).

In the example shown in Fig. 3.3 A, the potential increases from the initial value ($E_{initial}$) up to a maximum (E_{max}) at time t_1 . At this point the potential switches back and it decreases till reaching the minimum value (E_{min}) at t_2 . The potential now increases again till it reaches the final value (E_{final}). The scan rate is given by the variation of the potential with time. The graphical representation of the changes in current, as a result of the changing potential, is typically called a cyclic voltammogram (Fig. 3.3B). In the cyclic voltammograms, the peaks present represent an increase in current towards more positive or negative values, as a result of oxidation [O] or reduction [R] reactions taking place, respectively. In the frame of the current work, the interpretation of the data took a more qualitative rather than quantitative approach. In this sense, the mathematical description of peak current and potential will not be presented at this point.

Cyclic voltammograms were recorded in association with the hydrogen solubility measurements (section 3.4.1) typically at 50 mV/s and between -1.0 and 0.2 V vs. Hg/HgO. All measurements were performed in NaOH 0.1M and the number of cycles was varied, depending if it is before or after H solubility measurement. Further discussion of this issue will be given in chapter 5.

3.2.5.2. Other techniques

Chronoamperometric measurements were also used. In this technique, the potential is fixed and the current is monitored. Chronoamperometry was used for the measurement of hydrogen

solubility in PdCuAu alloys (further details in section 3.4.1) and for the electrodeposition of PdCuAu alloys thin films (section 3.1.1)

3.2.6. Mass of the deposits prepared by electro- or sputter deposition

Two different methods were used in order to measure the mass of the deposits prepared by electro- or sputter deposition. One of the methods is based on the mass difference between the substrate with and without the alloy film (gravimetric method) and the other one is based on the elemental analysis by Nuclear Activation Analysis (NAA).

3.2.6.1. Gravimetric method

The mass of the deposit was calculated by taking the difference between the mass of the samples (substrate+film) and the mass of the bare substrate. The latter was obtained by first immersing the samples (substrate with film on top) in aqua regia for three hours, rinsing with distilled water and drying it with paper tissues. Finally, the substrates were kept overnight inside a dry box before taking their mass. The gravimetric method was used only with the electrodeposited samples. Average values of the mass of the deposit were *ca.* 0.40 mg. The variation of mass observed on a bare titanium substrate was below the detection limit of the balance, which is 0.10 mg, indicating that the aqua regia does not dissolve the Ti to a significant extent.

3.2.6.2. Nuclear Activation Analysis (NAA)

NAA is an analytical technique that allows elemental analysis. The samples are bombarded with neutrons that excite the sample's nuclei [44]. Upon deexcitation, the nuclei will return to the ground state with the emission of gamma rays with a characteristic half-life time. This allows the identification of the emitting element, and the intensity of emitted radiation allows its quantification, by using standards of known concentration.

In the cases where the gravimetric method gave weight values below the detection limit of the balance (0.10 mg), NAA was used for better accuracy. Hence, the acidic solutions obtained from immersing the samples in aqua regia were sent for analysis at the SLOWPOKE laboratory (École Polytechnique Montreal). As the copper content was below the detection limit for this technique, the amount of copper in the alloys was inferred from the NAA measurements of Pd and

Au and the EDX measurements. Alternatively, NAA can be performed on solid samples, allowing to bypass the aqua regia treatment. This was done for the samples prepared by sputter deposition. Average values of the mass of the sputter deposit samples were about 0.15 mg. The uncertainty of the results is $\pm 5\%$.

3.2.7. Gas chromatography (GC)

Gas chromatography is a separation technique where a gas mixture is passed through a column with a help of an eluting or carrier gas [45]. The separation of the gas mixture occurs as the result of different adsorption or solubility of the gases in the stationary phase of the column.

In the current work, GC was used to quantify the amount of He present inside the permeation chamber when performing gas separation measurements (section 3.3.3). Agilent Technologies 490 micro GC was used with a 10-meter MS5A column (Agilent# 494001360) and using Ar as the carrier gas (35 psig). Separation was performed at 45°C (column and injector temperature). Injection time was 60 ms and the run time was 60 s with a sampling frequency of 10 Hz. A thermal conductive detector was used. Under these conditions the retention time for He is (0.306 ± 0.006) s while that of H₂ is (0.34 ± 0.01) s. The retention times for the 2 gases are very close, which renders the separation impossible when any of the two is present in high concentrations. For this reason samples were diluted 1:10 before injection. For quantification purposes, the peak areas were measured using the integration software provided with the GC (Agilent OpenLAB CDS –EZ Chrom edition). A standard of 0.1% He in H₂ was used as a reference. Average peak area of seven independent injections is $(4.6 \pm 0.1) \times 10^4$ a.u. All He concentrations presented in this work are calculated in respect to the latter value.

3.3. Measurement of hydrogen related properties

The hydrogen solubility can be defined on a more quantitative basis by the ratio between the number of hydrogen moles (nH) that can be introduced in the alloys' lattice and the number of moles of the PdCuAu alloy (nM) (equation 3.16):

$$H_{solubility} = \frac{nH}{nM} \times 100 \quad (\text{Equation 3.16})$$

As defined by equation 3.16, the hydrogen solubility is given as a percentage. In the present work, two methods were used to calculate nH : potential step chronoamperometry (section 3.3.1) and electrochemical *in situ* X-ray diffraction analysis (section 3.3.2). nM is given by the mass of the deposit (section 3.2.6) divided by its molar mass. The molar mass of the film was calculated using the EDX composition of the films and the atomic weight of each metal. When using the X-ray diffraction based-method, there is no need to evaluate nM (further details are given in section 3.2.6).

3.3.1. Electrochemical method for the measurement of hydrogen solubility

In potential step chronoamperometry, a sufficiently negative potential that promotes hydrogen absorption by the film is first applied. Afterwards, the potential is switched to more positive values, where hydrogen is oxidized and desorbed. The latter step gives rise to a current that decreases with time. The coulombic charge corresponding to the integration of this oxidation current is a measure of the amount of hydrogen atoms that were previously absorbed or dissolved in the material [13].

The measurements were performed using the electrochemical cell described in section 3.1.1.2, where the experimental details for the electrodeposition experiments are reported. All experiments were performed in 0.1 M NaOH (Fisher Scientific) and an Hg/HgO electrode was used as the reference electrode (with a Luggin capillary). A platinum wire was chosen as the counter-electrode. The amount of hydrogen dissolved in solution may lead to an overestimation of the hydrogen dissolved by the metallic film [13]. This occurs because H₂ molecules dissolved in the electrolyte can also be oxidized. In order to minimize this effect, the NaOH solution was continuously renewed with an extensively Ar-purged solution. This was done with the help of two peristaltic pumps (Variable flow Mini-pump, Control Company, Fisher Scientific) – one being used to remove the hydrogen-containing NaOH solution from the electrochemical cell, the other one to replenish the cell with the Ar-purged NaOH solution. Using as working electrode a metal that does not absorb hydrogen, for example a platinum foil, a 2.5 mC charge is measured, which is due to three sources, these being, the hydrogen that was adsorbed at the Pt surface, the remaining H₂ in solution and the double layer charge that arises when switching from the more negative potential to the more positive potential. In general, with this method a systematic bias between 1.5-2.5 mC is present in all measurements.

In each case, the samples were first activated by applying $E_{\text{negative}} = -1400$ mV for $t_{\text{negative}} = 3$ min, followed by $E_{\text{positive}} = -400$ mV, for $t_{\text{positive}} = 3$ min. This procedure was repeated 5 times. To measure the electrochemical hydrogen isotherms, E_{negative} was varied from -650 to -1400 mV by steps of 50 mV (with $t_{\text{negative}} = 3$ min) while keeping $E_{\text{positive}} = -400$ mV (with $t_{\text{positive}} = 3$ min). The current measured while $E_{\text{positive}} = -400$ mV originates from the oxidation of the hydrogen atoms absorbed in the metal alloy during the precedent E_{negative} step. Therefore, from the charge associated with the oxidation current, Q_{ox} , the number of moles of hydrogen (nH) can be determined by dividing Q_{ox} by the Faraday's constant. The detection limit of this technique is $Q_{ox} \cong 1$ mC, which represents 1×10^{-8} moles of hydrogen. This translates to $\frac{nH}{nM} \cong 1\%$ since, on the average, all the deposits were composed of at least 1×10^{-6} moles of metal.

3.3.2. Electrochemical *in situ* X-ray diffraction analysis for the measurement of hydrogen solubility (E *in situ* XRD)

3.3.2.1. Background information

E *in situ* XRD was used for alloys that show an oxidation current lower than the detection limit of the electrochemical method, this is $Q_{ox} < 1$ mC. This technique is based on the fact that the introduction of hydrogen in the lattice of the alloy will cause its volume to expand [46]. In other words, the volume of the expanded lattice (V_f) is given by the lattice initial volume (V_i) plus the volume occupied by the hydrogen atoms. Considering the volume expansion of one unit cell we can write:

$$V_f = V_i + x \times V_H \quad (\text{Equation 3.17})$$

Where, x represents the number of hydrogen atoms that were dissolved in the lattice and V_H is the hydrogen molar volume (2.9 \AA^3 per atom, [47]); $x \times V_H$ represents then the total volume occupied by the hydrogen atoms. XRD measurements before and after H introduction will allow the calculation of the initial and final volumes by determining the respective lattice parameters. This means that the only unknown in equation 3.16 is x . Resolving equation 3.16 in function of x gives:

$$x \times V_H = V_f - V_i \Leftrightarrow x = \Delta V / V_H$$

(Equation 3.18)

From equation 3.18 one may calculate the number of hydrogen moles dissolved in the films by dividing with the Avogadro constant. The following relation may thus be written, by adapting equation 3.16:

$$H_{solubility} = \frac{nH}{nM} \times 100 = \frac{\Delta V}{V_H N_A n M} \times 100 = \frac{\Delta V}{V_H M} \times 100 \quad (\text{Equation 3.19})$$

In equation 3.19, M represents the number of metal atoms involved in the hydrogen solubility process. As we are considering one single unit cell, M is equal to four in the case of a fcc lattice, and two in the case of a bcc lattice. Equation 3.19 enables the calculation of the hydrogen solubility by measuring the lattice constant before and after the electrochemical promoted-H absorption, without having to measure the mass of metal alloy involved in the process.

3.3.2.2. Experimental details

A custom made cell that works both as an electrochemical cell and as a reflection unit in X-ray diffraction was used. A full description of its construction and operation is available in the literature [48]. Figure 3.4 shows the experimental set-up and of the working electrode (the PdCuAu film).

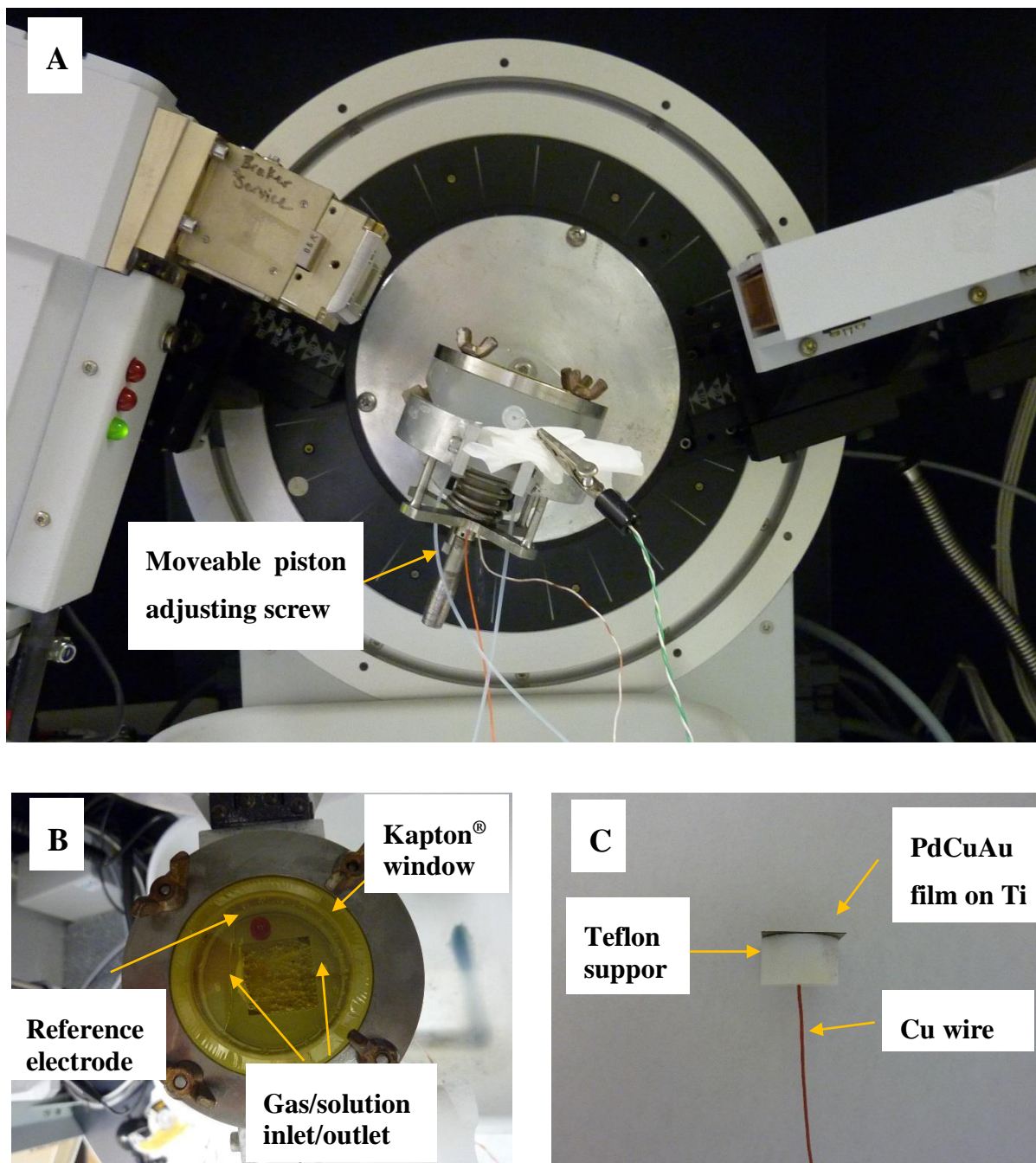


Figure 3. 4 – Experimental set-up for E *in situ* XRD A – general view, B – top view of cell; C – working electrode.

The device used in this set up is composed of two parts, a fixed one – the cell body – and a moveable piston (Fig. 3.4A). The working electrode is supported on the piston and the cell is sealed on top with a Kapton[®] window foil 7.5 μm thick (SPEX[®]SamplePrep; Fig 3.4B). There are

two openings on the cell that can be used to introduce or remove either gas or liquid from the cell with the help of two peristaltic pumps (Variable flow Mini-pump, Control Company, Fisher Scientific). The working electrode (WE), a PdCuAu film on titanium, was supported on a Teflon[®] disk (Fig. 3.4C). The connection to the potentiostat was made with the help of a copper wire, which was attached to the backside of the titanium substrate with conductive silver epoxy (Epotek, Epoxy Technology)

In the present case, the measurements were performed in 0.1M H₂SO₄, using a Pt wire as the counter electrode (CE) and palladium hydride as the reference electrode (RE). The reference electrode was prepared by applying -50 mA for 30 minutes in H₂SO₄ 0.1 M to a Pd wire using Pt as the counter electrode and a saturated calomel electrode as the reference. After assembling the electrodes (WE, CE and RE), the cell was filled with the electrolyte and was sealed at the top with the Kapton window. The higher stability of the Kapton[®] film in acidic media when compared to alkaline [49] justifies the used of H₂SO₄ instead of NaOH electrolyte. There are two possible configurations for the operation of E *in situ* XRD cell that are easily interchanged by maintaining the piston at the bottom of the cell (position 1) or moving it up (position 2) closer to the Kapton[®] window. In position 1, the working electrode is fully immersed in the electrolyte, and the cell can operate as an electrochemical cell. It was in position 1 that hydrogen absorption and desorption were promoted. In position 2, the XRD measurements can be performed. In the latter case, a thin film of the electrolyte remains between the WE and the Kapton[®] window, guaranteeing a complete electric circuit. Before any XRD measurement takes place, the position of the cell is carefully adjusted to the point where half of the intensity of the X-ray beam is detected. At this point, the WE is at the reference plane of the diffractometer.

Prior to any electrochemical experiments, the cell is set to position 2 and a first diffractogram (XRD1) at open circuit potential (OCP) is recorded. The diffractograms were measured from $2\theta = 35$ to 45° or $2\theta = 75$ to 81° , and using a grazing incidence angle of 5° . The angular step size was of 0.04° and the data acquisition time was of 6 s per step. Each diffractogram was repeated 4 times. After the first XRD measurement, the cell is pulled down to position 1 where the PdCuAu alloy films are saturated in hydrogen by applying -600 mV. After 15 minutes, the cell is pushed upwards to position 2 and put in contact with the Kapton[®] window. The reduction current consequently decreases. The position of the cell is then carefully adjusted and the XRD

measurements start again (XRD2). Afterwards, the cell is pulled back down to position 1 and the potential is switched to +300 mV in order to promote the oxidation of the absorbed H. This potential is kept for another 15 minutes, after which the cell is moved upwards into position 2 and a new XRD experiment takes place (XRD3). In summary, three diffractograms (XRD1 – pristine sample; XRD2 – charged sample; XRD3 – discharged sample) were taken per sample. This procedure was repeated for all the different samples. In one case, a diffractogram from 20-100° while maintaining -600 mV was recorded to verify for other possible changes in the crystallographic structure.

3.3.3. Gas phase method for the measurement of hydrogen permeability

3.3.3.1. Background

The PdCuAu membranes that were prepared from mechanically alloyed powders (section 3.2) were subjected to high pressure and temperature conditions in order to measure how much hydrogen can be transported through them. The mechanism for hydrogen separation by dense metallic membranes was discussed in section 2.2. In the cases where the diffusion through the membrane is the limiting step and the H₂ in the gas phase is in equilibrium with the hydrogen dissolved in the membrane, the Richardson relation (equation 2.7), already mentioned in section 2.2 is valid:

$$J_{H_2} = \frac{\phi}{L} \left[(P_{H_2}^{retentate})^{\frac{1}{2}} - (P_{H_2}^{permeate})^{\frac{1}{2}} \right]$$

Where J_{H_2} is the hydrogen flux in mol.m⁻².s⁻¹, ϕ is the hydrogen permeability in mol.m⁻¹.s⁻¹.Pa^{-0.5}, L is the membrane's thickness in meters, and p_{H_2} is the H₂ pressure (on the retentate or permeate side of the membrane, as indicated) in Pa. This equation establishes a linear relation between the gas flux and the gradient of pressure being applied on the membrane, and represents the basis for the assessment of the membrane's permeability. If measurements of the flux at different feed pressures are made, a linear regression of the data will allow the assessment of the hydrogen permeability by multiplying the slope of the straight line with the thickness of the membrane.

3.3.3.1. Experimental details

Hydrogen separation is made inside the permeation chamber. The membrane divides the permeation chamber in two parts, the retentate (high pressure) and permeate side (low pressure). A schematic representation of the permeation chamber is made in Fig. 3.5.

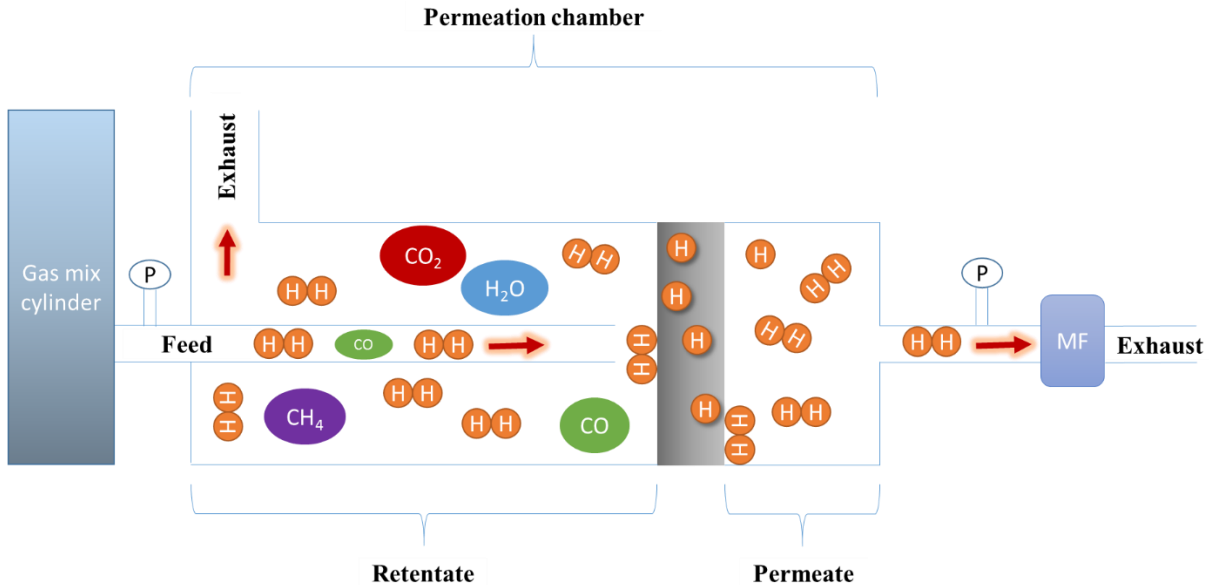


Figure 3.5 – Schematic representation of the experimental setup used for hydrogen permeability measurement. The retentate and the permeate sides of the permeation chamber are represented, as well as the cylinder with the gas mixture, the pressure gauges (P) and mass flow meters (MF). The arrows indicate the direction of gas flow.

In a typical permeation experiment, hydrogen gas is supplied by a gas cylinder (on the left of Fig. 3.5) to the retentate side of permeation chamber. The gas is in fact brought to the permeation chamber with a gas line that is about 2 cm apart from the membrane. This allows an effective initial purge of the permeation chamber, while keeping constant the gas composition close to membrane during the permeation experiment. A constant flow of feed gas is kept, and the excess is vented through the exhaust. The hydrogen that passes through the membrane reaches the permeate side of the permeation chamber where the pressure and flow of gas can be monitored. All the measuring devices and gas lines converge to the gas panel that was designed in our

laboratory and built and assembled by COGI-TECH (Quebec, Canada). The gas panel is shown in Fig. 3.6.



Figure 3. 6 – Gas panel evidencing the mass flow meters (yellow dotted square on the right) and the pressure gauges (white dotted squares).

The gas panel (Fig. 3.6) is made of the gas lines connecting to the gas cylinders and respective pressure gauges, back flash arrestors, and gas lines that transport the gas from and to the permeation chamber. There are two digital pressure gauges (Model DPG 409-250G-W from Omegadyne, Inc; 0-250 psig), one for each side of the permeation chamber and there are three mass flow meters connected to the permeate side of the membrane (MF1 H₂ 0.0-20.0 m/min, MF2 H₂ 0.0-100.0 ml/min and MF3 He 0.00-5.00 ml/min, all from Aalborg, model XFM17). The permeation chamber is placed inside a furnace that allows temperature control. These are shown in Fig.3.7.

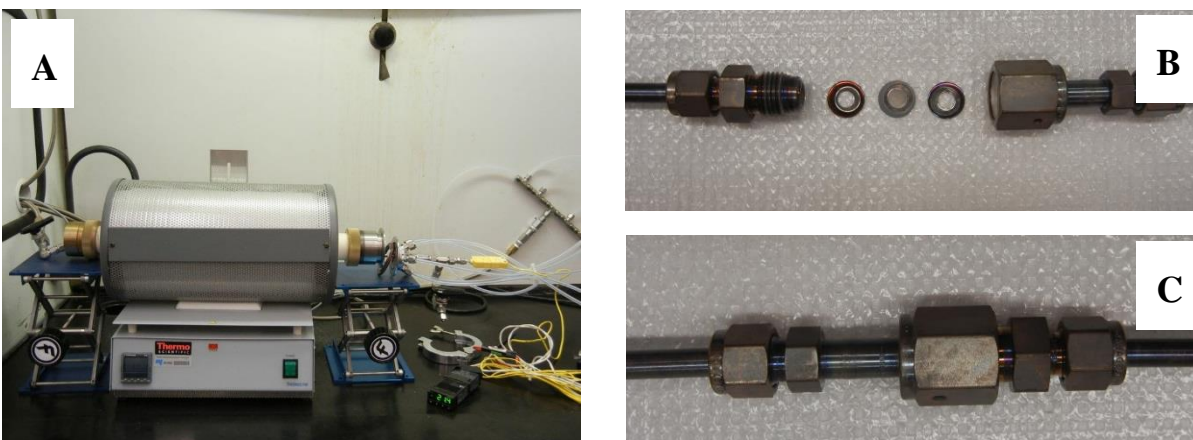


Figure 3. 7 – Furnace (A) and permeation chamber unassembled (B) and assembled (C). The disk at the center of panel B is the membrane (1.1 cm diameter). On each side of the membrane, the stainless steel gaskets that were used can be seen.

The membranes are assembled between two stainless steel gaskets inside a VCR[®] chamber (Fig. 3.7 B). The permeation chamber is then introduced inside the furnace (Fig 3.7 A, Thermolyne from Thermo Scientific) and connected to the gas panel. In a permeation test and after assembling the permeation chamber, the system was purged of air with alternating vacuum pumping (5 min; -30 inHg) and exposure to Ar at 30 psig. This was repeated three times. A first He leak test was then performed to check the integrity of the membrane, by introducing He at 30-60 psig while the variation of pressure and flow was monitored. A membrane was considered leak free if the He flow remained at 0.00 ml/min and if no increase in pressure was observed in the permeate side. The temperature was then increased for the working temperature (358, 411 or 464°C) and it was let to stabilize for one hour. The permeation test could then start. The last step of any permeation test was another He leak test, following the same procedure as described above. All gases used (Ar, He and H₂) were 5.0 pure and were purchased from Air Liquide. All data log (pressure and flow) was performed with a PC that was connected to both pressure gauges and flow meters.

Two different types of single-gas permeation experiments were performed, namely, (i) measurement of the hydrogen permeability at constant temperature (358, 411 or 464°C) and with increasing pure H₂ pressure (30, 45 and 60 psig pure H₂); (ii) flow stability measurements at constant temperature (464°C) and pressure (45 psig pure H₂) for 3 hours. The first type of experiments were used for the calculation of the hydrogen permeability. The membranes were also

tested in the presence of gas mixtures containing 6.09% He, 941 ppm H₂S and balance H₂ (Air Liquide) at 464°C. These experiments were performed in 3 different steps: first a baseline for H₂ flow was made by pressurizing the system with 30 psig pure H₂ for 30 or 60 min; after the gas mixture at 30-32 psig was introduced for another 30 minutes; and finally the feed gas was switched back for pure 30 psig H₂ to check if poisoning of the membrane was reversible or not. In order to characterize the reaction products of the interaction of the membranes with the H₂S component in the gas mixture, the membranes were exposed one last time for 15 minutes to 30-32 psig of the H₂S-He-H₂ mixture.

3.4. References

- [1] Goupil G, Jucken S, Poirier D, Legoux JG, Irissou E, Davis B, et al. Cold sprayed Cu–Ni–Fe anode for Al production. *Corrosion Science*. 2015;90:259-65.
- [2] Lee TH, Park CY, Lee G, Dorris SE, Balachandran U. Hydrogen transport properties of palladium film prepared by colloidal spray deposition. *Journal of Membrane Science*. 2012;415-416:199-204.
- [3] Balachandran U, Lee TH, Park CY, Emerson JE, Picciolo JJ, Dorris SE. Dense cermet membranes for hydrogen separation. *Separation and Purification Technology*. 2014;121:54-9.
- [4] Paunovic M, Schlesinger M. *Fundamentals of Electrochemical Deposition*. 2nd ed: John Wiley & Sons; 2006.
- [5] Schwarzacher W. *Electrodeposition: A technology for the future*. Electrochemical Society Interface. 2006;15:32-3.
- [6] Rao CRK, Trivedi DC. Chemical and electrochemical depositions of platinum group metals and their applications. *Coordination Chemistry Reviews*. 2005;249:613-31.

- [7] Xiao F, Hangarter C, Yoo B, Rheem Y, Lee K-H, Myung NV. Recent progress in electrodeposition of thermoelectric thin films and nanostructures. *Electrochimica Acta*. 2008;53:8103-17.
- [8] Paunovic M, Schlesinger M, Synder D. Fundamental Considerations. In: Schlesinger M, Paunovic M, editors. *Modern Electroplating, Fifth Edition*: John Wiley & Sons; 2010.
- [9] Brenner A. *Electrodeposition of Alloys: Principles and Practice - Volume I*: Academic Press; 1963.
- [10] Perret P, Brousse T, Bélanger D, Guay D. Electrochemical Template Synthesis of Ordered Lead Dioxide Nanowires. *Journal of The Electrochemical Society*. 2009;156:A645-A51.
- [11] Hyde AC. *Surface treatment of titanium*. Imp Metal Ind Kynoch Ltd; 1972.
- [12] Allemand M. MSc. thesis: Synthèse et caractérisation de films minces électrodéposés de cuivre-palladium: Université du Québec; 2011.
- [13] Martin MH, Galipaud J, Tranchot A, Roué L, Guay D. Measurements of hydrogen solubility in $\text{Cu}_x\text{Pd}_{100-x}$ thin films. *Electrochimica Acta*. 2013;90:615-22.
- [14] Allemand M, Martin MH, Reyter D, Roué L, Guay D, Andrei C, et al. Synthesis of Cu-Pd alloy thin films by co-electrodeposition. *Electrochimica Acta*. 2011;56:7397-403.
- [15] Musil J, Vlček J. Magnetron sputtering of alloy-based films and its specificity. *Czechoslovak Journal of Physics*. 1998;48:1209-24.
- [16] Kelly PJ, Arnell RD. Magnetron sputtering: a review of recent developments and applications. *Vacuum*. 2000;56:159-72.

- [17] Rossnagel S. Sputtering and Sputter Deposition. In: Seshan K, editor. Handbook of Thin Film Deposition Processes and Techniques (Second Edition). Norwich, NY: William Andrew Publishing; 2001. p. 319-48.
- [18] Depla D, Mahieu S, Greene JE. Sputter Deposition Processes. In: Martin PM, editor. Handbook of Deposition Technologies for Films and Coatings (Third Edition). Boston: William Andrew Publishing; 2010. p. 253-96.
- [19] Brodie I, Muray J. Layering Technologies. In: Brodie I, Muray J, editors. The Physics of Micro/Nano-Fabrication: Springer US; 1992. p. 315-451.
- [20] Wasa K. Sputtering Systems. In: Wasa K, Kanno I, Kotera H, editors. Handbook of Sputtering Technology (Second Edition). Oxford: William Andrew Publishing; 2012. p. 77-139.
- [21] Adachi H, Wasa K. Thin Films and Nanomaterials. In: Wasa K, Kanno I, Kotera H, editors. Handbook of Sputtering Technology (Second Edition). Oxford: William Andrew Publishing; 2012. p. 3-39.
- [22] Adler T, Houska CR. Affect of annealing on uniform and nonuniform strains in a sputtered Mo film on Si. Journal of Applied Physics. 1979;50:3288.
- [23] Gilman PS, Benjamin JS. Mechanical alloying. Annu Rev Mater Sci. 1983;13:279-300.
- [24] Suryanarayana C. Mechanical alloying and milling. Progress in Materials Science. 2001;46:1-184.
- [25] Lü L, Lai MO, Zhang S. Modeling of the mechanical-alloying process. Journal of Materials Processing Technology. 1995;52:539-46.

- [26] Tsai Y-C, Lin C-C, Lin W-L, Wang J-H, Chen S-Y, Lin P, et al. Palladium based cermet composite for hydrogen separation at elevated temperature. *Journal of Power Sources*. 2015;274:965-70.
- [27] Buehler^R *SumMet*TM - A Guide to Materials Preparation and Analysis. 2nd ed 2007.
- [28] Cullity BD. *Elements of X-Ray Diffraction*. 2 ed: Addison-Wesley Publishing Company, Inc.; 1978.
- [29] Behrens M, Schlögl R. *X-Ray Diffraction and Small Angle X-Ray Scattering. Characterization of Solid Materials and Heterogeneous Catalysts: Wiley-VCH Verlag GmbH & Co. KGaA*; 2012. p. 609-53.
- [30] Klug HP, Alexander LE. *X-ray Diffraction Procedures for Polycrystalline and Amorphous Materials: John Wiley & Sons, Inc.*; 1954.
- [31] Holzwarth U, Gibson N. The Scherrer equation versus the 'Debye-Scherrer equation'. *Nat Nano*. 2011;6:534-.
- [32] Scherrer P. Bestimmung der Größe und der inneren Struktur von Kolloidteilchen mittels Röntgenstrahlen. *Gottinger Nachrichten Math Phys*. 1918;2:98-100.
- [33] Williamson GK, Hall WH. X-ray line broadening from filed aluminium and wolfram. *Acta Metallurgica*. 1953;1:22-31.
- [34] Rosenberg Y, Machavariani VS, Voronel A, Garber S, Rubshtein A, Frenkel AI, et al. Strain energy density in the x-ray powder diffraction from mixed crystals and alloys. *Journal of Physics-Condensed Matter*. 2000;12:8081-8.

- [35] Every AG, McCurdy AK. Table 3. Cubic system. Elements. In: Nelson DF, editor. Second and Higher Order Elastic Constants: Springer Berlin Heidelberg; 1992. p. 11-7.
- [36] Baer DR, Thevuthasan S. Chapter 16 - Characterization of Thin Films and Coatings. In: Martin PM, editor. Handbook of Deposition Technologies for Films and Coatings (Third Edition). Boston: William Andrew Publishing; 2010. p. 749-864.
- [37] Gignac LM, Wells OC. Characterization of Semiconductor Nanostructures by Scanning Electron Microscopy. Handbook of Instrumentation and Techniques for Semiconductor Nanostructure Characterization 2011. p. 1-42.
- [38] Ohring M. Chapter 10 - Characterization of thin films and surfaces. In: Ohring M, editor. Materials Science of Thin Films (Second Edition). San Diego: Academic Press; 2002. p. 559-640.
- [39] Ratner BD, Castner DG. Electron Spectroscopy for Chemical Analysis. Surface Analysis – The Principal Techniques: John Wiley & Sons, Ltd; 2009. p. 47-112.
- [40] Moulder JF, Sickle WF, Sobol PE, Bomben KD. Handbook of X-ray Photoelectron Spectroscopy: A Reference Book of Standard Spectra for Identification and Interpretation of XPS Data: Physical Electronics Division, Perkin-Elmer Corporation; 1992.
- [41] Watts JF, Wolstenholme J. An introduction to surface analysis by XPS and AES: John Wiley & Sons, Ltd; 2003.
- [42] Bard AJ, Faulkner LR. Electrochemical Methods: Fundamentals and Applications 2nd ed: John Wiley & Sons, Inc.; 2001.
- [43] Brett CMA, Brett AMO. Electrochemistry: Principles, Methods and Applications: Oxford University Press; 1993.

- [44] Parry SJ. Activation Spectrometry in Chemical Analysis. Canada: John Wiley & Sons; 1991.
- [45] Christian GD. Chromatographic Methods. Analytical Chemistry. Canada: John Wiley & Sons, Inc.; 1994.
- [46] Baranowski B, Majchrzak S, Flanagan TB. Volume increase of fcc metals and alloys due to interstitial hydrogen over a wide-range of hydrogen contents. Journal of Physics F-Metal Physics. 1971;1:258-61.
- [47] Galipaud J, Martin MH, Roué L, Guay D. Measurement of hydrogen solubility in Pd_xCu_{100-x} thin films prepared by pulsed laser deposition: An electrochemical in situ X-ray diffraction analysis. Journal of Physical Chemistry C. 2013;117:2688-98.
- [48] Chabanier C, Guay D. Activation and hydrogen absorption in thermally prepared RuO₂ and IrO₂. Journal of Electroanalytical Chemistry. 2004;570:13-27.
- [49] Summary of Properties for Kapton Polyimide Films ; 2015. DuPont.

4. Hydrogen solubility in PdCuAu alloy thin films prepared by electrodeposition

Thin films of PdCuAu alloys were prepared by electrodeposition and characterized. The hydrogen solubility capacities of these alloys were measured by an electrochemical method. The characterization of the samples will be given first (section 4.1), followed by the H solubility measurements (section 4.2) and finally the conclusions (section 4.3).

4.1. Synthesis and characterization

The simple pulsed electrodeposition procedure used in this work allowed the production of single phase face centered cubic ternary PdCuAu alloys over a wide composition range and with diverse morphologies. The preparation of PdCuAu alloys by electrodeposition involved the electrolysis of a solution containing the ionic precursors of each metal (Pd^{2+} , Cu^{2+} and Au^{3+}) that were prepared from the nitrate salts of Pd and Cu, and from gold hydroxide. The standard reduction potential of these cations are: 1.498, 0.951 and 0.3419 V vs. SHE [1] for Au, Pd and Cu, respectively. The reduction potentials indicate that Au is the easiest metal to deposit followed by Pd, and finally by Cu. These reactions occur at the working Ti-electrode, pre-treated with oxalic acid to remove surface oxides. At the counter Ti-electrode, oxygen is evolving as a result of water oxidation, as it is typical in insoluble anodes [2]. H_2 evolution at the working electrode is not controlled and may have an important role in the morphology of the deposits, especially the ones richer in palladium. We will come back to this point later on. The films prepared in this work were first characterized by EDX/SEM and XRD, prior to the study of their capability to absorb hydrogen.

4.1.1. Composition analysis by EDX

In the current work, solutions containing all three metals at the same time with different concentrations were used with the aim of producing ternary alloys of various compositions. The procedure used here was adapted from the literature [3]. By varying the electrolytic bath composition, we were able to produce deposits with a variety of compositions. In Fig.4.1, the

composition of the film, as measured by EDX, is plotted as a function of the electrolytic bath composition, for Pd (Fig. 4.1A), Cu (Fig. 4.1B) and Au (Fig 4.1C).

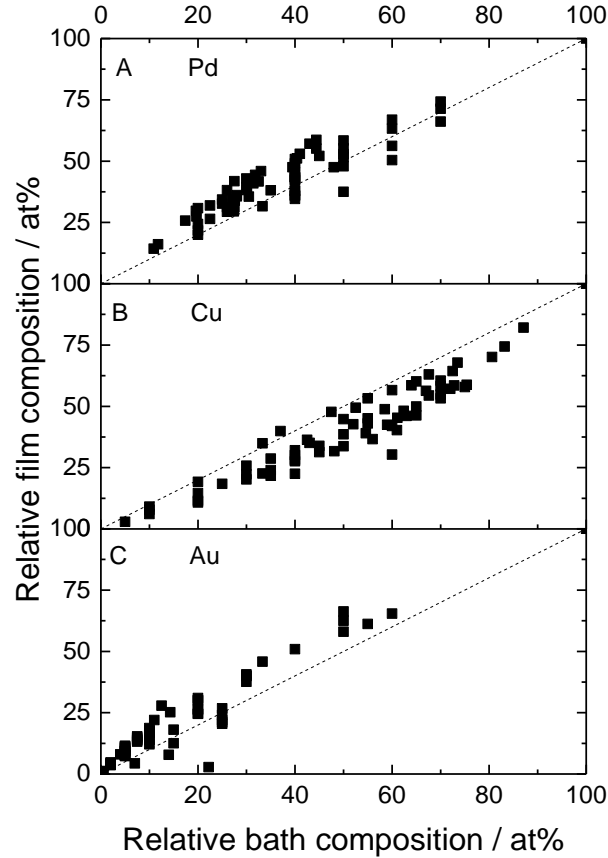


Figure 4. 1 – Variation of the relative composition of the film vs the relative composition of the bath: in (A) Pd, (B) Cu and (C) Au. The composition of the films was determined by EDX.

As seen in Fig. 4.1C, the films are slightly enriched in gold as compared to the composition of the solution. In contrast, the Cu and Pd composition of the films are slightly less than expected from the composition of the solution. To put things on a more quantitative basis, let us define the following equation

$$f_M = \frac{\sum ([M]_{film} - [M]_{solution})}{N} \quad (\text{Equation 4.1})$$

Where M is one of the elements Pd, Cu or Au, N is the number of data points in Figure 4.1, $[M]_{film}$ and $[M]_{solution}$ are the concentrations of M (in at.%) in the film and in the

electrodeposition bath, respectively. Accordingly, f_M is a measure of the deviation of the film composition with respect to the composition of the solution.

From the data of Fig. 4.1, $f_{Pd} = 0.07$, $f_{Cu} = -0.14$, and $f_{Au} = 0.07$. It is clear from that analysis that Pd and Au are deposited at the expense of Cu. In the absence of gold cations, M. Allemand and coworkers [3] verified that the composition of the film is the same as the composition of the starting electrolytic bath. However, the results obtained here for the ternary alloys are consistent with the general rule in electrodeposition that the more noble metals are easiest to deposit than others [2, 4], and hence it is expected *a priori* that the films would be richer in gold and palladium since the films were deposited at -0.258 V vs. SHE .

4.1.2. XRD characterization

The crystallographic structure of the films was analyzed by XRD and the patterns of a few representative samples are shown in Fig. 4.2.

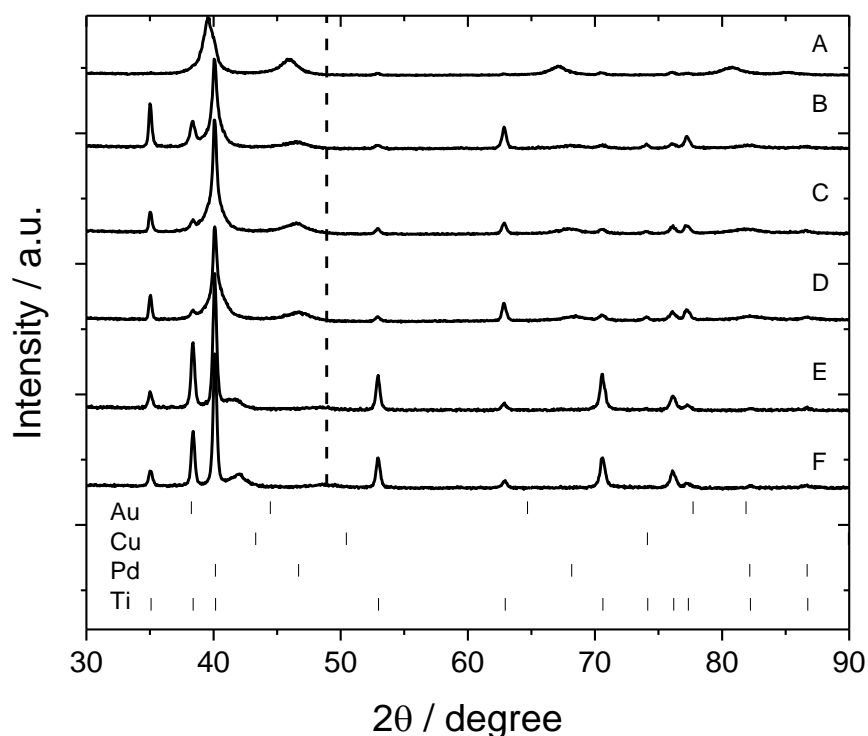


Figure 4. 2 – XRD patterns of CuPdAu ternary alloy thin films prepared by pulsed electrodeposition on Ti substrates. Six different compositions are shown and are organized from

the highest (top curve) to the lowest Au content (bottom curve). The composition of the alloys are (A) Pd_{50.4}Cu_{9.1}Au_{40.6}, (B) Pd_{43.5}Cu_{22.5}Au₃₁, (C) Pd_{47.9}Cu_{25.8}Au_{26.3}, (D) Pd_{63.3}Cu_{20.2}Au_{16.5}, (E) Pd_{38.2}Cu_{57.1}Au_{4.7}, and (F) Pd_{31.2}Cu_{67.8}Au₁. The peak position of the pure elements is shown at the bottom for reference.

Analysis of Fig. 4.2 shows that the diffractograms of all samples have the characteristic diffraction peaks of the substrate (Ti, hexagonal close-packed structure, JCPDS card no. 65-9622). In some cases, the XRD patterns also showed the presence of titanium hydride (JCPDS card no. 78-2216; fcc), which could be formed during the acid pre-treatment of the substrates. Apart from these peaks that are related to the substrate, all samples exhibit one series of diffraction peaks that can be indexed to a face centered cubic (fcc) phase. For comparison, the characteristic diffraction peaks of pure Pd (JCPDS card no. 65-8601), Cu (JCPDS card no. 85-1326) and Au (JCPDS card no. 65-6174) are given at the bottom of the figure. None of the diffraction peaks of the pure metals are seen in the XRD patterns (unless they were intentionally prepared), indicating that a ternary alloy was prepared. Indeed, the position of the characteristic diffraction peaks of the fcc phase vary with the composition of the film, as it is expected if a palladium-copper-gold solid solution is formed. For example, the position of the (200) peak shifts from $2\theta = 45.8^\circ$ (curve A) to $2\theta = 48.9^\circ$ (curve F) as the gold content is decreased from 40.6 to 1.0 at.%. Accordingly, the lattice parameter of the fcc phase changes with the composition of the material.

The lattice parameter of all samples was determined using the position of the (200) peak, and equation 3.3. The (200) diffraction peak was used because it is easily discernible in the XRD diffractograms of all samples, whereas the other peaks can sometimes overlap with the substrate peaks, as is the case of peak (111), or be of low intensity and not well defined as is the case of peaks (220), (311) or (222). The ternary contour plot in Figure 4.3 shows the variation of the lattice parameter with the composition of the samples.

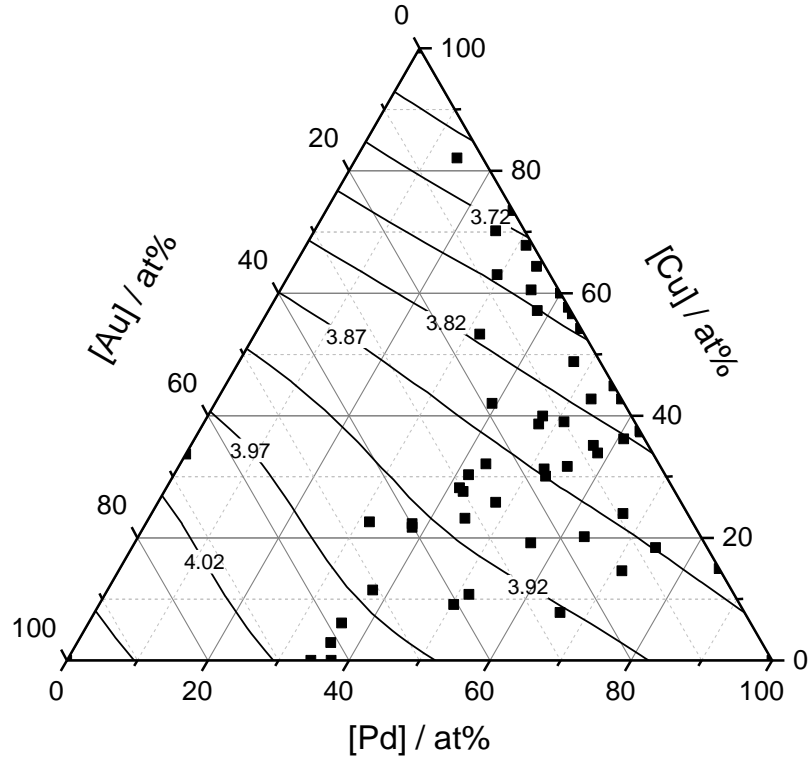


Figure 4. 3 – Ternary contour plot showing the variation of the experimentally determined lattice parameter (maximum standard error of 0.01\AA) with the film composition.

As seen in Fig. 4.3, increasing the Au content has the effect of expanding the lattice parameter of the deposit, while increasing the Cu content has the effect of compressing the lattice parameter of the fcc phase. This is because the atomic radius of Cu is 2.556\AA , smaller than Pd (2.751\AA), while that of Au is 2.884\AA , larger than Pd [5]. It is thus possible to vary the relative Cu and Au content of the alloy while keeping the lattice parameter constant. This means that, in the fcc structure, it is possible to change the size of the octahedral sites, which is directly related to the lattice parameter, by changing the relative Cu and Au content. As the amount of palladium remains unchanged so will the number of Pd atoms in the near neighbor shell and in the next near neighbor shell of the site. This will prove to be important later on.

In Fig. 4.4, a comparison is made between the experimental lattice parameters determined from the diffractograms and the expected lattice parameter. The latter ones are calculated using the composition of the alloy and the following relation:

$$a_{expected} = \frac{x}{100}a_{Pd} + \frac{y}{100}a_{Cu} + \frac{100 - (x + y)}{100}a_{Au} \quad (\text{Equation 4.2})$$

Where a_{Pd} , a_{Cu} and a_{Au} are the lattice parameters of the pure palladium (3.89 Å), copper (3.62 Å) and gold (4.07 Å), respectively, and x and y are the atomic percent compositions in Pd and Cu, as measured by EDX. The assumption that the lattice parameter of an alloy varies linearly with the composition is known as the Vegard's law [6, 7].

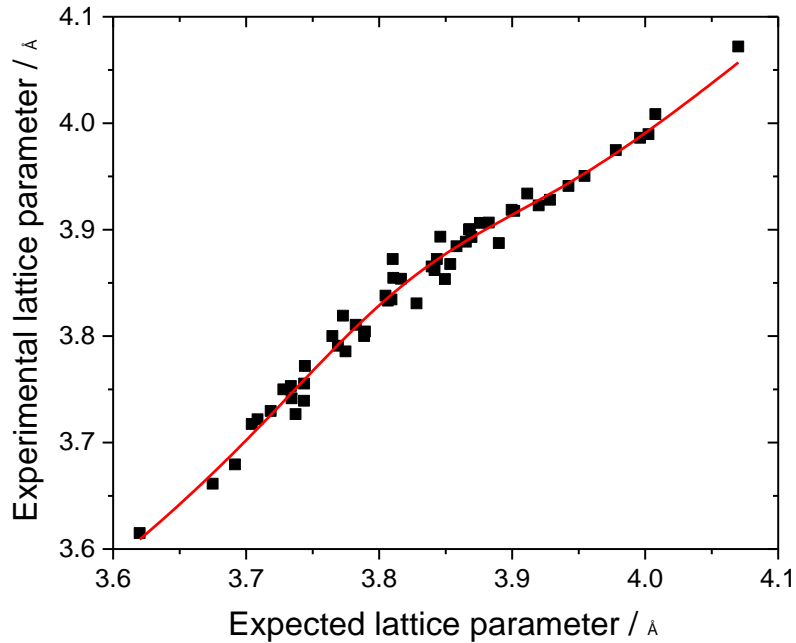


Figure 4. 4 – Variation of the experimentally measured lattice parameter with respect to the lattice parameter expected from the composition of the film assuming that Vegard's law holds true. The Gaussian shaped curve that is superimposed on the one-to-one straight line is centered at 3.82 Å and has a half width at half maximum of 0.10 Å.

As seen in Fig. 4.4, the difference between the expected and the experimental lattice parameter displays a bell-shaped dependence with the expected lattice parameter, centered at 3.82 Å and with a maximum deviation of *ca* 0.04 Å.

Uniform strain can cause a shift of the diffraction lines and this could be the cause of the discrepancy between the experimental and the expected lattice parameters. This is even more critical for materials like Cu, Pd and Au since they have relatively large Zener anisotropy ratio (2.8 for Pd, 2.9 for Au and 3.2 for Cu [8]). To verify this hypothesis, samples were heat treated at 400°C under Ar for 4 hours and their lattice parameters were compared before and after heat treatment. For those samples that kept the same fcc structure after heat-treatment, the average lattice parameter difference, $\Delta a = a_{as-deposited} - a_{heat-treated}$, is 0.004Å, which is a factor of 10 lower than the maximum difference noted previously. This indicates that strain – known to be relaxed upon heat treatment– is not fully responsible for the lattice deviation observed in Fig. 4.4.

Y. Rosenberg *et al.*[9] have shown that AuCu alloys display a similar behavior (deviation of the lattice parameter expected from the expected value calculated from the known composition of the alloy and assuming Vegard's law). The authors attributed this deviation to changes in the deformation energy which depends on the alloy composition. More precisely, the deformation energy is related to the relative size dispersion, γ , of the atoms in a substitutionally disordered crystal. By considering the size of the atoms, the probability of the same type of atoms to occupy a specific site in the crystal lattice, they were able to model γ as a function of the AuCu alloy composition [9]. It was shown that both γ and the deformation energy display the same trend with respect the composition of the alloy, with a maximum for [Cu] = [Au] = 50 at.%. This means that the maximum difference between the actual lattice parameter and the one expected from Vegard's law is observed at the alloy composition for which the deformation energy and γ are maximum. Following the same approach, the relative size distribution for a ternary alloy can be written as:

$$\gamma = \frac{\langle(\Delta d)^2\rangle}{\langle d \rangle^2} = \frac{d_1^2x + d_2^2y + d_3^2(1-x-y) - [d_1x + d_2y + d_3(1-x-y)]^2}{[d_1x + d_2y + d_3(1-x-y)]^2} \quad (\text{Equation 4.3})$$

where d_1 , d_2 and d_3 represent the atomic radii of Pd (2.7510Å) , Cu (2.5560Å) and Au (2.8839Å), respectively. In this equation, x , y and $(1-x-y)$ are the probabilities of a site being occupied by a Pd, Cu and Au atom, respectively. This equation shows a maximum at $x = 0$ and $y = 0.47$. For this composition, which corresponds to Pd₀Cu₄₇Au₅₃ and to an expected lattice parameter of 3.86

\AA , the deformation energy, and hence Δa , should be maximum. This is consistent with the data presented in Fig. 4.4, where Δa is maximum for a lattice parameter of $3.82 \pm 0.04 \text{\AA}$. Accordingly, the deviation from Vegard's law is the result of the deformations imposed on the crystal lattice by the different sizes of the atoms.

The crystallite size of the different deposits may be calculated using the Scherrer equation (equation 3.4 in section 3.2.1.1), applied to peak (200). The results are presented in figure 4.5.

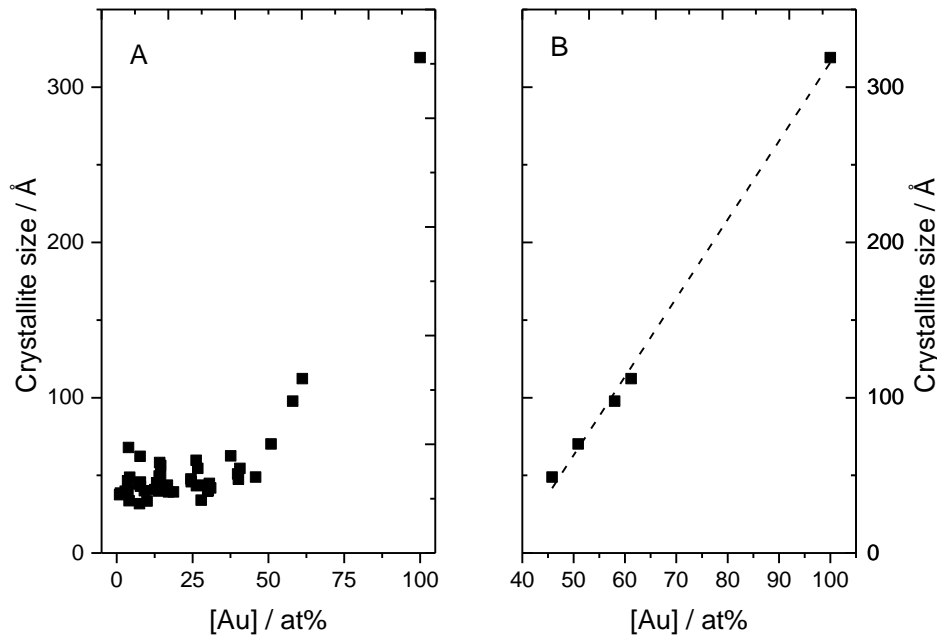


Figure 4. 5 – Crystallite size as a function of gold composition for PdCuAu alloys over the entire composition range (A,) and for gold concentrations above 45 at% (B,).

As it can be seen in Fig. 4.5, the crystallite size is $(45 \pm 8) \text{\AA}$ for compositions below 45 at% Au. For higher gold compositions, the crystallite size increases linearly to a maximum of 318\AA for pure gold.

4.1.3. Morphology analysis by SEM

The morphologies of the as-deposited alloy thin films were observed by SEM. As shown by Allemand *et al.* [3], the morphology of the deposit may vary with the film composition, the deposition time and the applied potential. In the current study, the deposition conditions were the

same for all deposits, except for the composition of the electrolytic bath. A few representative examples of the SEM micrographs are shown in Fig. 4.6.

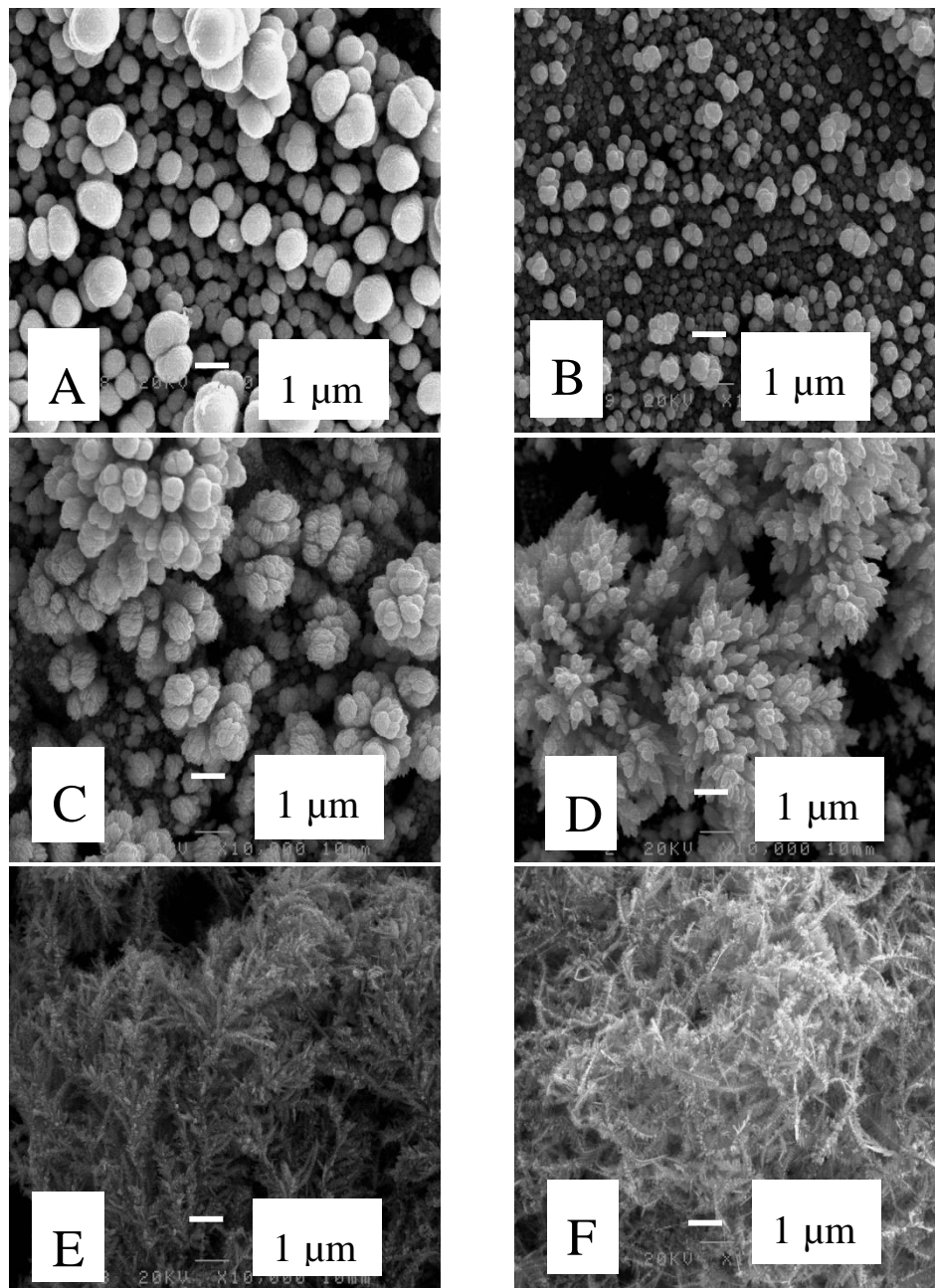


Figure 4. 6 – SEM micrographs of PdCuAu thin films that are arranged in order of increasingly higher Pd content. In (A) $\text{Pd}_{14.3}\text{Cu}_{82.1}\text{Au}_{3.6}$, (B) $\text{Pd}_{38.2}\text{Cu}_{57.1}\text{Au}_{4.7}$, (C) $\text{Pd}_{56.2}\text{Cu}_{19.2}\text{Au}_{24.6}$, (D) $\text{Pd}_{66.1}\text{Cu}_{7.8}\text{Au}_{26.2}$, (E) $\text{Pd}_{74.3}\text{Cu}_{18.4}\text{Au}_{7.3}$, and (F) $\text{Pd}_{100}\text{Cu}_{0.0}\text{Au}_{0.0}$.

It was found from a detailed analysis of all films prepared in this study that the Pd content is the main parameter that determines the morphology of the films. Accordingly, the SEM micrographs of Fig. 4.6 are shown as a function of increasingly higher Pd content, namely, 4.6A – Pd_{14.3}Cu_{82.1}Au_{3.6}, 4.6B – Pd_{38.2}Cu_{57.1}Au_{4.7}, 4.6C – Pd_{56.2}Cu_{19.2}Au_{24.6}, 4.6D – Pd_{66.1}Cu_{7.8}Au_{26.2}, 4.6E – Pd_{74.3}Cu_{18.4}Au_{7.3} and 4.6F – Pd₁₀₀Cu_{0.0}Au_{0.0}. At the lowest Pd content, the films are composed of small spheres of less than 1 μm in diameter. As the Pd content increases, the spheres are clustering together (see Fig 4.6C) and a needle-like morphology is clearly discernible at still higher Pd content (see Fig. 4.6D and 4.6E). For pure Pd, a spaghetti-like structure is observed (see Fig. 4.6F). The morphology of the films is not adequate for gas phase separation, as many pores are present, especially in the case of more dendrimeric structures. However, these films were prepared to use in the measurement of hydrogen solubility in aqueous solution, where the presence of pores is not important. Nonetheless, the preparation of denser structures can be attained by modifying the electrodeposition conditions [10, 11].

Micrographs of higher magnification were also taken for pure palladium and are shown in figure 4.7.

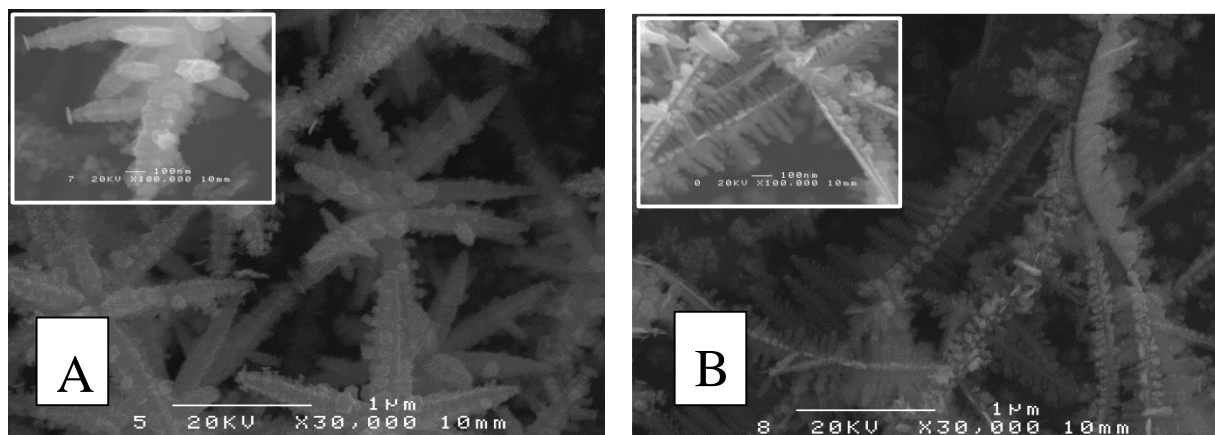


Figure 4. 7 – High magnification micrographs (30,000 times and 100,000 times in the insets) of a pure palladium film electrodeposited on a titanium substrate.

Figure 4.7 reveals that the spaghetti structure of palladium shown in Fig. 4.6F is in fact a mixture of two different structures. Figure 4.7A shows branched nanostructures where 8-9 branches are grown from the center. In figure 4.7B, fern-leaf like structures can be observed. The

morphology of electrodeposited palladium shown here is notoriously different from other published results. In particular, Reyter and coworkers [11] described the formation of a smooth palladium surface prepared on a Ni substrate from the electrolysis of PdCl₂ 10 mM solution at -500 mV vs. SCE for 20 minutes. These differences could be the result of different amounts of hydrogen that is being co-deposited. Co-deposition of hydrogen can lead to the preferential growth of certain planes, favoring in this way different morphologies.

4.1.4. Characterization of annealed samples

It is known from the literature that the binary Pd-Cu system displays a domain of composition where the bcc structure is stable at low temperature [12]. The existence of a bcc phase is attractive since this structure displays distinct hydrogen permeability properties than those of the fcc phase with the same composition [13-15]. All samples prepared in the present work were annealed at 400 °C during 4 h and analyzed by XRD after being cooled down to room temperature. A typical example of the XRD pattern of a sample (Pd_{35.6}Cu_{60.5}Au_{3.9}) undergoing the fcc to bcc transition is shown in Fig. 4.8.

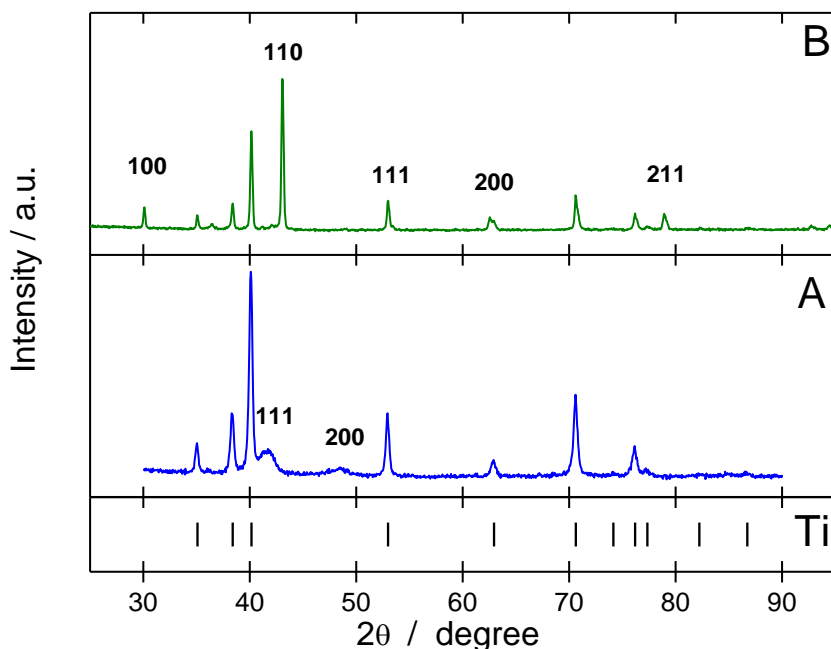


Figure 4. 8 – Comparison of XRD patterns of film with composition Pd_{35.6}Cu_{60.5}Au_{3.9} (A) before (fcc phase) and (B) after (bcc phase) heat treatment at 400°C.

From Fig. 4.8, both XRD patterns display the characteristic peaks of the Ti substrate. Before annealing, the characteristic diffraction peaks of the fcc phase (Fig. 5A) are present at $2\theta = 41.7^\circ$ (111), 48.5° (200) and 70.8° (220) (that later peak is superimposed on the (103) peak of Ti). After heat treatment at 400°C , the diffraction peaks of the fcc phase are no longer discernible. Instead, new peaks are visible at $2\theta = 30.1^\circ$ (100), 43.1° (110), 53.5° (111), 62.6° (200), 78.9° (211) and 94.5° (220) that are characteristic of a bcc phase (CsCl type lattice). The lattice parameter changes from 3.75 \AA in the fcc phase to 2.97 \AA in the bcc phase.

A similar fcc to bcc phase transition was observed in the following range of compositions (at%): $29.5 \leq \text{Pd} \leq 45.8$; $45.3 \leq \text{Cu} \leq 63.0$; and $0.0 \leq \text{Au} \leq 17.4$, with $[\text{Pd}] + [\text{Cu}] + [\text{Au}] = 100$. This region is shown in Fig. 4.9, along with the lattice parameter of the bcc phase.

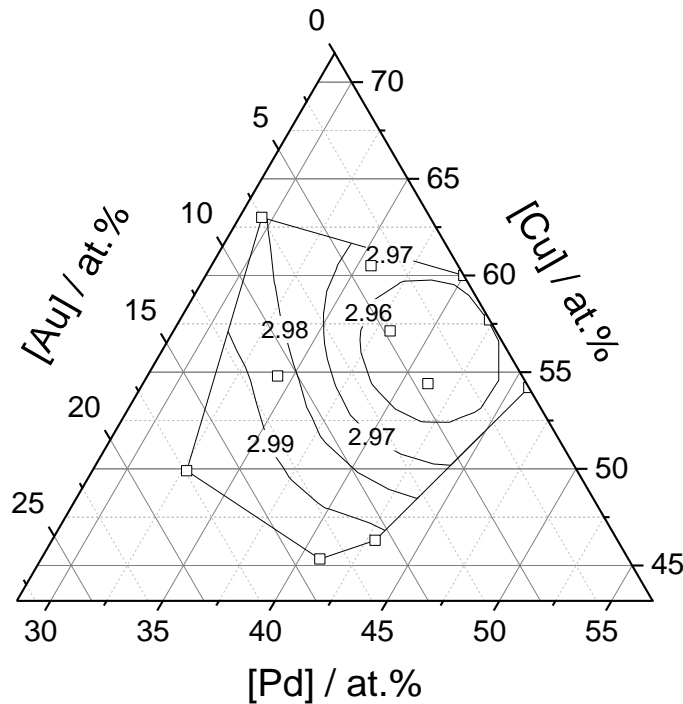


Figure 4. 9 – Ternary contour plot showing the variation of the experimentally determined lattice parameter for the bcc phase region with the film composition. The white squares are the EDX compositions of the samples used to construct this plot.

As noted previously, the lattice parameter of the bcc phase increases as the Au content of the alloy is increased. Again, this is consistent with the fact that the atomic radius of Au atom is larger than that of Cu atom. It is noteworthy that replacing some of the Cu atoms by Au atoms extends the range of concentration over which the bcc phase is stable. Indeed, according to Subramanian *et al.* [12], the bcc phase is stable for $34 \leq \text{Pd} \leq 47$ at% in the PdCu system at 400 °C, while this range is as large as $29.5 \leq \text{Pd} \leq 45.8$ at% in the present work, when some of the Cu atoms are replaced by Au atoms. This means that gold has a stabilizing effect on the bcc structure.

Outside of the composition range where the fcc to bcc phase transition is observed, the crystallographic structure of the film remains either fcc ($Fm\bar{3}m$) or changes to tetragonal ($P4/mmm$, tetra-auricupride structure). In some cases, such as $(\text{Pd}_{16.1}\text{Cu}_{74.4}\text{Au}_{9.4})$, ordering of the fcc phase was observed. In this case, the heat treatment gave rise to a simple cubic structure ($Pm\bar{3}m$, AuCu_3 structure), where Pd and Au share the same site. These results are summarized in Fig. 4.10, which represents a phase diagram for PdCuAu alloys for temperatures below 400°C.

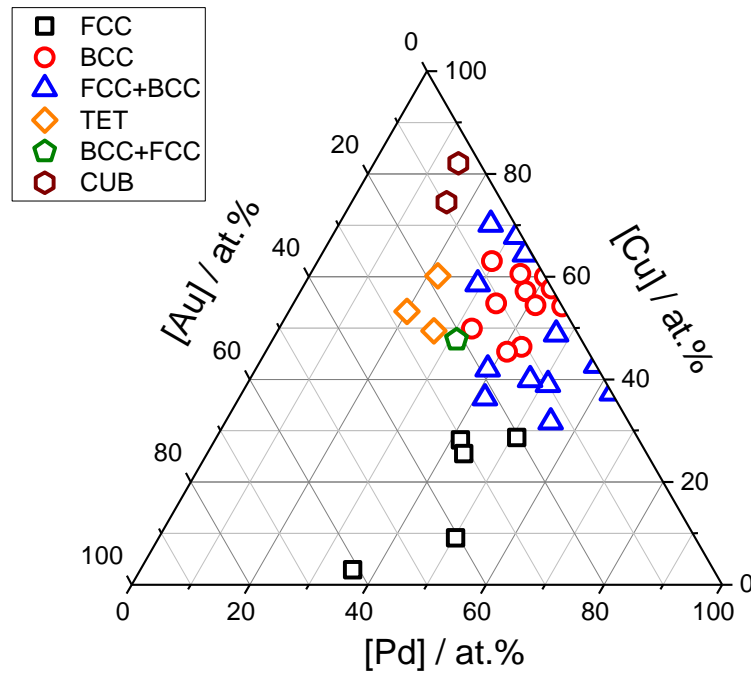


Figure 4. 10 – Ternary diagram showing final crystallographic phases after 4 hour-heat treatment at 400°C and under Ar. EDX compositions are used. FCC – face-centered cubic; BCC – body-centered cubic; TET – tetragonal; CUB – simple cubic

The results above are consistent with data from the literature since it is known that the introduction of gold in the mixture does not preclude the formation of the bcc phase. Indeed, according to the ternary Pd-Cu-Au phase diagram [16], three distinctive structures are thermodynamically stable at 400°C, namely a disordered fcc phase, a tetragonal phase, and a bcc phase with a CsCl type lattice (B2). At 400 °C, the present domain of existence of the bcc phase is identical to that expected from the work of Prince *et al.* [16].

In the following, we are going to pay a special attention to films whose compositions are falling within a restricted domain where the fcc to bcc phase transition occurs. SEM micrographs of Pd_{38.8}Cu_{56.2}Au_{5.0} thin film before (fcc phase) and after heat-treatment at 400°C (bcc) are displayed in Fig. 4.11A and 4.11B, respectively. As seen in these micrographs, there is no major change (except for a welding of the particles) in the morphology of the film as a result of the heat-treatment step.

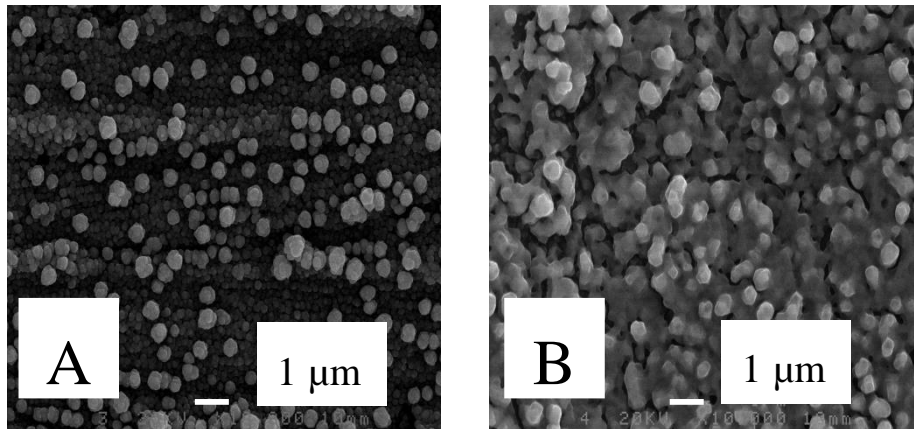


Figure 4. 11 – SEM micrographs of Pd_{38.8}Cu_{56.2}Au_{5.0} thin film (A) before (fcc phase) and (B) after heat-treatment at 400 °C (bcc phase).

4.2. Hydrogen solubility measurements

The solubility of hydrogen in the PdCuAu ternary alloys was assessed by an electrochemical method in an aqueous alkaline media at room temperature. M. Martin *et al.* [17], have shown that CuPd-based alloys are stable in alkaline media in the potential range of interest here, whereas leaching of Cu atoms is observed at the same potential in acidic electrolyte. However, we will see in chapter 5 (section 5.2) that some copper dissolution should not be completely ruled out even in alkaline solution.

At sufficiently negative potential, the absorption of hydrogen in the ternary alloy occurs through a two-step process, where the adsorption/reduction reaction of hydrogen at the metal surface occurs first, followed by the diffusion of hydrogen atoms into the bulk of the material where it is absorbed [18] (section 2.3). At the opposite, at sufficiently positive potential, desorption/oxidation of hydrogen atoms arises. Under the conditions that were defined elsewhere [17], the coulombic charge associated with the oxidative current is a measure of the amount of hydrogen atoms that were previously absorbed in the alloy. In order to verify if equilibrium is reached during reduction and if all hydrogen was oxidized at positive potentials, the times of reduction and oxidation were varied as illustrated in Fig. 4.12.

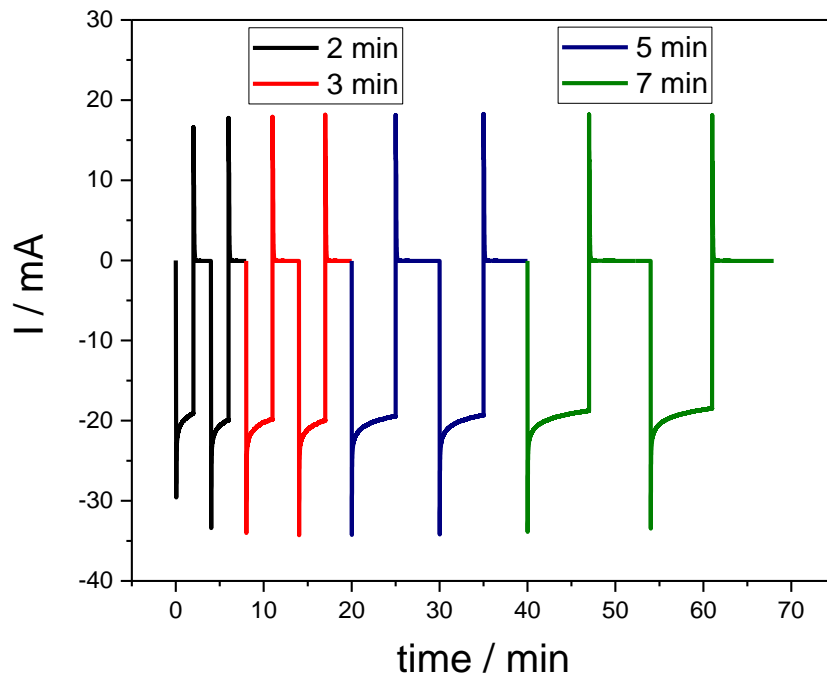


Figure 4. 12 – Variation of the reduction and oxidation times: 2, 3, 5 and 7 minutes. Each time was applied twice.

In Fig. 4.12, a negative potential (-1400 mV vs. Hg/HgO) is first applied for 2 minutes giving rise to -20 mA reduction current. Afterwards the potential is switched to -400 mV vs. Hg/HgO giving rise to a sharp increase in current to 15 mA (oxidation current). The oxidation potential is kept for 2 minutes before repeating the experiment. Reduction/oxidation times were then increased to 3, 5 and 7 minutes, and each time was applied twice. The charge measured during oxidation was: 68 and 69 mC, for the two 2-minute oxidation, 70 mC for the two 3-minute oxidation, 71 for the two 5-minute oxidation and 70 mC for the two 7-minute oxidation. Thus, in all cases equilibrium is reached during reduction and the oxidation time is long enough to achieve complete oxidation of hydrogen. All further experiments were performed by setting reduction and oxidation time equal to three minutes each.

In the following, H-absorption is performed at a significantly negative potential, *i.e.* from -650 to -1400 mV (vs. Hg/HgO). After this absorption period, the potential is stepped to -400 mV (vs. Hg/HgO) to oxidize all the H absorbed in the Pd-based material; the oxidation current is then

integrated and this charge is converted into the number of absorbed hydrogen moles to measure the solubility of H in the alloy. It must be mentioned that no oxidation of the PdCuAu film was witnessed at -400 mV, during the desorption step. The pros and cons of the method used in the present study were discussed in detail elsewhere [17].

Typical examples of the hydrogen absorption isotherms are given in Fig. 4.13 for pure Pd and for three different fcc ternary alloys, namely Pd₆₉Cu₁₇Au₁₄, Pd₄₈Cu₂₆Au₂₆, and Pd₄₂Cu₂₈Au₃₀.

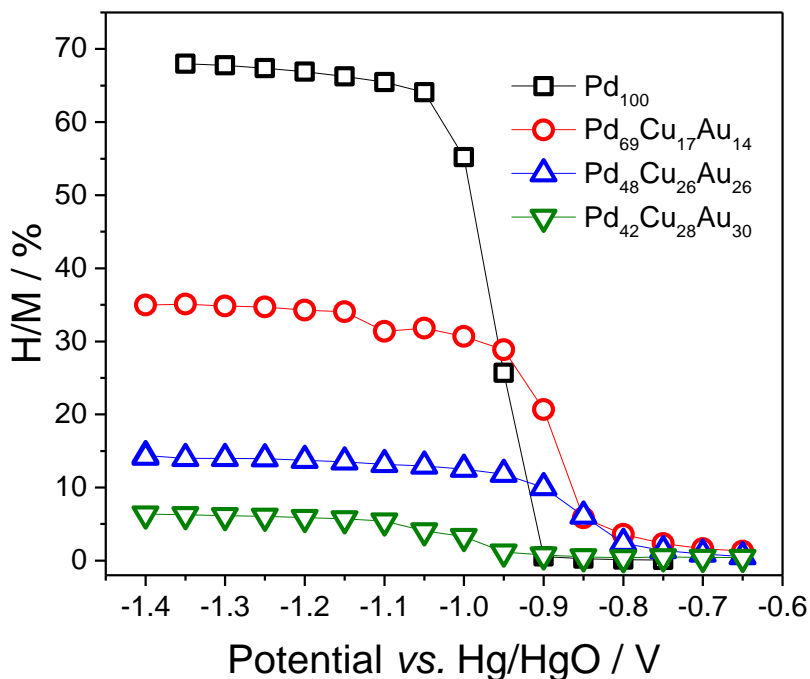


Figure 4. 13 – Variation of the hydrogen solubility with the applied potential for PdCuAu alloys at different compositions. All measurements were performed in NaOH 0.1M.

As seen in Fig. 4.13, the hydrogen solubility for pure palladium increases as the absorption potential is made more negative (from -650 to -850 mV; α phase region). The hydrogen solubility increases abruptly at *ca.* -950 mV ($\alpha+\beta$ mixed region) to reach a plateau (β phase region) at still more negative absorption potentials. The shape of the curves for the alloys is not markedly different from that measured on pure Pd thin film, except for the maximum H/M value that varies by a factor of 10 between Pd and Pd₄₂Cu₂₈Au₃₀, indicating that hydrogen solubility is far more important in the former compared to the latter material. And also, the difference between the

maximum hydrogen dissolved in the α and in the β region seems to become less important upon decreasing the amount of palladium in the alloy. In the following, the maximum hydrogen solubility, $(H/M)_{\max}$, was taken as the value measured at -1400 mV (*vs.* Hg/HgO). For example, pure palladium shows a $(H/M)_{\max}$ value of 68%, which is in good agreement with the already published results [17, 19-21], while that of Pd₄₂Cu₂₈Au₃₀ is 6.3%.

In this work, the effects of the alloy composition and of the crystalline structure of the film on the hydrogen solubility were studied. The hydrogen solubility was first measured with respect to the palladium content by varying it between 45 and 100% Pd. These results are shown in Fig.4.14.

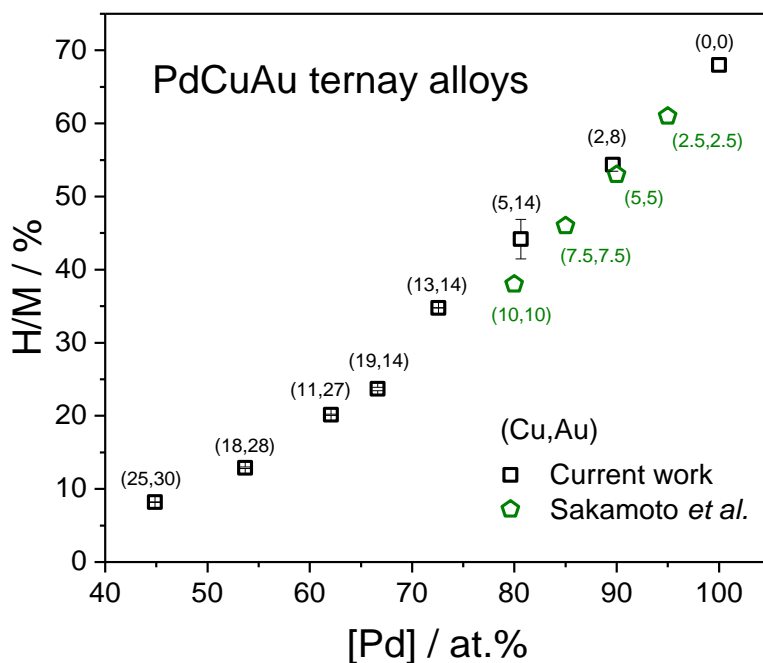


Figure 4. 14 – Variation of the hydrogen solubility of PdCuAu alloys with the palladium content. All films are made of a fcc phase with a lattice parameter (3.885 ± 0.005) Å. The data taken from reference [22] is also shown for comparison. The copper and gold contents are shown in at.% in brackets.

As seen in Fig. 4.14, the hydrogen solubility increases steadily with the Pd content, from 8.2 % for [Pd] = 45 at.% to 68.0 % for [Pd] = 100 at.%. For comparison, the results obtained by

Sakamoto *et al.* [22] from measurements in the gas phase at 30°C are also shown. In the range where a comparison is possible ([Pd] ≥ 80 at.%), both sets of results are identical within the experimental error. In the present study, we were able to considerably extend the range over which the hydrogen solubility can be assessed in the fcc phase. A decrease of the palladium content in the alloy results in a decrease of the hydrogen solubility. To the best of our knowledge, the hydrogen solubility in PdCuAu alloys had never been measured at concentrations lower than 80 at.% Pd.

The lattice parameter of the samples used to draw Fig. 4.14 is almost the same (3.885 ± 0.015) Å, very close to the lattice parameter of pure Pd, which is 3.88674 Å). This assertion holds true for the data taken from the work of Sakamoto *et al.* [22] as well. Accordingly, it is clear that the concentration of palladium is the key factor in determining the hydrogen solubility of this type of alloys.

The fact that the lattice parameters of the fcc alloy does not change as the Pd content is varied from 45 to 100 at% depends on a delicate balance between the Cu and Au content of the film since, as it was discussed previously, the insertion of Cu atoms in the structure tends to decrease the lattice parameter, while that of Au atoms have the opposite effect. In order to differentiate the effect of copper from that of gold, hydrogen solubility measurements were also performed at constant palladium concentration and by changing the relative amounts of Cu/Au. The results are summarized in Fig. 4.15.

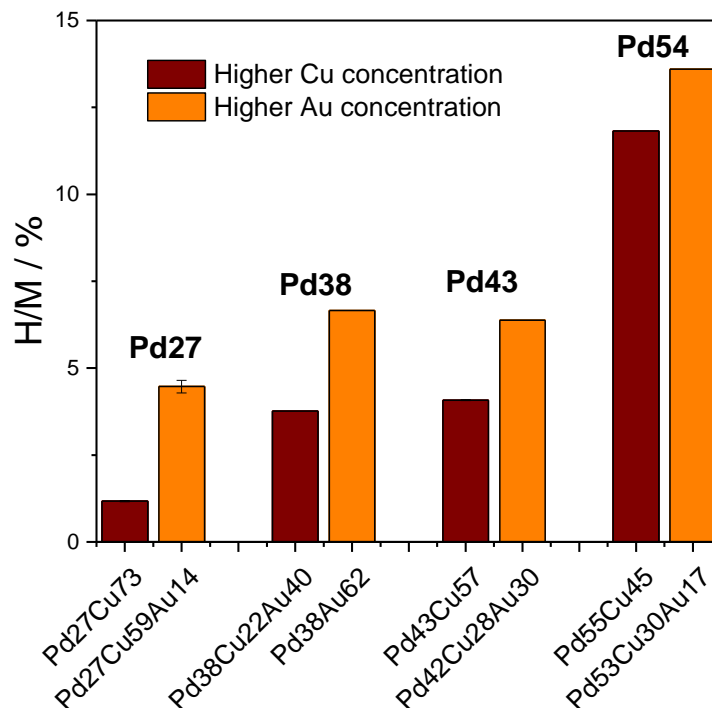


Figure 4. 15 – Effect of copper and gold on the hydrogen solubility of PdCuAu alloys at constant palladium content.

In Fig. 4.15, it can be observed that for a constant palladium content of 27 at.%, the hydrogen solubility increases from 1.17 to 4.5 % as the gold content is increased from 0 to 14 at.%. Similar trends are observed in samples with [Pd] = 38, 43 and 54 at.%. At constant palladium concentration, an increase in the hydrogen solubility is observed as some copper atoms are replaced by gold atoms in the alloy.

The previous observation is consistent with first-principle models of hydrogen permeation PdCu-based ternary alloys [23]. The increase of the hydrogen solubility in Pd-Cu-Au has been described as the result of the repulsive interaction of Cu-H pairs and the attractive interaction of Au-H pairs [22], combined with the increase in the lattice parameter that results from the replacement of Cu atoms by Au atoms. For example, at [Pd] = 27 at.%, the lattice parameter of the fcc alloy increases from 3.68 to 3.82 Å when the gold content increases from 0 to 14.1 at.%. The same trend is observed in all cases depicted in Fig. 4.15. This occurs because the atomic radius of Au atoms (2.884 Å) is much larger than that of Cu (2.556 Å).

In order to study the effect of the alloy structure on the hydrogen solubility, samples that are made of a pure bcc phase after annealing at 400 °C were also tested. Two representative examples of electrochemical isotherms of samples with the same composition ($\text{Pd}_{33}\text{Cu}_{50}\text{Au}_{17}$) but different structure (fcc and bcc) are shown in Fig. 4.16.

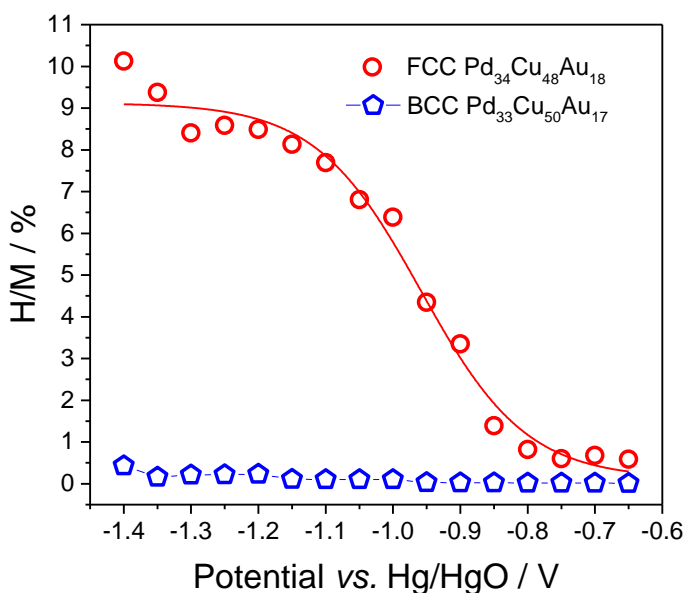


Figure 4. 16 – Variation of the hydrogen solubility with the applied potential for PdCuAu alloy in the fcc and in the bcc phase. All measurements were performed in NaOH 0.1M.

As seen in Fig. 4.16, the maximum hydrogen solubility of the sample in the bcc phase is *ca.* 0.5%, whereas it is 10.2% for the fcc phase. This observation is similar to that made on binary PdCu alloys when the fcc to bcc phase transformation is performed [17]. H atoms are mostly located at the octahedral interstitial sites of the fcc phase, while in the bcc phase H occupies mostly the tetrahedral sites [24]. In general the binding energies of hydrogen to the octahedral sites is more negative than the corresponding energies to the tetrahedral sites, due to the higher coordination number (meaning the number of possible neighboring palladium atoms) of the hydrogen atom when located in the octahedral sites. H is therefore more stabilized in the fcc phase than in the bcc phase, which results in the higher solubility shown by the fcc phase.

In Fig. 4.16, the maximum charge recorded during the potential step measurement used to assess the amount of hydrogen atoms dissolved in the $\text{Pd}_{33}\text{Cu}_{50}\text{Au}_{17}$ bcc alloy is 1.3 mC, which is

of the same order as the detection limit of the method. Hence, while it is clear that a change in the structure of the alloy has a marked effect on the hydrogen solubility, it is difficult to proceed any further with a study of the effect of the Au content on the hydrogen solubility of the bcc alloys. This point will be further addressed in chapter 5.

4.3. Conclusion

PdCuAu alloy thin films were prepared by co-electrodeposition over a large composition range. The interplay of the amount of copper and gold allows the production of alloys that have the same lattice parameter but are of different compositions. Introducing in the same lattice atoms that are of different sizes was shown to cause strain. The alloys prepared have various morphologies that mostly depend on the palladium content, possibly as a result of the increased co-deposited H in samples richer in Pd. As-deposited samples invariably show the fcc crystallographic structure. Other crystallographic phases were identified by heat treating the samples. As an example, the bcc phase can be obtained and in fact the ternary PdCuAu alloys were shown to have an extended composition range where the bcc phase is stable, in comparison with binary PdCu alloys. Three factors were identified that determine the hydrogen solubility of the alloy, namely the palladium content, the Au/Cu ratio and, finally, the crystallographic structure (fcc vs. bcc).

4.4. References

- [1] CRC Handbook of Chemistry and Physics. 73rd ed: CRC Press, Inc.; 1992-1993.
- [2] Brenner A. Electrodeposition of Alloys: Principles and Practice Academic Press Inc.; 1963.
- [3] Allemand M, Martin MH, Reyter D, Roué L, Guay D, Andrei C, et al. Synthesis of Cu-Pd alloy thin films by co-electrodeposition. *Electrochimica Acta*. 2011;56:7397-403.
- [4] Hernández SC, Yoo BY, Stefanescu E, Khizroev S, Myung NV. Electrodeposition of iron-palladium thin films. *Electrochimica Acta*. 2008;53:5621-7.
- [5] Cullity BD. Elements of X-Ray Diffraction. 2 ed: Addison-Wesley Publishing Company, Inc.; 1978.
- [6] Denton A, Ashcroft N. Vegard's law. *Physical Review A*. 1991;43:3161-4.
- [7] Vegard L. Die Konstitution der Mischkristalle und die Raumfüllung der Atome. *Z Physik*. 1921;5:17-26.
- [8] Faurie D, Djemia P, Le Bourhis E, Renault PO, Roussigné Y, Chérif SM, et al. Elastic anisotropy of polycrystalline Au films: Modeling and respective contributions of X-ray diffraction, nanoindentation and Brillouin light scattering. *Acta Materialia*. 2010;58:4998-5008.
- [9] Yu R, Machavariani VS, Voronel A, Garber S, Rubshtein A, Frenkel AI, et al. Strain energy density in the x-ray powder diffraction from mixed crystals and alloys. *Journal of Physics: Condensed Matter*. 2000;12:8081.
- [10] Allemand M, Martin MH, Reyter D, Roué L, Guay D, Andrei C, et al. Synthesis of Cu-Pd alloy thin films by co-electrodeposition. *Electrochimica Acta*. 2011;56:7397-403.

- [11] Reyter D, Bélanger D, Roué L. Elaboration of Cu–Pd Films by Coelectrodeposition: Application to Nitrate Electroreduction. *The Journal of Physical Chemistry C*. 2009;113:290-7.
- [12] Subramanian PR, Laughlin DE. Cu-Pd (Copper-Palladium). *Journal of Phase Equilibria*. 1991;12:231-43.
- [13] Mckinley DL. Metal alloy for hydrogen separation and purification. United States: US patent 3,350,845; 1967.
- [14] Howard BH, Killmeyer RP, Rothenberger KS, Cugini AV, Morreale BD, Enick RM, et al. Hydrogen permeance of palladium-copper alloy membranes over a wide range of temperatures and pressures. *Journal of Membrane Science*. 2004;241:207-18.
- [15] Kamakoti P, Morreale BD, Ciocco MV, Howard BH, Killmeyer RP, Cugini AV, et al. Prediction of Hydrogen Flux Through Sulfur-Tolerant Binary Alloy Membranes. *Science*. 2005;307:569-73.
- [16] Prince A, Raynor GV, Evans DS. *Phase Diagrams of Ternary Gold Alloys: The Institute of Metals*; 1990.
- [17] Martin MH, Galipaud J, Tranchot A, Roué L, Guay D. Measurements of hydrogen solubility in $\text{Cu}_x\text{Pd}_{100-x}$ thin films. *Electrochimica Acta*. 2013;90:615-22.
- [18] Kleperis J, Wójcik G, Czerwinski A, Skowronski J, Kopczyk M, Beltowska-Brzezinska M. Electrochemical behavior of metal hydrides. *Journal of Solid State Electrochemistry*. 2001;5:229-49.
- [19] Ebisuzaki Y, O'Keeffe M. The solubility of hydrogen in transition metals and alloys. *Progress in Solid State Chemistry*. 1967;4:187-211.

- [20] Flanagan TB, Chisdes DM. Solubility of hydrogen (1 atm, 298 K) in some copper/palladium alloys. *Solid State Communications*. 1975;16:529-32.
- [21] Maeland AJ, Flanagan TB. Comparison of hydrogen and deuterium solubility in palladium-rich alloys, gold-palladium. *J Phys Chem*. 1967;71:1950-2.
- [22] Sakamoto Y, Ishimaru N, Mukai Y. Thermodynamics of Solution of Hydrogen in Pd-Cu and Pd-Cu-Au Solid Solution Alloys. *Berichte der Bunsen-gesellschaft fuer physikalische Chemie*. 1991;95:680-8.
- [23] Semidey-Flecha L, Ling C, Sholl DS. Detailed first-principles models of hydrogen permeation through PdCu-based ternary alloys. *Journal of Membrane Science*. 2010;362:384-92.
- [24] Kamakoti P. A comparison of hydrogen diffusivities in Pd and CuPd alloys using density functional theory. *Journal of Membrane Science*. 2003;225:145-54.

Cet article a dû être retiré de la version électronique en raison de restrictions liées au droit d'auteur.

Vous pouvez le consulter à l'adresse suivante :

DOI : [10.1021/acs.jpcc.5b10711](https://doi.org/10.1021/acs.jpcc.5b10711)

6. Hydrogen permeability of PdCuAu membranes prepared from mechanical alloyed powders

PdCuAu bulk ternary alloys were prepared by ball milling together pure palladium, copper and gold (section 6.1). The powders thus obtained were used in the preparation of membranes (section 6.2) that were later studied for their hydrogen permeability properties (section 6.3). In particular, experiments were performed in the presence of pure hydrogen gas (section 6.3.1) and in the presence of H₂S (section 6.3.2). Finally, the conclusions will be presented (section 6.4).

6.1. Synthesis and characterization of PdCuAu alloys

High-energy ball milling was used in the preparation of PdCuAu ternary alloys from pure Pd, Cu and Au powders. NaCl was added as a process control agent (PCA) in order to avoid extensive welding. The powders were milled together for 18 hours inside Ar-filled stainless steel vessels while using stainless steel balls as the grinding medium. A ball-to-powder mass ratio of 2:1 was used. Four different compositions were prepared, all with the same target palladium content (40 at.%) and with increasing amounts of gold (0, 3, 7 and 11 at.%), with the copper content being adjusted accordingly. In Table 6.1, the measured EDX composition after ball milling is compared with the nominal compositions.

Table 6. 1 – Nominal and EDX compositions for the 4 synthesis performed.

Synthesis #	Nominal composition (at.%)	EDX composition (at%)
1	Pd ₄₀ Cu ₆₀	Pd ₃₉ Cu ₆₁
2	Pd ₄₀ Cu ₅₇ Au ₃	Pd ₄₁ Cu ₅₆ Au ₃
3	Pd ₄₀ Cu ₅₃ Au ₇	Pd ₄₀ Cu ₅₃ Au ₇
4	Pd ₄₀ Cu ₄₉ Au ₁₁	Pd ₃₉ Cu ₅₁ Au ₁₀

As shown in Table 6.1, all EDX compositions are in agreement with the target compositions. Na and Fe contaminations are also present at levels less than 5 and 2 at.%, respectively. Na was purposely added to the preparation as PCA. However, Fe represents a true contamination originating from the mill and the balls which are all made of stainless steel. More than one batch for each composition was produced, but the results were found to be equivalent and within the same composition regardless of the batch number. Typical micrographs of the powders obtained with ball milling are shown in Fig. 6.1.

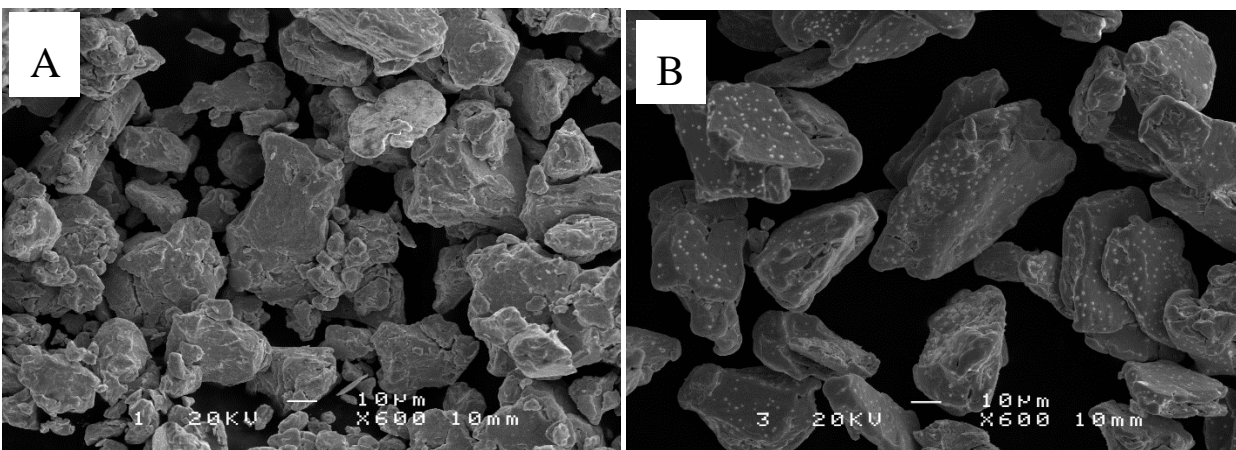


Figure 6. 1 – Micrographs of A) Pd₄₀Cu₅₃Au₇ (synthesis 3 in Table 6.1) and B) pure Pd, both at 600 times magnification, after 18 hours of ball milling. Grains of NaCl are clearly visible in micrograph B.

As seen in Fig.6.1, ball milling leads to the formation of a variety of structures, many oval-shaped, with the largest ones measuring about 70 μm along the longer axis. The powders were characterized by XRD after synthesis. Afterwards they were annealed for 5 hours under Ar 5% H₂ at 400°C and were again analyzed by XRD. No significant differences in morphology were observed upon annealing. The diffractograms of the various samples are shown in Fig. 6.2 for the before and after annealing treatment.

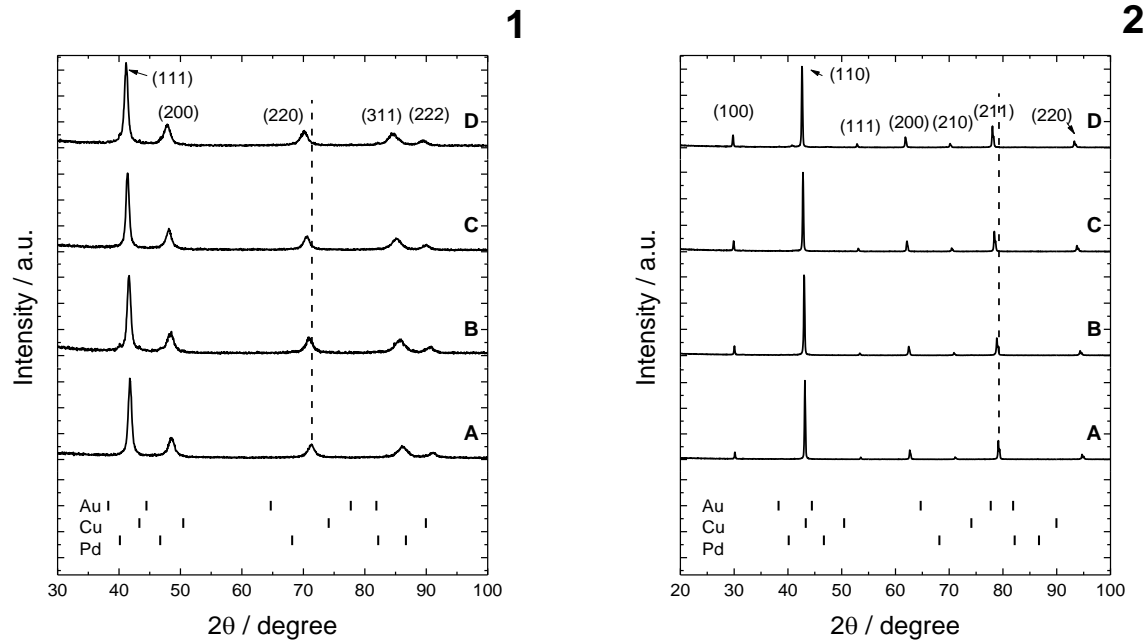


Figure 6. 2 – Diffractograms of the as-milled powders (panel 1) and after 5-hour heat treatment (panel 2) arranged by increasing gold content from 0% (A) to 10% (D) (A – Pd₃₉Cu₆₁; B – Pd₄₁Cu₅₆Au₃; C – Pd₄₀Cu₄₃Au₇; D – Pd₃₉Cu₅₁Au₁₀).

As seen on the left panel of Fig. 6.2 there is only one phase present after 18 hours of mechanical alloying. Indeed, all diffractograms show the characteristic peaks of a face centered cubic phase. For example, in the case of alloy Pd₃₉Cu₆₁ (Fig. 6.2A, left side) peaks are observed at 41.7 (111); 48.5 (200); 71.3 (220); 86.2 (311) and 91.1° (222). A phase transition to body centered cubic (CsCl-type structure) phase occurs with annealing as it can be observed on the right panel of Fig. 6.2. The conversion is complete for all samples except for the alloy with the highest gold content (D – Pd₃₉Cu₅₁Au₁₀), where the fcc peaks of the initial phase can still be seen. The bcc phase is in fact the thermodynamic stable phase for the given compositions and at room temperature [1, 2]. In this sense the solubility limits of the fcc were extended, similarly with what happens with the electrodeposited and the sputter deposited samples. Not only mechanical alloying is able to extent the solubility limits[3], but also there is a low variation of enthalpy during fcc to bcc phase transition (around 2 kJ·mol⁻¹[4]).

Taking a closer look at Fig. 6.2 we observed that, as the gold content increases from 0 (Fig.6.2A) to 10 at.% (Fig. 6.2D), all peaks shift towards lower 2θ values. This occurs for both phases, fcc and bcc, and is schematically represented by the dotted lines in panels 1 and 2. For example, for the fcc phase, peak (220) shifts from 71.3° (Fig. 6.2A) to 70.1° (Fig. 6.2D). For the bcc phase, peak (211) shifts from 79.2° (Fig. 6.2A) to 78.1° (Fig. 6.2D). These changes occur as the gold content is increased from 0 to 10 at.%, and they indicate that the lattice parameter is increasing as copper is replaced with gold. This is due to the larger lattice parameter of gold (4.07 \AA) in respect to that of copper (3.62 \AA), which causes the alloy lattice to expand as the gold content is increased. This feature was also observed and discussed in chapters 4 and 5. The lattice parameters were calculated from the position of each individual peak and using equation 3.3. The results are displayed in Fig. 6.3.

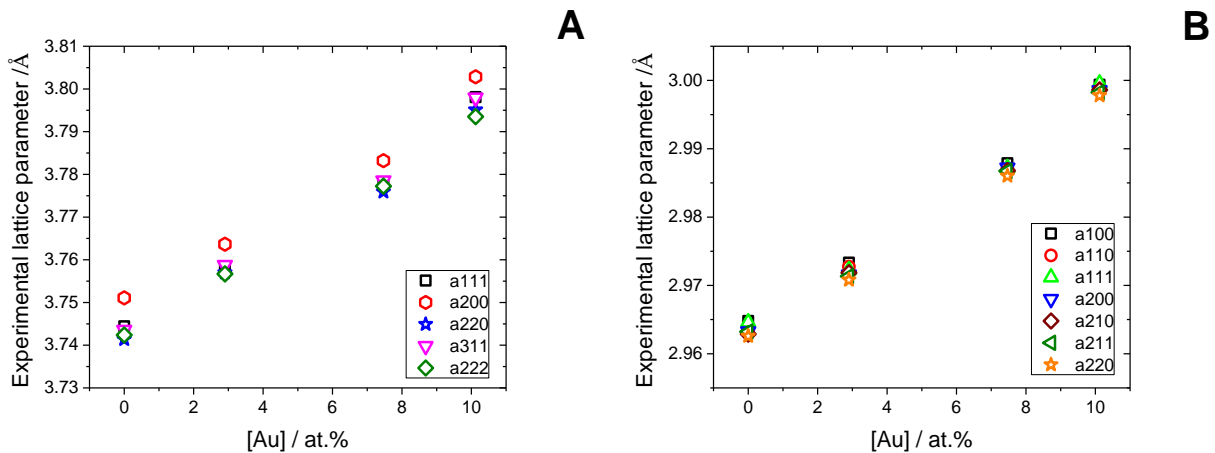


Figure 6. 3 – Experimental lattice parameter as a function of gold content for as-milled powders (A) and annealed samples (B).

As seen in Fig 6.3 and already anticipated in the previous paragraph, the lattice parameter increases with the gold content for both fcc and bcc phases. Interestingly, the increase in lattice parameter observed is about 1.4 and 1.2%, for the fcc and bcc phases, respectively, as the gold content varies from 0 to 10 at%. For each composition, the values calculated according to each direction are the same within experimental error, except for $a_{[200]}$ in the case of the fcc phase. For each composition, the values for the [200] direction are slightly higher (*ca.* 0.007 \AA) than the values for the remaining directions. Although small, the difference is significant as the error in

determining the lattice parameter is commonly below 0.001\AA for the present samples. This may indicate that there is extra strain on the [200] direction. Extensive cold welding occurs during ball milling that results in deformation of the powder and ultimately leading to the formation of the alloy. As Zener anisotropy ratios of Pd, Cu and Au, 2.8, 3.2 and 2.9, respectively, are relatively large, deformation is more likely to occur according to the [100] direction.

For the fcc phase, the experimental lattice parameter can be compared to the one calculated with Vegard's law. The comparison between the two lattice parameters is shown in Fig. 6.4.

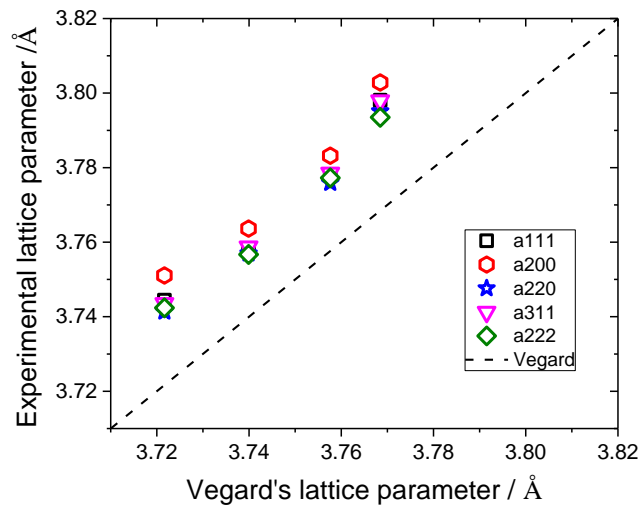


Figure 6. 4 – Comparison between the experimental and Vegard's lattice parameter for the mechanically alloyed powders.

As shown in Fig. 6.4 there is a positive deviation from Vegard's law. The same behavior was already observed in Chapters 4 and 5 and arises from the deformations imposed on the crystal lattice by the different sizes of the atoms. The fact that this deviation is positive is also indicating that the enthalpy of mixing of the three elements is positive [5].

6.2. Membrane preparation from ball milled powders and characterization

6.2.1. Preparation method

The PdCuAu alloys produced by mechanical alloying may be used in two different ways, either to prepare a thin film on a porous substrate (supported membrane) or to prepare a pellet (standalone membrane). Several strategies are available for the production of supported membranes, such as colloidal spray deposition [6], paste-painting [7] or cold spray deposition [8]. The main difference between these techniques is the combined use of solvents (organic or aqueous) and surfactants in the first two cases that could lead to undesired oxidation of the PdCuAu powder. In this sense, cold spray deposition is attractive but unfortunately it is a technique best suitable for larger scale applications (in the present case, we are interested in having membranes with a diameter of about 1.1 cm or less). Having ruled out supported membranes, a method was devised for the production of standalone membranes from the PdCuAu alloyed powders. This method was already described in section 3.2 but a schematic description of it is given here for easier reference (Fig. 6.5).

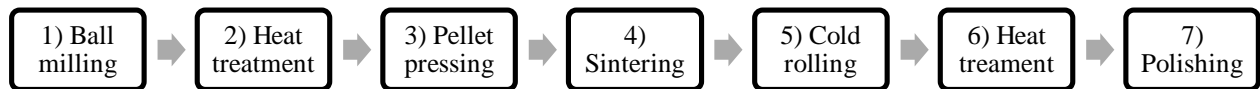


Figure 6. 5 – Method for the production of PdCuAu membranes from mechanically alloyed PdCuAu powder (same as Fig. 3.2).

As seen in Fig. 6.5, seven steps are required to produce the membranes. Steps 1, 3 and 4 are common to the method developed by Tsai and coworkers in the preparation of a cermet membrane with palladium and $\text{BaCe}_{0.4}\text{Zr}_{0.4}\text{Gd}_{0.1}\text{Dy}_{0.1}\text{O}_{3-x}$ [9]. One important difference between the two methods is that in their case ball milling was used only as a way of mixing the two powders, while in the current work ball milling was used as a way to produce the ternary alloy. The first two steps represent the preparation of the bcc PdCuAu powders and were discussed in section 6.1. In short, the powders Pd, Cu, Au plus NaCl (process control agent) were ball milled together resulting in the formation of the fcc alloy (step 1). With heat treatment (step 2), transition to the bcc occurred,

partially or fully in accordance with the composition of starting alloy. Steps one and two are omitted when preparing a pure Pd membrane from commercially available palladium powder. After the first heat treatment (step 2), the powders are pressed into 1.1 cm disks (steps 3). At this stage, the pellets are rather fragile and no characterization was attempted. Upon sintering at 900°C for one hour, the pellets gain cohesiveness and bend easily without breaking. After sintering, the pellets are cold rolled in order to homogenize and reduce their thicknesses. The final thickness of the membranes after cold rolling varies from membrane to membrane and depends not only on the amount of the powder that was pressed but also on the number of times the membrane was pressed between the rolls. Nonetheless, cold rolling reduces the thickness on average by 30%. As the thickness is reduced, the diameter of the membranes is increased from 1.1 cm to a final average of 1.2 cm. After cold rolling the membranes are heat treated one last time (step 6) and finally they are polished (step 7). The need for steps 6 and 7 will be justified in sections 6.2.3 and 6.2.2, respectively.

6.2.2. EDX/SEM analysis

After the final heat treatment, the pellets were characterized by EDX/SEM. The EDX composition measured on three different spots of the membrane surface gave equivalent values to the ones already reported in table 6.1, with a standard deviation lower than 1 at.%. No other elements apart from Pd, Cu or Au were detected in these measurements and neither was sodium. Sodium was only detected when XPS was used (section 6.3.2.3). The EDX results attest for the homogeneity in the composition of the membranes. EDX mapping was also used to look for any element segregation. Results are shown in Fig. 6.6.

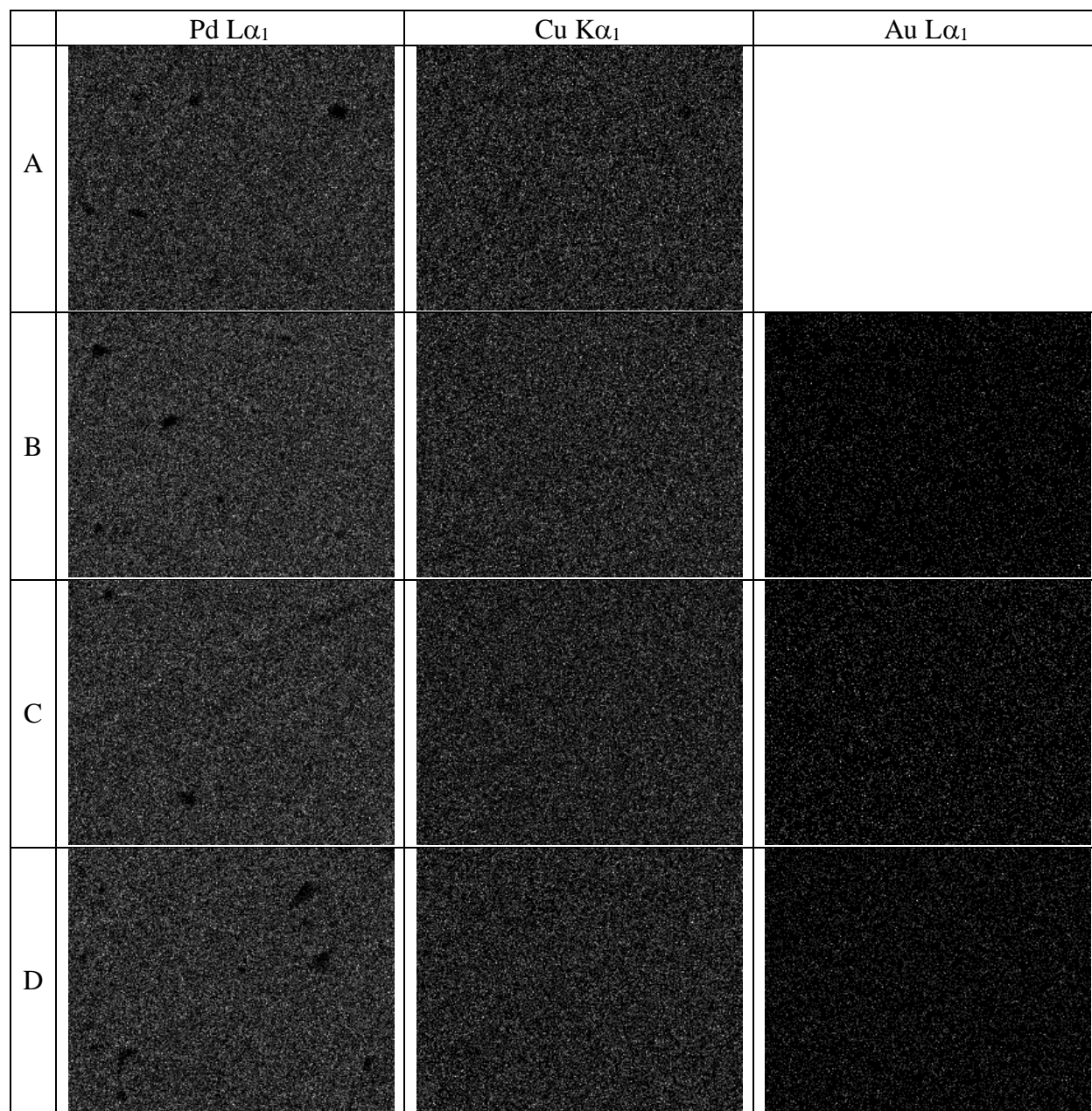


Figure 6. 6 – EDX mapping of the membranes’ surface. Each row represents one different composition (A – Pd₄₀Cu₆₀; B – Pd₄₀Cu₅₇Au₃; C – Pd₃₉Cu₅₃Au₇; D – Pd₄₀Cu₄₉Au₁₁) and each column represents one element (from left to right, Pd $L\alpha_1$, Cu $K\alpha_1$ and Au $L\alpha_1$).

As it can be observed in Fig 6.6, all elements are distributed evenly on the surface of the membrane and no segregation was observed. This is important and guarantees equal hydrogen transport at all location of the membrane surface. Each pellet was also analyzed by SEM after the second heat treatment. The corresponding micrographs are shown in Fig. 6.7.

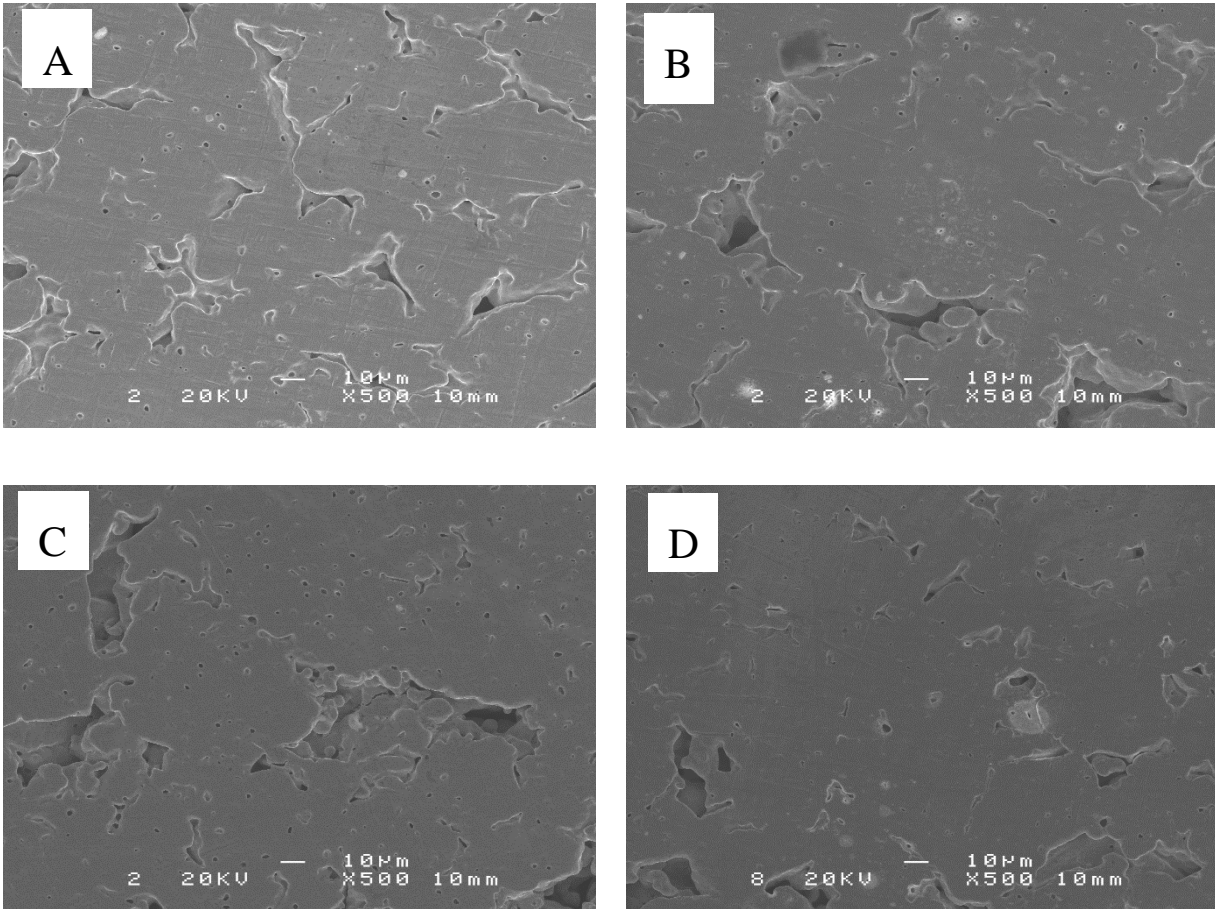


Figure 6. 7 – SEM micrographs at 500 times magnification of membranes after the second heat treatment (step 6 in Fig. 6.5); A – Pd₄₀Cu₆₀; B – Pd₄₀Cu₅₇Au₃; C – Pd₃₉Cu₅₃Au₇; D – Pd₄₀Cu₄₉Au₁₁.

As seen in Fig. 6.7 all pellets are identical regardless of their composition. Many pores are visible at the surface. However, there is no evidence that these pores run uninterruptedly through all the thickness of the pellet. Nonetheless, this is not the best scenario for a selective dense membrane. Consequently, a polishing procedure was developed to obtain almost mirror finish like-

surfaces even if some minor scratches were visible. A comparison of the pellets before and after polishing is shown as an example in Fig. 6.8 for a membrane with composition Pd₃₉Cu₅₃Au₇.

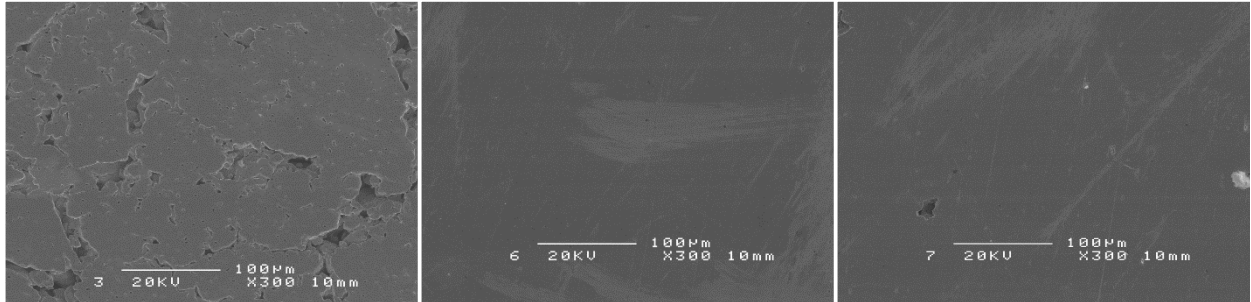


Figure 6. 8 – SEM micrograph before (left) and after (center and right) polishing was performed. Membrane with composition Pd₃₉Cu₅₃Au₇ is shown as an example.

As observed in Fig 6.8 practically all pores are removed during polishing. Polishing is in fact displacing material and by doing this it is covering each pore effectively. Each side of the membrane was polished, resulting in an overall 25% reduction in thickness, from 344 to 257 μm, in the present case. The reduction in thickness achieved with polishing varies from membrane to membrane but it is usually not greater than 25%.

6.2.3. XRD analysis

The membrane with the composition Pd₄₀Cu₄₃Au₇ was analyzed by XRD after steps 2 (first heat treatment), 4 (sintering), 5 (cold rolling) and 6 (second heat treatment). The results are displayed in Fig. 6.9 for 2θ between 41.0 and 44.5°, showing in detail the changes occurring with peak (110).

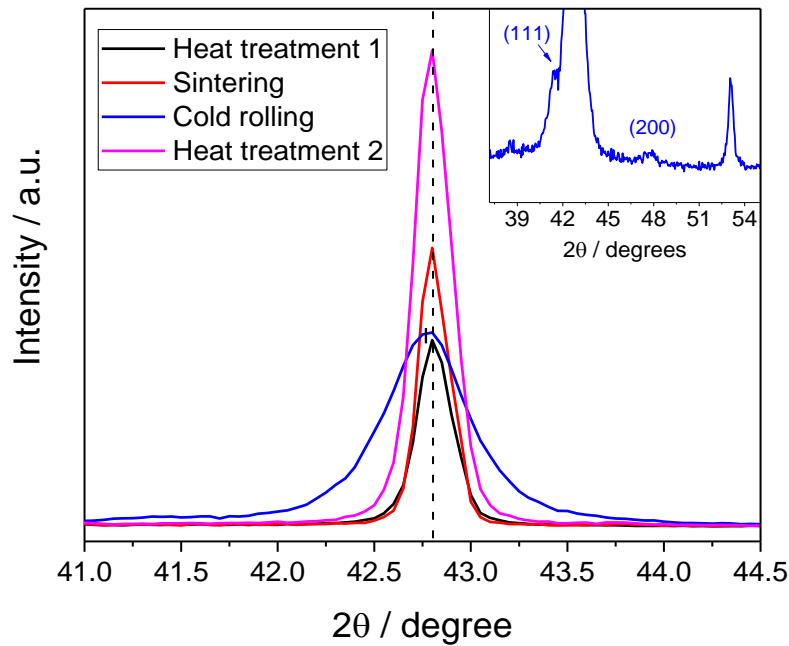


Figure 6. 9 – X-ray diffractogram of Pd₄₀Cu₄₃Au₇ powder after the first heat treatment (step 2), and pellet after sintering (step 4), cold rolling (step 5) and after second heat treatment (step 6). The dotted line indicates the average peak center (42.8°) for all samples except the one that underwent cold rolling. The inset shows the diffratogram of the cold rolled sample between 38 and 59° in order to emphasize the presence of the fcc peaks.

The dotted line seen in Fig 6.9 represents the average position of peak (110) with $2\theta = (42.809 \pm 0.003)^\circ$ and average FWHM $(0.21 \pm 0.02)^\circ$ for all samples except the one that was cold rolled (values presented are average \pm standard deviation). In the case of the cold rolled sample, the (110) peak is shifted by 0.042° to the left and is now positioned at $2\theta = (42.767 \pm 0.001)^\circ$. The peak is also broader and its FWHM is $(0.513 \pm 0.003)^\circ$. These results indicate that cold rolling introduces strain (uniform strain and microstrain) in the lattice of the alloy. However, this strain is removed after the second heat treatment. An estimation of the crystallite size and the microstrain was made using the Williamson-Hall method and considering that the microstrain is anisotropic (equations 3.8 and 3.9). Under these conditions the crystallite size of the cold rolled sample is (102 ± 44) nm, while the microstrain varies between $(2.9 \pm 0.2) \times 10^{-3}$ and $(8.1 \pm 0.5) \times 10^{-3}$ (microstrain

is dimensionless), for the (111) and (100) directions respectively. As a comparison, the sample after the second heat treatment shows similar crystallite sizes (112 ± 33) nm but lower microstrain, this is $(1.3\pm 0.1)\times 10^{-3}$ and $(2.1\pm 0.2)\times 10^{-3}$ for the (111) and (100) directions respectively (for the heat treated sample a uniform deformation energy was considered in the calculations, as defined in equations 3.12 and 3.13). Indeed, the microstrain is about 2 to 4 times lower after the second heat treatment.

Apart from introducing strain in the lattice, cold rolling also promotes partial conversion of the bcc to the fcc phase (inset of Fig. 6.9). This issue was further explored in Fig.6.10, where diffractograms of $\text{Pd}_{40}\text{Cu}_{43}\text{Au}_7$ are shown for $\text{Pd}_{40}\text{Cu}_{43}\text{Au}_7$ after different treatments (ball milling, cold rolling and final heat treatment).

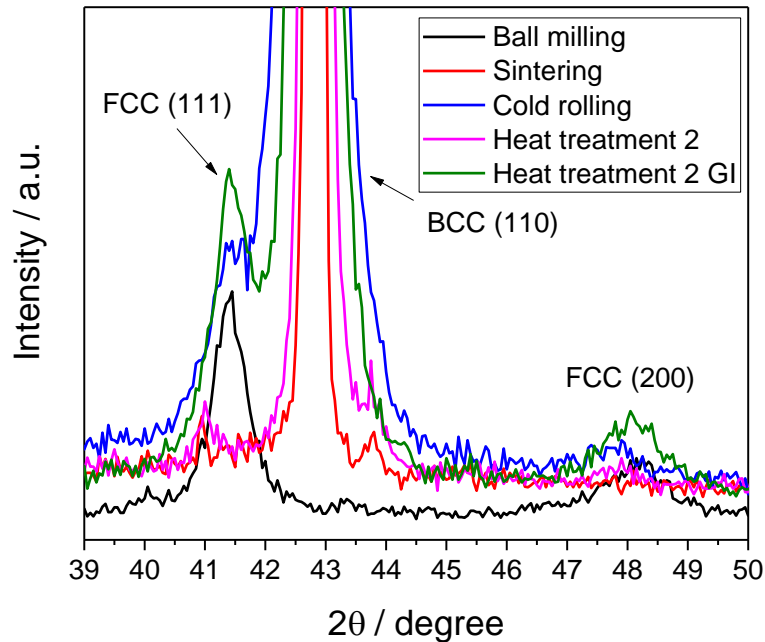


Figure 6. 10 – X-ray diffractogram of $\text{Pd}_{40}\text{Cu}_{43}\text{Au}_7$ powder after ball milling (step 1), and of $\text{Pd}_{40}\text{Cu}_{43}\text{Au}_7$ pellet after cold rolling (step 5) and after second heat treatment (step 6). The latter was acquired in both Bragg-Brentano (curve in magenta) and in grazing incidence (GI) with $\theta=5^\circ$ (curve in green) configurations. The (111) and (200) fcc peaks are visible, as is also the (110) bcc peak.

As illustrated in Fig. 6.10, both the (111) and (200) peak of the fcc phase formed after cold rolling (curve in blue) matches well with the same peak observed after ball milling (curve in black). This is a clear indication that this phase is formed under the cold rolling conditions since these peaks are totally absent from the XRD pattern of the sample after sintering, the step right before cold rolling. The presence of these peaks in the XRD pattern recorded in the Bragg-Brentano configuration after the second heat treatment (curve in magenta) is difficult to ascertain, suggesting that conversion of the fcc to the bcc phase has occurred. However, the XRD pattern of the same sample taken in grazing incidence mode clearly shows the presence of the (111) and (200) peak of the fcc phase, leaving little doubt that the initial fcc phase is still present, to a small extent, in the membrane after the second heat treatment. This remaining fcc phase is mostly concentrated at the surface of the pellet and will reveal important when discussing the effects that H₂S on the membrane (section 6.3.2.1).

The second heat treatment is effective in reducing the strain introduced by cold rolling and in favoring the conversion to the bcc phase, although not fully complete. XRD analyses were performed on pellets of all compositions (Pd₄₀Cu₆₀; Pd₄₀Cu₅₇Au₃; Pd₃₉Cu₅₃Au₇; Pd₄₀Cu₄₉Au₁₁) after the second heat treatment. The results are shown in Fig. 6.11.

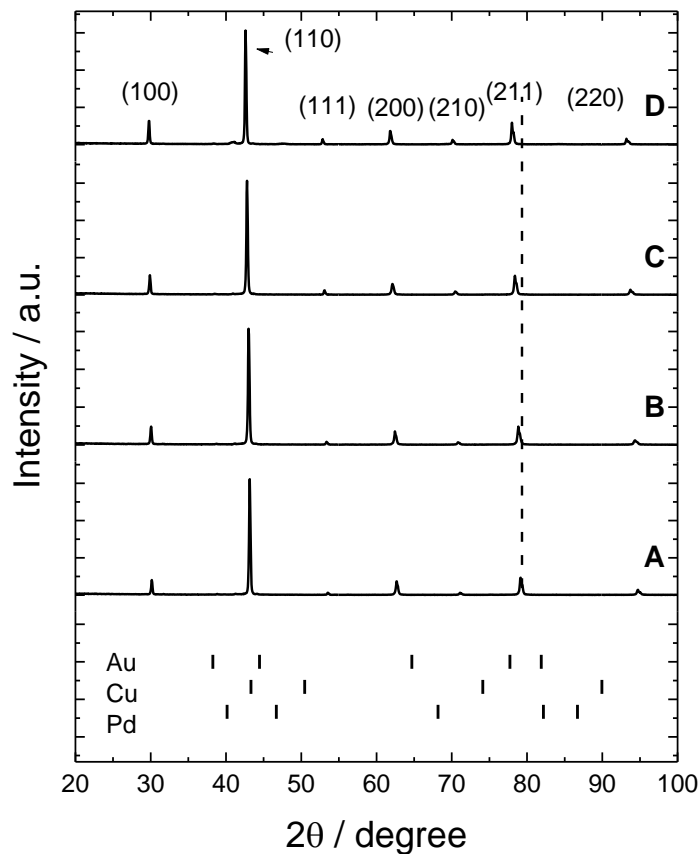


Figure 6. 11 – Bragg-Brentano X-ray diffractograms of the membranes after the second heat treatment (step 6 in diagram of Fig. 6.5) arranged by increasing gold content from 0% (A) to 10% (D) (A – Pd₄₀Cu₆₀; B – Pd₄₀Cu₅₇Au₃; C – Pd₃₉Cu₅₃Au₇; D – Pd₄₀Cu₄₉Au₁₁).

As seen in Fig. 6.11, bcc is the main phase present in all samples, except sample D that also shows low intensity fcc peaks. From Fig. 6.10 we also know that a small amount of fcc phase is also present in sample C. The peak positions of the bcc phase shown in Fig. 6.11 are equivalent to those in panel 2 of Fig. 6.2. Consequently, the lattice parameters after the first and the second heat treatments are very close to each other. In fact, the average difference in lattice parameter is (0.0002 ± 0.0003) Å, well within the experimental error. Williamson-Hall analysis was performed on the diffractograms shown in Fig. 6.11. For comparison, the samples after ball milling (diffractograms were shown in Fig. 6.2) were also analyzed. The strain energy density and the crystallite size were calculated using equation 3.13, this is considering that the microstrain is

anisotropic and depends on a uniform density of deformation energy. The results are shown in Fig. 6.12.

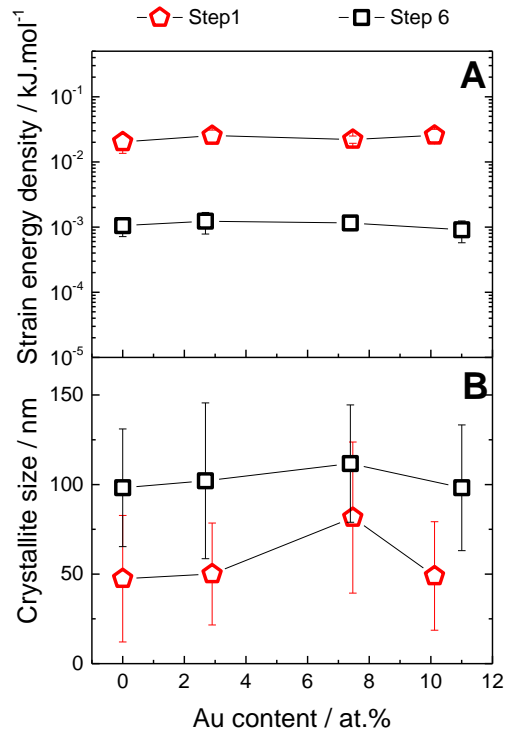


Figure 6. 12 – Williamson-Hall analysis (equation 3.13) applied to PdCuAu alloys after ball milling (step 1) and after the second heat treatment (step 6). Results for the strain energy density (A) and the crystallite size (B) are shown.

In general, as displayed in Fig. 6.12, the samples after ball milling present smaller crystallite sizes and higher strains than the samples after the final heat treatment. There is, however, no clear trend with composition. The quality of the linear regressions, R^2 value, varies between 0.8556 and 0.9667.

6.2.4. Conclusions

The method used for the preparation of membranes does not result in any composition change while maintaining the bcc structure. Surface imperfections that could otherwise impact the selectivity of the membrane are removed by a simple polishing procedure. More than one pellet per composition was prepared and their characteristics, as observed by EDX, SEM and XRD were found to be dependent only on the composition. Indeed, the method used to prepare the pellets is very reproducible. Having prepared the membranes the next step is to evaluate their performance in gas phase.

6.3. Permeability measurements

6.3.1. Single gas experiments

In the previous section it was demonstrated that we are able to successfully prepare membranes from mechanically alloyed PdCuAu powders. As discussed before, the method is very reproducible and all membranes show that Pd, Cu or Au are distributed homogeneously on the surface. Moreover, all prepared membranes are pure bcc, except for the membranes with the highest gold content that shows some fcc contamination. In order to measure the H₂ permeability of our membranes, we need first to guarantee that the membranes are pore free. The method chosen to do so was to pressurize the membrane under He (30-60 psig) inside the permeation chamber and at the temperature chosen for the H₂ testing. Afterwards and during 15 minutes, the flow of gas and the pressure buildup in the permeate side of the chamber were monitored. Only the membranes that showed 0.00 ml/min He flow and no pressure increase in the permeate side were considered pore free. Alternative methods would have consisted of immersing the permeation chamber in liquid and check for the formation of bubbles upon pressurization of the retentate side or the membrane could had been inspected visually for light transmission, as an evidence of the presence of pinholes [10]. However, these two alternatives do not provide a quantification of the extent of the leak, and were therefore not used.

On average, four out of ten membranes passed the initial He test. There are two main reasons why the membranes could fail the He leak test: 1) either there are too many pinholes or defects or 2) the VCR lock is cutting through the membrane causing it to rupture. A more careful

polishing could resolve the former whereas the latter could be circumvented by sandwiching the membrane between two stainless steel gaskets.

The sealing method – the VCR lock – may bring additional problems to the stability of the membrane. As the VCR cuts through the membrane (or the membrane plus the two stainless steel gaskets mentioned above), part of the membrane will not be in contact with H₂. Instead, that part of the membrane will be in contact with atmospheric gases. The consequence of this is illustrated in Fig. 6.13 for a membrane that failed the He leak test after the H₂ permeability experiment.

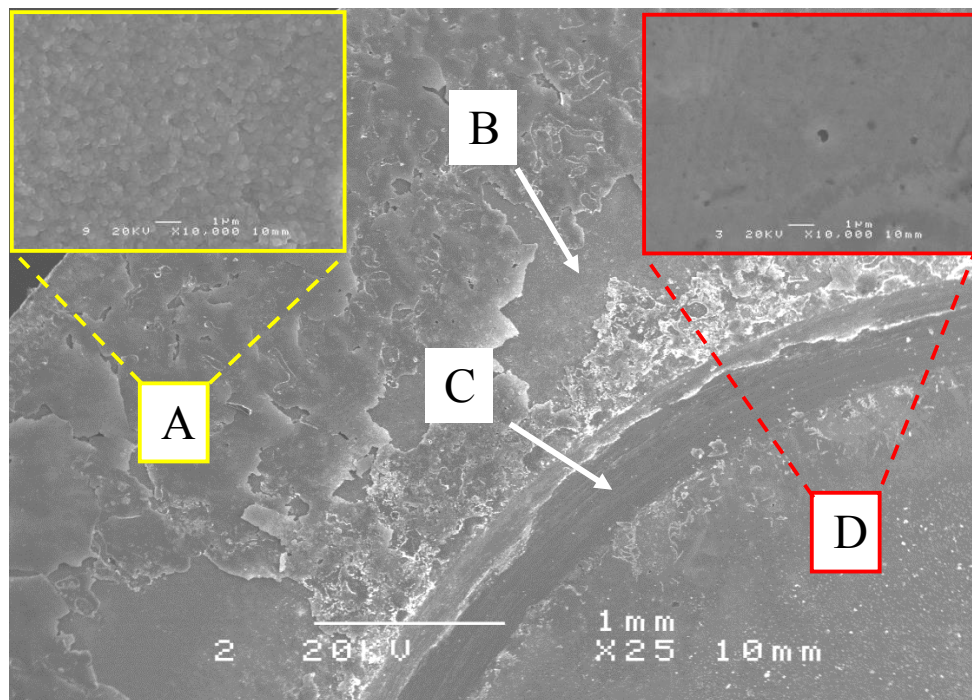


Figure 6. 13 – Micrograph of membrane with composition Pd_{38.9}Cu_{54.5}Au_{6.6} that failed the He leak test after the H₂ permeation experiment. Regions A and B are shown in more detail in the insets.

Four different regions are distinguishable in Fig. 6.13: regions A) and B) are on the edge of the membrane and outside the VCR lock, region C) is the indentation caused by the VCR lock and region D) shows the center of the membrane center that is always in contact with hydrogen. Regions A) and B) are blueish-grey in color while the remaining of the membrane has a more metallic look, similar to the pre-testing appearance. Region A seems to be a layer that easily peels off revealing region B. EDX analysis shows that region A is essentially formed of a dense copper

layer ($\text{Pd}_{2.7}\text{Cu}_{97.1}\text{Au}_{0.2}$) and region B is copper-rich ($\text{Pd}_{17.4}\text{Cu}_{80.1}\text{Au}_{2.5}$) when compared to the membrane's initial composition. The composition at the center of the membrane, region D in Fig. 6.13, remains unchanged with the H_2 testing ($\text{Pd}_{39.5}\text{Cu}_{53.6}\text{Au}_{6.9}$ post-testing vs. $\text{Pd}_{38.9}\text{Cu}_{54.5}\text{Au}_{6.6}$ pre-testing; the difference is within experimental error). We may conclude that copper is segregating to the surface of the membrane when air is present at high temperature (450°C), as suggested by the previous EDX results. As copper atoms migrate out of the PdCuAu ternary alloy, the lattice parameter increases as a consequence of the larger Au and Pd content. The expansion of the lattice in the outer parts of the membrane may have an impact on its integrity and contribute to the formation of fractures. However, in the present case, the membrane most likely failed by the formation of pinholes visible in the magnified view of region D, the area in contact with H_2 .

6.3.1.1. Evaluation of the effect of composition in the permeability

The membranes that successfully passed the He leak test were evaluated under H_2 and their permeability was measured. With this purpose, the membranes were pressurized under 30, 45 and 60 psig H_2 for 30, 15 and 15 minutes, respectively, at 464°C . The variation of the hydrogen flow with time is shown in Fig. 6.14 for six different membranes, namely a reference Pd 250 μm commercial foil from Alfa Aesar (A), a Pd pellet prepared from commercial Pd powder (B; 250 μm) and the four PdCuAu alloys prepared, $\text{Pd}_{40}\text{Cu}_{60}\text{Au}_0$ (C; 327 μm), $\text{Pd}_{40}\text{Cu}_{57}\text{Au}_3$ (D; 300 μm), $\text{Pd}_{40}\text{Cu}_{53}\text{Au}_7$ (E; 277 μm); $\text{Pd}_{40}\text{Cu}_{49}\text{Au}_{11}$ (F; 304 μm).

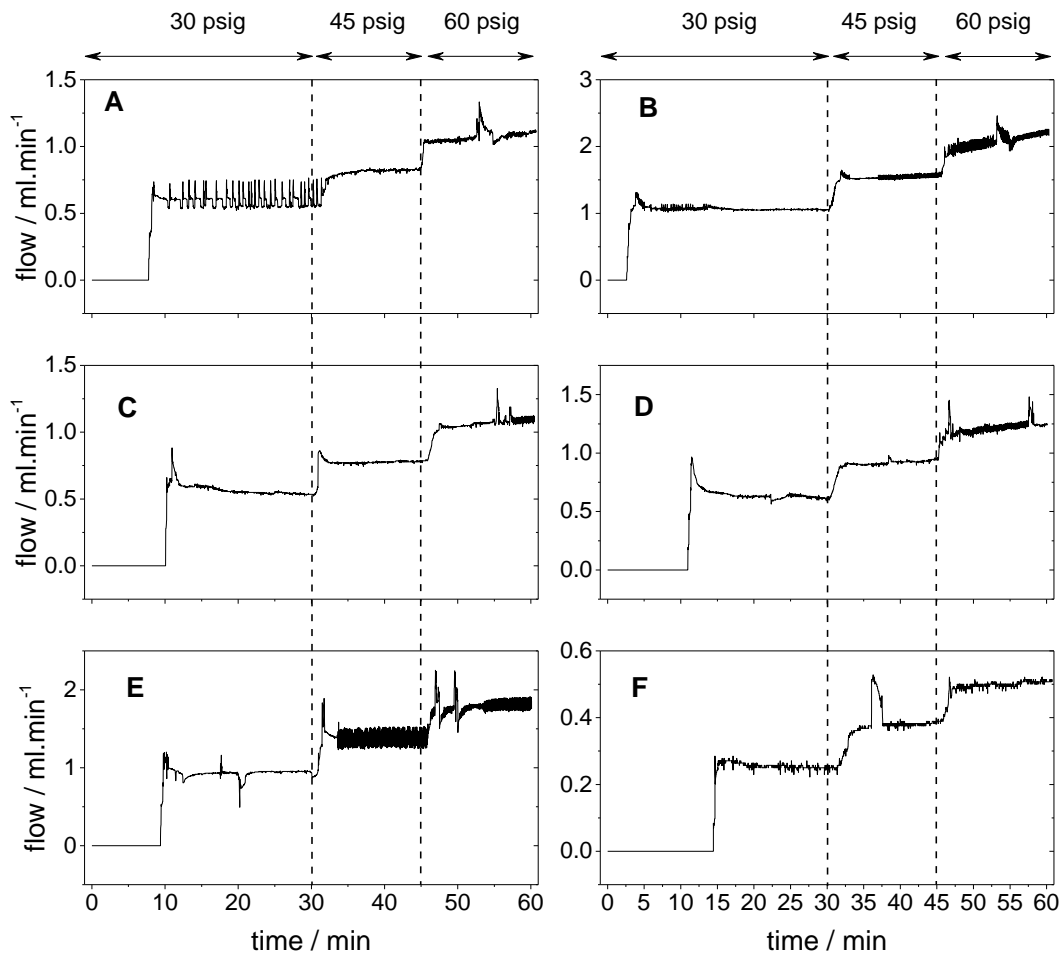


Figure 6. 14 – Variation of H₂ flow with time at 30, 45 and 60 psig H₂ feed pressure and 464°C. The permeate side was not submitted to any pressure control and no sweeping gas was used. Measurements were made with the following membranes: Pd 250 μm commercial foil form Alfa Aesar (A), a Pd pellet prepared from commercial Pd powder (B; 250 μm) and the four PdCuAu alloys prepared, Pd₄₀Cu₆₀Au₀ (C; 327 μm), Pd₄₀Cu₅₇Au₃ (D; 300 μm), Pd₄₀Cu₅₃Au₇ (E; 277 μm); Pd₄₀Cu₄₉Au₁₁ (F; 304 μm).

As seen in Fig. 6.14, all membranes respond similarly under hydrogen gas in the sense that they all show a waiting period for the flow to start and they all show an increase in flow as a result of the increase in pressure. The initial delay in flow may vary from 3 to 15 minutes for the commercial Pd powder pressed pellet (B in Fig. 6.14) and for the membrane with composition

Pd₄₀Cu₄₉Au₁₁ (F in Fig. 6.14), respectively. In fact, membranes with higher flow show shorter delaying times (compare for example membranes B and F in Fig. 6.14). However, the delay time is also an artifact introduced by the measuring device. The flow meter that was used requires a minimum pressure of about -0.39 psig before registering a flow. Below this threshold value, no flow will be registered with the mass flow meter. Notwithstanding, the increase in pressure in the permeate side can attest for the existence of flow right after pressurization of the chamber. For example, for membrane A, the pressure increased about 0.07 psig/min in the first 8 minutes. After the delay period, there is a sudden increase in flow that stabilizes with time. Occasionally, such as in the case of the Pd commercial foil (A in Fig. 6.14), the flow shows some variation around an average value. This also seems to be instrument related, because changing the measurement to another flow meter usually stops the variation or could be due to the pressure control system. As stated before, an increase in pressure leads to an increase in flow. For example in the case of membrane A, changing the pressure from 30, to 45 and to 60 psig, ultimately increases the flow from 0.59, to 0.70 and to 0.83 ml/min, respectively. Moreover, the flow is usually quite constant at each pressure, apart from the instruments variation already stated. Curiously, for membrane B, there seems to be a slight increase in flow with time, in the last 15 minutes. We will come back to this point later on.

To simplify the comparison between the membranes shown in Fig. 6.14, their permeability was calculated using the Richardson equation (equation 2.8) already discussed in section 2.2 and repeated here for easier reference:

$$J_{H_2} = \frac{\phi}{L} \left[(P_{H_2}^{retentate})^{\frac{1}{2}} - (P_{H_2}^{permeate})^{\frac{1}{2}} \right] \quad (\text{Equation 2.8})$$

The Richardson equation establishes a linear relation between the hydrogen flow (or flux, J_{H_2}) with the square root of the pressure gradient across the membrane. From the slope of the linear relation and knowing the thickness L of the membrane, the permeability ϕ can be calculated. In the present case, the pressure and flow registered at 30, 45 and 60 minutes for each membrane were used in the calculations. The results are shown in Fig. 6.15.

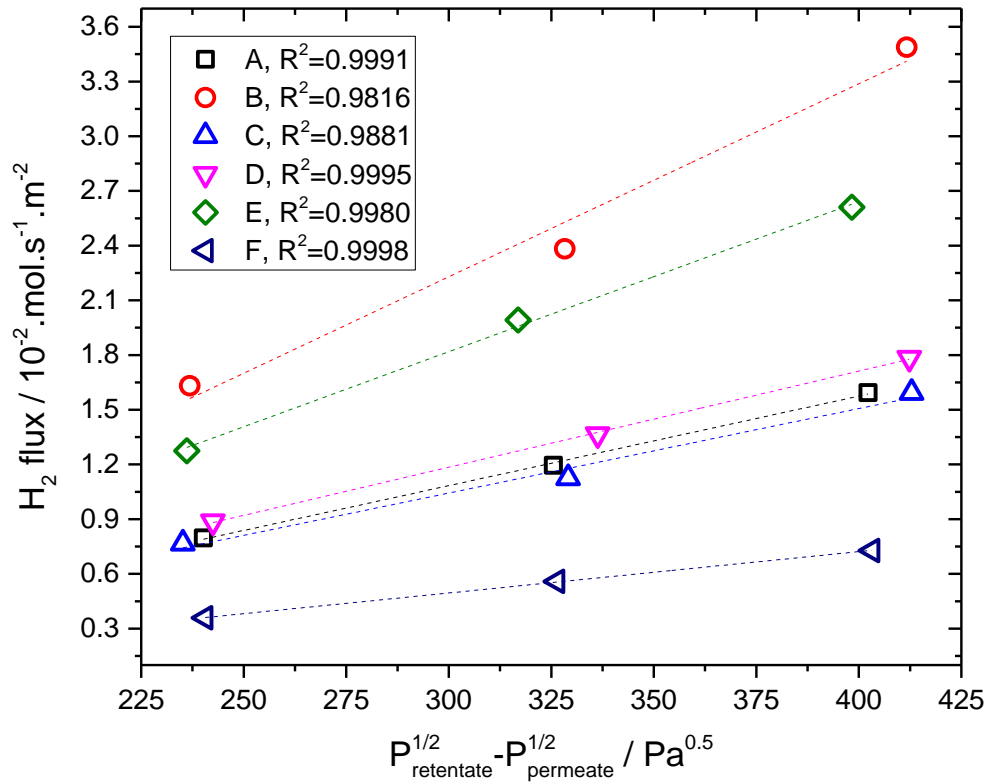


Figure 6. 15 – Hydrogen flux in function of the difference of the square root of pressure drop across the membrane at 464°C. The dotted lines represent the calculated linear regressions. All membranes showed 0.00 ml·min⁻¹ He flow before and after the H₂ testing. Measurements were made with the following membranes: Pd 250 μm commercial foil form Alfa Aesar (A), a Pd pellet prepared from commercial Pd powder (B; 250 μm) and the four PdCuAu alloys prepared, Pd₄₀Cu₆₀Au₀ (C; 327 μm), Pd₄₀Cu₅₇Au₃ (D; 300 μm), Pd₄₀Cu₅₃Au₇ (E; 277 μm); Pd₄₀Cu₄₉Au₁₁ (F; 304 μm).

As it can be observed in Fig. 6.15, most membranes show good linearity between flux and $\Delta P^{0.5}$, with $R^2 > 0.999$. These high correlation coefficient values confirm the applicability of the Richardson equation to our system, and that the assumptions used in its derivation (steady state conditions with a linear concentration gradient across the membrane) are valid. Moreover, it indicates that the H₂ transport through the membrane is diffusion limited as anticipated. Only two

membranes show a lower R^2 : the membrane prepared from Pd commercial powder (B in Fig. 6.15) and the one with the composition $\text{Pd}_{40}\text{Cu}_{60}$ (C in Fig. 6.15). In the latter case, the linearity is improved to $R^2=0.991$ if the average of the flow in the last 5 minutes of the experiment at 60 psig is used instead of the last flow value at 60 minutes. Using average values is particularly important whenever the flow shows this type of variation. In the case of membrane B, the flow of H_2 seems to increase with time when the pressure is set to 60 psig in the last 15 minutes of the experiment (Fig. 6.14B). In fact, the flow starts at 1.98 ml/min when the 60 psig pressure is first applied, and then it increases to 2.18 ml/min at the end. The difference between the two values is 0.20 ml/min. If we consider that the error of the flow meter is half of the smallest scale division, that is, 0.005 ml/min, then the 0.20 ml/min difference can be considered significant. Taking into account the first value (1.98 ml/min) instead of the last value (2.18 ml/min) in the linear regression the quality of the linear regression improves substantially from $R^2=0.9816$ to $R^2=0.9999$. From the slopes of the curves shown in Fig.6.15, the hydrogen permeability was calculated for each membrane. The results are summarized in table 6.2 along with the thickness and an estimation of the He permeability. The ideal selectivity values of the membranes are also shown.

Table 6. 2 – Membranes’ properties including, composition, thickness, H₂ and He permeability at 464°C, and ideal selectivity factors. H₂ and He permeability is given in mol·m⁻¹·s⁻¹·Pa^{-0.5}.

Membrane	EDX composition (at%)	Thickness (μm)	R ²	ϕ _{H₂}	ϕ _{Helium}	α*
A	Pd ₁₀₀	250	0.9991	1.2×10 ⁻⁸	< 4.5×10 ⁻¹¹	> 267
B	Pd ₁₀₀	250	0.9816 (0.9994)	2.6×10 ⁻⁸ (2.0×10 ⁻⁸)	< 4.5×10 ⁻¹¹	> 578
C	Pd ₄₀ Cu ₆₀ Au ₀	327	0.9881 (0.9907)	1.5×10 ⁻⁸ (1.5×10 ⁻⁸)	< 5.7×10 ⁻¹¹	> 263
D	Pd ₄₀ Cu ₅₇ Au ₃	300	0.9995	1.6×10 ⁻⁸	< 5.2×10 ⁻¹¹	> 308
E	Pd ₄₀ Cu ₅₃ Au ₇	277	0.9980 (0.9999)	2.3×10 ⁻⁸ (2.1×10 ⁻⁸)	< 4.8×10 ⁻¹¹	> 396
F	Pd ₄₀ Cu ₄₉ Au ₁₁	304	0.9998	6.9×10 ⁻⁹	< 5.3×10 ⁻¹¹	> 130

The experimentally determined hydrogen permeability of the standard Pd foil (A in table 6.1) is 1.2×10⁻⁸ mol·m⁻¹·s⁻¹·Pa^{-0.5} at 464°C. The same experiment was repeated twice under the same conditions giving (1.3±0.2) × 10⁻⁸ mol·m⁻¹·s⁻¹·Pa^{-0.5} (average ± standard deviation of the three measurements). These values are in good agreement with published results [6, 10-13]. For example, McKinley [11] reported 1.5×10⁻⁸ mol·m⁻¹·s⁻¹·Pa^{-0.5} for his 25.4 μm Pd foil at 450°C and 75 psig H₂, Braun *et al.* [12] presented a 14 μm membrane prepared by electroless deposition on ZrO₂-modified porous stainless steel support with 1.53×10⁻⁸ mol·m⁻¹·s⁻¹·Pa^{-0.5} at 450°C and up to

15 psig of pressure drop, and Mundschau *et al.* [13] showed a 250 μm Pd foil with $2.2 \times 10^{-8} \text{ mol} \cdot \text{m}^{-1} \cdot \text{s}^{-1} \cdot \text{Pa}^{-0.5}$ at 430°C and at a differential pressure up to 435 psig. The accordance of our results with the literature values validates the hydrogen permeation set up and testing protocol. As with all the membranes presented in table 6.1, the Pd foil was submitted to two He leak tests, one before and the other after the H₂ permeability testing. In both He tests, the He flow was under the detection limit, which is 0.005 ml/min or $7 \times 10^{-5} \text{ mol} \cdot \text{m}^{-2} \cdot \text{s}^{-1}$. The detection limit for He is comparable with what is found in the literature. For example, Coulter and coworkers showed a detection limit of $2.8 \times 10^{-5} \text{ mol} \cdot \text{m}^{-2} \cdot \text{s}^{-1}$ [10]. Having a He flow lower than 0.005 ml/min translates into a maximum He permeability of $4.5 \times 10^{-11} \text{ mol} \cdot \text{m}^{-1} \cdot \text{s}^{-1} \cdot \text{Pa}^{-0.5}$. This means that the selectivity factor, this is the ratio of the H₂ permeability with that of He (equation 2.12), is in this case higher than 267 for the Pd foil standard. Selectivity factors were calculated for all membranes using the same approach. The results are also listed in table 6.1 and are all higher than 130.

In the case of the membranes prepared from the commercial powder (B in table 6.1) and the mechanically alloyed powders (C to F in table 6.1), the permeability varies from 6.9×10^{-9} and $2.1 \times 10^{-8} \text{ mol} \cdot \text{m}^{-1} \cdot \text{s}^{-1} \cdot \text{Pa}^{-0.5}$ for membranes F and E, respectively. In some cases, the linear correlation factor (in brackets) improves when considering average flow values. For an easier comparison with published results, the data of table 6.1 are represented in a plot using the McKinley values as a reference [11]. This is shown in Fig. 6.16.

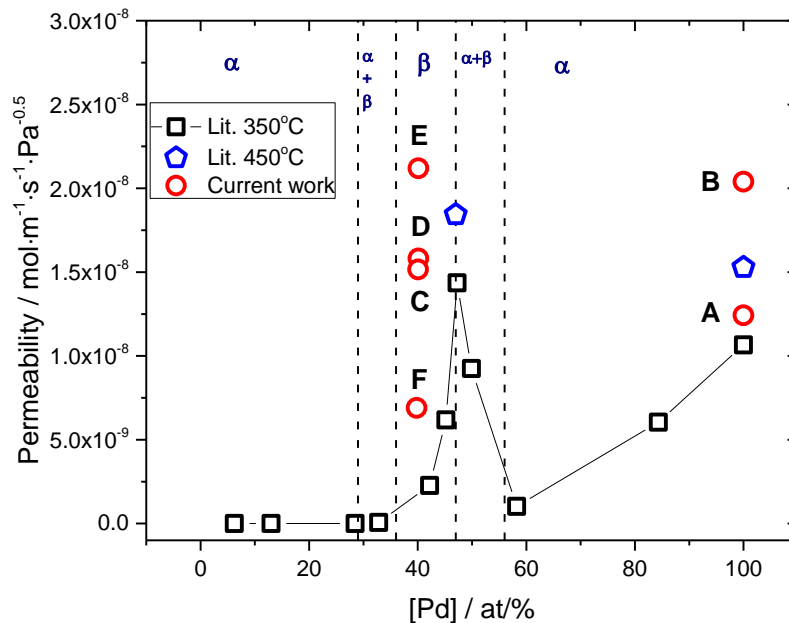


Figure 6. 16 – Experimentally determined H₂ permeability of membranes prepared from the consolidation of PdCuAu mechanically alloyed powders (membranes C to F in Figs. 6.13 and 6.14 and table 6.1). Literature permeability values for PdCu alloys 25.4 foils μm [11] are also shown, along with indication of the crystallographic phase for the PdCu alloys (α - fcc phase; β - bcc phase) [1].

As it can be seen in Fig. 6.16 all the PdCuAu alloys have higher hydrogen permeability than the PdCu alloy foils used by McKinley [11]. The difference could be the result of four different effects: 1) temperature, 2) membrane selectivity, 3) fabrication method or 4) composition (the presence of gold). A discussion of the four hypotheses follows. In the case of temperature (hypothesis 1), unfortunately there is no data at 450°C for the entire composition range. However, looking at the data of Pd₁₀₀ and Pd₄₇, there is an increase of 43 and 28%, respectively (blue pentagons in Fig. 6.16) when the temperature is increased from 350 to 450°C. If we consider that an equivalent permeability increase occurs for the other compositions of the McKinley data, then the increase in temperature alone does not account for the higher permeability of the mechanically alloyed samples. For example, the hydrogen permeability of McKinley's Pd₄₂Cu₅₈ is 2.3×10^{-9}

$\text{mol}\cdot\text{m}^{-1}\cdot\text{s}^{-1}\cdot\text{Pa}^{-0.5}$ at 350°C , and is estimated to be 3.3×10^{-9} $\text{mol}\cdot\text{m}^{-1}\cdot\text{s}^{-1}\cdot\text{Pa}^{-0.5}$ at 450°C , if an increase of 43% is considered. In the current work, the ternary alloy with the closest palladium content shows a hydrogen permeability equal to 6.9×10^{-9} $\text{mol}\cdot\text{m}^{-1}\cdot\text{s}^{-1}\cdot\text{Pa}^{-0.5}$, which is about two times higher than the estimated value presented previously. Therefore, the difference in temperature between our study and McKinley's should not be the factor determining the difference between the two sets of values.

The selectivity of the membrane (hypothesis 2) may be playing a role as well. As mentioned above the detection limit for He in our system is 0.005 ml/min. In essence, any flow that is below this value will go unnoticed. Gas chromatography measurements show the presence of (6.2 ± 0.2) ppmv He in the permeate side when membrane B (Pd compressed commercial powder) is pressurized with 45 psig He for 15 minutes. This value increased to (14.3 ± 0.4) ppmv He after 1 hour. As a comparison, no He was detected when using the Pd foil membrane. The presence of He in the permeate side of the membrane could be due to the presence of defects (for instance pinholes) or to problems with sealing of the membrane inside the permeation chamber. It is estimated that this amount of He downstream of the membrane (6-15 ppmv) reflects an overestimation of the hydrogen permeability by 2%. However, this overestimation does not account for the difference between the data in this work and the one from McKinley.

Mechanical alloying (hypothesis 3) introduces a variety of crystal defects such as dislocations, vacancies, stacking faults and increased number of grain boundaries that could all be contributing to the increase of H_2 permeability. In fact, it has been hypothesized in the literature that hydrogen diffusion occurs not only through the Pd crystals but also through grain boundaries [14]. The high density of grain boundaries as a result of smaller crystallites size introduced by mechanical alloying could then justify the higher permeability of the samples tested in this work. However, as shown previously in Fig. 6.12, the average crystallites size after ball milling is increased upon submitting the samples to the different heat treatments required for the preparation of the membranes, from (57 ± 14) to (102 ± 5) nm. Moreover, the crystallite size for the commercial Pd foil is estimated to be (88 ± 45) nm, which is equivalent to the crystallite size of the other samples. As a result, the crystallite size or the grain boundaries densities should not be playing an important role either.

Probably the decisive factor to explain the differences in permeability shown in Fig.6.16 is the composition of the alloy (hypothesis 4), or in other words, the replacement of copper with gold. This is further illustrated in Fig. 6.17.

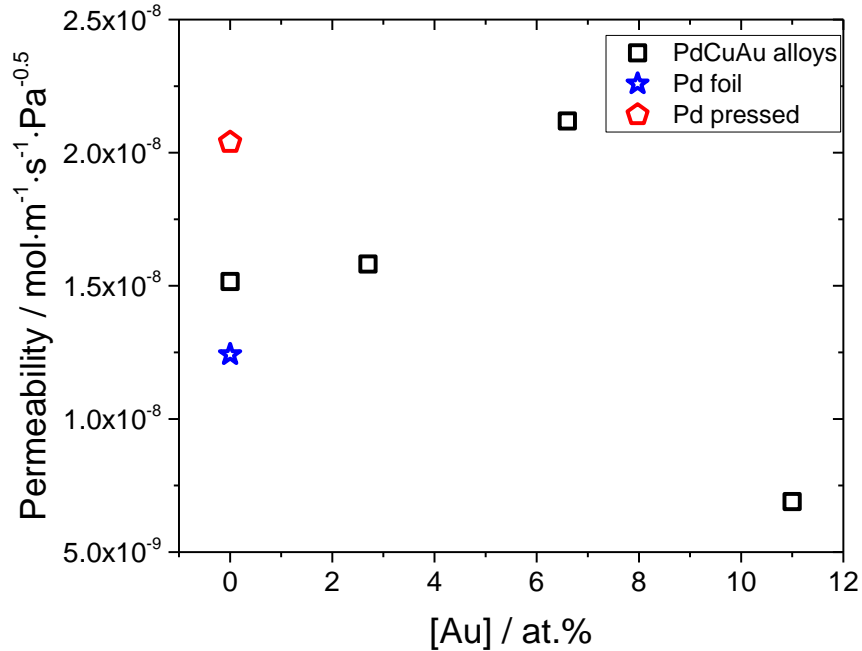


Figure 6. 17 – H₂ permeability of the PdCuAu ternary alloy membranes at 464°C in function the gold content. As a reference, results for Pd foil and for a pellet prepared from Pd powder are also shown.

As shown in Fig 6.17, the amount of gold seems to influence hydrogen permeability. In fact, very high concentrations of Au, namely 11 at.% Au, seem to be detrimental for permeability, whereas at 7 at.% Au the permeability is at its apex. Overall, the presence of gold increases the permeability when compared to PdCu alloys, but a too high concentration of gold is ultimately detrimental.

The stability of flow with time at constant H₂ feed pressure was verified. The results are shown in Fig. 6.18.

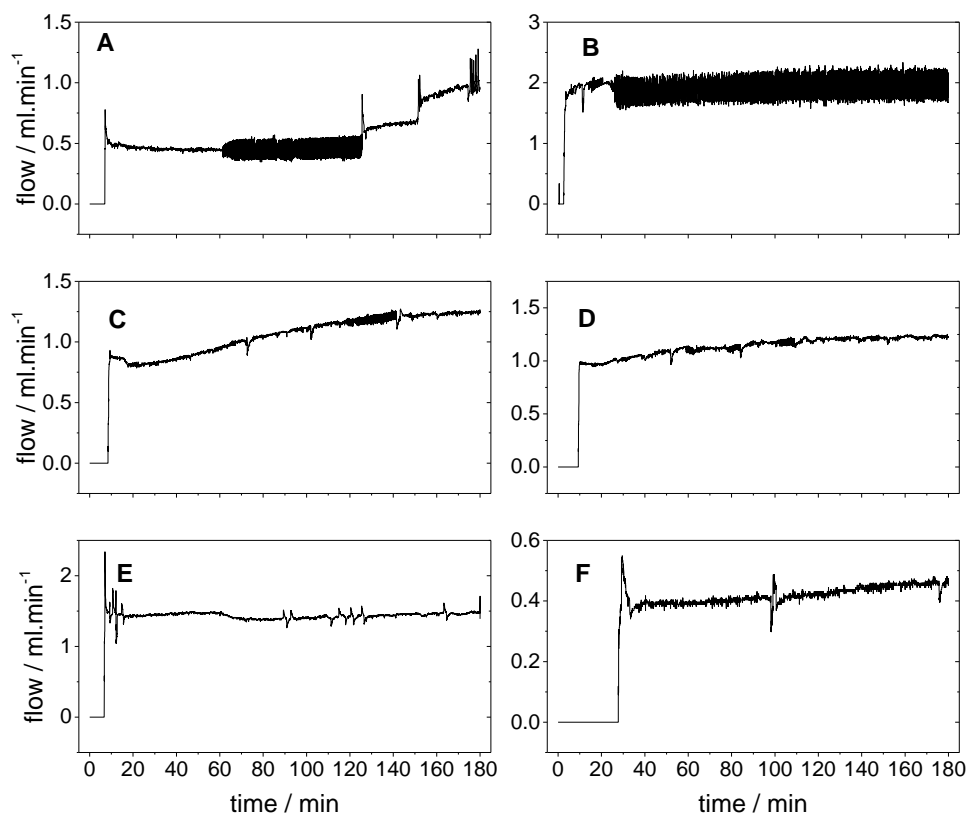


Figure 6. 18 – Variation of H₂ flow with time at 464°C. The H₂ feed pressure was constant at 45 psig for all experiments, except for sample A which was kept at 30, 45 and 60 psig for 2, 0.5 and 0.5 hours, respectively. The permeate side was not submitted to any pressure control and no sweeping gas was used. Measurements were made with the following membranes: Pd 250 μm commercial foil form Alfa Aesar (A), a Pd pellet prepared from commercial Pd powder (B; 250 μm) and the four PdCuAu alloys prepared, Pd₄₀Cu₆₀Au₀ (C; 327 μm), Pd₄₀Cu₅₇Au₃ (D; 300 μm), Pd₄₀Cu₅₃Au₇ (E; 277 μm); Pd₄₀Cu₄₉Au₁₁ (F; 304 μm).

All experiments displayed in Fig. 6.18 were performed at constant H₂ pressure (45 psig), except experiment A with the commercial 250 μm Pd foil. In the latter case, the membrane was pressurized at 30, 45 and 60 psig for 2, 0.5 and 0.5 hours, respectively. Apart from the effect of instrumental variation already mentioned, the flow observed is remarkably constant with time excluding perhaps for membrane C. For the latter membrane, an increase in flow is observed from

0.86 to 1.26 ml/min at 15 and 180 min, respectively. This increase could be related to the transport of hydrogen through pinholes or defects, even if this went undetected in the He leak test.

6.3.1.2. Effect of temperature in the permeability

The membrane that displayed the highest permeability, membrane E ($\text{Pd}_{40}\text{Cu}_{53}\text{Au}_7$, confirm Fig. 6.16) was further tested at different temperatures, namely at 358, 411 and 464°C. The natural logarithm of the permeability values was plotted in function of $1/T$, as shown in Fig.6.19. The results with Pd 250 μm foil are also shown for comparison.

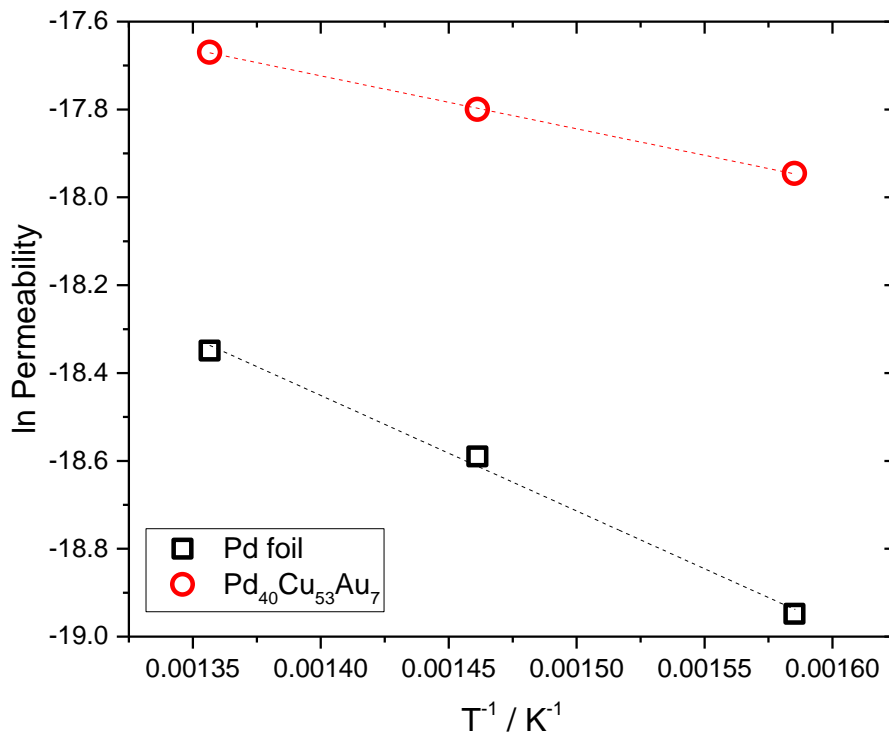


Figure 6. 19 – Permeability vs. $1/T$ for Pd 250 μm foil from Alfa Aesar and $\text{Pd}_{40}\text{Cu}_{53}\text{Au}_7$ membrane. The dotted lines represent the best linear regression of the data, considering an Arrhenius-type relationship.

As displayed in Fig. 6.19, the natural logarithm of the permeability varies linearly with the inverse of the absolute temperature, for both membranes. From the Arrhenius equation (equation

2.11), one can then calculate the activation energy and the pre-exponential factor. The results are shown in table 6.3, along with literature results for comparison.

Table 6. 3 – Pre-exponential factor and activation energy for the H₂ permeation assuming that an Arrhenius-type relationship between the logarithm of the permeability and 1/T is valid. Both experimental results and literature values are shown. All values are calculated considering that the H₂ permeability is a diffusion-limited process.

Membrane	Temperature (°C)	Pre-exponential factor (mol·m ⁻¹ ·s ⁻¹ ·Pa ^{-0.5})	Activation energy (kJ·mol ⁻¹)	Reference
Pd foil 250 μm	358-464	3.9×10 ⁻⁷	21.9	Current work
Pd ₄₀ Cu ₅₃ Au ₇	358-464	1.2×10 ⁻⁷	10.0	Current work
Pd 25.4 μm foil	250-550	1.9×10 ⁻⁷	15	[11]
Pd 25.4 μm foil	250-500	1.4×10 ⁻⁷	12.4	[15]
Pd 25 μm foil	350-700	4.7×10 ⁻⁷	19.2	[16]
Pd electroless plating 14 μm	350-450	3.9×10 ⁻⁷	19.4	[12]
Pd foil 1000 μm	350-900	3.31×10 ⁻⁷	13.81	[17]
Pd foil 800-2025 μm	500-900	1.42×10 ⁻⁷	12.81	[18]
Pd 940 μm	496-946	3.82×10 ⁻⁷	20.50	[19]

Pd 10-150 μm	350-773	1.47×10^{-8}	11.92	[20]
Pd 100 μm foil	330-530	2.20×10^{-7}	14.8	[6]
Pd 100 μm foil	350-900	1.2×10^{-7}	13	[21]
<hr/>				
Pd ₄₂ Cu ₅₈ 20 μm foil	400-625	8.8×10^{-8}	21.9	[22]
Pd ₄₇ Cu ₅₃	250-400	1.1×10^{-7}	9.5	[11]
Pd ₄₀ Cu ₆₀ 100 μm foil	350-464	7.3×10^{-8}	27	[21]
Pd ₅₅ Cu ₄₁ Au ₄ 10 μm from sputter deposition	300-500	2.1×10^{-7}	27	[10]
<hr/>				
Pd ₉₄ Au ₆ 25.4 μm foil	250-500	9.2×10^{-8}	10.6	[15]
Pd ₉₅ Au ₅ 10 μm sputtered film	250-500	1.9×10^{-7}	13.4	[15]
Pd ₉₄ Au ₆ 25 μm sputtered film	250-500	6.4×10^{-8}	9.0	[15]
<hr/>				

The activation energy for pure Pd (21.9 $\text{kJ}\cdot\text{mol}^{-1}$) and pre-exponential factor ($3.9 \times 10^{-7} \text{mol}\cdot\text{m}^{-1}\cdot\text{s}^{-1}\cdot\text{Pa}^{-0.5}$) are within the same order of magnitude as published results. Indeed, literature values vary between 12 to 21 $\text{kJ}\cdot\text{mol}^{-1}$ for the activation energy, and 1.5×10^{-8} to $3.9 \times 10^{-7} \text{mol}\cdot\text{m}^{-1}\cdot\text{s}^{-1}\cdot\text{Pa}^{-0.5}$ for the Arrhenius pre-exponential factor. These results validate once again the laboratory set up used in this work. Membrane E (Pd₄₀Cu₅₃Au₇) presents an activation energy (10.0 $\text{kJ}\cdot\text{mol}^{-1}$) and pre-exponential factor ($1.2 \times 10^{-7} \text{mol}\cdot\text{m}^{-1}\cdot\text{s}^{-1}\cdot\text{Pa}^{-0.5}$) closer to Pd₄₇Cu₅₃ than to Pd₄₂Cu₅₈ alloys. These results may be justified by the favorable effect of replacing copper with gold on the permeability.

6.3.2. H₂ permeability in the presence of H₂S

The presence of H₂S in a gas mixture is known to reduce the H₂ permeability of both Pd [23-26] and bcc PdCu membranes [24, 26, 27]. The impact of H₂S gas in the hydrogen permeability of membrane E (Pd₄₀Cu₅₃Au₇) – the membrane with the highest hydrogen permeability in single-gas experiments – was evaluated. Unfortunately, after having been used in the series of experiments described previously (pure H₂ gas), membrane E did not pass the initial He leak test (0.26 ml/min He at 60 psig He) and so a new membrane with the same composition was prepared (membrane E-2 Pd₃₉Cu₅₄Au₇). As a reference, Pd foil 250 μm was used. The membranes were first pressurized under 30 psig of pure H₂ for 30 or 60 minutes. Afterwards, a mixture of H₂-6% He with 941 ppm H₂S was introduced into the permeation chamber for a period of 30 minutes, also at 30 psig total pressure. The He content of the permeate was analyzed by gas chromatography before switching back to 30 psig H₂ for another 30 minutes. The evolution of flow with time is shown in Fig. 6.20.

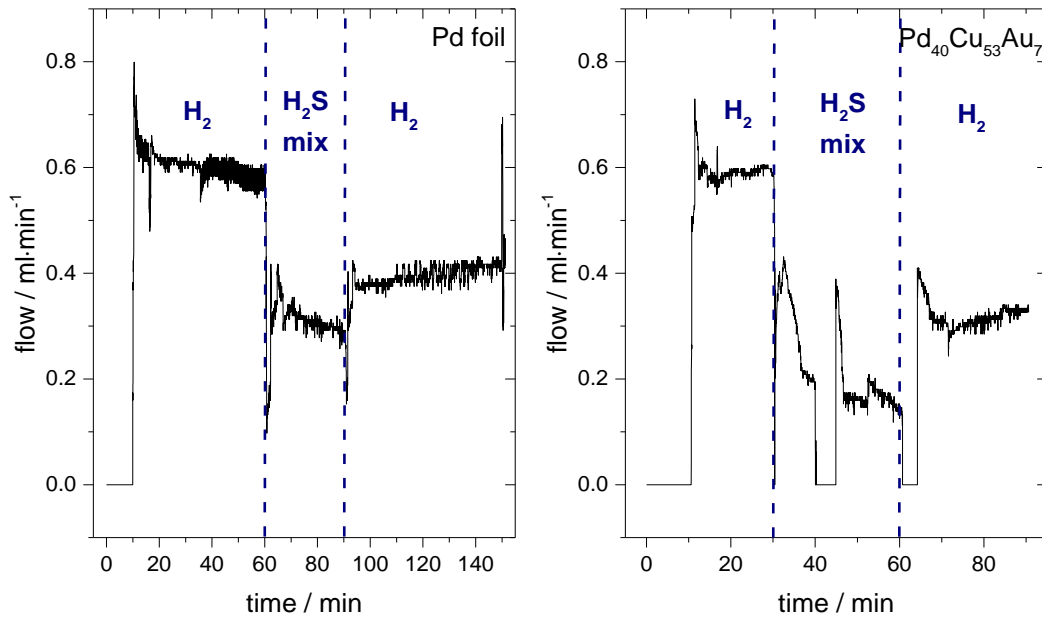


Figure 6. 20 – Variation of flow with time when the membranes are exposed to either pure H₂ or a mixture of H₂ and 941 ppm H₂S. Two different membranes were analyzed: Pd 250 μm foil from

Alfa Aesar (left panel) and Pd₃₉Cu₅₄Au₇ membrane E-2 (right panel). Experiments were performed at 464°C.

As displayed in Fig. 6.20, the H₂ flow decreases when introducing the H₂S, and recovers, although not fully, when switching back to pure H₂. This is true for both membranes. During the first step of the experiment when only pure H₂ is used, both membranes presented permeability values, 8.8×10^{-9} and 9.7×10^{-9} mol·m⁻¹·s⁻¹·Pa^{-0.5}, for Pd and membrane E-2 respectively, that are slightly lower than the ones previous calculated and shown in table 6.2. The difference may arise from the fact that these calculations were made only at one single pressure (30 psig), whereas before different pressures were used instead. Upon introduction of the H₂S mixture, the H₂ permeability in Pd is reduced by half. In the case of the PdCuAu alloy membrane, after 10 minutes of exposure to H₂S, the permeability is zero for about 5 minutes and afterwards it increases and ends up stabilizing at 2.5×10^{-9} mol·m⁻¹·s⁻¹·Pa^{-0.5}. The fact that the permeability decreases to zero is an important issue and will be discussed later on. When switching back to pure H₂ the permeabilities are 6.1×10^{-9} and 5.6×10^{-9} mol·m⁻¹·s⁻¹·Pa^{-0.5}, for the Pd and the E-2 membrane, respectively. This means the permeabilities of the former membrane and the latter membranes are reduced to 69% and 58% of their initial values, respectively. Comparison with literature values is not straightforward as experimental conditions, such as temperature, H₂S concentration and time of reaction, vary greatly from work to work. Nonetheless, a summary of the published data is shown in table 6.4.

Table 6. 4 – Literature results for the effect of H₂S in the H₂ permeability of Pd and Pd alloys.

Membrane	°C	Feed composition	Time	Pressure	Result	Ref.
Pd 14 μm electroless deposition	400	100 ppm H ₂ S/H ₂	24h	7.25 psig	85% decrease in flux	[23]
Pd foil 25.4 μm foil	350	4 ppm H ₂ S/H ₂	3-4 days	75 pig	70% reduction in permeability	[24]

Pd foil 25 μm	350	1000 ppm $\text{H}_2\text{S}/\text{H}_2$	3h	Atmospheric pressure	Pd_4S formation; flux not measured	[28]
Pd 25 μm foil	350	1000 ppm-10% $\text{He}-\text{H}_2$	6h	30 psig	90% reduction in flux: Pd_4S is formed	[26]
$\text{Pd}_{47}\text{Cu}_{53}$ 25.4 μm foil	350	4 ppm $\text{H}_2\text{S}/\text{H}_2$	1-2 days	75 psig	95% reduction in permeability	[24]
$\text{Pd}_{47}\text{Cu}_{53}$ 25 μm foil	350	1000 ppm-10% $\text{He}-\text{H}_2$	5 min	30 psig	Flux below detection limit; 3 nm surface S layer	[26]
$\text{Pd}_{47}\text{Cu}_{53}$ 25 μm foil	500	50 ppm 1000 ppm		115 psia	23% and 85% reduction in flux	[29]
$\text{Pd}_{40}\text{Cu}_{60}$ 100 μm foil	385-500 > 560	1000 ppm $\text{H}_2\text{S}/\text{H}_2$	<110 hours	75 psig maximum	85-40% reduction in permeability Less than 10% reduction in permeability	[30]
$\text{Pd}_{55}\text{Au}_{45}$ 25.4 μm foil	350	4 ppm $\text{H}_2\text{S}/\text{H}_2$	6 days	75 psig	20% reduction in permeability	[24]
$\text{Pd}_{69}\text{Cu}_{14}\text{Au}_{17}$ 14 μm electroless deposition	400	100 ppm $\text{H}_2\text{S}/\text{H}_2$	24h	7.25 psig	57% reduction in flux	[23]

As seen in table 6.4, Pd foil shows a decrease in flow that can be as high as to 90% of the pre-H₂S-treatment values for membranes in contact with 1000 ppm H₂S at 350°C for 3h [26]. The 50% decrease registered in the current work is most probably the result of the higher working temperature (464°C), shorter incubation time (30 minutes) or lower H₂S content (941 vs. 1000 ppm). In a separate experiment, another Pd foil was tested under H₂S 941 ppm for 3 hours at 450°C. Afterwards, the temperature was decreased and kept at 350°C for another 3 hours, while maintaining the membrane under the mixture of H₂ and H₂S. Under these conditions, the permeability decreased by 54 and 78% of the initial pre-sulfur test values, when temperatures were 450 and 350°C, respectively. The temperature and H₂S concentration seem to be the determining factors ruling the loss in permeability in the palladium membranes.

The behavior shown by membrane E-2, that is, zero flow after about 10 minutes under H₂S gas mixture, is similar to what was described by O'Brien and coworkers [26] for their Pd₄₇Cu₅₃ foil). In their case, no flow was registered after 5 min under 1000 ppm H₂S at 350°C. In other words, both membranes, membrane E-2 and Pd₄₇Cu₅₃, are poisoned to such an extent by the sulfurous gas mixture that no gas is able to flow through them. Unfortunately, this leads to the conclusion that the replacement of Cu with Au did not prevent poisoning of the bcc membrane. Five minutes further into the experiment, there is a sudden increase in flow, even if the membrane is still under the H₂S gas mixture. The development of defects on the membrane could cause this burst in gas. Indeed, chromatography measurements made at the end of the H₂S incubation period revealed the presence of 2% He, indicating that pores were formed. The final 15-minute He leak test gave flow < 0.005 ml·min⁻¹, this is, below the detection limit. However, a 0.13 psig increase in pressure in the retentate side, leads to the conclusion that the membrane indeed failed during testing. The presence of pores will be later confirmed with SEM. Comparatively, no He is detected in the permeate by gas chromatography when Pd foil is used. In summary, when the E-2 membrane is first in contact with H₂S, S-compounds are most probably being adsorbed on the surface limiting the flow of H₂ and, ultimately, reducing it to zero. The flow then remains undetected till the formation of pores allows the recovery of gas permeation once again.

In order to characterize the reaction products formed at the surface the membranes upon exposure to H₂S, the gas mixture was re-introduced for another 15 minutes, at the end of the

experiments shown in Fig.6.20. During this time the gas flow was not recorded. Both membranes, Pd and Pd₃₉Cu₅₄Au₇, were then characterized by XRD, SEM/EDX and XPS.

6.3.2.1. XRD analysis

After exposure to H₂S, the Pd foil and membrane E-2 were characterized by XRD on the retentate and permeate sides. The diffractograms are shown in Fig. 6.21.

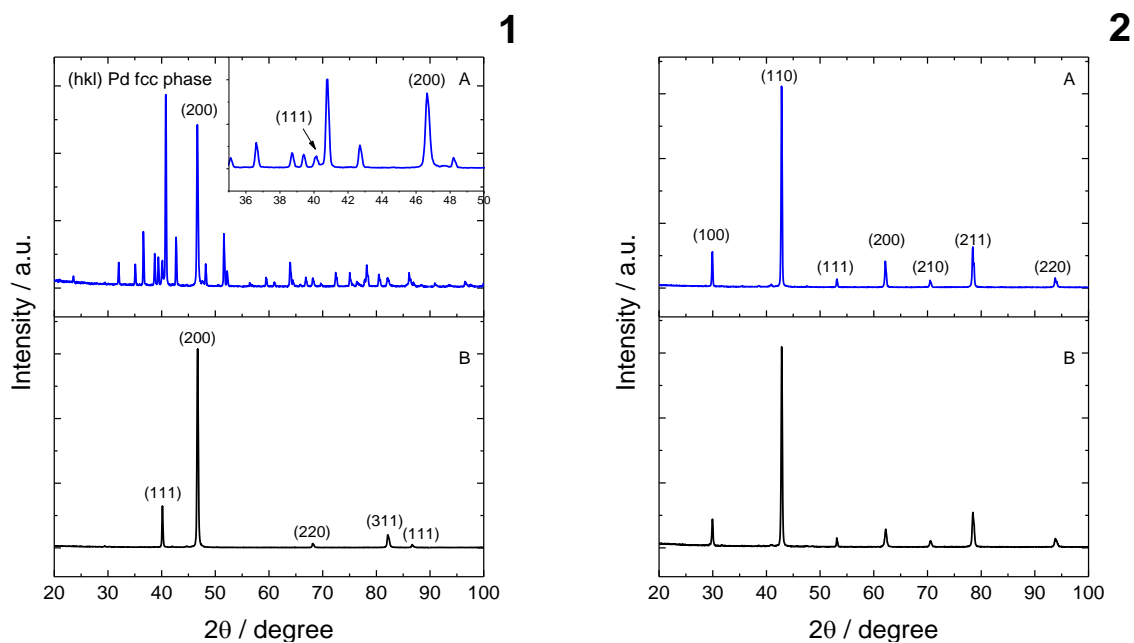


Figure 6. 21 – Diffractograms of Pd 250 μm foil (panel 1) and membrane E-2 Pd₃₉Cu₅₄Au₇ (panel 2) after exposure to H₂S. Both retentate (panels A) and permeate (panels B) sides of the membrane were analyzed.

As seen on panel 1 of Fig. 6.21, there is a remarkable difference between the retentate (panel 1-A) and the permeate (panel 1-B) sides of the Pd foil. The permeate side remains pure fcc Pd (JCPDS 03-065-6174), whereas the retentate side, the one in direct contact with the H₂S gas mixture, consists of two different phases, Pd fcc and tetragonal Pd₄S (JCPDS 01-073-1387). The presence of Pd₄S in Pd foils treated with H₂S is extensively described in the literature [12, 26, 28, 31]. Pd₄S acts as a barrier for the H₂ permeability. Indeed, the H₂ permeability of Pd₄S is 9×10^{-10} mol·m⁻¹·s⁻¹·Pa^{-0.5} [16] at 450°C, about 2 orders of magnitudes less than that of the pure Pd. Thus,

it is not surprising that the H₂ flux decreases when sulfur compounds are present in the feed gas stream. The permeability calculated in the current work for the Pd foil when in contact with the H₂S ($4.5 \times 10^{-9} \text{ mol} \cdot \text{m}^{-1} \cdot \text{s}^{-1} \cdot \text{Pa}^{-0.5}$) is higher than the Pd₄S permeability, indicating the membrane's surface is not fully covered with the sulfurous compound. Another important aspect is that Pd₄S has larger lattice parameter ($a=5.1147$ and $c=5.5903$ Å) than pure Pd (3.8874 Å). The volume expansion caused by the introduction of S into the Pd lattice may introduce additional stress into the membrane causing it to fail. In the present case, the Pd membrane did not fail but SEM analysis showed the formation of cracks (this will be shown in Fig.6.23). Contrary to the Pd foil, membrane E-2 does not go through any phase change either on the feed or permeate side as seen in panel 2 of Fig. 6.21. In fact, XRDs of both sides are very similar to the XRD of a pristine sample, and do not show any evidence of sulfurous compounds. Any changes occurring on membrane E-2 are surely mostly limited to the surface. This was further investigated by grazing incidence XRD with $\theta = 5^\circ$. The corresponding diffractograms are shown in Fig. 6.21.

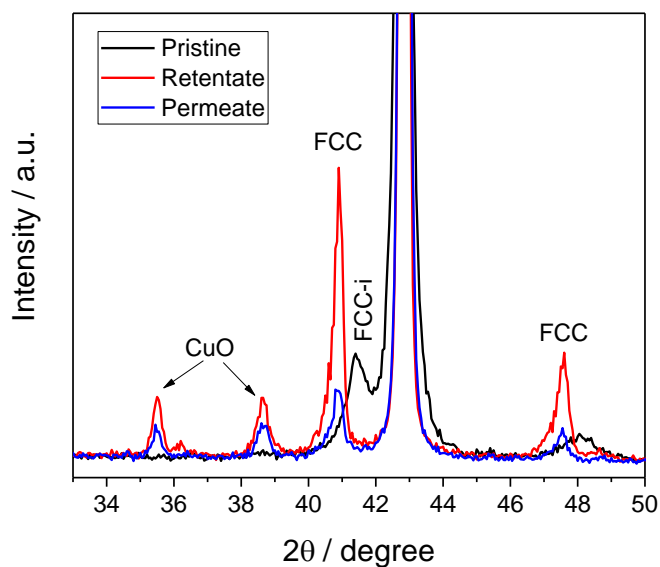
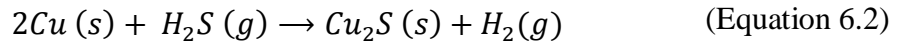
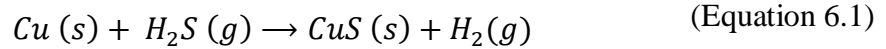
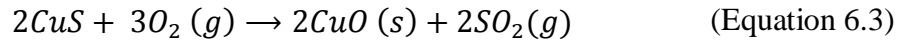


Figure 6. 22 – Grazing incidence X-ray diffractograms ($\theta = 5^\circ$) for membrane E-2 Pd₃₉Cu₅₄Au₇, after exposure to H₂S, for both retentate and permeate sides. A comparison is made with the pristine sample.

In Fig 6.22, three diffractograms acquired in grazing incidence are shown, namely of the membrane before testing (pristine sample) and of the retentate and permeate sides after testing. Features of the pristine sample are the same already seen in 6.10, this is two phases are present, the predominant bcc phase and the fcc phase (denoted fcc-1, in Fig 6.22) that matches the fcc phase of the alloy after ball milling. Three phases are observed in both retentate and permeate sides of the membrane after exposure to H₂S, namely the bcc phase of the pristine membrane, a new fcc phase and a CuO phase (JCPDS card no. 48-1548) not seen previously. The new fcc phase has the following lattice parameters: (3.823±0.001) and (3.826±0.002) Å, for the retentate and permeate sides, while the lattice parameter of the fcc-1 phase is (3.781±0.004) Å. This gives ~0.04 Å difference in the lattice parameters. It seems that fcc-1 phase was replaced by another fcc phase after the H₂S testing. Most surprising is that no phase with sulfurous compounds was identified. Also surprising is the fact that copper oxide is formed during the permeation test even if O₂ is not present and high H₂ pressure was used. This suggests that CuO is formed post-testing. Indeed, copper may react with H₂S to give CuS or Cu₂S [32]:



Upon removal of the membrane from the permeation chamber, CuS can react with the oxygen in the air to form CuO [33-36], while Cu₂S is stable against oxidation below 200°C [37]. The formation of CuO is illustrated by equation 6.3:



As seen in equation 6.3, sulfur dioxide gas is formed along with CuO. Based on what was described above, the following degradation mechanism is proposed: Cu in the fcc-1 phase, reacts with H₂S during the permeation experiment, resulting in the formation of CuS. As copper is leaving the alloy, a new PdCuAu fcc phase with a larger lattice parameter is being formed simultaneously. Outside the permeation chamber, CuS reacts to give CuO.

6.3.2.2. SEM/EDX analysis

The morphology of the samples after H₂S treatment was analyzed by SEM. The corresponding micrographs are shown in Fig. 6.23.

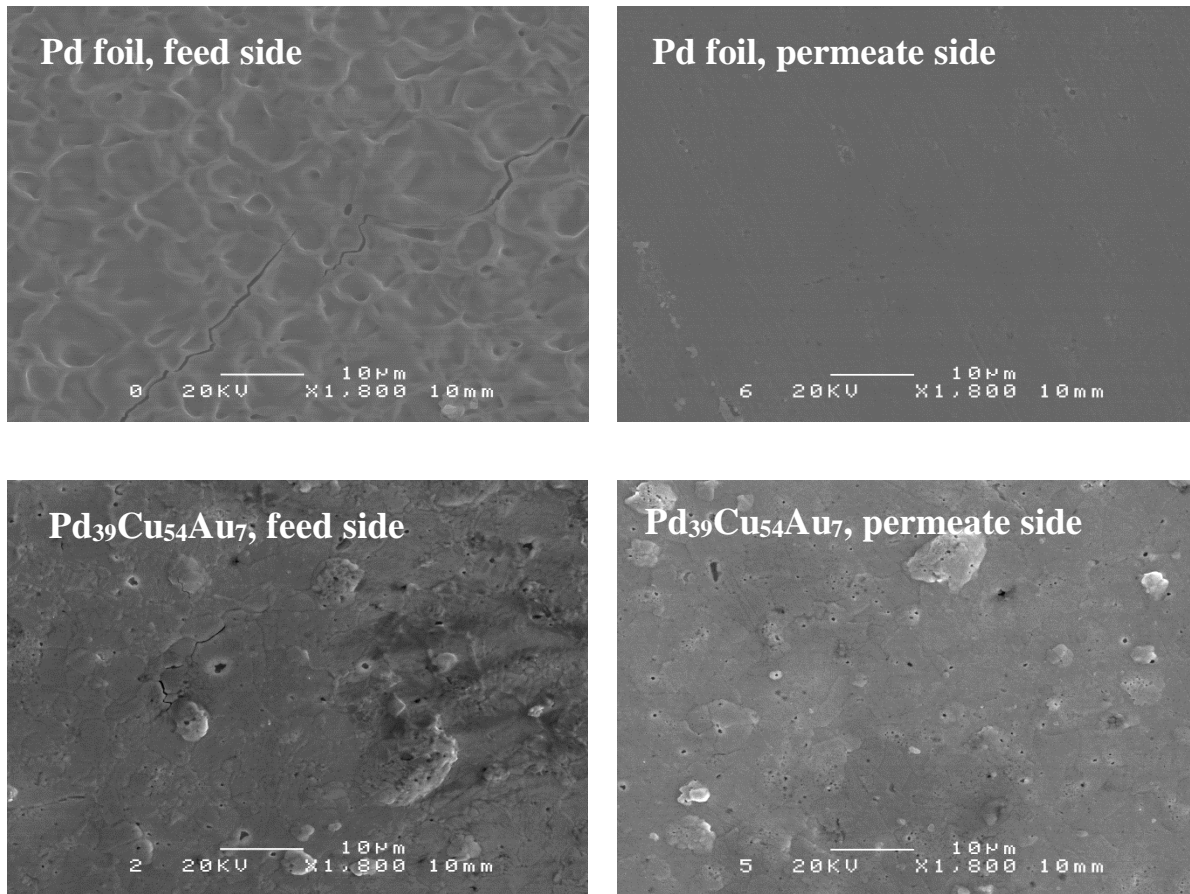


Figure 6. 23 – SEM micrographs for the Pd 250 μm foil (top) and membrane E-2 Pd₃₉Cu₅₄Au₇ (bottom). Both retentate (left) and permeate sides (right) of the membranes are shown.

As seen in Fig. 6.23, the feed side of the Pd foil becomes rougher, whereas the permeate side maintains its homogeneous metallic surface. Some cracks are also observed on the feed side of Pd. The formation of cracks or pinholes in pure Pd when in contact with H₂S gas is already described in the literature [13, 38-41] and results from the stress caused by the lattice mismatch between pure fcc Pd ($a=3.8874 \text{ \AA}$) and tetragonal Pd₄S ($a=5.1147 \text{ \AA}$; $c=5.5903 \text{ \AA}$), as already mentioned in section 6.3.2.1. EDX analysis confirms that Pd₄S is formed on the surface of the feed side (measured composition P_{4.37}S) and pure Pd is present on the permeate side. In the case of

membrane E-2, both feed and permeate side present pores as anticipated by the GC data. Cracks are also visible in the feed side but not on the permeate side. EDX analysis of membrane E-2 was performed not only on the surface but also on a cross section. Most surprisingly, no sulfur was detected in any of the analyses. The results for Pd, Cu and Au are compared in Fig. 6.24.

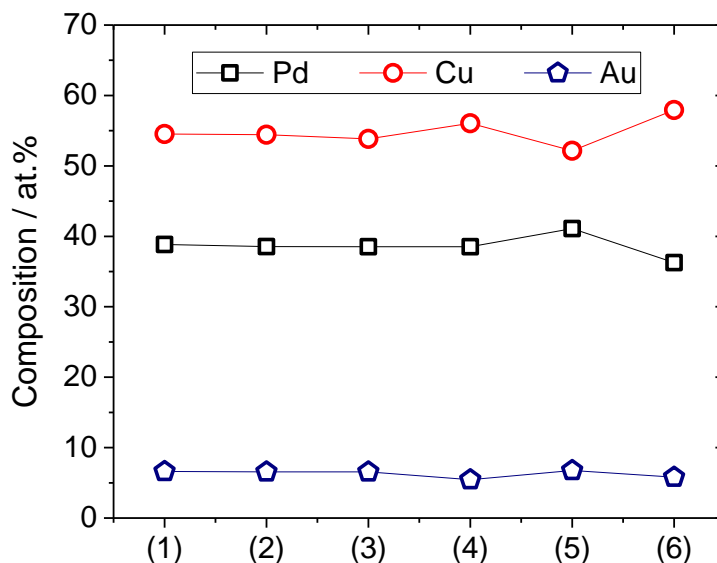


Figure 6. 24 – Variation of composition as determined by EDX measurements for membrane E-2. The data were taken on both surfaces of the membrane and at various locations on the cross section: (1) surface of pristine sample; (2) surface of retentate upon exposure to H₂S treatment; (3) surface of permeate upon exposure to H₂S; (4) cross section close to retentate side; (5) middle of cross section; (6) cross section close to permeate side.

As it can be seen in Fig. 6.24, the compositions of the retentate and permeate sides are practically the same and are both equal to the compositions of a pristine sample. There is a slight Cu depletion in the middle of the cross section and slight enrichment in Cu in the cross section close to retentate and permeate sides of the membrane. The reverse is true for Au. The data suggests that Cu is migrating from the bulk of the membrane to both surfaces (feed and permeate) most probably due to the presence of H₂S (as the membrane failed, both sides of the membrane

were in fact in contact with H₂S). Further analysis with XPS will help elucidating this issue (section 6.3.2.3).

6.3.2.3. XPS analysis

Table 6.5 reports the binding energy and the composition of sample E-2, analyzed on the retentate and permeate sides, with and without etching. The results are compared with a pristine sample. No analysis of the Pd foil was performed, as the nature of the sulfurous compound was already revealed by XRD and EDX.

Table 6. 5 – Binding energy and composition of membrane E-2 after being in contact with H₂S gas mixture. Analyses were made on the retentate and permeate sides of the membrane with and without etching. The results are compared to the pristine sample. (1) refers to the bulk EDX composition of the pristine sample, and reference values are from [42].

Sample	Binding energy (eV)					Alloy composition (at.%)			Overall content (at.%)	
	Pd 3d _{3/2}	Cu 2p _{3/2}	Au 4f _{7/2}	Na 1s	S 2p	Pd	Cu	Au	Na	S
Reference	340.3	932.7	84.0	1072.1	164.0	40 ⁽¹⁾	53 ⁽¹⁾	7 ⁽¹⁾	3 ⁽¹⁾	---
Pristine	340.4	931.8	83.5	1071.3	---	60.1	27.1	12.8	6.5	---
Pristine etch 6 nm	340.2	931.6	83.4	1071.8	---	47.3	44.6	8.1	0.8	---
Retentate	340.4	931.6	83.7	1071.4	162.5	41.1	51.8	7.0	18.4	15.8
Retentate etch 2 nm	340.3	931.7	83.6	1072.1	161.9	45.7	48.3	6.0	11.1	5.7
Permeate	340.2	931.4	83.6	1071.5	162.3	49.0	41.6	9.4	15.84	9.7
Permeate etch 2 nm	340.3	931.8	83.6	1071.9	161.8	43.0	49.7	7.7	5.8	7.7

As seen in table 6.5, the binding energies of copper follow the same trend already mentioned in section 5.2.3, that is, the binding energy of the reduced copper is lower than the binding energy of metallic copper found in the literature (931.8 vs. 932.7 eV). The same is true for gold (83.5 vs. 84.0 eV). However, for Pd, both the literature and the experimental binding energies are practically the same (340.4 vs. 340.3 eV). After the H₂S testing similar trends in the Pd, Cu and Au binding energies were observed, on both retentate and permeate sides. These results are in accordance with the ones of Tarditi et al. [43], except for the palladium binding energy where they observed a maximum -0.4 eV shift.

The pristine sample, shows surface enrichment in palladium. Indeed, the bulk Pd concentration is 40 at.%, whereas 60.1 at.% was measured. This is, however, exactly the reverse of what was observed in section 5.2.3. In fact, we commented before on the surface segregation of copper that could arise as a result of annealing, probably promoted by the presence of vestigial oxygen in the Ar-purged furnace. In the present case, the pristine sample was annealed under Ar with 5% H₂. As a consequence of the favorable interaction of palladium with hydrogen, palladium segregates at the surface (in this context defined as the region probed by XPS ~7 atomic layers), in a similar way as oxygen promotes the segregation of copper. Recently, Tarditi and coworkers [43] have commented on the same effect when PdCuAu ternary alloys were heat treated under pure H₂. Etching the surface for 6 nm reveals a composition (Pd_{47.3}Cu_{44.6}Au_{6.1}) that is closer to the expected composition (Pd₄₀Cu₅₃Au₇) than it is to the surface one (Pd_{60.1}Cu_{27.1}Au_{12.8}). The sodium content was also measured and is equal to 6.5 and 0.8 at.% for the pristine sample, at the surface and at 6 nm depth, respectively. This strongly suggests that sodium is segregating on the surface as well. Overall, the XPS results suggest that the surface is enriched in both palladium and sodium when compared to the bulk

After the H₂S testing the retentate and permeate sides of the membrane show a strong sodium segregation. Indeed, sodium content increases from 6.5 at.% in the pristine sample to concentrations above 15 at.% in the H₂S-treated sample. Sulfur contents are also high, 15.8 and 9.7 at.% in the retentate and permeate side of the membrane. O'Brien and coworkers [26] also registered a sulfur content as high as 30 at.% on their 25 μm Pd₄₇Cu₅₃ membrane exposed to 1000 ppm H₂S for six hours at 350°C. Etching the surface for 2 nm, lowers the sodium or sulfur contents

on either sides of the membrane. The retentate side of the membrane was further etched to approximately 40 nm deep. The concentration profile of the different elements is shown in Fig. 6.25.

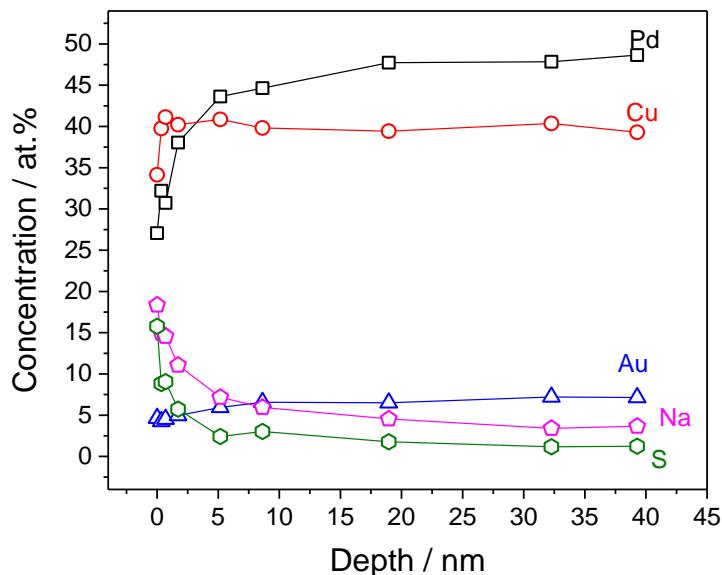


Figure 6. 25 – Pd, Cu, Au, Na and S concentration profile of membrane E-2 that was in contact with H₂S 941 ppm gas mixture. Analysis started at the retentate side of the membrane here referenced as 0 nm depth. Depth was estimated using equation 3.15.

As displayed by Fig. 6.25, the palladium, copper and gold content increases in the first 5 nm while that of sulfur and sodium decreases. Afterwards, the composition of the membrane remains approximately constant. At 40 nm depth the sulfur content is about 1%. Most likely, as the result of membrane failure during the H₂S experiment, the sulfur content will remain around 1% till reaching the permeate side of the membrane, where its concentration will increase again. At 40 nm the palladium content is higher than that of copper, indicating copper depletion is more pronounced in the center of the membrane, as already anticipated with the EDX results (Fig. 6.22). The nature of the sulfur bound to the surface was investigated with the high resolution spectra of Cu 2p_{3/2} and S 2p spectra, shown in figures 6.26 and 6.27, respectively.

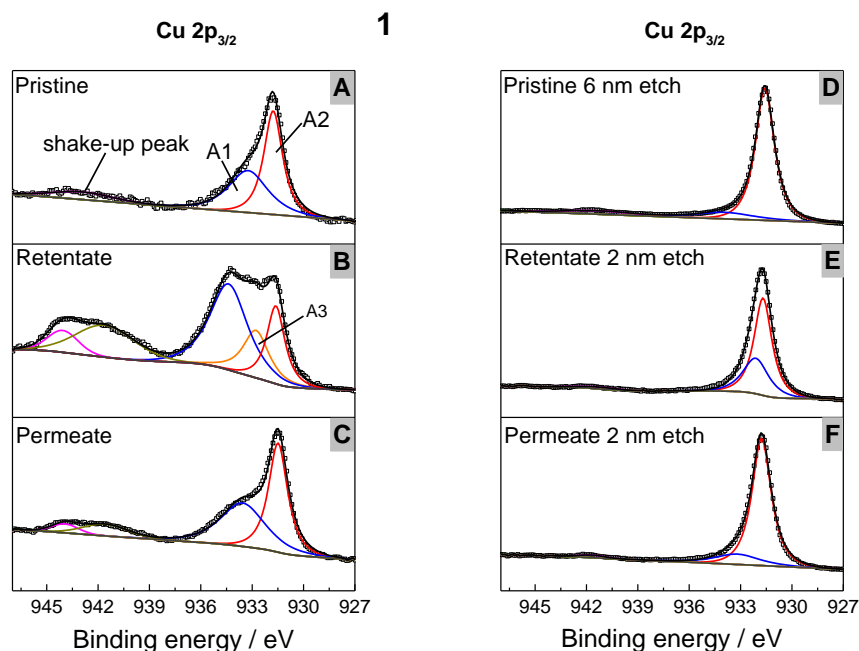


Figure 6. 26 – Cu $2p_{3/2}$ high resolution spectra for membrane E-2 after being in contact with H_2S 941 ppm. Both sides of the membrane were analyzed and are compared with a pristine sample. Analyzes were performed without (panel 1) and with etching (panel 2).

The Cu $2p_{3/2}$ spectra of the pristine sample (panel A Fig. 6.26) reveals the presence of shake-up peaks, which are characteristic of copper in oxidation state +2. As a consequence, the broad peak is better deconvoluted by two peaks, A2 and A1, corresponding to the reduced and oxidized forms of copper, respectively. This is similar to what was observed with the samples prepared by sputter deposition in section 5.2.3. The measured binding energies for the pristine sample are 931.8 (A2) and 933.2 (A1) eV. The binding energy of the latter peak identifies it with CuO [44]. About 20% of all copper on the surface is in the form of CuO, according to equation 5.4. Etching the surface for 6 nm (panel D, Fig. 6.23), decreases this value to 13%. Changes occur at the surface with the H_2 - H_2S experiment on both sides of the membrane (panels B and C of Fig. 6.26). Indeed, the very broad peak in panel B, for the retentate side of the membrane, seems to be the sum of three peaks, rather than two, with the binding energies 931.6, 932.8 and 934.7 eV. These correspond to the reduced alloyed copper (42% of total), Cu_2S or CuS (literature values are 932.6 and 932.5, respectively [45]) and $Cu(OH)_2$ [44, 45]. The peak at 162.6 eV (peak C3) in panel A of Fig.6.27 confirms that CuS is present rather than Cu_2S as it will be discussed below. In the

case of the permeate side of the membrane the binding energies are 931.5 (reduced copper), and 933.6 (CuO) eV. Upon etching we get the following binding energies 931.7 (reduced copper) and 932.1 (CuS) eV for the retentate side, while for the permeate side we have 931.8 (reduced copper) and 933.2 eV (CuO). From the information above we may conclude that in the presence of H₂S, XPS and XRD (section 6.3.2.1) data support the formation of CuS rather than Cu₂S. The high resolution spectra of S 2p allowed the identification of other sulfur containing species (Fig. 6.27).

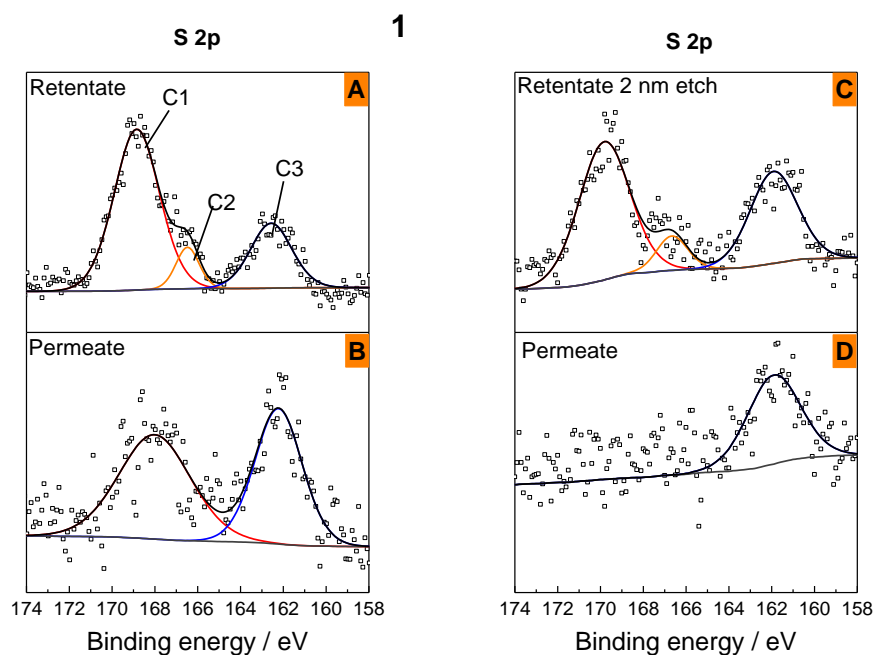


Figure 6. 27 – S 2p high resolution spectra for membrane E-2 after being in contact with H₂S 941 ppm. Both sides of the membrane were analyzed. Analyzes were performed without (panel 1) and with etching (panel 2).

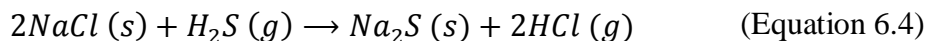
As seen in panel A of Fig. 6.27, the retentate sample shows 3 three different S 2p peaks (162.6, 166.5 and 168.9 eV), while the permeate side (panel B) only displays two peaks (162.2 and 168.0 eV). In fact each peak is the sum of two unresolved components (S 2p_{1/2} and S 2p_{3/2}) [45]. After etching for 2 nm (panels C and D), three peaks remain in the retentate side (161.9, 166.7 and 169.8 eV), however only one peak is visible on the permeate side (161.9 eV). The identification of each peak is not straightforward as sulfur exists in many different oxidation states (-2, 0, +2,+3,+4 and +6). Broadly speaking, the reduced sulfur (-2 or 0) shows peaks below ~164

eV while higher binding energies are associated with oxidized sulfur. To facilitate the discussion the binding energies of sulfur 2p peaks are summarized in table 6.6.

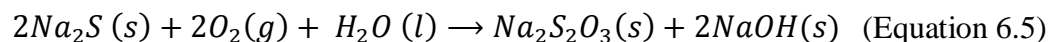
Table 6. 6 – Published results of the S 2p binding energy for common sulfur compounds with copper or sodium.

Compound	Sulfur oxidation state	Binding energy (eV)	Type of compound	Ref.
Cu ₂ S	-2	161.8	sulfide	[45]
CuS	-2	162.5	sulfide	[45]
CuSO ₄	+6	168.8	sulfate	[45]
CuSO ₄	+6	169.9	sulfate	[46]
Na ₂ S	-2	162.0	sulfide	[47]
Na ₂ S ₂ O ₃	-2 and +6	162.7 (-2) and 168.6 (+6)	thiosulfate	[48]
Na ₂ S ₂ O ₃	-2 and +6	162.7 (-2) and 168.4 (+6)	thiosulfate	[47]
Na ₂ SO ₃	+4	167.6	sulfite	[48]
Na ₂ SO ₃	+4	166.8	sulfite	[47]
Na ₂ SO ₄	+6	169.4	sulfate	[48]
Na ₂ SO ₄	+6	168.4	sulfate	[47]

As different compounds have similar binding energies each peak of Fig. 6.27 is probably not the result of one single sulfur species but of several. In Fig. 6.25 was shown that sodium and sulfur have the same depth profile, thus suggesting that somehow they are both connected. At high temperature and pressure the following reaction of NaCl with H₂S is plausible:



As seen in equation 6.4, Na₂S can be formed under the H₂S test conditions. However, Na₂S is not stable and readily reacts with air moisture [49] according to the equation:



The sulfur compound that is formed in equation 6.5 is a thiosulfate that contains two sulfur atoms, one with oxidation state -2 and the other with oxidation +6. Consequently, in XPS this compound shows two peaks at 162.7 (-2) and 168.6 (+6) eV with approximately the same intensity [50]. This is most probably the origin of the peaks at 162.2 and 168.0 eV for the permeate side of the membrane (Fig. 6.27 panel B). The Na 1s high resolution spectrum shows a strong peak at 1071.5 eV. However, sodium thiosulfate, sodium sulfate and sodium chloride all have overlapping binding energies [42, 51], making it difficult to ascertain the compound responsible for the origin of the peak. Upon etching (panel D) only one peak is present that could be the due to Na₂S. At 2 nm depth, Na₂S could resist oxidation as access to air moisture is more limited in comparison to the surface.

The retentate side of the membrane shows three S 2p peaks at 0 and 2 nm depth (panels A and C, respectively). In both cases, peak C1 (at higher binding energies) is higher in intensity than peak C3 (at lower binding energies). This means that sodium thiosulfate alone does not completely explain the origin of these peaks. However, on the basis of the binding energies, the presence of the thiosulfate cannot be excluded either (C3 – 162.6, and C1 – 168.9 eV). At 162.6 eV, CuS may also play a role while CuSO₄ is probably contributing to the peak at 168.9 eV. CuS is not stable and reacts with air moisture, leading to the formation of copper sulfate [52] or CuO. Even if sodium sulfate also has binding energies compatible with peak C1, its presence is not likely, owing to the fact that the formation of the sulfate from Na₂S would require the use of hydrogen peroxide.

Evidence of CuSO_4 in the Cu 2p $3/2$ high resolution spectra is not clear, unless 4 components are used to deconvolute the broad peak presented in Fig. 6.24 B. If that is the case, the extra component would have 935.2 eV of binding energy which matches exactly with the data reported by Chawla et al. [45] for copper sulfate.

At 2 nm depth (Fig. 6.27 C), there are some variations in the binding energies. Indeed peak C1 is now at 169.8 eV, while peak C3 is at 161.9 eV. Peak C1 can still be identified with the sulfate, as literature values fall between 168.8 and 169.9 eV. Based on the binding energy only, peak C3 is more likely to be Cu_2S or Na_2S . However, the peak at 932.1 eV for the Cu 2p $_{3/2}$ is indicating that we should have CuS instead. Lastly, peak C2, present at 166.5 and 166.7 eV for the 0 and 2 nm depth, respectively, corresponds very well with Na_2SO_3 published binding energies.

The exposure of the membrane to H_2S results in the formation of different Na-S and Cu-S compounds. In these conditions, no Pd-S and Au-S compounds were identified. XPS measurements support the formation of the following compounds: Na_2S , $\text{Na}_2\text{S}_2\text{O}_3$, Na_2SO_3 , CuS and CuSO_4 . The oxidized forms of sulfur were most probably formed post-testing, from the reaction with moisty air.

6.4. Conclusions

PdCuAu ternary alloys were successfully prepared by mechanical alloying of the pure metal powders. The fcc phase was invariably formed even if the compositions were within the limits of the bcc phase, which is the thermodynamically stable phase at room temperature. The bcc phase is formed upon annealing at 400°C for 5h. A method was developed to prepare membranes from the ball milled powders that involves seven steps, including sintering, cold rolling, polishing and heat treatments. The permeability of these membranes was measured and it was found to be composition dependent. The membrane that performed the best under pure H_2 was $\text{Pd}_{40}\text{Cu}_{53}\text{Au}_7$. This membrane presents a decrease in the activation energy for H_2 permeability when compared with a pure Pd foil (10.0 vs. 21.9 $\text{kJ}\cdot\text{mol}^{-1}$). The permeation measurements performed in presence of H_2S show that gold does not provide any protective effect towards sulfur poisoning. Several sulfurous compounds were formed on the surface of the membrane not only with copper but also with sodium. The latter was added as a process control agent in the mechanical alloying procedure.

6.5. References

- [1] Subramanian PR, Laughlin DE. Cu-Pd (Copper-Palladium). *Journal of Phase Equilibria*. 1991;12:231-43.
- [2] Honrado Guerreiro B, Martin MH, Roué L, Guay D. Hydrogen solubility in PdCuAu alloy thin films prepared by electrodeposition. *International Journal of Hydrogen Energy*. 2014;39:3487-97.
- [3] Suryanarayana C. Mechanical alloying and milling. *Progress in Materials Science*. 2001;46:1-184.
- [4] Galipaud J, Martin MH, Roué L, Guay D. Measurement of hydrogen solubility in Pd_xCu_{100-x} thin films prepared by pulsed laser deposition: An electrochemical in situ X-ray diffraction analysis. *Journal of Physical Chemistry C*. 2013;117:2688-98.
- [5] Hahn JD, Wu F, Bellon P. Cr-Mo solid solutions forced by high-energy ball milling. *Metall and Mat Trans A*. 2004;35:1105-11.
- [6] Lee TH, Park CY, Lee G, Dorris SE, Balachandran U. Hydrogen transport properties of palladium film prepared by colloidal spray deposition. *Journal of Membrane Science*. 2012;415-416:199-204.
- [7] Balachandran U, Lee TH, Park CY, Emerson JE, Picciolo JJ, Dorris SE. Dense cermet membranes for hydrogen separation. *Separation and Purification Technology*. 2014;121:54-9.
- [8] Goupil G, Jucken S, Poirier D, Legoux JG, Irissou E, Davis B, et al. Cold sprayed Cu-Ni-Fe anode for Al production. *Corros Sci*. 2015;90:259-65.
- [9] Tsai Y-C, Lin C-C, Lin W-L, Wang J-H, Chen S-Y, Lin P, et al. Palladium based cermet composite for hydrogen separation at elevated temperature. *Journal of Power Sources*. 2015;274:965-70.

- [10] Coulter KE, Way JD, Gade SK, Chaudhari S, Sholl DS, Semidey-Flecha L. Predicting, Fabricating, and Permeability Testing of Free-Standing Ternary Palladium-Copper-Gold Membranes for Hydrogen Separation. *Journal of Physical Chemistry C*. 2010;114:17173-80.
- [11] Mckinley DL. Method for hydrogen separation and purification. United States: US Patent 3,439,474; 1969.
- [12] Braun F, Tarditi AM, Miller JB, Cornaglia LM. Pd-based binary and ternary alloy membranes: Morphological and perm-selective characterization in the presence of H₂S. *Journal of Membrane Science*. 2014;450:299-307.
- [13] Mundschau MV, Xie X, Evenson CR, Sammells AF. Dense inorganic membranes for production of hydrogen from methane and coal with carbon dioxide sequestration. *Catalysis Today*. 2006;118:12-23.
- [14] Abate S, Genovese C, Perathoner S, Centi G. Performances and stability of a Pd-based supported thin film membrane prepared by EPD with a novel seeding procedure. Part 1—Behaviour in H₂:N₂ mixtures. *Catal Today*. 2009;145:63-71.
- [15] Gade SK, Coulter KE, Way JD. Effects of fabrication technique upon material properties and permeation characteristics of palladium-gold alloy membranes for hydrogen separations. *Gold Bulletin*. 2010;43:287-97.
- [16] O'Brien CP, Gellman AJ, Morreale BD, Miller JB. The hydrogen permeability of Pd₄S. *Journal of Membrane Science*. 2011;371:263-7.
- [17] Morreale BD, Ciocco MV, Enick RM, Morsi BI, Howard BH, Cugini AV, et al. The permeability of hydrogen in bulk palladium at elevated temperatures and pressures. *Journal of Membrane Science*. 2003;212:87-97.

- [18] Holleck GL. Diffusion and solubility of hydrogen in palladium and palladium-silver alloys. *The Journal of Physical Chemistry*. 1970;74:503-11.
- [19] Katsuta H, Farraro RJ, McLellan RB. The diffusivity of Hydrogen in palladium. *Acta Metallurgica*. 1979;27:1111-4.
- [20] Hurlbert RC, Konecny JO. Diffusion of Hydrogen through Palladium. *The Journal of Chemical Physics*. 1961;34:655-8.
- [21] Howard BH, Killmeyer RP, Rothenberger KS, Cugini AV, Morreale BD, Enick RM, et al. Hydrogen permeance of palladium-copper alloy membranes over a wide range of temperatures and pressures. *Journal of Membrane Science*. 2004;241:207-18.
- [22] Matsumura Y. A basic study of high-temperature hydrogen permeation through bcc Pd–Cu alloy foil. *Separation and Purification Technology*. 2014;138:130-7.
- [23] Tarditi AM, Imhoff C, Braun F, Miller JB, Gellman AJ, Cornaglia L. PdCuAu ternary alloy membranes: Hydrogen permeation properties in the presence of H₂S. *Journal of Membrane Science*. 2015;479:246-55.
- [24] Mckinley DL. Metal alloy for hydrogen separation and purification. United States: US patent 3,350,845; 1967.
- [25] Tarditi AM, Braun F, Cornaglia LM. Novel PdAgCu ternary alloy: Hydrogen permeation and surface properties. *Applied Surface Science*. 2011;257:6626-35.
- [26] O'Brien CP, Howard BH, Miller JB, Morreale BD, Gellman AJ. Inhibition of hydrogen transport through Pd and Pd₄₇Cu₅₃ membranes by H₂S at 350°C. *Journal of Membrane Science*. 2010;349:380-4.

- [27] Morreale B. Effect of hydrogen-sulfide on the hydrogen permeance of palladium-copper alloys at elevated temperatures. *Journal of Membrane Science*. 2004;241:219-24.
- [28] Braun F, Miller JB, Gellman AJ, Tarditi AM, Fleutot B, Kondratyuk P, et al. PdAgAu alloy with high resistance to corrosion by H₂S. *International Journal of Hydrogen Energy*. 2012;37:18547-55.
- [29] Gabitto J, Tsouris C. Sulfur poisoning of metal membranes for hydrogen separation. *International Review of Chemical Engineering*. 2009;1:394-411.
- [30] Morreale BD, Ciocco MV, Howard BH, Killmeyer RP, Cugini AV, Enick RM. Effect of hydrogen-sulfide on the hydrogen permeance of palladium–copper alloys at elevated temperatures. *J Membr Sci*. 2004;241:219-24.
- [31] Mundschau MV, Xie X, Evenson Iv CR, Sammells AF. Dense inorganic membranes for production of hydrogen from methane and coal with carbon dioxide sequestration. *Catal Today*. 2006;118:12-23.
- [32] Iyoha O, Enick R, Killmeyer R, Morreale B. The influence of hydrogen sulfide-to-hydrogen partial pressure ratio on the sulfidization of Pd and 70 mol% Pd–Cu membranes. *Journal of Membrane Science*. 2007;305:77-92.
- [33] Kong X, Li Y. High sensitivity of CuO modified SnO₂ nanoribbons to H₂S at room temperature. *Sensors and Actuators B: Chemical*. 2005;105:449-53.
- [34] Wagh MS, Patil LA, Seth T, Amalnerkar DP. Surface cupricated SnO₂–ZnO thick films as a H₂S gas sensor. *Materials Chemistry and Physics*. 2004;84:228-33.
- [35] Yuanda W, Maosong T, Xiuli H, Yushu Z, Guorui D. Thin film sensors of SnO₂–CuO–SnO₂ sandwich structure to H₂S. *Sensors and Actuators B: Chemical*. 2001;79:187-91.

- [36] Xue X, Xing L, Chen Y, Shi S, Wang Y, Wang T. Synthesis and H₂S Sensing Properties of CuO–SnO₂ Core/Shell PN-Junction Nanorods. *The Journal of Physical Chemistry C*. 2008;112:12157-60.
- [37] Wang S, Huang Q, Wen X, Li X-y, Yang S. Thermal oxidation of Cu₂S nanowires: A template method for the fabrication of mesoscopic CuxO (x = 1,2) wires. *Physical Chemistry Chemical Physics*. 2002;4:3425-9.
- [38] Kulprathipanja A, Alptekin GO, Falconer JL, Way JD. Pd and Pd–Cu membranes: inhibition of H₂ permeation by H₂S. *Journal of Membrane Science*. 2005;254:49-62.
- [39] Edlund DJ, Pledger WA. Thermolysis of hydrogen sulfide in a metal-membrane reactor. *Journal of Membrane Science*. 1993;77:255-64.
- [40] Kajiwara M, Uemiya S, Kojima T. Stability and hydrogen permeation behavior of supported platinum membranes in presence of hydrogen sulfide. *International Journal of Hydrogen Energy*. 1999;24:839-44.
- [41] Chen C-H, Ma YH. The effect of H₂S on the performance of Pd and Pd/Au composite membrane. *Journal of Membrane Science*. 2010;362:535-44.
- [42] Moulder JF, Sickle WF, Sobol PE, Bomben KD. *Handbook of X-ray Photoelectron Spectroscopy: A Reference Book of Standard Spectra for Identification and Interpretation of XPS Data*: Physical Electronics Division, Perkin-Elmer Corporation; 1992.
- [43] Tarditi AM, Imhoff C, Miller JB, Cornaglia L. Surface composition of PdCuAu ternary alloys: a combined LEIS and XPS study. *Surface and Interface Analysis*. 2015;47:745-54.

- [44] Biesinger MC, Lau LWM, Gerson AR, Smart RSC. Resolving surface chemical states in XPS analysis of first row transition metals, oxides and hydroxides: Sc, Ti, V, Cu and Zn. *Applied Surface Science*. 2010;257:887-98.
- [45] Chawla SK, Sankarraman N, Payer JH. Diagnostic spectra for XPS analysis of Cu-O-S-H compounds. *Journal of Electron Spectroscopy and Related Phenomena*. 1992;61:1-18.
- [46] Kurmaev EZ, Fedorenko VV, Galakhov VR, Bartkowski S, Uhlenbrock S, Neumann M, et al. Analysis of oxyanion (BO_3^{3-} , CO_3^{2-} , SO_4^{2-} , PO_4^{3-} , SeO_4^{4-}) substitution in Y123 compounds studied by X-ray photoelectron spectroscopy. *J Supercond*. 1996;9:97-100.
- [47] Siriwardane RV, Cook JM. Interactions of SO_2 with sodium deposited on CaO. *Journal of colloid and interface science*. 1986;114:525-35.
- [48] Peisert H, Chassé T, Streubel P, Meisel A, Szargan R. Relaxation energies in XPS and XAES of solid sulfur compounds. *Journal of Electron Spectroscopy and Related Phenomena*. 1994;68:321-8.
- [49] Greenwood NN, Earnshaw A. *Chemistry of the Elements*. Second ed: Butterworth-Heinemann; 1997.
- [50] Liang X, Hart C, Pang Q, Garsuch A, Weiss T, Nazar LF. A highly efficient polysulfide mediator for lithium–sulfur batteries. *Nature communications*. 2015;6.
- [51] Wagner CD. Chemical shifts of Auger lines, and the Auger parameter. *Faraday Discussions of the Chemical Society*. 1975;60:291-300.
- [52] Murata K, Ikeda S, Utsunomiya T, Yasui A. X-ray photoelectron spectrometric and x-ray fluorometric studies of sulphur compounds on the surface of copper plates exposed to the atmosphere. *Talanta*. 1976;23:529-33.

7. Conclusions and Future work

7.1. Conclusions

Palladium-copper-gold ternary alloys were prepared over a wide composition range by three different methods, namely, electrodeposition (chapter 4), sputter deposition (chapter 5) and mechanical alloying (chapter 6). In all three methods, the solubility limits of the fcc phase were extended at room temperature. Only upon heat treatment, and in accordance with the composition, the thermodynamically stable bcc phase is obtained. This is probably a consequence of the low enthalpy variation between the ordered bcc phase and the disordered fcc solid solution phase [1]. The lattice of the PdCuAu alloys is deformed due to the different sizes of the atoms. This explains the positive deviation observed when the experimental lattice parameters are compared to the ones calculated using Vegard's law.

The morphologies of electrodeposited samples are dependent on the palladium content, going from more spherical structures at low Pd concentrations (for example Pd_{14.3}Cu_{82.1}Au_{3.6}) to more needle-like structures at higher Pd content (for example Pd_{74.3}Cu_{18.4}Au_{7.3}). This could be due to the co-deposition of hydrogen that is favored at higher palladium concentrations.

EELS analysis of a cross-section of films prepared by sputter deposition reveals a periodical layer structure imposed on the films by applying rotation on the substrate while operating the three metal targets – palladium, copper and gold – at the same time. Annealing will most likely homogenize the films. The substrates were rotated as a way to guarantee that surface composition was homogeneous along the surface of the samples (from point to point).

Annealing may cause not only changes in the crystallographic structure but also in the surface composition. The former effect is regulated by the Pd, Cu and Au relative content, while the latter effect is regulated by the atmosphere under which annealing is made. Generally, the presence of oxygen or H₂S stimulates copper segregation to the surface, while the presence of hydrogen promotes Pd segregation at the surface.

Two hydrogen related properties were studied, namely, solubility and permeability. The palladium content is the key factor ruling the amount of hydrogen that can be dissolved in the alloy. The alloys richer in Pd were also the ones that showed the highest hydrogen solubility. The replacement of Cu with Au was found to increase the solubility of hydrogen. Annealing is in general detrimental to the solubility, either because it promotes phase transition, specifically to the bcc structure, or as a consequence of increased crystallite size (less grain boundaries). Moreover, the solubility of the fcc and bcc phase is affected to the same extent by the palladium content. The introduction of hydrogen into the PdCuAu host lattice leads to volume expansion. To maintain the mechanical integrity of a membrane, it is preferable that the hydrogen solubility is limited, to avoid great volumes changes.

A new method to prepare membranes from mechanical alloyed powders was developed, that consists in pressing the powders into disks. These are subsequently sintered, cold rolled, annealed and polished. Membranes prepared in this way show higher hydrogen permeability values but lower selectivity than reference literature membranes. The permeability is also composition dependent and it was the highest for Pd₄₀Cu₅₃Au₇. At the temperature and concentrations (of gold and H₂S) used in this work, the presence of gold does not seem to confer any protection against H₂S poisoning. In fact, the H₂S-promoted segregation of copper overcomes any potential beneficial effect of gold. Furthermore, NaCl is not a spectator in the permeation, but it seems to react providing a mix of sulfur-containing compounds. Removal of NaCl by aqueous extraction is feasible before pellet pressing. However, it may induce oxidation of copper or palladium that could result in partial dealloying.

7.2. Future Work

In the preceding chapters, more specifically, chapters 5 and 6, copper segregation was shown to occur as the result of annealing, promoted by the presence of oxygen or hydrogen sulfide. A more detailed studied could be done using high temperature *in situ* XRD. In the presence of different gases (H₂, H₂S, O₂, CO, CO₂, CH₄, or others) surface modifications could be monitored by grazing incidence XRD while changing the temperature. The information gathered by XRD could be complimented by EDX, XPS and LEIS (Low-Energy Ion Scattering) data.

Alternative methods for the production of membranes from mechanical alloyed powders could be developed. Most interestingly would be the use of supported membranes in order to reduce the membranes' thickness. In this way, the amount of alloy material would be reduced and, consequently price reduction could be achieved. Methods such as colloidal spray deposition [2], paste-painting [3] or cold spray deposition [4] could be used.

Another interesting approach would be to prepare Pd-bcc alloys that do not have copper. The alloy Pd₅₀Al₅₀ shows a bcc structure above 745°C [5, 6]. It could be interesting to verify if the behavior of PdAl is identical to PdCu alloys when it comes to H₂ permeability (this is to verify if PdAl is showing an increase in H₂ permeability upon transition to bcc structure). At such high temperatures H₂S poisoning is less worrisome, as the studies of Morreale and coworkers [7] have shown for PdCu alloys.

7.3. References

- [1] Galipaud J, Martin MH, Roué L, Guay D. Measurement of Hydrogen Solubility in Pd_xCu_{100-x}Thin Films Prepared by Pulsed Laser Deposition: An Electrochemical in Situ X-Ray Diffraction Analysis. *The Journal of Physical Chemistry C*. 2013;117:2688-98.
- [2] Lee TH, Park CY, Lee G, Dorris SE, Balachandran U. Hydrogen transport properties of palladium film prepared by colloidal spray deposition. *Journal of Membrane Science*. 2012;415-416:199-204.
- [3] Balachandran U, Lee TH, Park CY, Emerson JE, Picciolo JJ, Dorris SE. Dense cermet membranes for hydrogen separation. *Separation and Purification Technology*. 2014;121:54-9.
- [4] Goupil G, Jucken S, Poirier D, Legoux JG, Irissou E, Davis B, et al. Cold sprayed Cu-Ni-Fe anode for Al production. *Corros Sci*. 2015;90:259-65.
- [5] Hume-Rothery W. The platinum metals and their alloys *Platinum Metals Review*. 1966;10:94-100.

[6] Grushko B. Again regarding the Al–Pd phase diagram. *Journal of Alloys and Compounds*. 2013;557:102-11.

[7] Morreale B. Effect of hydrogen-sulfide on the hydrogen permeance of palladium-copper alloys at elevated temperatures. *Journal of Membrane Science*. 2004; 241:219-24.

A1. Résumé: Alliages de Palladium-Cuivre-Or pour la Purification de l'Hydrogène

A1.1 Introduction

L'hydrogène moléculaire joue un rôle primordial dans l'industrie chimique, le raffinage du pétrole, ainsi que dans le secteur alimentaire [1]. De plus, l'hydrogène est considéré comme un vecteur énergétique majeur et propre avec l'utilisation, par exemple, des piles à combustible [2]. La production mondiale d'hydrogène est largement axée sur le vaporeformage, notamment du gaz naturel [3], même si d'autres alternatives, comme l'électrolyse de l'eau, sont disponibles. Pour l'implémentation d'une économie fondée sur l'hydrogène, les coûts de production de l'hydrogène doivent être réduits. Plus spécifiquement, les procédés de purification de l'hydrogène doivent être simplifiés. À cet égard, l'utilisation de membranes denses à base de palladium est particulièrement attrayante, car cela permettrait de réduire les pertes d'énergie et la complexité du processus par rapport aux procédés actuels de purification. Cependant, le coût élevé du palladium et son empoisonnement en présence de H_2S empêchent l'application de ce type de membrane à l'échelle industrielle [4]. Dans le cadre de ce projet, des membranes à base d'alliages palladium-cuivre-or (PdCuAu) ont été évaluées pour la purification de l'hydrogène.

Plusieurs études ont été publiées sur les alliages PdCu, PdAu et PdCuAu et leurs applications dans la purification de l'hydrogène [5-12]. Toutefois, la majorité de ces études sont axées sur la phase cubique à face centrée (fcc de l'anglais *face-centered cubic*) tandis que la phase cubique centrée (bcc de l'anglais *body-centered cubic*) est pratiquement inexplorée. Les alliages PdCuAu de phase cubique centrée devraient avoir une perméabilité aussi élevée que celle des alliages binaires PdCu-bcc, tout en procurant une résistance plus élevée à l'empoisonnement par H_2S grâce à la présence de l'or. Dans cette étude approfondie sur les alliages PdCuAu fcc et plus particulièrement bcc, trois méthodes de synthèse différentes (électrodéposition, dépôt par pulvérisation et broyage mécanique) ont été utilisées pour les préparer. La solubilité et la perméabilité de l'hydrogène ont été mesurées. L'influence de la composition et de la structure cristallographique a été évaluée.

A1.2 Points théoriques

En termes généraux, une membrane est une barrière qui permet le passage sélectif d'une substance spécifique, tout en bloquant les autres. Dans la séparation des gaz, les membranes métalliques denses sont un type particulier de membranes qui fonctionnent via un mécanisme de solution-diffusion, en contraste avec des membranes poreuses qui sont basées sur des mécanismes de séparation par exclusion de tailles. Ces mécanismes sont illustrés à la Fig. 1.

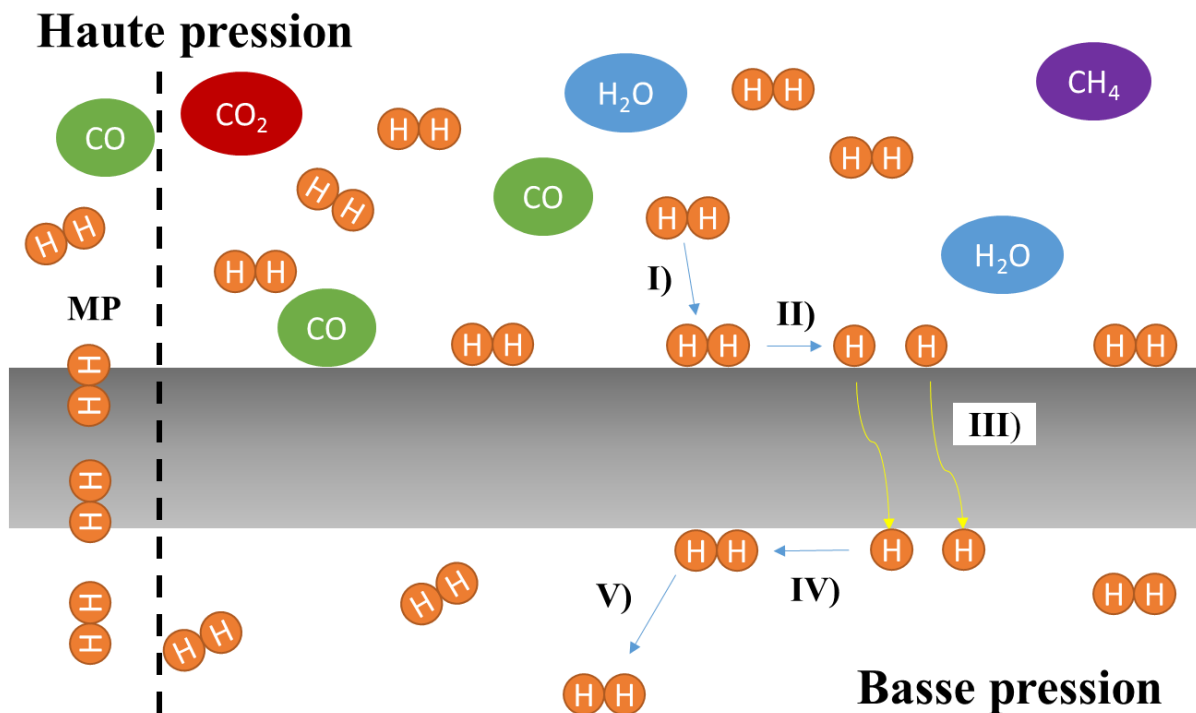


Figure 1 – Illustration schématisée du mécanisme de perméation de l'hydrogène à travers une membrane poreuse (MP, à gauche) et une membrane métallique dense (à droite). Le mécanisme de solution-diffusion comprend 5 étapes: I – adsorption de l'hydrogène moléculaire; II - dissociation de l'hydrogène moléculaire en hydrogène atomique; III - diffusion; IV - recombinaison atomique; et V) désorption de l'hydrogène moléculaire reconstituée.

Indépendamment du type de membrane, poreuse ou métallique dense, le processus de séparation nécessite l'application d'une différence de pression entre l'amont et l'aval de la

membrane. En ce sens, le flux d'hydrogène, c'est-à-dire la quantité d'hydrogène transportée à travers la membrane par unité de temps et unité de surface ($\text{mol}\cdot\text{s}^{-1}\text{m}^{-2}$), est dirigé vers la face de la membrane où la pression d'hydrogène est plus basse. Comme le montre la Fig. 1, le mécanisme de solution-diffusion consiste en 5 étapes. Tout d'abord, sur le côté de haute pression, H_2 est adsorbé sur la surface de la membrane. Ensuite, la liaison H-H est clivée par le palladium (étape II) et les atomes d'hydrogène se solubilisent dans les interstices octaédriques du réseau cubique à faces centrées du métal ou des alliages métalliques. En fait, en dépit du fait que le palladium et l'hydrogène ont des électronégativités comparables, il est généralement admis que l'orbitale électronique 4d du Pd accepte les électrons de l'atome d'hydrogène et que ce sont les protons H^+ qui se déplacent dans les interstices octaédriques. Aux températures auxquelles ces membranes sont généralement utilisées ($> 300^\circ\text{C}$), les atomes d'hydrogène sautent entre les sites voisins sous l'effet de l'activation thermique (étape III) [13]. Finalement, en atteignant l'autre côté de la membrane, les atomes d'hydrogène se recombinent pour former de l'hydrogène moléculaire (étape IV) qui se désorbe de la surface de la membrane (étape V). Comme les atomes d'hydrogène sont les seuls qui soient capables de se dissoudre et de diffuser à travers le palladium, les membranes de palladium sont ainsi hautement sélectives et peuvent théoriquement produire de l'hydrogène pur à 100%. Dans le cas des membranes poreuses (désignés par MP dans la partie gauche de la Fig. 1), c'est la taille relative des molécules de gaz par rapport à la taille des pores qui gouverne le processus de séparation. Le palladium n'entre pas dans la composition de ce type de membranes qui peuvent être produites à partir de matériaux moins dispendieux tels que le carbone. Les membranes poreuses sont plus économiques, mais elles fournissent habituellement une séparation de moindre qualité et, par le fait même, sortent du cadre de ce projet. En fait, l'existence de pores dans les membranes métalliques denses est hautement indésirable, car leur présence va réduire la sélectivité des membranes denses.

Le flux de H_2 à travers la membrane, J_{H_2} est donné par l'équation de Richardson:

$$J_{\text{H}_2} = \frac{\phi}{L} \left[(P_{\text{H}_2}^{\text{amont}})^{\frac{1}{2}} - (P_{\text{H}_2}^{\text{aval}})^{\frac{1}{2}} \right] \quad (\text{Équation 1})$$

avec

$$\phi = \frac{D_H K_S}{2} \quad (\text{Équation 2})$$

Dans les équations 1 et 2, ϕ correspond à la perméabilité de l'hydrogène ($\text{mol}\cdot\text{m}^{-1}\cdot\text{s}^{-1}\cdot\text{Pa}^{0.5}$), L est l'épaisseur de la membrane (m), $P_{H_2}^{amont}$ et $P_{H_2}^{aval}$ sont respectivement les pressions partielles de H_2 en amont et en aval de la membrane (Pa), D_H est le coefficient de diffusion et K_S est la solubilité de l'hydrogène. En utilisant l'équation 1, la perméabilité de la membrane peut être calculée. La perméabilité est une propriété importante de la membrane, car elle permet de quantifier la capacité de la membrane à transporter l'hydrogène.

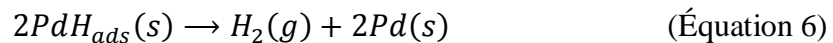
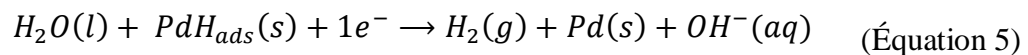
Le palladium peut absorber d'hydrogène soit en phase gazeuse ou en solution aqueuse lorsqu'on applique une différence de potentiel. Pour l'absorption électrochimique d'hydrogène, qui est utilisée dans ce travail, le palladium est immergé dans l'électrolyte et est connecté à un potentiostat. Lors de l'application d'un potentiel négatif, l'absorption d'hydrogène se produit. L'absorption électrochimique de l'hydrogène est un processus en deux étapes [14, 15]. En premier lieu, l'hydrogène est adsorbé sur la surface métallique:



où PdH_{ads} représente l'hydrogène adsorbé sur la surface du palladium. L'équation 3 est également connue comme étant la réaction Volmer. Par la suite, l'hydrogène adsorbé en surface diffuse dans le volume de l'électrode de palladium:



où PdH_{abs} représente l'hydrogène qui s'est inséré dans la maille cristalline du palladium par diffusion. L'hydrogène ainsi adsorbé peut se recombiner pour générer de l'hydrogène moléculaire gazeux, soit selon l'équation 5 (réaction de Heyrovsky) ou l'équation 6 (réaction de Tafel):



Les équations 5 et 6 sont des réactions secondaires qui ne contribuent pas à l'absorption de l'hydrogène. Dans le cadre des présents travaux, l'absorption électrochimique de l'hydrogène a été utilisée dans le but d'en étudier la solubilité. L'hydrogène absorbé a été quantifié par l'une de deux méthodes suivantes: *i*) désorption électrochimique où la charge de l'oxydation de l'hydrogène absorbé est mesurée ; *ii*) méthode électrochimique jumelée à la diffractométrie des rayons X *in situ* où les changements dans le paramètre de maille de l'électrode sont mesurés lorsque l'hydrogène est absorbé. Ensuite, des membranes ont été préparées et testées en présence d'hydrogène gazeux à haute pression. De cette façon, la perméabilité des membranes a peut être mesurée.

A1.3 Résultats

A1.3.1 Mesure de la solubilité de l'hydrogène dans les films minces de PdCuAu préparés par électrodéposition

Les alliages PdCuAu, sous la forme de films minces sur substrats de titane, ont été préparés par électrodéposition pulsée via l'électrolyse d'une solution contenant les précurseurs ioniques de chaque métal (Pd^{2+} , Cu^{2+} and Au^{3+}). Ces solutions aqueuses ont été préparées à partir des sels de nitrate de Pd ($\text{Pd}(\text{NO}_3)_2$) et de Cu ($\text{Cu}(\text{NO}_3)_2$), et de l'hydroxyde d'or ($\text{Au}(\text{OH})_3$). Cette procédure simple a permis la production des alliages ternaires PdCuAu avec une phase unique cubique centrée sur une gamme étendue de compositions. Les diagrammes de diffraction des rayons X sont présentés à la Fig. 2.

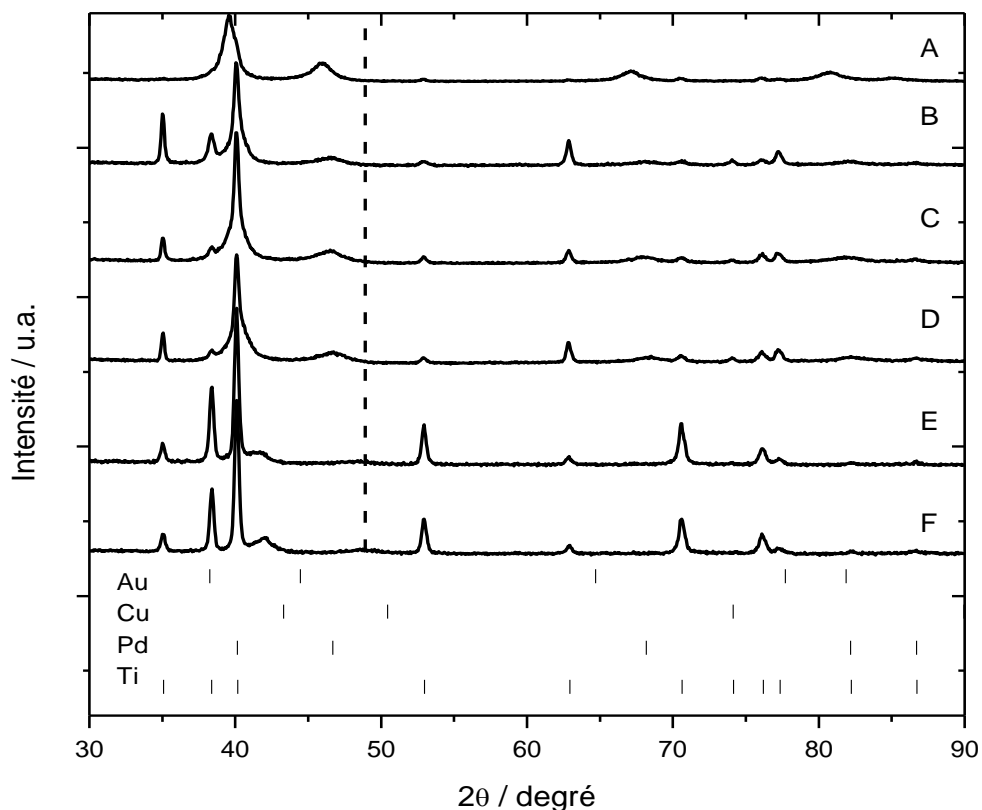


Figure 2 – Patrons de diffraction d’alliages PdCuAu électrodéposés sur substrats de titane. Six compositions différentes sont représentées et sont organisées en fonction de leur teneur en or, allant de la plus élevée (courbe A) à la plus faible (courbe F). Les compositions des alliages sont les suivantes: (A) $\text{Pd}_{50,4}\text{Cu}_{9,1}\text{Au}_{40,6}$; (B) $\text{Pd}_{43,5}\text{Cu}_{22,5}\text{Au}_{31}$; (C) $\text{Pd}_{47,9}\text{Cu}_{25,8}\text{Au}_{26,3}$; (D) $\text{Pd}_{63,3}\text{Cu}_{20,2}\text{Au}_{16,5}$; (E) $\text{Pd}_{38,2}\text{Cu}_{57,1}\text{Au}_{4,7}$; et (F) $\text{Pd}_{31,2}\text{Cu}_{67,8}\text{Au}_1$. La position des pics de chaque élément pur est affichée dans la partie inférieure à titre de référence.

L’analyse de la Fig. 2 montre que les patrons de diffraction (θ - 2θ) de tous les échantillons ont des pics de diffraction caractéristiques au substrat (Ti, structure hexagonale compacte, JCPDS no. 65-9622). Dans certains cas, une phase d’hydrure de titane (JCPDS no. 78-2216) a été identifiée, qui est fort probablement une conséquence du prétraitement acide des substrats. Mis à part ces pics, tous les échantillons présentent une série de pics de diffraction qui peuvent être indexés à une phase fcc. À titre de comparaison, les positions des pics de diffraction

caractéristiques des métaux purs Pd (JCPDS no. 65-8601), Cu (JCPDS no.85-1326) et Au (JCPDS no. 65-6174) sont données au bas de la figure. Aucun de ces pics n'est observé dans les diagrammes de XRD (sauf si les éléments purs ont été préparés intentionnellement). La position des pics de diffraction caractéristiques de la phase fcc varie en fonction de la composition des films, ce qui est attendu si une solution solide palladium-cuivre-or est formée. Par exemple, le pic (200) est décalé de $2\theta = 45,8^\circ$ (courbe A) à $2\theta = 48,9^\circ$ (courbe F) alors que la teneur en or est réduite de 40,6 à 1,0 %at. Par conséquent, le paramètre de maille de la phase fcc va aussi changer en fonction de la composition des alliages.

La morphologie des alliages tels que déposés a été observée par microscopie électronique à balayage (MEB). Les études d'Allemand *et coll.* [16] ont montré que la morphologie des films minces peut varier en fonction de leur composition, du temps de déposition et du potentiel appliqué. Dans la présente étude, les conditions de déposition ont été les mêmes pour tous les dépôts, à l'exception de la composition du bain électrolytique. Quelques exemples représentatifs des micrographies MEB sont présentés à la Fig. 3.

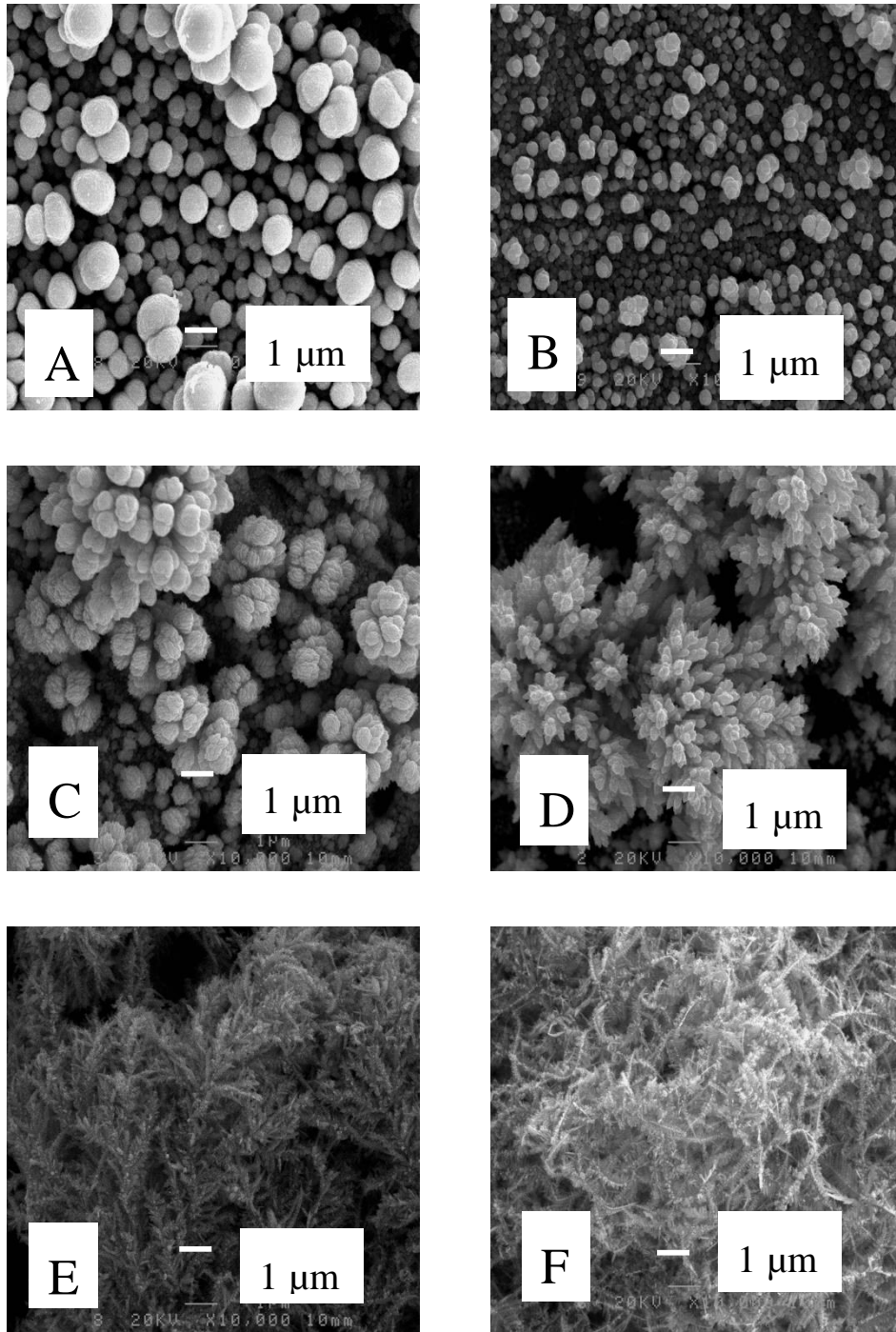


Figure 3 – Micrographies MEB de films minces PdCuAu arrangées en ordre croissant de leur contenu respectif en Pd : (A) $\text{Pd}_{14,3}\text{Cu}_{82,1}\text{Au}_{3,6}$; (B) $\text{Pd}_{38,2}\text{Cu}_{57,1}\text{Au}_{4,7}$; (C) $\text{Pd}_{56,2}\text{Cu}_{19,2}\text{Au}_{24,6}$; (D) $\text{Pd}_{66,1}\text{Cu}_{7,8}\text{Au}_{26,2}$; (E) $\text{Pd}_{74,3}\text{Cu}_{18,4}\text{Au}_{7,3}$; et (F) $\text{Pd}_{100,0}\text{Cu}_{0,0}\text{Au}_{0,0}$.

Il a été montré que la teneur en Pd est le principal paramètre qui influence la morphologie des films minces. Par conséquent, les micrographies MEB à la Fig. 3 sont présentées en fonction du teneur en Pd, soit 3A – Pd_{14,3}Cu_{82,1}Au_{3,6}; 3B – Pd_{38,2}Cu_{57,1}Au_{4,7}; 3C – Pd_{56,2}Cu_{19,2}Au_{24,6}; 3D – Pd_{66,1}Cu_{7,8}Au_{26,2}; 3E – Pd_{74,3}Cu_{18,4}Au_{7,3} et 3F – Pd_{100,0}Cu_{0,0}Au_{0,0}. A la plus faible teneur en Pd, les films sont constitués de petites sphères de moins de 1 µm de diamètre. En augmentant le contenu en Pd, les sphères s'agglomèrent ensemble (figure 3C). Pour des concentrations encore plus élevées, une morphologie en forme d'aiguilles est clairement observée (Fig. 3D et 3E). Le Pd pur a une structure en forme de spaghettis (Fig. 3F).

Dans ce travail, les effets de la composition de l'alliage sur la solubilité de l'hydrogène ont été étudiés. Un procédé électrochimique a été utilisé pour mesurer l'absorption d'hydrogène par l'alliage. En bref, l'absorption est promue à un potentiel significativement négatif, soit de -650 à -1400 mV (vs. Hg/HgO). Après avoir appliqué le potentiel de réduction pendant 3 minutes, le potentiel est porté à -400 mV pendant 3 minutes afin d'oxyder tout le H absorbé dans le film d'alliage de Pd. Le courant d'oxydation est ensuite intégré et cette charge est convertie en nombre de moles d'hydrogène absorbées (nH ou H). La solubilité de l'hydrogène (en pourcentage, H/M) est obtenue en divisant cette valeur par le nombre de moles d'alliage métallique (nM ou M) Lors de l'étape de désorption, aucun signe de l'oxydation du film PdCuAu n'a été détectée. La solubilité de l'hydrogène a été mesurée par rapport à la teneur des films en palladium et en variant celle-ci entre 45 et 100% at. Les résultats sont présentés à la Fig. 4

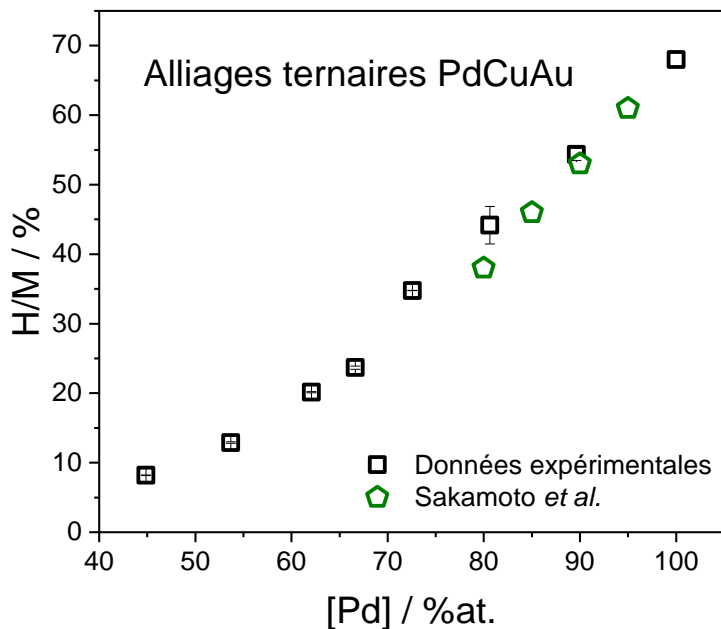


Figure 4 – Variation de la solubilité de l’hydrogène (H/M) en fonction de la teneur en palladium, pour les alliages PdCuAu. Tous les films ont une phase cubique à face centrée avec un paramètre de maille de $(3,885 \pm 0,005)$ Å. Les données tirées de la référence [8] sont également présentées pour des fins de comparaison.

Comme on le voit sur la Fig. 4, la solubilité de l’hydrogène augmente proportionnellement avec le contenu de Pd, de 8,2% pour $[Pd] = 45$ % at. à 68,0% pour $[Pd] = 100$ % at.. À titre de comparaison, les résultats obtenus par Sakamoto *et coll.* [8] à partir de mesures en phase gazeuse à 30 °C sont également indiqués. Dans la gamme où une comparaison est possible ($[Pd] \geq 80\%$ at.), les deux séries de résultats sont identiques, en considérant l’erreur expérimentale. La Fig. 4 montre que la solubilité de l’hydrogène dépend de la concentration en Pd et augmente lorsque la teneur en Pd augmente. Les paramètres de maille des échantillons à la Fig. 4 sont presque les mêmes, soit $(3,885 \pm 0,015)$ Å, ce qui est très proche du paramètre de maille du palladium pur ($3,88674$ Å). Cette affirmation vaut aussi pour les données tirées du travail de Sakamoto *et coll.* [8]. Par conséquent, il est clair que la concentration en palladium est le facteur clé dans la détermination de la solubilité de l’hydrogène pour ce type d’alliage. L’insertion des atomes de Cu dans la structure métallique tend à diminuer le paramètre de maille, tandis que celle des atomes d’or a l’effet inverse.

Afin de différencier les effets du cuivre de ceux de l'or, des mesures de solubilité de l'hydrogène ont été effectuées en maintenant la concentration de palladium constante et en modifiant les quantités relatives de Cu/Au. Les résultats sont résumés à la Fig. 5.

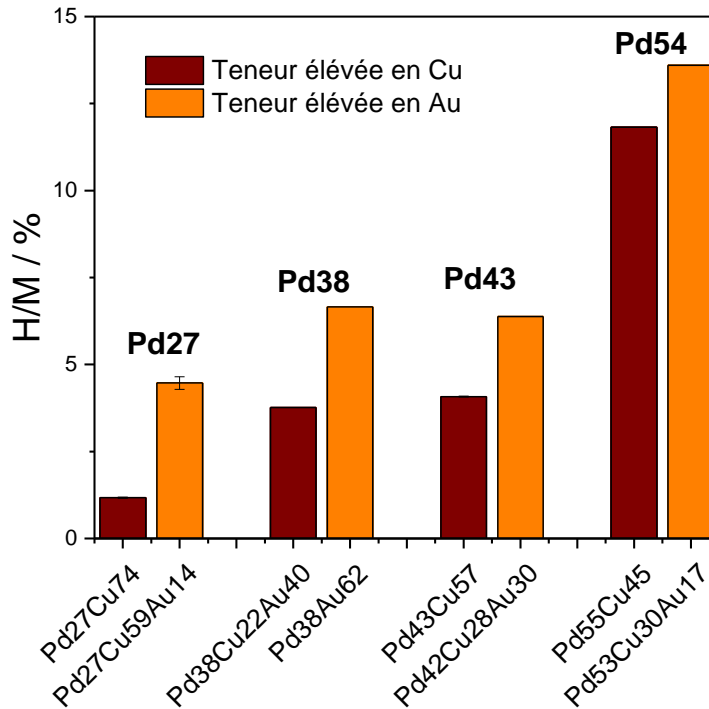


Figure 5 – Effet du cuivre et de l'or sur la solubilité de l'hydrogène dans les alliages PdCuAu ayant une teneur en palladium constante.

On montre à la Fig. 5 que pour une même teneur en palladium, par exemple 27 %at., la solubilité de l'hydrogène augmente de 1,17 à 4,5% lorsque la teneur en or est augmentée de 0 à 14 %at. Des tendances similaires sont observées pour les échantillons avec [Pd] = 38, 43 et 54 %at. Donc, pour un même contenu en palladium, une augmentation de la solubilité de l'hydrogène dans l'alliage est observée lorsqu'un certain nombre d'atomes de cuivre sont remplacés par des atomes d'or. La précédente observation est en accord avec les calculs théoriques de la perméation de l'hydrogène dans des alliages ternaires à base de PdCu [11]. L'augmentation de la solubilité de l'hydrogène dans Pd-Cu-Au a été décrite comme le résultat de l'interaction de répulsion de paires Cu-H et l'interaction attractive de paires Au-H [8], associée à l'augmentation du paramètre de maille qui résulte du remplacement des atomes de Cu par des atomes d' Au. Par exemple, pour [Pd] = 27 %at., le paramètre de maille de l'alliage fcc augmente de 3,68 à 3,82 Å lorsque la teneur en

or augmente de 0 à 14,1 %at.. La même tendance est observée pour tous les exemples représentés à la Fig. 5. Cela se produit parce que le rayon atomique de l'or (2.884 Å) est beaucoup plus large que celui du cuivre (2.556 Å).

A1.3.2 Mesures de solubilité de l'hydrogène dans films minces de PdCuAu préparés par pulvérisation cathodique magnétron

Des couches minces de PdCuAu ont été préparées par pulvérisation cathodique et caractérisées. Le dépôt des films minces a été effectué sur des substrats de titane en pulvérisant simultanément les trois cibles (Pd, Cu et Au) pendant 3 minutes. Les substrats ont été mis en rotation à 10 tours par minute (rpm) pour la durée du processus de dépôt. Les échantillons ainsi préparés ont été utilisés pour évaluer l'impact de la composition métallique et d'un recuit thermique sur la solubilité de l'hydrogène. Dans cet esprit, deux techniques différentes pour la mesure de la solubilité de H ont été utilisées : *i*) une méthode électrochimique pour les échantillons dont la composition de Pd est supérieure à 45 %at., et *ii*) un procédé électrochimique jumelée à la diffractométrie des rayons X *in situ* pour des échantillons avec une teneur en palladium inférieur à 45 % at. Tous les échantillons ainsi déposés ont une structure fcc. La distribution de chaque métal dans les films préparés a été mesurée par spectroscopie de perte d'énergie (EELS de l'anglais *electron energy loss spectroscopy*) sur une section transversale du film perpendiculaire au substrat. Les signaux relatifs au Pd, Cu et Au sont présentés à la Fig. 6 pour l'alliage de composition Pd_{50,8}Cu_{46,0}Au_{3,2}.

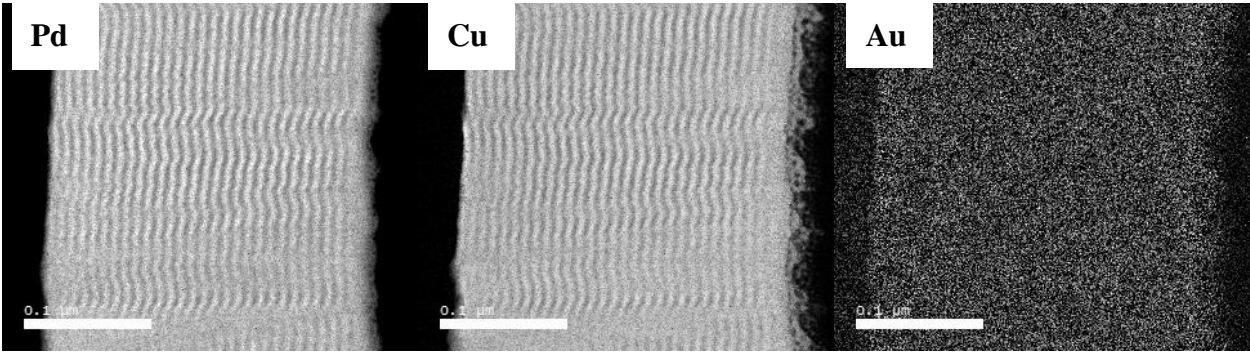


Figure 6 – Cartes élémentaires de Pd M45-edge, Cu L23-edge and Au M45-edge mesurées par spectroscopie de perte d'énergie. Une section transversale du film perpendiculaire au substrat est montrée pour l'alliage de composition $\text{Pd}_{50,8}\text{Cu}_{46,0}\text{Au}_{3,2}$. Les signaux relatifs sont présentés ici.

Comme on le voit à la Fig. 6, les cartes élémentaires de Pd et Cu montrent une structure en couches alors que l'or a une distribution homogène sur l'entièreté du film. Il est estimé que les couches les plus sombres ont environ 5% de plus de palladium ou de cuivre que les couches plus claires. L'oscillation dans le contenu en palladium et en cuivre est une conséquence de la rotation des substrats. En effet, comme les substrats sont en rotation au-dessus des cibles métalliques, ils seront parfois plus près de la cible de palladium et plus éloignés de la cible de cuivre, ou vice-versa. Comme les substrats tournent à 10 rpm, les substrats font 30 tours complets au cours du dépôt et, par conséquent, ils se rapprochent 30 fois de la cible de palladium (ou du cuivre) et s'en éloignent 30 fois. Ainsi, 30 couches enrichies en l'un des éléments sont intercalées avec 30 autres couches appauvries en ce même élément. Étonnamment, 27 couches de chaque peuvent être facilement distinguées, ce qui confirme que la rotation est bien la cause de cet effet de superposition. Le profil oscillant de la composition dans des échantillons préparés par dépôt par pulvérisation a déjà été décrit dans la littérature [17, 18]. Si la position des substrats demeurait fixe par rapport aux cibles, la composition serait homogène sur toute l'épaisseur des films, mais malheureusement la composition varierait selon la position à la surface de l'échantillon. En effet, Coulter et ses collaborateurs [12] ont montré qu'en absence de rotation la composition de surface peut varier jusqu'à 6 % at.. Aucune oscillation dans le profil de l'or n'a été observée, probablement en raison de sa teneur plus faible (3,2 % at.), ce qui nuit à la précision de la mesure. Dans le présent travail, nous nous sommes intéressés à mesurer la solubilité de l'hydrogène dans les films. Dans une première approche, il est important d'avoir une composition homogène en surface, car la

couche la plus externe du film est la première qui interagit avec l'hydrogène. Pour cette raison, tous les échantillons ont été préparés en utilisant la rotation, indépendamment du fait que cette procédure résulte dans une structure en couches. Comme le recuit favorise un mélange de ces différentes couches [17], l'impact du traitement à température élevée sur la solubilité de l'hydrogène a également été évalué.

Les alliages ternaires PdCuAu ont été recuits à 400 °C sous atmosphère d'argon pendant des périodes de 4, 8 ou 48 heures. Selon leur composition, une transition de phase fcc à bcc peut se produire. Cette transition est illustrée à la Fig. 7 pour un alliage de composition Pd_{32,2}Cu_{63,3}Au_{4,5} qui a été recuit pendant 4 heures.

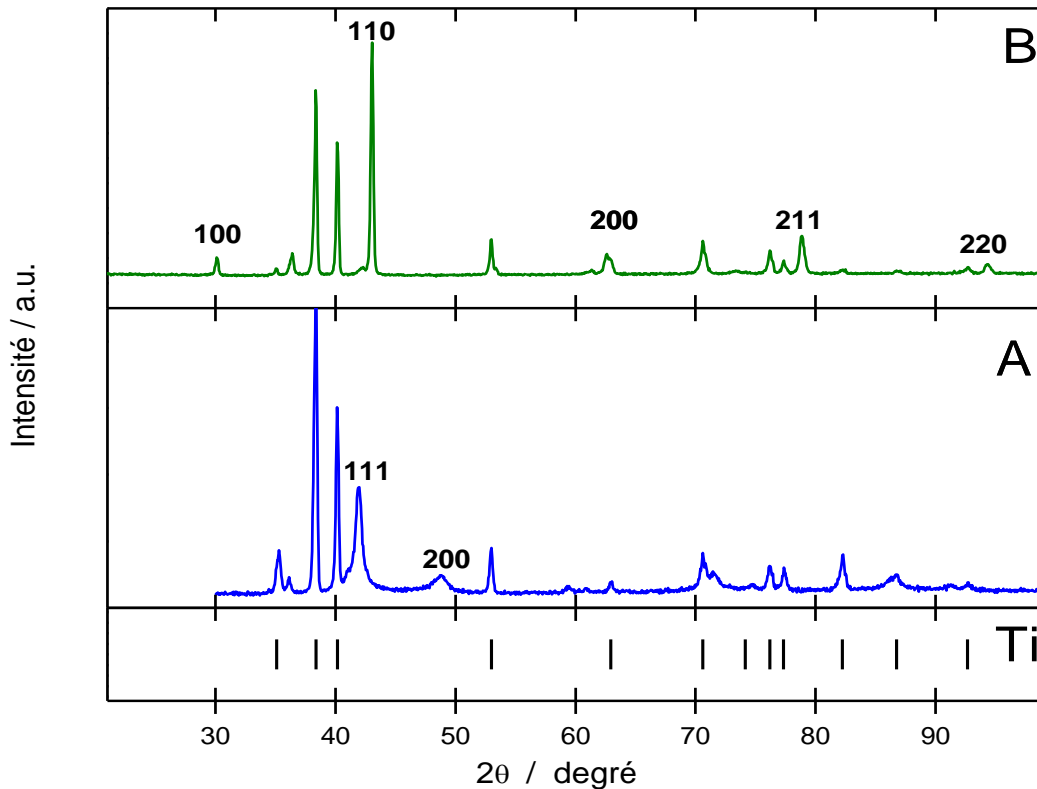


Figure 7 – Patrons de diffraction des rayons X d’alliage ternaire Pd_{32,2}Cu_{63,3}Au_{4,5} avant (A) et après (B) être recuit à 400°C sous l’argon pendant 4 heures. Avant le recuit, l’échantillon montre des pics caractéristiques de la phase fcc, tandis qu’après le recuit une seule phase bcc est observée.

Comme on peut voir à la Fig. 7, un traitement thermique de 4 heures est suffisant pour induire la transition complète de la phase fcc à la phase bcc (de type CsCl). En effet, les pics caractéristiques de la phase fcc, présents à $2\theta = 41,9$ (111) $48,7$ (200) $71,5$ (220) $86,6$ (311) et $91,2^\circ$ (222), sont remplacés par les pics caractéristiques de la phase bcc, ceux-ci à $2\theta = 30,1$ (100) $43,0$ (110) $78,9$ (211) et $94,3^\circ$ (220). Les pics du substrat de titane sont également visibles dans les deux diffractogrammes. Le pic supplémentaire à $36,1$ et $36,3^\circ$ aux figures 7A et B, respectivement, pourrait être attribuable à l'oxyde de titane (JCPDS pas. 72-4593). Dans les films déposés par pulvérisation, la transition de phase fcc à bcc a été observée dans les alliages avec une teneur en palladium entre $30,1$ et $43,9$ %at. ($49,9 \leq \text{Cu} \leq 65,7$ et $3,5 \leq \text{Au} \leq 6,1$ %at.). En dehors de cette gamme de compositions, les échantillons sont demeurés en phase fcc, mais avec des tailles de cristallites plus élevées. En outre, plus le temps de traitement thermique est augmenté, plus grosses sont les cristallites. En effet, lorsque l'alliage $\text{Pd}_{67,3}\text{Cu}_{29,1}\text{Au}_{3,7}$ est recuit pendant 0, 4, 8 et 48 heures, les tailles de cristallite sont respectivement 219, 325, 331 et 1225 Å. Le recuit favorise aussi la ségrégation métallique en surface. En général, le recuit sous atmosphère d'argon a entraîné une ségrégation du cuivre à la surface tandis que le recuit sous H_2 conduit à la migration du palladium à la surface. (Dans ce contexte, la surface est définie comme la région superficielle des films sondée par spectroscopie des photoélectrons induits par rayon-X (XPS de l'anglais *X-ray photoelectron spectroscopy*), c'est-à-dire les premières ~ 7 couches atomiques.

La solubilité de l'hydrogène des alliages PdCuAu, avant et après recuit, est présentée à la Fig.8.

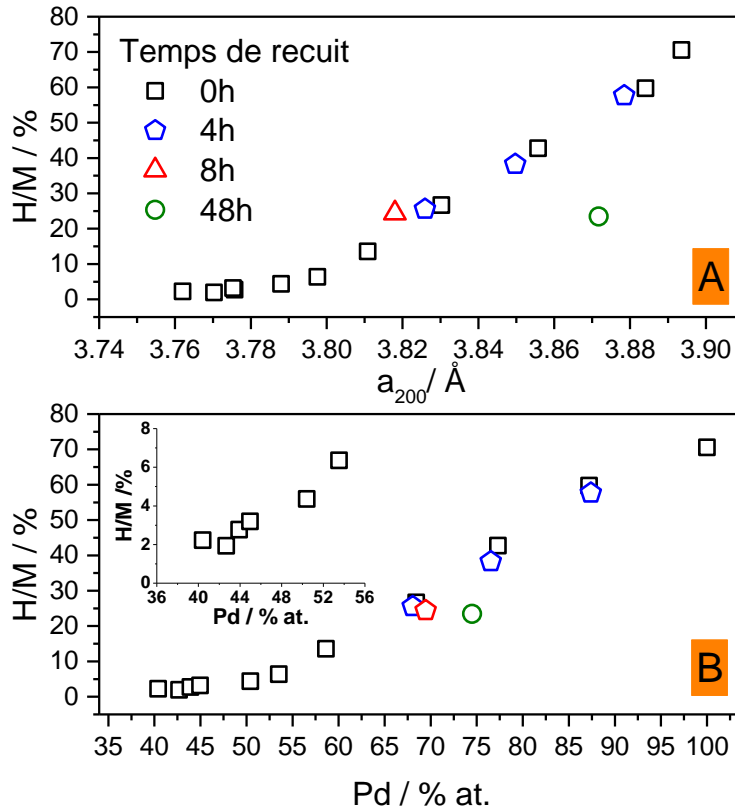


Figure 8 – Solubilité de l’hydrogène dans la phase fcc en fonction du paramètre de maille (A) et de la concentration en palladium (B). Les résultats sont pour des échantillons avant et après recuit à 400°C sous argon et pendant plusieurs périodes de temps.

Tous les alliages qui sont présentés à la Fig. 8 ont une structure cristallographique fcc. L'augmentation de la teneur en palladium (ou du paramètre de maille) entraîne une augmentation de la solubilité de l'hydrogène. Ceci est similaire à ce qui a été observé à la Fig. 4 pour les échantillons préparés par électrodeposition. Les échantillons qui ont été recuits montrent une solubilité de l'hydrogène qui est différente. Par exemple, l’alliage de composition $\text{Pd}_{67,3}\text{Cu}_{29,1}\text{Au}_{3,7}$ a une solubilité de 26,7, 25,5, 24,4 et 23,5% lorsque les échantillons sont recuits pendant 0, 4, 8 et 48 heures, respectivement. En même temps, la taille des cristallites augmente avec le recuit, passant de 219, 325, 331 et 1225 Å après 0, 4, 8 et 48 heures de recuit. La solubilité de l’hydrogène dans le film diminue donc avec l’augmentation de la taille des cristallites. Ceci peut-être parce qu’il y a moins de joints de grains où l’hydrogène pourrait également être dissout. Ces résultats sont en

accord avec ceux d'Adams *et coll.*[19] qui ont étudié la sorption de l'hydrogène dans les nanostructures PdCd.

La solubilité de l'hydrogène dans la phase bcc a également été étudiée, mais cette fois en utilisant un procédé électrochimique jumelé à la diffractométrie des rayons X *in situ*. Cette méthode consiste en trois étapes différentes. Tout d'abord, un premier diffractogramme de l'échantillon est prélevé. Ensuite, l'absorption d'hydrogène est favorisée via l'application d'un potentiel suffisamment négatif (-600 mV par rapport à l'électrode de référence d'hydrure de palladium). À ce moment, un nouveau diffractogramme est enregistré. Finalement, l'hydrogène est désorbé en appliquant un potentiel de +300 mV vs. hydrure de palladium tout en enregistrant un nouveau diffractogramme. Lorsque l'hydrogène est absorbé par le palladium, le volume de la maille cristalline augmente. La mesure de la dilatation en volume de la maille cristalline permet de connaître la quantité d'hydrogène dissout dans l'alliage. Les valeurs de solubilité qui ont été calculées sont présentées à la Fig. 9.

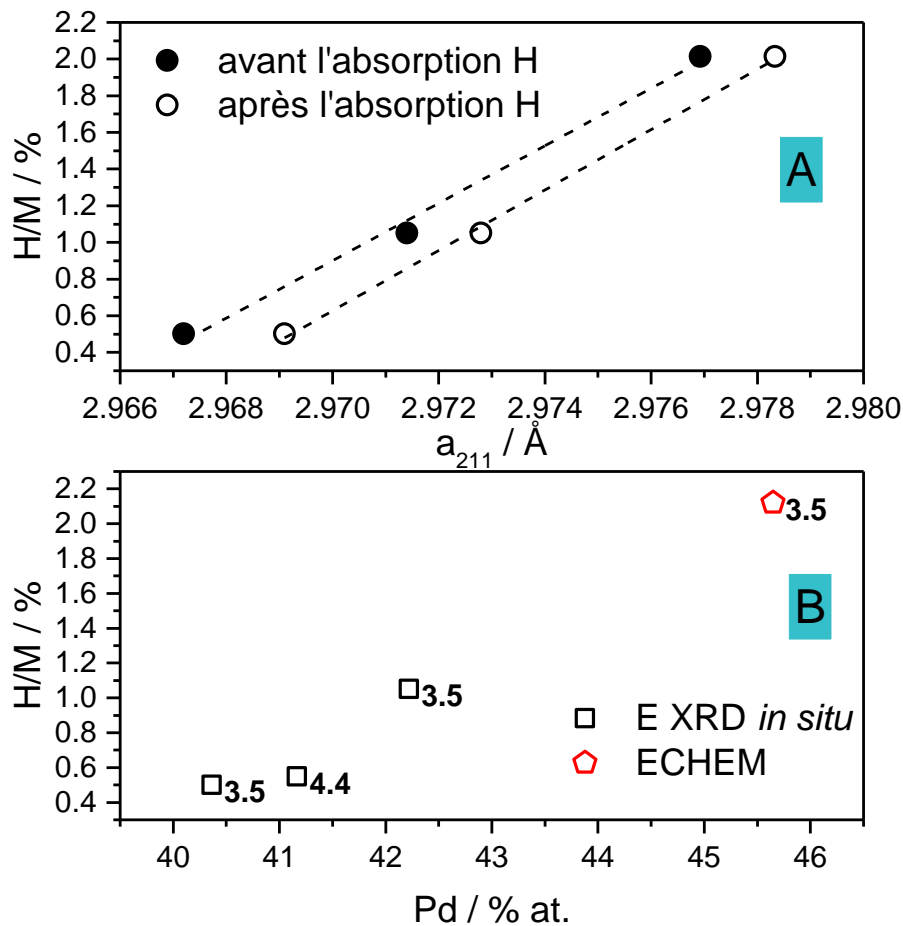


Figure 9 – Solubilité de l'hydrogène dans les alliages avec la phase bcc en fonction du paramètre de maille (A) et de la teneur en palladium (B). La concentration en Au des échantillons est indiquée sur le graphique.

À la Fig. 9A, la solubilité de l'hydrogène est tracée en fonction du paramètre de maille (mesurée avant et après les mesures de solubilité), alors que la Fig. 9B montre la solubilité de l'hydrogène en fonction de la teneur en palladium. De la même manière qu'avec la phase cubique à face centrée, la solubilité de l'hydrogène augmente proportionnellement avec la teneur en palladium. L'effet de l'or ne peut pas être évalué de manière exhaustive, car seulement un échantillon avec une teneur différente en or a été préparé, mais la solubilité de l'hydrogène dans l'échantillon contenant 4.4 %at. d'or ne semble pas supérieure à celle des échantillons contenant 3.5 %at. d'or. Les échantillons avec la même teneur en or (3,5 at.%) ont été représentés sur la Fig. 9A en fonction du paramètre de maille. Non seulement la relation entre la solubilité de l'hydrogène

et le paramètre de maille est linéaire, mais l'amplitude de l'augmentation du paramètre de maille est semblable pour les trois échantillons (en moyenne 0,06%). Il semble que l'absorption de l'hydrogène provoque une déformation plastique sur les films d'alliage. Toutefois, cela pourrait être une conséquence indirecte de l'absorption d'hydrogène. En effet, un hydrure de titane est également formé lors de l'application du potentiel négatif. L'hydrure de titane a un volume de maille qui est supérieur à celle du titane métallique. Cela pourrait expliquer pourquoi les films d'alliage ne reviennent pas à leur paramètre de maille initiale d'avant l'absorption de H : parce que l'expansion de la maille cristalline des films est également accompagnée d'une expansion de maille du substrat.

À la Fig. 10, une comparaison est faite entre la solubilité de l'hydrogène de la phase bcc et celle de la phase fcc en fonction de la teneur en palladium.

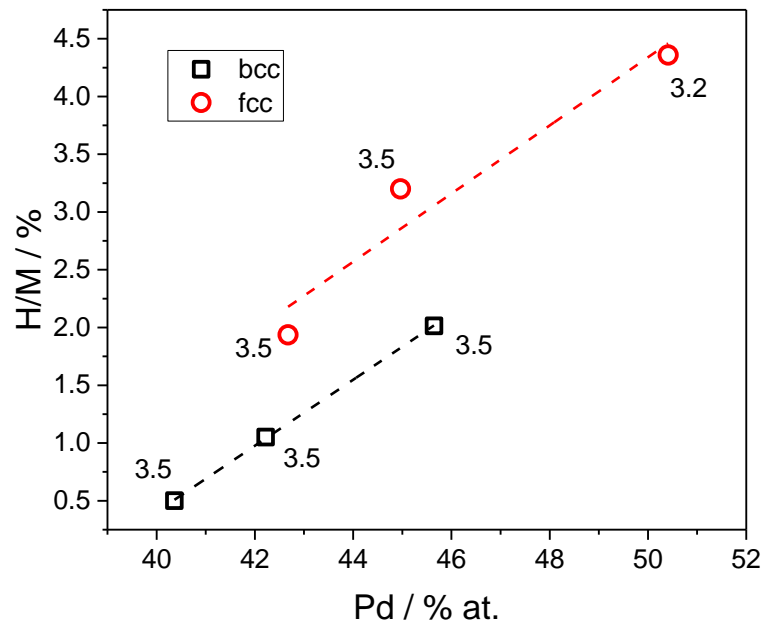


Figure 10 – Comparaison de la solubilité de l'hydrogène entre la phase bcc et la phase fcc en fonction de la teneur en palladium des alliages. Les droites pointillées représentent la meilleure régression linéaire pour chaque ensemble de données. Les valeurs à côté des points représentent la teneur en or des alliages.

Comme on le voit à la Fig. 10, les résultats pour les phases fcc et bcc montrent que la solubilité de l'hydrogène varie de façon linéaire avec la teneur en palladium, pour des alliages avec approximativement la même concentration en or. Les droites pointillées représentent des régressions linéaires. Les pentes calculées sont respectivement 0,295 et 0,286 pour les phases bcc et fcc. Cela signifie que l'augmentation de la teneur en Pd de la phase fcc a exactement le même effet sur la solubilité de H que l'augmentation de la teneur en Pd de la phase bcc. Cela correspond au comportement attendu, en première approximation, si la teneur en Pd est le principal facteur déterminant de la solubilité de H.

A1.3.3 Mesures de perméabilité de l'hydrogène dans les membranes de PdCuAu

Le broyage mécanique de haute énergie a été utilisé pour la préparation d'alliages ternaires PdCuAu à partir de poudres de Pd, Cu et Au pur. NaCl a été ajouté en tant qu'agent de contrôle du processus et éviter un soudage excessif. Les poudres ont été broyées ensemble pendant 18 heures à l'intérieur de récipients en acier inoxydable remplis d'argon. Des billes en acier inoxydable ont été utilisées en tant qu'agents de broyage. Un rapport massique billes-poudre 2:1 a été utilisé. Quatre compositions différentes ont été préparées, toutes avec la même teneur de palladium (40 %at.) et avec des quantités croissantes d'or (0, 3, 7 et 11 %at.). La teneur en cuivre a été ajustée en conséquence. Tous les échantillons préparés dans ces conditions ont une structure fcc. La structure bcc est obtenue suite à un recuit des échantillons fcc. Les poudres bcc ont été consolidées sous la forme de pastilles, de façon à les utiliser comme membranes pour des expériences de séparation de l'hydrogène. La méthode de fabrication des pastilles consiste en 7 étapes, représentées schématiquement à la Fig. 11.



Figure 11 – Méthode pour la préparation de membranes PdCuAu à partir de poudre de PdCuAu issue de broyage mécanique.

Les étapes 1, 3 et 4 de la Fig. 11 sont communes à la méthode mise au point par Tsai et collaborateurs pour la préparation d'une membrane de cermet avec du palladium et $\text{BaCe}_{0.4}\text{Zr}_{0.4}\text{Gd}_{0.1}\text{Dy}_{0.1}\text{O}_{3-x}$ [20]. Une différence importante entre les deux méthodes est que dans leur cas, le broyage mécanique a été utilisé seulement comme un moyen de mélanger les deux poudres, alors que dans le présent travail, il a été utilisé comme moyen de produire l'alliage ternaire. Les deux premières étapes correspondent à la préparation des poudres PdCuAu de phase bcc. En bref, les poudres de Pd, Cu, Au plus NaCl sont broyées ensemble pour former les alliages fcc (étape 1). En fonction de la composition de départ des alliages, une transition partielle ou complète à la phase bcc est survenue lorsqu'un traitement thermique est appliqué (étape 2). Les étapes un et deux sont naturellement omises lors de la préparation d'une membrane de Pd pur à partir de poudre de palladium disponible commercialement. Après le premier recuit (étape 2), les poudres sont pressées en disques de 1,1 cm de diamètre (étape 3). A ce stade, les pastilles sont assez fragiles et aucune caractérisation n'a été tentée. Après une heure de frittage à 900 °C sous argon 5% H_2 , les pastilles gagnent en cohésion et peuvent se plier facilement sans se briser. Après le frittage, les pastilles sont laminées à froid afin d'homogénéiser et de réduire leur épaisseur. L'épaisseur finale de la membrane après le laminage à froid varie de membrane en membrane et ne dépend pas uniquement de la quantité de poudre qui est utilisée, mais également du nombre de fois que la membrane a été pressée entre les rouleaux. Néanmoins, le laminage à froid réduit l'épaisseur en moyenne de 30%. Lorsque l'épaisseur est réduite, le diamètre de la membrane est augmenté de 1,1 cm à une moyenne finale de 1,2 cm. Après le laminage à froid, les membranes

sont recuites une dernière fois (étape 6) et sont finalement polies (étape 7). La dernière étape supprime les imperfections à la surface.

La perméabilité des membranes PdCuAu a été mesurée en phase gazeuse. Pour ce faire, les membranes ont été pressurisées sous 30, 45 et 60 psig de H₂ pendant 30, 15 et 15 minutes, respectivement, à 464 °C. Dans ces conditions, le flux d'hydrogène a été enregistré et, en utilisant l'équation 1, la perméabilité à l'hydrogène des membranes a été calculée. Les résultats sont présentés à la Fig. 12.

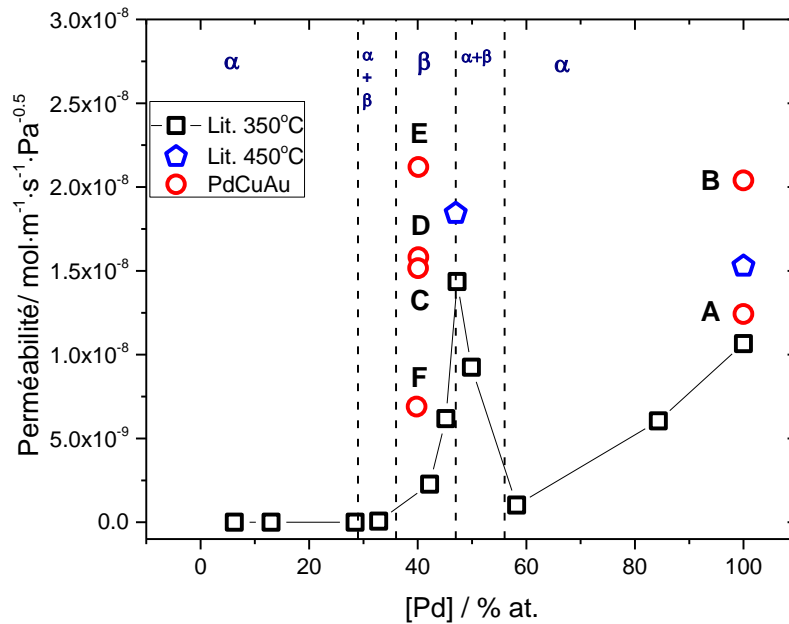


Figure 12 – Perméabilité de membranes PdCuAu préparés à partir de poudres PdCuAu provenant du broyage mécanique. Pour des fins de comparaison, les valeurs de perméabilité pour les alliages PdCu (feuilles de 25,4 μm) extraites de la littérature [21] sont également représentées, avec l'indication de leur phase cristallographique correspondante (α - la phase fcc; β - la phase bcc) [22]. A – Pd commercial (feuille de 250 μm), B – membrane de Pd préparée à partir de poudre de Pd commerciale (250 μm), C – Pd₄₀Cu₆₀Au₀ (327 μm), D – Pd₄₀Cu₅₇Au₃ (300 μm), E – Pd₄₀Cu₅₃Au₇ (277 μm); F – Pd₄₀Cu₄₉Au₁₁ (304 μm).

Comme on peut le voir à la Fig. 12, tous les alliages PdCuAu ont une perméabilité à l'hydrogène plus élevée que les alliages PdCu utilisés par McKinley [21]. La différence pourrait être le résultat de quatre effets: 1) la température, 2) la sélectivité de la membrane, 3) le procédé de fabrication ou 4) la composition (la présence d'or). De toutes ces possibilités, l'effet de l'or est le plus important. Des concentrations très élevées d'or, à savoir 11 %at. (membrane F), semblent être nuisible à la perméabilité, alors qu'à 7 %at. d' Au (membrane E), la perméabilité est maximale. Dans l'ensemble, la présence de l'or augmente la perméabilité par rapport aux alliages PdCu, mais une concentration trop élevée d'or devient néfaste.

La présence de H₂S dans un mélange de gaz est reconnue pour réduire la perméabilité du Pd [5, 10, 23, 24] et des membranes de PdCu bcc [5, 24, 25]. L'impact de H₂S sur la perméabilité de la membrane E (Pd₄₀Cu₅₃Au₇) – la membrane dont la perméabilité est la plus élevée (Fig.11) – a été étudiée. Malheureusement, après avoir été utilisée dans la série d'expériences décrite précédemment, la membrane E a développé des fuites (0,26 ml/min He à 60 psig) et ainsi une nouvelle membrane de même composition a été préparée (membrane E-2 Pd₃₉Cu₅₄Au₇). A titre de référence, une feuille de Pd de 250 µm d'épaisseur a également été utilisée. Les membranes ont été soumises à une pression de 30 psig de H₂ pur pour 30 ou 60 minutes. Par la suite, un mélange de H₂-6% He avec 941 ppm de H₂S à 30 psig de pression totale a été introduit dans la chambre de perméation pour une période de 30 minutes. . Le contenu du perméat a été analysé par chromatographie en phase gazeuse avant de revenir à 30 psig de H₂ pendant 30 minutes de plus. L'évolution du débit en fonction du temps est représentée à la Fig. 6.13.

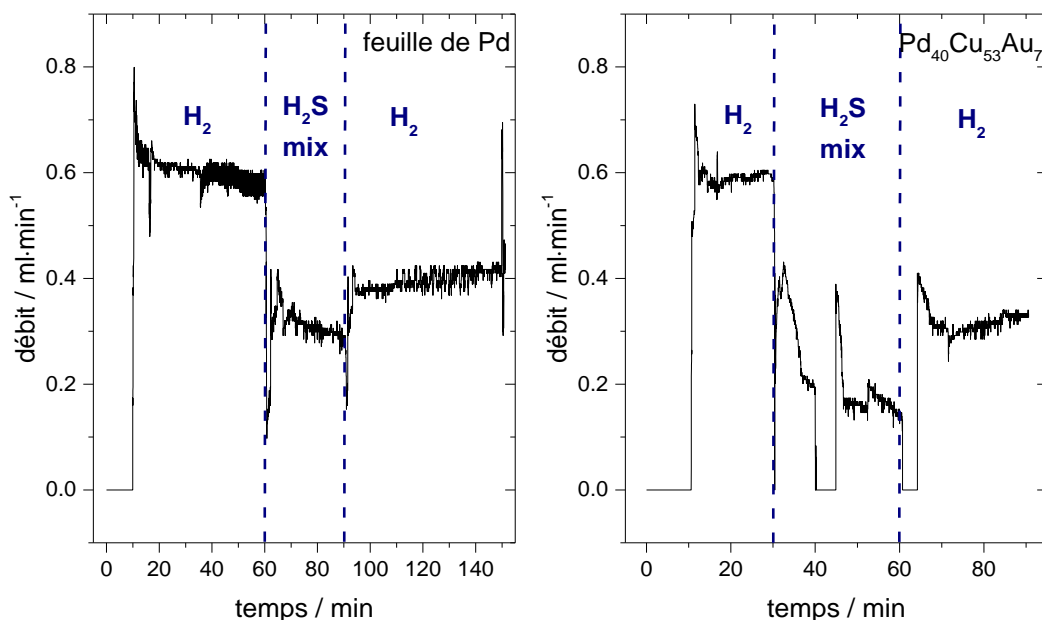


Figure 13 – Variation avec le temps du débit d’hydrogène lorsque les membranes sont exposées à H₂ pur ou à un mélange de H₂ avec 941 ppm de H₂S. Deux membranes différentes ont été analysées: Pd commercial (feuille de 250 µm, panneau de gauche) et membrane E-2 Pd₃₉Cu₅₄Au₇ (panneau de droite). Les mesures ont été effectuées à 464°C.

Comme le montre la Fig. 13, le débit d’hydrogène diminue lors de l’introduction du H₂S, et retourne vers sa valeur initiale, mais pas entièrement, lors du passage de nouveau à H₂ pur. Ceci est vrai pour les deux membranes. Au cours de la première étape de l’expérience, quand seulement H₂ pur est utilisé, les deux membranes Pd et E-2 exhibent les valeurs de perméabilité respectives de $8,8 \times 10^{-9}$ et $9,7 \times 10^{-9} \text{ mol} \cdot \text{m}^{-1} \cdot \text{s}^{-1} \cdot \text{Pa}^{-0.5}$. Ces valeurs sont légèrement inférieures à celles présentées à la Fig.12. La différence peut résulter du fait que ces calculs ont été effectués seulement à une pression (30 psig), alors qu’auparavant des pressions différentes ont plutôt été utilisées. Lors de l’introduction du mélange H₂S, la perméabilité du Pd est réduite de 50%. Dans le cas de la membrane E-2, et après 10 minutes d’exposition à H₂S, la perméabilité est égale à zéro pendant environ 5 minutes et augmente ensuite pour se stabiliser à $2,5 \times 10^{-9} \text{ mol} \cdot \text{m}^{-1} \cdot \text{s}^{-1} \cdot \text{Pa}^{-0.5}$. Le fait que la perméabilité tombe à zéro est une question importante et sera discuté plus tard. Lors du retour à H₂ pur, les perméabilités du Pd et de la membrane E-2 sont respectivement 6.1×10^{-9} et 5.6×10^{-9}

$\text{mol}\cdot\text{m}^{-1}\cdot\text{s}^{-1}\cdot\text{Pa}^{-0.5}$. Ces perméabilités en présence de H_2S correspondent à 69% et 58% de leurs valeurs initiales, pour le Pd et la membrane E-2, respectivement. Dans la littérature, la perte de perméabilité du palladium en présence de H_2S peut atteindre jusqu'à 90% des valeurs pré- H_2S lorsque les membranes sont en contact avec 1000 ppm de H_2S à 350 °C pendant 3 h [24]. La diminution de 50% observée dans le cours du présent travail est probablement le résultat de la température plus élevée (464°C), la réduction du temps d'incubation (30 minutes) et de la teneur inférieure en H_2S (941 vs. 1000 ppm). Dans une expérience séparée, une autre membrane de Pd a été testée sous 941 ppm de H_2S pendant 3 heures à 450 °C. Ensuite, la température a été abaissée et maintenue à 350 °C pendant encore 3 heures, tout en gardant la membrane sous le mélange de H_2 et H_2S . Dans ces conditions, la perméabilité était à 54% (450°C) et 78% (350°C) des valeurs initiales avant le test avec H_2S . La température et la concentration de H_2S sont en effet des facteurs déterminants qui contribuent à l'empoisonnement.

Après 10 minutes de contact avec le mélange H_2 - H_2S , la membrane E-2 présente un débit nul. Ce comportement est similaire à ce qui a été décrit par O'Brien et ses collaborateurs [24] pour un alliage $\text{Pd}_{47}\text{Cu}_{53}$. Dans leur cas, aucun débit n'a été enregistré après 5 minutes de traitement sous 1000 ppm de H_2S à 350°C. Cela signifie que ces deux membranes, E-2 et $\text{Pd}_{47}\text{Cu}_{53}$, ont été empoisonnées par le mélange de gaz sulfureux à un point tel qu'aucun gaz ne peut les traverser. Malheureusement, cela mène à conclure que le remplacement du Cu par Au n'a pas empêché l'empoisonnement de la membrane bcc. Cinq minutes plus tard durant l'expérience, il y a une augmentation soudaine du débit d'hydrogène, en dépit de la présence du mélange de gaz H_2S . Le développement de défauts pourrait justifier cette récupération du débit. En effet, des mesures de chromatographie en phase gazeuse faites à la fin du test avec H_2S ont révélé la présence de 2% de He, ce qui indique que des pores ont été formés (le mélange de gaz utilisé est composé de H_2 -6% He avec 941 ppm de H_2S , telle que mentionnée ultérieurement). En résumé, tout indique que la membrane a développé des pores pendant le test, sinon le débit serait resté à zéro pendant le temps que la membrane était en contact avec le H_2S .

Des mesures de XRD, EDX et XPS ont montré que la membrane de palladium pur réagit avec H_2S pour produire Pd_4S . Ceci est en accord avec ce qui est décrit dans la littérature [24, 26-28]. Le Pd_4S agit comme une barrière à la perméabilité de l'hydrogène. En effet, la perméabilité

du Pd₄S vis-à-vis de H₂ est $9 \times 10^{-10} \text{ mol} \cdot \text{m}^{-1} \cdot \text{s}^{-1} \cdot \text{Pa}^{-0.5}$ [29] à 450°C, c'est-à-dire d'environ deux ordres de grandeur inférieure à celle du Pd pur. Il n'est donc pas surprenant que le débit de H₂ diminue lorsque les composés de soufre sont présents dans le flux de gaz d'alimentation. La perméabilité calculée, dans le cadre de ce travail, de la membrane de Pd lorsqu'il est en contact avec H₂S ($4.5 \times 10^{-9} \text{ mol} \cdot \text{m}^{-1} \cdot \text{s}^{-1} \cdot \text{Pa}^{-0.5}$) est plus élevée que la perméabilité du Pd₄S, indiquant que la surface de la membrane n'est pas entièrement recouverte par le composé sulfureux. Dans le cas de la membrane E-2 plusieurs composés ont été formés, y compris: Na₂S, Na₂S₂O₃, Na₂SO₃, CuS, CuSO₄ et CuO. (Ces deux derniers sont probablement formés par la décomposition du CuO dans l'air).

A1.4 Conclusions et perspectives

Des alliages ternaires de palladium-cuivre-or ont été préparés sur une gamme étendue de compositions à partir de trois méthodes de synthèse différentes, à savoir, l'électrodéposition (section A1.3.1), la pulvérisation cathodique (section A1.3.2) et le broyage mécanique (section A1.3.3). Dans les trois procédés, les limites de solubilité de la phase fcc ont été étendues à température ambiante. La phase bcc se forme uniquement après un traitement thermique et dépendamment de la composition de la membrane. Ceci est probablement une conséquence de la faible variation d'enthalpie entre la phase bcc ordonnée et la phase fcc désordonnée [30]. La maille cristalline des alliages PdCuAu est déformée en raison des différentes tailles des atomes. Cela explique l'écart positif observé lorsque les paramètres de maille expérimentaux sont comparés à ceux calculés à l'aide de la loi de Vegard [31]. Les morphologies des échantillons électrodéposés dépendent de la teneur en palladium, allant de structures plus sphériques aux faibles concentrations de Pd (par exemple Pd_{14,3}Cu_{8,1}Au_{3,6}), à diverses structures en forme d'aiguilles aux teneurs plus élevée en Pd (par exemple Pd_{74,3}Cu_{18,4}Au_{7,3}). Cela pourrait être dû à la co-déposition de l'hydrogène qui est favorisée à des concentrations plus élevées de palladium.

L'analyse par EELS de la section transversale des films préparés par pulvérisation cathodique révèle une structure en couches périodiques, une conséquence du fait que les substrats sont en rotation lorsqu'on utilise les trois cibles métalliques – le palladium, le cuivre et l'or – en même temps. Le recuit peut toutefois homogénéiser les films. La rotation des substrats a été un moyen de garantir que la composition de la surface était homogène.

Le recuit peut provoquer non seulement des modifications au niveau de la structure cristallographique, mais aussi dans la composition de surface. Le premier effet est régi par la teneur relative en Pd, Cu et Au, tandis que le dernier effet est régi par l'atmosphère sous lequel le recuit est effectué. En général, la présence d'oxygène ou d'H₂S favorise une ségrégation de cuivre à la surface, tandis que la présence d'hydrogène favorise la ségrégation du Pd à la surface. Une étude plus détaillée pourrait être faite en utilisant la diffraction des rayons X *in situ* à haute température. En présence de différents gaz (H₂, H₂S, O₂, CO, CO₂, CH₄ ou autres) les modifications en surface pourraient être surveillées par XRD en incidence rasante tout en changeant la température ou la nature du gaz. Les informations ainsi recueillies par XRD pourraient être complétées via d'autres techniques comme l'XPS.

La solubilité et la perméabilité de l'hydrogène ont été étudiées. La teneur en palladium est le facteur clé qui détermine la quantité d'hydrogène qui peut être dissout dans l'alliage. En effet, les alliages les plus riches en Pd étaient également ceux qui ont montré les solubilités de l'hydrogène les plus élevées. Le remplacement de Cu par Au a également augmenté la solubilité de l'hydrogène. Le recuit est généralement nuisible à la solubilité, soit parce qu'elle favorise la transition de phase, en particulier vers la structure bcc, ou à cause de l'augmentation de la taille des cristallites (diminution des joints de grains). En outre, la solubilité dans les phases fcc et bcc est affectée de la même façon par la teneur en palladium. L'introduction d'hydrogène dans l'alliage PdCuAu conduit à l'expansion de volume de la maille cristalline. Pour maintenir l'intégrité mécanique d'une membrane, il est préférable que la solubilité de l'hydrogène soit plus limitée, pour éviter des changements de volume trop importants. Donc, la solubilité plus faible dans la phase bcc serait un avantage par rapport à la phase fcc.

Une nouvelle méthode a été développée pour préparer des membranes à partir de poudres obtenues par broyage mécanique. Cette méthode consiste à presser les poudres en disques qui sont ensuite frittés, laminés à froid, recuits et polis. Les membranes préparées de cette manière montrent des valeurs plus élevées de perméabilité vis-à-vis de l'hydrogène, mais une plus faible sélectivité par rapport aux membranes citées dans la littérature. La perméabilité est également une fonction de la composition des membranes. La perméabilité la plus élevée a été obtenue avec la membrane Pd₄₀Cu₅₃Au₇. Toutefois, la présence de l'or ne semble conférer aucune protection contre

empoisonnement au H₂S. En fait, le H₂S a promu la ségrégation du cuivre à la surface, annulant ainsi tout bénéfice potentiel ayant pu être apporté par l'or. En outre, le NaCl a réagi aussi avec l'H₂S. L'enlèvement de NaCl par extraction aqueuse est faisable avant le pressage. Cependant, il peut induire l'oxydation du cuivre ou du palladium qui risquerait de provoquer la destruction partielle de l'alliage.

D'autres procédés pour la production de membranes à partir de poudres alliées mécaniques pourraient être développés. Le plus intéressant serait l'utilisation de membranes supportées afin de réduire l'épaisseur des membranes. De cette manière, la quantité de matériau d'alliage serait minimisée et, par conséquent, la réduction de coût pourrait être atteinte. Des méthodes telles que le dépôt par pulvérisation à dispersion colloïdale [32], l'application d'une pâte contenant le matériau d'intérêt [33] ou le dépôt par pulvérisation à froid [34] peuvent être utilisées.

Une autre approche intéressante serait de préparer les alliages Pd-bcc qui n'utilisent pas de cuivre. L'alliage Pd₅₀Al₅₀ montre une structure bcc au-dessus de 745°C [35, 36]. Il pourrait être intéressant de vérifier si ces membranes ont un comportement similaire au PdCu bcc en ce qui concerne la perméabilité. À des températures aussi élevées, l'empoisonnement au H₂S est moins problématique pour les alliages PdCu, comme l'ont montré que les études de Morreale et collaborateurs [25].

A1.5 Références

- [1] Ramachandran R, Menon RK. An overview of industrial uses of hydrogen. *International Journal of Hydrogen Energy*. 1998;23:593-8.
- [2] Winter C-J. Hydrogen energy — Abundant, efficient, clean: A debate over the energy-system-of-change. *International Journal of Hydrogen Energy*. 2009;34:S1-S52.
- [3] Ockwig NW, Nenoff TM. Membranes for Hydrogen Separation. *Chemical reviews*. 2007;107:4078-110.
- [4] Nenoff TM, Spontak RJ, Aberg CM. Membranes for Hydrogen Purification: An Important Step toward a Hydrogen-Based Economy. *MRS Bulletin*. 2006;31:735-44.
- [5] McKinley DL. Metal alloy for hydrogen separation and purification. United States: US patent 3,350,845; 1967.
- [6] Howard BH, Killmeyer RP, Rothenberger KS, Cugini AV, Morreale BD, Enick RM, et al. Hydrogen permeance of palladium-copper alloy membranes over a wide range of temperatures and pressures. *Journal of Membrane Science*. 2004;241:207-18.
- [7] Honrado Guerreiro B, Martin MH, Roué L, Guay D. Hydrogen solubility in PdCuAu alloy thin films prepared by electrodeposition. *International Journal of Hydrogen Energy*. 2014;39:3487-97.
- [8] Sakamoto Y, Ishimaru N, Mukai Y. Thermodynamics of Solution of Hydrogen in Pd-Cu and Pd-Cu-Au Solid Solution Alloys. *Berichte der Bunsen-gesellschaft fuer physikalische Chemie*. 1991;95:680-8.

- [9] Peters TA, Kaleta T, Stange M, Bredesen R. Development of thin binary and ternary Pd-based alloy membranes for use in hydrogen production. *Journal of Membrane Science*. 2011;383:124-34.
- [10] Tarditi AM, Imhoff C, Braun F, Miller JB, Gellman AJ, Cornaglia L. PdCuAu ternary alloy membranes: Hydrogen permeation properties in the presence of H₂S. *Journal of Membrane Science*. 2015;479:246-55.
- [11] Semidey-Flecha L, Ling C, Sholl DS. Detailed first-principles models of hydrogen permeation through PdCu-based ternary alloys. *Journal of Membrane Science*. 2010;362:384-92.
- [12] Coulter KE, Way JD, Gade SK, Chaudhari S, Sholl DS, Semidey-Flecha L. Predicting, Fabricating, and Permeability Testing of Free-Standing Ternary Palladium-Copper-Gold Membranes for Hydrogen Separation. *Journal of Physical Chemistry C*. 2010;114:17173-80.
- [13] Fletcher S. PhD Thesis:Thin Film Palladium-Yttrium Membranes for Hydrogen Separation. Birmingham: The University of Birmingham; 2009.
- [14] Kleperis J, Wójcik G, Czerwinski A, Skowronski J, Kopczyk M, Beltowska-Brzezinska M. Electrochemical behavior of metal hydrides. *Journal of Solid State Electrochemistry*. 2001;5:229-49.
- [15] Birry L, Lasia A. Effect of crystal violet on the kinetics of H sorption into Pd. *Electrochimica Acta*. 2006;51:3356-64.
- [16] Allemand M, Martin MH, Reyter D, Roué L, Guay D, Andrei C, et al. Synthesis of Cu-Pd alloy thin films by co-electrodeposition. *Electrochimica Acta*. 2011;56:7397-403.

- [17] Plantin P, Thomann AL, Brault P, Renault PO, Laaroussi S, Goudeau P, et al. Oscillating composition of Fe–W alloy thin films grown by magnetron co-sputtering. *Surface and Coatings Technology*. 2007;201:7115-21.
- [18] Ramos AS, Vieira MT. Intermetallic compound formation in Pd/Al multilayer thin films. *Intermetallics*. 2012;25:70-4.
- [19] Adams BD, Wu G, Nigro S, Chen A. Facile Synthesis of Pd-Cd Nanostructures with High Capacity for Hydrogen Storage. *Journal of the American Chemical Society*. 2009;131:6930-1.
- [20] Tsai Y-C, Lin C-C, Lin W-L, Wang J-H, Chen S-Y, Lin P, et al. Palladium based cermet composite for hydrogen separation at elevated temperature. *Journal of Power Sources*. 2015;274:965-70.
- [21] Mckinley DL. Method for hydrogen separation and purification. United States: US Patent 3,439,474; 1969.
- [22] Subramanian PR, Laughlin DE. Cu-Pd (Copper-Palladium). *Journal of Phase Equilibria*. 1991;12:231-43.
- [23] Tarditi AM, Braun F, Cornaglia LM. Novel PdAgCu ternary alloy: Hydrogen permeation and surface properties. *Applied Surface Science*. 2011;257:6626-35.
- [24] O'Brien CP, Howard BH, Miller JB, Morreale BD, Gellman AJ. Inhibition of hydrogen transport through Pd and Pd₄₇Cu₅₃ membranes by H₂S at 350°C. *Journal of Membrane Science*. 2010;349:380-4.
- [25] Morreale B. Effect of hydrogen-sulfide on the hydrogen permeance of palladium-copper alloys at elevated temperatures. *Journal of Membrane Science*. 2004;241:219-24.

- [26] Braun F, Tarditi AM, Miller JB, Cornaglia LM. Pd-based binary and ternary alloy membranes: Morphological and perm-selective characterization in the presence of H₂S. *Journal of Membrane Science*. 2014;450:299-307.
- [27] Mundschau MV, Xie X, Evenson Iv CR, Sammells AF. Dense inorganic membranes for production of hydrogen from methane and coal with carbon dioxide sequestration. *Catal Today*. 2006;118:12-23.
- [28] Braun F, Miller JB, Gellman AJ, Tarditi AM, Fleutot B, Kondratyuk P, et al. PdAgAu alloy with high resistance to corrosion by H₂S. *International Journal of Hydrogen Energy*. 2012;37:18547-55.
- [29] O'Brien CP, Gellman AJ, Morreale BD, Miller JB. The hydrogen permeability of Pd₄S. *Journal of Membrane Science*. 2011;371:263-7.
- [30] Galipaud J, Martin MH, Roué L, Guay D. Measurement of Hydrogen Solubility in Pd_xCu_{100-x} Thin Films Prepared by Pulsed Laser Deposition: An Electrochemical in Situ X-Ray Diffraction Analysis. *The Journal of Physical Chemistry C*. 2013;117:2688-98.
- [31] Denton A, Ashcroft N. Vegard's law. *Physical Review A*. 1991;43:3161-4.
- [32] Lee TH, Park CY, Lee G, Dorris SE, Balachandran U. Hydrogen transport properties of palladium film prepared by colloidal spray deposition. *Journal of Membrane Science*. 2012;415-416:199-204.
- [33] Balachandran U, Lee TH, Park CY, Emerson JE, Picciolo JJ, Dorris SE. Dense cermet membranes for hydrogen separation. *Separation and Purification Technology*. 2014;121:54-9.
- [34] Goupil G, Jucken S, Poirier D, Legoux JG, Irissou E, Davis B, et al. Cold sprayed Cu-Ni-Fe anode for Al production. *Corros Sci*. 2015;90:259-65.

[35] Hume-Rothery W. The platinum metals and their alloys *Platinum Metals Review*. 1966;10:94-100.

[36] Grushko B. Again regarding the Al–Pd phase diagram. *Journal of Alloys and Compounds*. 2013;557:102-11.